

**Hybridization of Electrochemical Energy Storage:
Nanohybrid Materials and Hybrid Cell Architectures
for High Energy, Power, and Stability**

Dissertation
zur Erlangung des Grades
des Doktors der Naturwissenschaften
der Naturwissenschaftlich-Technischen Fakultät
der Universität des Saarlandes

von
Simon Fleischmann

Saarbrücken

2018

Tag des Kolloquiums: 30.11.2018

Dekan: Prof. Dr. G. Kickelbick

Berichterstatter: Prof. Dr. V. Presser

PD Dr.-Ing. G. Falk

Prof. Dr.-Ing. C. Gachot

Vorsitz: Prof. Dr. G. Kickelbick

Akad. Mitarbeiter: Dr.-Ing. F. Aubertin

Table of contents

1 Motivation	1
2 Theoretical basis and state-of-the-art	3
2.1 Overview of electrochemical energy storage	3
2.2 Electrical double-layer capacitors	4
2.2.1 Setup and mechanism	4
2.2.2 Electrode materials	5
2.2.3 Electrolytes	7
2.3 Batteries	9
2.3.1 Overview	9
2.3.2 Lithium-ion batteries	10
2.4 Pseudocapacitance	13
2.4.1 Classification of pseudocapacitive materials	13
2.4.2 Developing pseudocapacitance in materials	15
2.4.3 Kinetic analysis of pseudocapacitive materials	16
2.5 Hybrid electrochemical energy storage	18
2.5.1 Hybrid materials for EES	19
2.5.2 Hybrid supercapacitor devices	20
2.6 Atomic layer deposition	24
2.6.1 Working principle	24
2.6.2 Applications	27
3 Outline	29
4 Results and Discussion	33
4.1	34
Enhanced electrochemical energy storage by nanoscopic decoration of endohedral and exohedral carbon with vanadium oxide via atomic layer deposition	34
4.2	54
Tailored mesoporous carbon/vanadium pentoxide hybrid electrodes for high power pseudocapacitive lithium and sodium intercalation	54
4.3	68
Tuning pseudocapacitive and battery-like lithium intercalation in vanadium dioxide/carbon onion hybrids for asymmetric supercapacitor anodes	68
4.4	88
Design of carbon/metal oxide hybrids for electrochemical energy storage	88
4.5	102

Vanadia–titania multilayer nanodecoration of carbon onions via atomic layer deposition for high performance electrochemical energy storage	102
4.6.....	116
Atomic layer deposited molybdenum oxide / carbon nanotube hybrid electrodes: Influence of crystal structure on lithium-ion capacitor performance	116
4.7	130
High voltage asymmetric hybrid supercapacitors using lithium- and sodium-containing ionic liquids.....	130
5 Conclusions and outlook	145
References.....	I

Acknowledgements

First and foremost, I would like to thank my supervisor Prof. Volker Presser who gave me the opportunity to work on my PhD thesis in the Energy Materials Group at the INM - Leibniz Institute for New Materials. Ever since I started in the group as a student intern in 2014, I enjoyed his exceptional support in every scientific or personal situation. Owing to his continuous trust and guidance, I enjoyed a very interesting and successful time as a PhD student. The thesis was part of the Carbon Metal Oxide Nanohybrid project (CarMON) supported by the Leibniz Association (SAW-2017).

I want to express my appreciation to PD Dr.-Ing. habil. Guido Falk from Saarland University for his efforts to be the second reviewer for my PhD thesis.

During my time at the INM, I had the pleasure to be part of a great institution and get to know a number of incredible people. I want to express my deepest gratitude to all current and former members of the Energy Materials Group, without whom my thesis would not have been possible. My special thanks to Dr. Marco Zeiger, Dr. Nicolas Jäckel, Aura Tolosa, Benjamin Krüner, Anna Schreiber, Pattarachai Srimuk, Öznil Budak, Hwirim Shim, Tobias Dörr, Juhan Lee, Valeria Lemkova, Mathias Widmaier, Dr. Mesut Aslan, Robert Drumm, and Dr. Daniel Weingarth for all the great help and good times inside and outside the laboratory. I also want to thank Prof. Eduard Arzt, head of the INM, for his continuing support.

The work would not have been possible without our excellent collaborators. I want to thank Dr. Angela Kruth and Dr. Antje Quade from the INP Greifswald and Prof. Christina Scheu, Dr. Anna Frank, and Dr. Stefan Hieke from the MPIE Düsseldorf for their support within the CarMON project. I am also grateful for the help and the great discussions with Dr. Lars Borchardt, Desirée Leistenschneider, and Christina Schneidermann from TU Dresden concerning the synthesis and properties of mesoporous carbon materials.

Finally, I would like to say thank you to all the people outside of work who supported me throughout my time as a PhD student. Thanks to all my friends from the 11m2. And most importantly, thank you Mama and Papa for all your unconditional support over the last 28 years.

Zusammenfassung

Der Erfolg der Energiewende hin zu erneuerbaren Energiequellen hängt stark von der Verfügbarkeit von elektrochemischen Energiespeichern ab, welche die derzeitige Lithium-Ionen Batterietechnologie in Leistung und Stabilität übertreffen. Diese Doktorarbeit untersucht die Materialhybridisierung von Kohlenstoffen mit Metalloxiden und die Konstruktion von Hybridzellen, die aus einer kapazitiven und einer Faradayschen Elektrode bestehen. Materialhybridisierung mittels Atomlagenabscheidung erzeugt nanoskopische Schichten von Metalloxiden auf Kohlenstoffsubstraten. Dadurch kann die hohe Kapazität Faradayscher Reaktionen dank der hohen Elektrode-Elektrolyt-Grenzfläche bei erhöhter Leistung abgerufen werden. Die Porosität des Kohlenstoffsubstrats spielt dabei eine entscheidende Rolle; ideale Kohlenstoffe weisen interne Mesoporen (2-50 nm) auf. Hybridzellen können durch den Einsatz dieser Hybridmaterialien als Faradaysche Elektrode verbessert werden. Die Kinetik und das Überpotenzial der Faradayschen Reaktion sind für eine schnelle und effiziente Zellperformanz von entscheidender Bedeutung. Die spezifische Energie von Hybridzellen kann darüber hinaus durch den Einsatz lithium- bzw. natrium-haltiger ionischer Flüssigkeit deutlich erhöht werden. Dieses neuartige Zellkonzept erhöht die maximal zugängliche Zellspannung, das Einsatztemperaturfenster und die Sicherheit der Hybridzelle.

Abstract

A successful transition from fossil to renewable energy sources requires electrochemical energy storage devices that surpass current lithium-ion battery technology in specific power and performance stability. In this PhD thesis, hybrid materials containing carbon and metal oxide components are synthesized, and hybrid cell architectures employing both a Faradaic and a capacitive electrode are explored. For material hybridization, atomic layer deposition is used to deposit nanoscopic layers of metal oxide on carbon substrates. This strategy allows to combine the high capacity of Faradaic reactions with the high power enabled by the large electrode-electrolyte interface. The porosity of the carbon substrate plays a major role in the resulting electrochemical performance; ideal carbon substrates show internal mesopores (2-50 nm). Hybrid supercapacitor devices are optimized by using these hybrid materials as the cell's Faradaic electrode. It is demonstrated that the kinetics and overpotentials of the Faradaic reactions are the determining factors to enable fast and efficient cell performance. Finally, the specific energy of hybrid supercapacitor cells is drastically increased by using lithium- or sodium-containing ionic liquid electrolyte. This novel concept increases the accessible cell voltage, operation temperature window, and safety of the hybrid supercapacitor cell.

1 Motivation

In the Paris Agreement of 2015, members of the United Nations Framework Convention on Climate Change committed to containing the mean global temperature rise below 2 °C, with respect to pre-industrial levels, to prevent "dangerous anthropogenic interference with the climate system".¹ Global warming is, inter alia, leading to rising sea levels, more extreme weather events like strong storms and precipitations, heat waves and droughts, and changes in animal and plant life cycles.²⁻⁴

To limit global warming, each participating country is putting forward nationally determined contributions that will be strengthened every five years, with developed countries being expected to take the most ambitious measures. The main objective is a drastic reduction of greenhouse gas (GHG) emissions, most importantly, of carbon dioxide. The Intergovernmental Panel on Climate Change concluded that the average global temperature is directly linked to the concentration of GHGs in the atmosphere, which had led to a rise of 0.85 °C in average global temperature between 1880 and 2012, when about $1.5 \cdot 10^{12}$ t of anthropogenic CO₂ emission was registered.^{5, 6} Moderate rises in average global temperature are projected to create even more severe regional changes in peak temperatures, particularly over land. A 2 °C rise in global mean temperature is projected to cause, for example, a rise of 3 °C in extreme temperature in the Mediterranean region;⁷ generally, drylands are experiencing more warming than humid lands.⁸ Consequently, even a moderate global temperature rise is projected to lead to more extreme weather events in many regions.⁹

The main source of anthropogenic GHG emissions is the burning of fossil fuels (coal, natural gas, oil) that are primarily used for power generation, mobility, and heating. Hence, a key component for combatting global warming is the transition from fossil fuels to renewable energy sources, like wind and solar power that are abundantly available. The intermittent character of wind and solar, however, leads to severe fluctuations in power output, posing enormous challenges for maintaining grid stability.¹⁰ While power from fossil fuels can be produced on demand, wind and solar power need to be harvested when available, creating a mismatch between the real-time power supply and demand. This creates the need for the construction of a "smart grid", which is relying on the implementation of electrochemical energy storage (EES) devices to buffer resulting fluctuations in a broad range from seconds to hours.^{11, 12} A decarbonization of the transportation sector requires EES technologies that fulfill

the requirements of high energy density (long range) and high power density (fast charging). All these future applications require EES offering a combined high specific energy, power, and cycling stability. Current state-of-the-art lithium-ion battery and supercapacitor technologies, however, cannot satisfy all of these demands, offering either high energy or high power and stability, respectively. Within the context of this PhD thesis, I will explore hybridization aiming to synergistically combine the merits of both technologies. Novel hybrid material design strategies will be explored, and hybrid cell architectures will be developed. Such next-generation hybrid EES technologies can be regarded as particularly significant for maintaining a sustainable planet Earth in the future.

2 Theoretical basis and state-of-the-art

2.1 Overview of electrochemical energy storage

There is a plethora of technologies to store and recover electrical energy, such as pumped hydroelectric energy storage, flywheels, batteries, or capacitors, which greatly differ in their working mechanisms, dimensions, and operational parameters.¹³ Among them, EES devices present today the most promising solution for mobile applications, grid stabilization, and miniaturized electronics.¹⁴ The core component of an EES cell consists of two electrodes immersed in an electrolyte that contains mobile charge carrier species. Depending on the charge storage mechanism (Faradaic or non-Faradaic) and the electrochemical signature (linear charge-voltage profile or clear redox-plateaus) of the cells, two archetypes of EES can be identified. **Supercapacitors** are characterized by a linear, capacitor-like signature between accumulated charge and voltage. When they solely store charge by non-Faradaic processes, they are classified as electrical double-layer capacitors (EDLCs), whereas pseudocapacitive charge storage also involves Faradaic reactions, while maintaining a clearly capacitor-like voltage profile. Charge storage in supercapacitors is usually dominated by surface or near-surface processes close to the interface of electrodes and electrolyte, reducing the kinetic limitations posed by solid-state diffusion and offering high specific power with charging/discharging times of seconds to minutes (**Fig. 1A**).

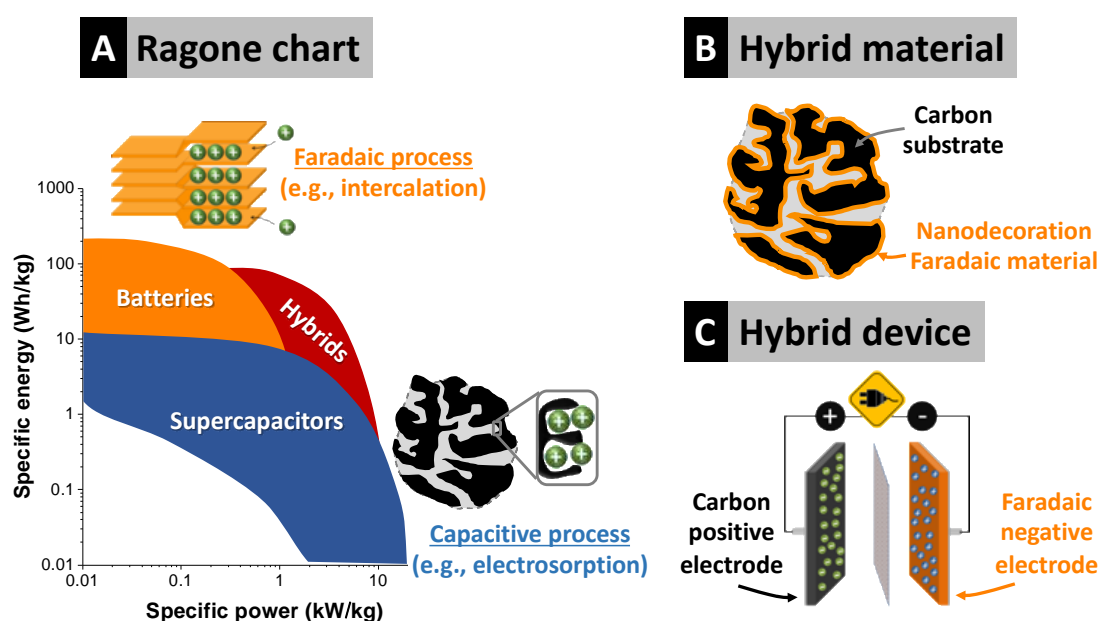


Figure 1: Ragone chart illustrating typical specific energy and power of supercapacitors, batteries, and hybrids thereof (A). Illustration of hybrid material (B), and a hybrid supercapacitor device (C).

Reproduced from Ref. ¹⁵ with permission from John Wiley and Sons.

Batteries store and recover charge by Faradaic reactions within the bulk volume of their electrodes and show non-linear voltage profiles with clear plateaus, where the chemical redox reactions occur. They typically provide high specific energy, but charge transfer kinetics are relatively slow due to sluggish solid-state diffusion processes, yielding limited specific power (**Fig. 1A**).

An optimized EES device combines high specific energy with high specific power ratings. A pathway to this goal is the synergistic combination of elements from both supercapacitor and battery technologies by hybridization.¹⁵ In the following chapters, each supercapacitor and battery technologies are introduced, and design strategies for hybridization both on the materials level (**Fig. 1B**) and on the device level (**Fig. 1C**) are discussed.

2.2 Electrical double-layer capacitors

2.2.1 Setup and mechanism

An EDLC is an EES device that consists of one (or several) pairs of high surface area electrodes immersed in an electrolyte, contacted with a current collector at each electrode, and a porous separator like glass fiber in between the electrodes to prevent short-circuiting (**Fig. 2A**). It stores energy by electrostatic ion adsorption at the polarized interface of the electrode surface and the electrolyte.¹⁶ The electrical double-layer (EDL) is formed by separation of charges, as first described by Helmholtz in 1853,¹⁷ resulting in the capacitance C :

$$C (F) = \frac{Q}{U} \left(\frac{As}{V} \right) = \varepsilon_0 \varepsilon_r \frac{A}{d} \quad (\text{Eq. 2.1})$$

with the accumulated charge Q , applied potential U , (ion accessible) electrode surface area A , interfacial charge separation distance d , and vacuum and electrolyte dielectric constants ε_0 and ε_r , respectively.

The accumulated charge in the EDL is directly proportional to the applied potential; consequently, the capacitance remains constant as the slope of the Q-U-diagram (**Fig. 2B**). The energy E stored in the EDL can be derived from the capacitance and the potential by:

$$E = 1/2 CU^2 = 1/2 QU \quad (\text{Eq. 2.2})$$

It is important to differentiate between the capacitance of one EDL and the capacitance of an EDLC device. Since the EDL is formed at each electrode-electrolyte interface, an EDLC cell consists of two EDLs connected in series, resulting in a cell capacitance C_{cell} of:

$$1/C_{cell} = 1/C_+ + 1/C_- \quad (\text{Eq. 2.3})$$

with C_+ and C_- being the capacitance of the EDL at the positive and negative electrode, respectively.

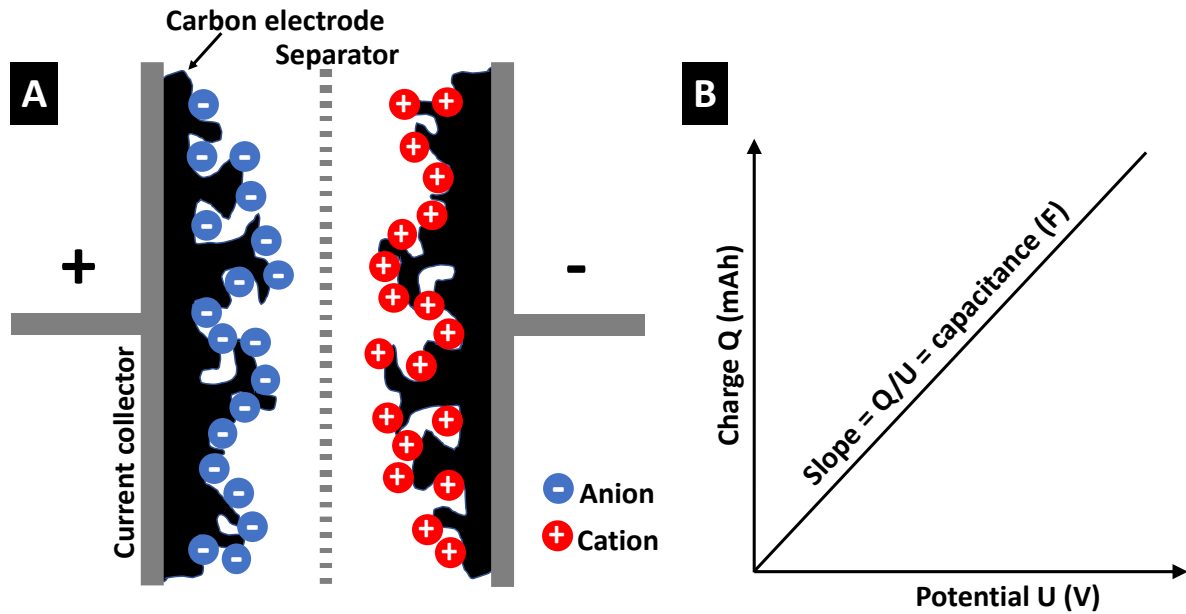


Figure 2: Schematic representation of a charged EDLC cell (A; inspired by Ref.¹²), the characteristic linear relationship between accumulated charge and potential of an EDL.

Assuming equal capacitances at the positive and negative electrodes (symmetrical setup), the cell capacitance is half the capacitance at each electrode in total values. When further normalizing to the total mass of both electrodes, the specific cell capacitance becomes¹²:

$$C_{cell,specific} \left(\frac{F}{g} \right) = 1/4 C_{electrode,specific} \quad (\text{Eq. 2.4})$$

2.2.2 Electrode materials

The formation of the EDL occurs in the absence of electron transfers between the ions of the electrolyte and the electrode, requiring chemically inert behavior of the electrode surface toward the ions in the applied potential range. The capacitance is, in first approximation, directly proportional to the surface area of the electrode, which is why porous materials with high specific surface areas are commonly used as electrodes in EDLCs. These requirements are met best by a variety of carbon materials. Most commonly, EDLC electrodes are based on **activated carbon** with a high intraparticle porosity and specific surface areas up to around 3000 m²/g.^{18, 19} These carbons are produced by carbonization and physicochemical activation

of naturally abundant, carbonaceous precursors, such as biomass.^{20, 21} Using activated carbon powder, electrodes are formed by mixing carbon particles with a binder like polytetrafluoroethylene or polyvinylidene fluoride to form either free-standing electrodes or to coat powder slurries directly onto a current collector. Typically, 2.5-20 mass% of conductive additives like carbon black are further added to increase the electron transport properties of the electrodes.²² The most important feature of activated carbons, which typically consist of particles that are several micrometers large, is their internal porosity while the outer surface area can be neglected. Inside the particles, pores in a broad range of sizes are formed by the activation process. These pores include macropores (>50 nm), mesopores (2-50 nm), and micropores (<2 nm).²³ The biggest contributors to the high specific surface area and pore volume are micropores, often below 1 nm in size, offering very large electrode-electrolyte interfaces. The capacitance of an EDL formed at a typical activated carbon electrode is in the range of 100-200 F/g, depending on the used electrode materials and electrolytes.²⁴

Increased surface areas of porous carbons linearly increase the capacitance only up to a certain point. The maximum capacitance of the EDL is not increased by pores with sizes below the ion size, which are no longer accessible for ion electrosorption.²⁵ The ability to accommodate charges inside the carbon pore walls is limited when carbons exceed a specific surface area of about 1200 m²/g.²⁶ This is due to the finite number of free electrons in non-metallic carbon, leading to a plateau of capacitance for higher surface areas.²⁶ An increase in capacitance was observed by Chmiola et al.²⁷ when the pore size of the carbon is tailored to fit the size of the desolvated electrolyte ion. In this case, a (partial) stripping of the solvation shell was observed that led to increased capacitance.^{27, 28} In contrast, a study of Centeno et al. did not observe this increase for carbon pore sizes between 0.7 nm and 15 nm.²⁹ Part of this controversy may relate to the use of dissimilar models to calculate the specific surface area and pore size distribution and by neglecting the influence of binder materials that may obstruct access to some pores.^{30, 31}

Activated carbons show predominantly internal pores within the particle volume.³²⁻³⁴ The main advantage of these carbons is their large surface area, yielding high capacitances; however, other factors like structural ordering and accessibility for electrolyte ions play an important role for the power handling of the electrode material. On the other hand, many carbon materials show exclusively outer surface area.³²⁻³⁴ Among them, carbon nanomaterials like graphene,^{35, 36} carbon onions,³⁷⁻³⁹ or carbon nanotubes^{40, 41} have attracted significant

interest for their higher electrical conductivity and easier access to the surface compared to activated carbons. This enables an increased power handling ability compared to activated carbons, but the specific surface area of carbons with outer surface area is mostly well below 1000 m²/g and limits the maximum capacitance. Carbon onions were demonstrated to offer a power handling ability close to conventional electrolytic capacitors (three orders of magnitude above activated carbon-based EDLCs) when employed in microelectronics,³⁸ but the capacitance at their EDL is only around 25-50 F/g, depending on the type of carbon onion.^{39, 42}

2.2.3 Electrolytes

Besides the electrode materials, the choice of the electrolyte strongly influences the EDLC performance. First, the electrolyte determines the maximum voltage window of an EDLC that is limited by the electrochemical stability window of the electrolyte.¹² Considering the relation between the square of the voltage and the resulting energy (Eq. 2.2), a higher maximum cell voltage drastically increases the specific energy of an EDLC. Second, the ionic conductivity of an electrolyte has a great effect on the power handling of the EDLC.¹²

Table 1: Summary of selected electrolyte type properties.^{12, 43, 44}

	Electrochemical stability window	Ionic cond. (at 25 °C)	Comments
Aqueous	ca. 1 V (dependent on pH)	ca. 1 S/cm	High power, environmentally friendly, cheap, non-flammable
Organic	ca. 2.7 V	15-60 mS/cm	Best compromise of stability and conductivity, flammable, toxic, requires water-free assembly
Ionic liquid	ca. 3.5-3.6 V	5-15 mS/cm	Highest energy, non-flammable, thermal stability, expensive, requires water-free assembly

An electrolyte usually consists of an organic or inorganic salt dissolved in a solvent, but there are also solvent-free electrolytes. Fundamentally, we can differentiate three groups of electrolytes based on the type and presence of a solvent: (1) aqueous electrolytes, (2) organic electrolytes, and (3) ionic liquids. Each type of electrolyte has its advantages and

disadvantages, making the appropriate choice of electrolyte dependent on the desired application. **Table 1** summarizes selected properties of each type of electrolyte.

pH-Neutral **aqueous electrolytes** with dissolved salts like Na_2SO_4 or Li_2SO_4 ,⁴⁵ and acidic or basic solutions like H_2SO_4 or KOH , respectively, are the most attractive choice for high power applications because of their high ionic conductivity. Their relatively cost-attractive, environmentally friendly, and non-flammable character also makes them suitable for large-scale applications. From an industrial point of view, the possibility of cell assembly without the need for component drying and water-free, inert atmospheres is of further economic advantage. The biggest drawback is the narrow electrochemical stability window that is thermodynamically limited to 1.23 V by the dissociation reaction with hydrogen and oxygen evolution reactions at the negative and positive electrodes, respectively. The electrode potential at which the reactions occur depends on the pH value, as illustrated in a Pourbaix diagram. Strategies like manipulating carbon surface functionalities, capitalizing on strong solvation of electrolyte ions, reversible hydrogen sorption at the negative electrode, or adjustment of electrolyte pH have enabled higher cell voltages in aqueous electrolytes up to about 2.2 V.⁴⁶⁻⁴⁸ EES using aqueous electrolytes may play an important role for large-scale, stationary energy storage facilities in the future, where economic factors and non-flammability play a more important role than space or weight restrictions.

The most popular **organic electrolytes** for EDLC applications are propylene carbonate (PC) and acetonitrile (ACN) with dissolved organic salts like tetraethylammonium tetrafluoroborate, which enable comparably high ionic conductivity and cell voltages up to 2.7-2.8 V.¹² Depending on the used salt and solvent, the ionic conductivity shows a maximum at a certain ion concentration, usually 1-2 M.^{12, 49} Though ACN enables higher powers than PC owing to its lower viscosity (0.369 Pa·s compared to 2.513 Pa·s), its low boiling point of 81.6 °C poses severe limitations to high-temperature usage.⁵⁰

Room temperature ionic liquids like N-butyl-N-methyl pyrrolidinium bis(trifluoromethanesulfonyl)imide (PYR₁₄ TFSI) or 1-ethyl-3-methylimidazolium tetrafluoroborate (EMIM BF₄) are salts that are liquid at room temperature and can be used as electrolytes without the addition of a solvent.^{51, 52} They exhibit a large electrochemical stability window up to about 3.6 V, thermal stability with stable operation temperatures of some ionic liquids between -50 °C and more than 100 °C, and a very low volatility.⁵³⁻⁵⁵ Tuning

of the ionic structure/size or changes in ionic liquid composition offer a wide range of possibilities to adjust the electrochemical properties. The size proportion of ionic liquid cations and anions, for example, was shown to influence the mechanism of EDL formation, having impact on the resulting electrode strain.⁵⁶ Especially formulated mixtures of ionic liquids are intensively studied for the possibility of further expansion of the voltage window,⁵⁷ or widening of the temperature range, for example, by eutectic mixtures.⁵⁸ Research related to ionic liquids in energy applications is still a relatively unexplored field and offers countless opportunities for further improvement of performance and safety aspects. Currently, the high prices of ionic liquids with high purity impede their widespread use in commercial applications.

2.3 Batteries

2.3.1 Overview

A battery generally consists of one or several pairs of electrodes, immersed in an ion-conducting electrolyte and kept apart by a separating membrane. Unlike a symmetric EDLC with two activated carbon electrodes, a battery cell contains two dissimilar electrodes with different chemical potentials. When connected with a consumer, the electrode with the more negative potential (anode) is oxidized, and electrons flow through the external circuit to the electrode with a more positive potential (cathode) that is reduced.⁵⁹ Simultaneously, ions flow in the reverse direction through the electrolyte. In the case of primary batteries, this reaction is irreversible (within the stable operation window provided by the system), while secondary batteries can be recharged by applying an external voltage that reverses the redox reaction.⁵⁹ The term “anode” is historically defined as the electrode where oxidation occurs, while a reduction reaction takes place at the cathode. In a primary battery, where the redox reaction only occurs in one direction, the nomenclature is appropriate. In secondary batteries, the negative (positive) electrode oxidizes (reduces) during discharging and reduces (oxidizes) during recharging. According to the definition of anode and cathode, the assignment would be dependent on whether the battery is charging or discharging. In the battery community though, the nomenclature is defined for the discharge reaction; hence, the negative electrode of a battery cell is always defined as the anode and the positive electrode as the cathode.

Modern battery research has a more than two centuries old history, starting in 1780 with Luigi Galvani's discovery of contracting frog leg muscles after contacting with iron and copper

plates. The reason was an electron flow through the muscle from the metal with the more negative potential (iron) to the more positive one (copper). Based on this discovery, the first battery, the Voltaic pile, was constructed by Alessandro Volta in 1800 and consisted of alternating piles of copper and zinc, separated by salt water soaked spacers.⁶⁰ Since then, various cell types relying on the same principle of redox reactions between two electrode materials with a chemical potential gradient have been developed, most notably, lead-acid, nickel-cadmium, and nickel-metal hydride secondary batteries. Dominating the market for high-end applications today is the lithium-ion battery, which is based on the insertion of lithium ions into host electrodes. The underlying concept was first presented by M. Stanley Whittingham, demonstrating intercalation of lithium ions into a titanium disulfide host.⁶¹ The first cell containing two intercalation electrodes was presented by the Goodenough group with a lithium cobalt oxide/titanium disulfide electrode couple.⁶² Commercialization of the lithium-ion battery was first realized in 1991 by the Sony Corporation.

2.3.2 Lithium-ion batteries

In a **lithium battery**, lithium ions are reversibly inserted or extracted from the host lattice of an electrode (lithium insertion compound $\text{Li}_x\text{M}_y\text{X}_z$) that undergoes reduction or oxidation, respectively, resulting in electron flow through the external circuit.⁶³ In this process, the insertion compound is used as the positive electrode (cathode), while the anode is metallic lithium (= lithium battery). A crucial step towards practical application was the replacement of the lithium metal anode with a second insertion compound electrode, to avoid detrimental effects of metallic lithium like dendrite formation, passivation layers on lithium and local overheating.⁶³ In the resulting **lithium-ion battery** (LIB), lithium ions are exchanged between two insertion compounds via the so-called rocking-chair principle.⁶³ Today's most common type of LIB consists of a graphite anode and a layered lithium metal oxide cathode (LiMO_2), such as LiCoO_2 or LiNiO_2 , immersed in an organic, lithium salt-containing, mixed carbonate electrolyte (such as 1 M LiPF_6 in ethylene carbonate/dimethyl carbonate, "LP30").⁶⁴ These cells exhibit a high cell voltage of ca. 3.8 V and a specific energy around 150 Wh/kg. A schematic representation of a LIB is given in **Fig. 3**.

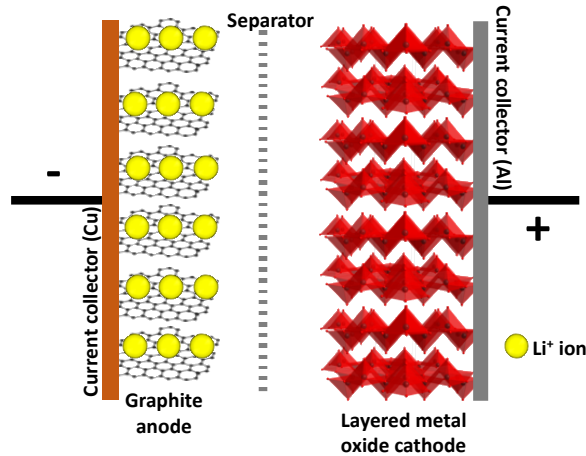
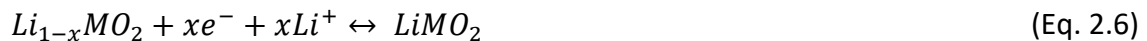


Figure 3: Schematic representation of an LIB with a graphite anode and a layered metal oxide cathode in the charged state.

The chemical reactions occurring at the anode (Eq. 2.5) and cathode (Eq. 2.6) during discharging are given as:



During the first charging cycle, the **graphite** anode is negatively polarized, and lithium ions intercalate between the two-dimensional graphene layers. This multi-step lithiation reaction of graphite yields a theoretic specific capacity of 372 mAh/g and typically occurs at an anode potential below ca. 0.2 V vs. Li^+/Li ,⁶⁵ resulting in a volume expansion of up to 10%.⁶⁶ This potential is below the negative stability limit of the carbonate electrolyte, causing an electrolyte reduction and the formation of the so-called **solid electrolyte interphase (SEI)**.⁶⁷ The SEI needs to be penetrable for lithium ions during further cycling but ideally passivates the anode to block any further electron transport to the electrolyte, preventing further decomposition.⁶⁸ Depending on the used electrolyte and electrode, SEI formation onsets at an anode potential of about 1.0-0.8 V vs. Li^+/Li .⁶⁹ Though the presence of a stable SEI enables long cyclability of the LIB, it presents several unwanted side effects: (1) During SEI formation, lithium ions from the cathode are irreversibly consumed, resulting in loss of active material.⁶⁸ (2) The insulating SEI layer adds an additional impedance, decreasing the lithium ion transfer kinetics.⁶⁷ (3) The SEI increases the risk of metallic lithium dendrite formation on its surface, especially during fast charging.⁷⁰ The latter issue poses serious challenges for the development of batteries for electric vehicles, where fast-charging possibilities are desired. Consequently,

alternative anode materials are in high demand that show an intercalation potential within the electrochemical stability window of the electrolyte.

Among alternative anode materials, **spinel lithium titanate** (LTO, $\text{Li}_4\text{Ti}_5\text{O}_{12}$) has been researched extensively. LTO shows a stable lithiation potential of 1.55 V vs. Li^+/Li , which is within the stability window of most organic electrolytes (**Fig. 4**). It is a so-called zero-strain material where intercalation occurs without notable volume expansion (only 0.2 %), enabling high cycling stability.^{71, 72} Due to the absence of SEI formation, LTO electrodes show an improved safety, especially for fast charging/discharging at low temperature.⁶⁴ The lithiation reaction of LTO is given by:



The reaction involves the transfer of three electrons and yields a specific capacity of 175 mAh/g. Because of its lower specific capacity and higher insertion potential compared to the graphite anode, LIBs with LTO anodes show lower specific energy. The improved power handling, stability, and safety aspects make the material of high interest for a number of applications, mostly in the mobility sector,⁶⁴ for which, among others, the Toshiba Corporation distributes an LIB using LTO under the brand name Super Charge Ion Battery (SCiB™).

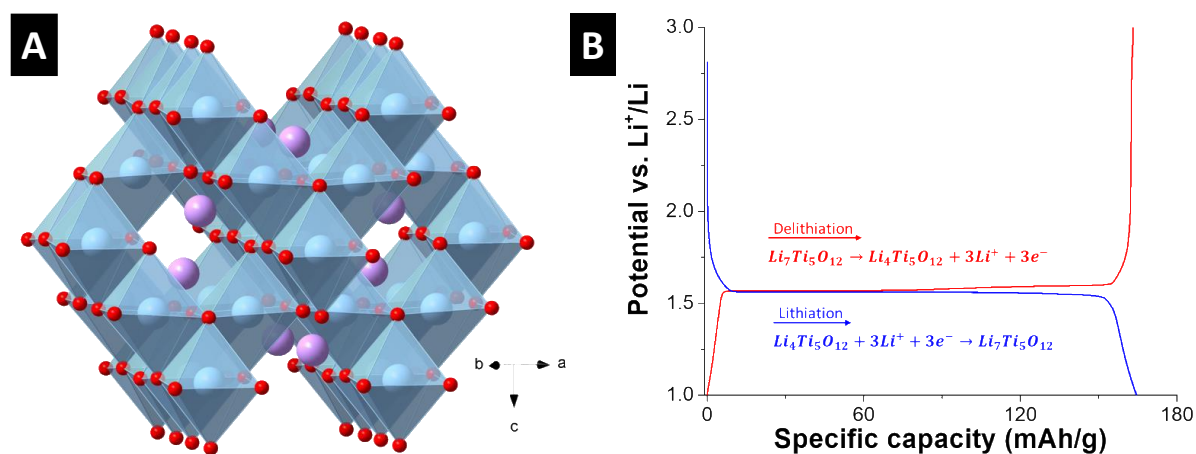


Figure 4: Crystal structure of spinel LTO (A) and characteristic intercalation plateau of galvanostatically cycled LTO electrode vs. Li-metal (B).

On the cathode side, an often-used material is **lithium cobalt oxide** (LiCoO_2), which yields a theoretic capacity of 274 mAh/g upon full delithiation ($\text{Li}_{1-x}\text{CoO}_2$, with $x=1$ for full delithiation). It has a high delithiation potential above 4 V vs. Li^+/Li , low self-discharge and good cycling stability.⁷³ Fully delithiated, the material shows strong lattice distortion leading to unstable cycling behavior, which is why delithiation is usually limited to $x=0.5$ at a cut-off voltage of

4.2 V vs. Li^+/Li .^{73, 74} Consequently, the available capacity is only half, around 137 mAh/g. Furthermore, the material is unstable at temperatures above ca. 200 °C, releasing oxygen that can react with organic electrolytes and cause thermal runaway.⁷³ Doping strategies or replacement of Co with other metals like nickel, manganese, or aluminum can improve the electrode properties; for example, $\text{LiNi}_{0.8}\text{Co}_{0.15}\text{Al}_{0.05}\text{O}_2$ (NCA) yields a larger stable delithiation window up to about 200 mAh/g.⁷³ Cathode materials with higher delithiation potentials like spinel $\text{LiNi}_{0.5}\text{Mn}_{1.5}\text{O}_4$ (ca. 4.75 V vs. Li^+/Li) that would lead to higher cell voltages and energies, pose the problem of electrolyte decomposition above potentials of about 4.3 V vs. Li^+/Li at the cathode.⁶⁴

Besides LIBs employing the rocking-chair principle of reversible lithium intercalation and deintercalation in both electrodes, electrode materials utilizing conversion or alloying reactions have also been explored. The fundamental difference is that the lithiation and delithiation reactions change the entire structure of the electrode materials by breaking their chemical bonds.⁷³ The key advantage of such materials is the very high theoretical capacity, owing to an increase in electron transfers per formula unit. Such battery chemistries involve fluorine or chlorine compounds,⁷³ silicon,⁷⁵ the lithium-sulfur battery⁷⁶ or the lithium-air (O_2) battery with oxygen as a gaseous cathode,⁷⁷ which could potentially increase the specific energy of conventional rocking-chair cells by up to an order of magnitude.⁷⁸ These conversion reactions often show a large overpotential, that is, a potential shift between oxidation and reduction reaction, leading to the decreased energy efficiency of the devices.⁷⁹ A further obstacle towards their practical use is the high volume change of conversion electrodes upon cycling.⁷³

2.4 Pseudocapacitance

2.4.1 Classification of pseudocapacitive materials

The process of charge storage in an electrode can be labeled “pseudocapacitive” when it exhibits a potential development that is similar to a capacitor, that is, a (quasi-)linear relationship between potential and stored charge while utilizing Faradaic charge transfer across the electrode-electrolyte interface (**Fig. 5**).⁸⁰ The Pseudocapacitive behavior is clearly distinguished from battery-like processes, where Faradaic charge transfer occurs mainly at a fixed potential or within a small potential window, showing clear plateaus in the voltage profile. Pseudocapacitance has first been described for RuO_2 ^{81, 82} and MnO_2 ⁸³⁻⁸⁵ in acidic and

neutral aqueous electrolytes, respectively, and for conducting polymers like polyaniline in aqueous H_2SO_4 .⁸⁶ Pseudocapacitive charge storage of these materials is often associated with **surface redox reactions** between the electrode and the ions in the electrolyte. These reactions are typically limited to the materials surfaces, as demonstrated for MnO_2 electrodes in an aqueous Na_2SO_4 electrolyte by observations of manganese binding energy via X-ray photoelectron spectroscopy.⁸⁴ Manganese reduces its oxidation state from Mn(+IV) to Mn(+III) in MnO_2 thin films via surface reactions with Na^+ and H^+ , whereas the oxidation state of Mn(+IV) in MnO_2 bulk electrodes remains constant.⁸⁴ The presence of structural water in RuO_2 ($\text{RuO}_2 \cdot 0.5\text{H}_2\text{O}$) can further increase this pseudocapacitive effect by making bulk reaction sites available for Faradaic reactions by enabling proton conduction.⁸² Pseudocapacitive behavior does not have to be limited to surface redox reactions, but can also involve intercalation reactions in the bulk electrode material. A well-explored material exhibiting this so-called **intercalation pseudocapacitance** is orthorhombic niobium pentoxide (T- Nb_2O_5) in lithium-containing organic electrolyte.^{87,88} Even though the electrochemical signature during intercalation reactions is not perfectly capacitor-like, the intercalation process is widely classified as pseudocapacitive (**Fig. 5**).⁸⁹ Guidelines for the identification of intercalation pseudocapacitance are (i) low dependency of the capacity from rate, (ii) small voltage hysteresis between lithiation and delithiation, and (iii) absence of phase transitions during lithiation that occurs across two-dimensional transport ways in the crystalline network.⁸⁹⁻⁹¹

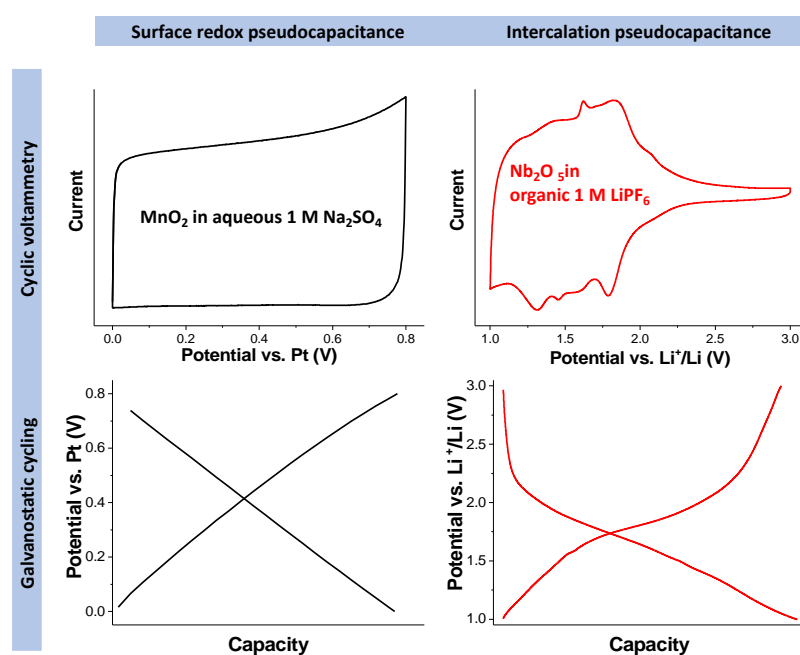


Figure 5: Typical cyclic voltammograms and galvanostatic cycles of surface redox pseudocapacitive (MnO_2) and intercalation pseudocapacitive (T- Nb_2O_5) materials.

More recently, two-dimensional materials like titanium carbide (transition metal carbide known as MXene; e.g., Ti_3C_2) and molybdenum disulfide (transition metal dichalcogenide; e.g., MoS_2) were described to exhibit pseudocapacitive behavior in aqueous NaCl solutions owing to both anion (Cl^-) and cation (Na^+) intercalation in their 2D electrode structure, depending on polarization.^{92,93} Other than the intercalation pseudocapacitance observed in $\text{T-Nb}_2\text{O}_5$, these materials show a distinctly capacitor-like voltage profile. Recent studies on the reversible mass change of Ti_3C_2 -MXene electrodes via electrochemical quartz crystal microbalance suggest a high dependence of its pseudocapacitive charge storage mechanism on the presence of nanoconfined water molecules between the electrode's 2D-sheets.⁹⁴ All these materials show pseudocapacitive properties because of their intrinsic properties and are often referred to as **intrinsic pseudocapacitive** materials.⁹¹

The term “pseudocapacitance” is often misused to describe materials that show clear redox plateaus, leading to misrepresentations of their capacity (for example, by reporting their performance in terms of capacitance).⁹⁵ It can also lead to confusion when describing device performances that show an “intermediate” battery/capacitor-like voltage profile since the voltage profile of a device does not provide adequate information about the nature of the processes at each individual electrode.⁹⁶ Brousse et al. argue that the discussion of pseudocapacitive behavior should be limited to describe processes at individual materials/electrodes (in half-cells), rather than to describe the performance of a full-cell or device.⁹⁶ Nonetheless, recent studies like from Jiang et al. use the term to describe “all pseudocapacitive MXene- RuO_2 asymmetric supercapacitor” devices.⁹⁷ In such a case, when both individual electrodes were shown to exhibit pseudocapacitive charge storage in half-cells, it may be preferred to label the device as a “pseudocapacitor”.

2.4.2 Developing pseudocapacitance in materials

Materials that exhibit battery-like electrochemical properties can show pseudocapacitive properties when they are appropriately nanostructured. This way, most of the crystal sites where intercalation reactions occur are at or near the electrode-electrolyte interface. In that case, the pseudocapacitive properties are not intrinsic to the material, but a result of its structure; the materials are referred to as **extrinsic pseudocapacitive**.^{91, 95} This effect was demonstrated using the battery material LiCoO_2 having crystallite sizes from large bulk crystals down to domains of just 6 nm. It was discovered that the potential profile is battery-like up to

about 15 nm and changes gradually to capacitor-like at 6 nm crystallite size.⁹⁸ The reason for the pseudocapacitive signal is a disordered structure in the near-surface region of the nanoparticle, which is responsible for a large dispersion of intercalation site energies,⁹⁸ resulting in (de-)intercalation reactions distributed over a wide potential window.

Another material that can exhibit pseudocapacitance is vanadium pentoxide (V_2O_5) in its amorphous and nanocrystalline orthorhombic form when it presents a high surface area with a large part of its volume exposed to the electrolyte. This high surface area is obtained by the synthesis of aerogels or deposition on a carbon substrate to further enhance the conductivity of the otherwise insulating metal oxide material.⁹¹ In a study by Boukhalifa et al., atomic layer deposition was used to deposit V_2O_5 onto carbon nanotubes, effectively creating a large electrode-electrolyte interface and still providing sufficient electrical conductivity.⁹⁹ The resulting V_2O_5 /carbon nanotube hybrid materials exhibited pseudocapacitive lithium intercalation behavior with high rate performance due to its nanostructure.⁹⁹ This approach of hybrid material synthesis is a promising strategy to develop extrinsic pseudocapacitance and will be discussed in chapter 2.5.

Intercalation pseudocapacitance has been reported for orthorhombic molybdenum trioxide (α - MoO_3) obtained via reducing to MoO_{3-x} by Kim et al.¹⁰⁰ The latter work demonstrated that the introduction of oxygen vacancies into the α - MoO_3 lattice expanded the interlayer spacing, effectively reducing lithium diffusion limitations. That way, the phase transformation occurring during the first lithiation cycle in α - MoO_3 was suppressed, and lithiation in MoO_{3-x} was possible without any phase transformations, which significantly enhanced the rate handling.¹⁰⁰ The study is of particular interest, as it showcases a further possible avenue besides nanostructuring to introduce extrinsic pseudocapacitance to a material.

2.4.3 Kinetic analysis of pseudocapacitive materials

Pseudocapacitive charge storage offers significantly enhanced power compared to battery-like processes due to reduced kinetic limitations otherwise encountered for solid-state diffusion. Using cycling voltammetry experiments at varying potential sweep rates, the kinetic limitations of the charge storage process can be analyzed (**Fig. 6A**).^{81, 101} The measured current I at a certain potential is a function of the sweep rate ν according to:

$$I = a\nu^b \quad (2.8)$$

with a and b being variables (Fig. 6B).

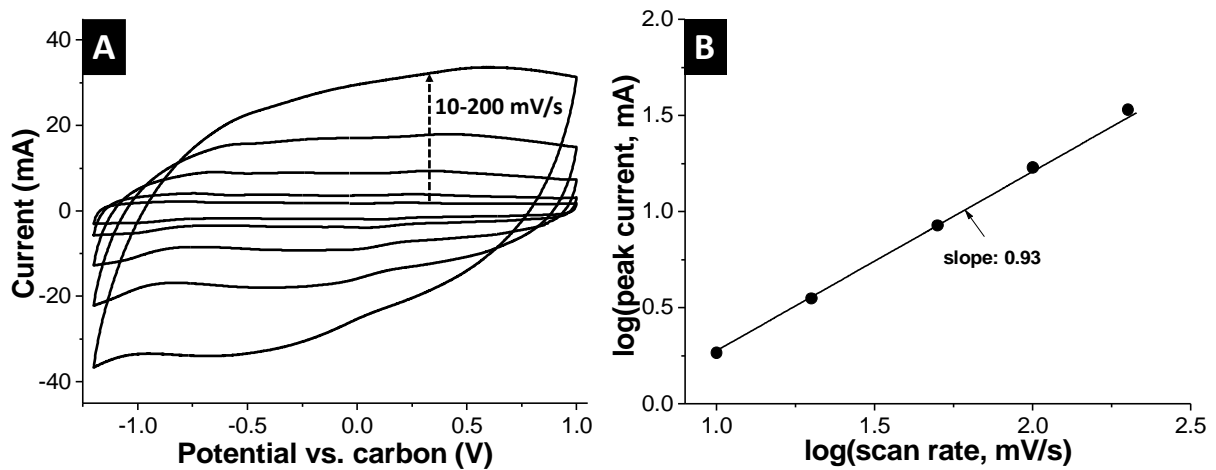


Fig. 6: Iso-potential kinetic analysis ($U = -0.75$ V vs. carbon) of an intercalation pseudocapacitive material (data adapted from Ref. ¹⁰²).

There are two defined conditions for the parameter b : (1) In the case of $b=1$, the current is directly proportional to the sweep rate, which is associated with a perfectly capacitive response. (2) If $b=0.5$, the current response is diffusion controlled and proportional to the square root of v , in accordance with the Randles-Sevcik equation:

$$I = 0.4463((nF)^{3/2}Ac \left(\frac{D}{RT}\right)^{1/2} v^{1/2} \quad (2.9)$$

with n as the number of electrons transferred, Faraday constant F , surface area A , concentration of diffusing species c , its diffusion coefficient D , universal gas constant R and temperature T .¹⁰³ Distinguishing quantitatively between diffusion-controlled and capacitive currents at a fixed potential is possible by splitting the components of equation (2.8) via equation (2.10):^{104, 105}

$$I(U) = k_1v + k_2v^{1/2} \quad (2.10)$$

By determining the parameters k_1 and k_2 at each potential, the individual contributions of diffusion-controlled and capacitive processes to the overall stored charge can be quantitatively separated by this so-called iso-potential method.¹⁰⁵

When applying this kinetic analysis tool, the absence of thermodynamic equilibrium during cyclic voltammetry must be considered. For that reason, the range of probed sweeping rates v_i must be chosen within an appropriate window for the tested system to avoid detrimental side effects influencing the calculations. As pointed out by Anjos et al., even pure EDLCs will

exhibit b -values close to 0.5 if the sweep rate is chosen too high, since effects like ion depletion and Faradaic side reactions pose kinetic limitations (unrelated to solid-state diffusion) to the system.¹⁰³ Another problem with the method is the potential-dependency of many redox reactions from the sweep rate. Opitz et al. recently demonstrated that an unphysical negative pseudocapacitive contribution is obtained ($b < 0.5$), when applying the iso-potential analysis to Nb-TiO₂ and LTO nanoparticles.¹⁰⁶ When calculating with the peak current I at a fixed potential U over various sweeping rates v_i , a shift in peak position or peak width will lead to errors in current contribution assignment.¹⁰⁶ Consequently, the use of iso-potential analysis can be a powerful tool, but correct application within an appropriate range of sweeping rates is critical.

The importance of sweeping rate adjustment is shown by Augustyn et al. for the analysis of T-Nb₂O₅ lithium intercalation pseudocapacitance. Thin film electrodes were investigated using sweep rates between 0.1-20 mV/s.⁸⁹ For faster operation up to 500 mV/s, when Ohmic polarization would significantly affect the results, they applied a cavity microelectrode with a conductive additive to avoid Ohmic losses that would have distorted the analysis.⁸⁹ That way it was possible to demonstrate the absence of kinetic solid-state diffusion limitations in the T-Nb₂O₅ system over a wide range of sweeping rates.

An example for the problematic use of this tool is the choice of unrealistically slow sweeping rates. In the case of very slow sweeping, the system is given enough time to approach thermodynamic equilibrium at each potential, even though solid-state diffusion is taking place. Then, the process can seem capacitor-like (b close to 1), when in fact it is battery-like. Thus, the investigation of a “high-power” pseudocapacitive material should use a range of sweeping rates that fits this description of high power, for example, by charging/discharging within minutes.⁹⁵

2.5 Hybrid electrochemical energy storage

As illustrated in **Fig. 1**, EDLC and battery technologies show distinct electrochemical properties. Combining them by a hybridization approach holds the potential of creating novel materials or cells with high specific energy, power and stability.¹⁰⁷ Synergistic interplay between the individual components can only be obtained if the characteristics detrimental to each technology can be suppressed.¹⁵ In this chapter, the merits of hybrid materials will be introduced (a thorough discussion takes place in the review-type paper in chapter 4.4) and

the working mechanisms of hybrid devices including potential pitfalls will be analyzed according to the state-of-the-art.

2.5.1 Hybrid materials for EES

Faradaic materials are often electrically insulating and require the addition of a conductive additive like carbon black when used as an electrode in an EES cell. In battery research as well as in commercialized products, this is conventionally achieved by a physical mixing process under the addition of a polymer binder material. The individual components of the electrode are connected via particle-particle contacts and held together by the binder. Such an electrode can be defined as a **composite electrode**, as its macroscopic properties are determined by the sum of their components properties (**Fig. 7**).^{15, 108} This approach can cause detrimental effects such as clustering of the individual components that disrupt electrical percolation, increase impedance and can lead to local stresses and degradation.^{15, 109} This effect was described by Kerlau et al., who studied the degradation of NCA/carbon black composite cathode materials by impedance spectroscopy, Raman spectroscopy, and atomic force microscopy.¹⁰⁹ They found that upon cycling, increased local contact resistances change the electron pathways within the composite electrode and lead to non-uniform charge distribution, loss of contact of NCA with the conductive backbone, and electrode degradation.¹⁰⁹

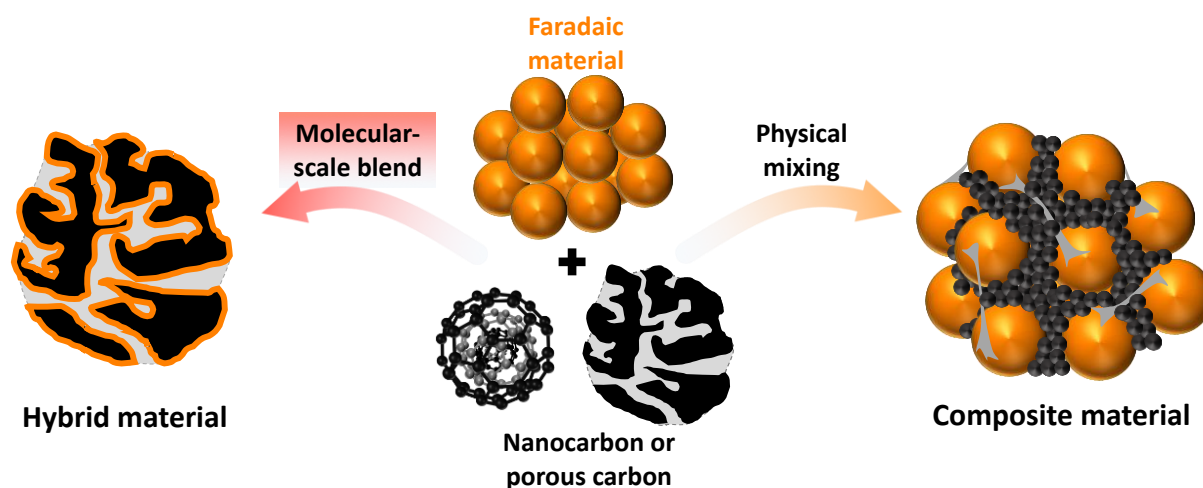


Figure 7: Schematic illustration of electrode synthesis strategies: Hybrid electrode material with chemical bonding between components on a molecular scale (left), physically mixed components yield composite electrode (right). Reproduced from Ref.¹⁵ with permission from John Wiley and Sons.

Consequently, the homogenous distribution of the electrode components is important to ensure stable cycling behavior. This can be accomplished by **material hybridization**, that is,

blending of the Faradaic material and conductive carbon on a molecular scale by creating of chemical bonding between the two phases (**Fig. 7**). That way, a much more stable and intimate interface between the components is created, and charge transfer properties are enhanced.¹⁵ One can use a high surface area carbon component (typical for EDLCs) as a substrate for deposition of Faradaic material which also leads to an additional nanostructuring of the Faradaic material. The latter reduces the intercalation distances to the reactive sites and may introduce pseudocapacitive properties.^{102, 110} Other pathways for hybrid material synthesis include the co-synthesis of both the Faradaic and the conductive phase via conversion or sol-gel reactions (**Fig. 8**).¹⁵ More discussion of this topic is provided in chapter 4.4.

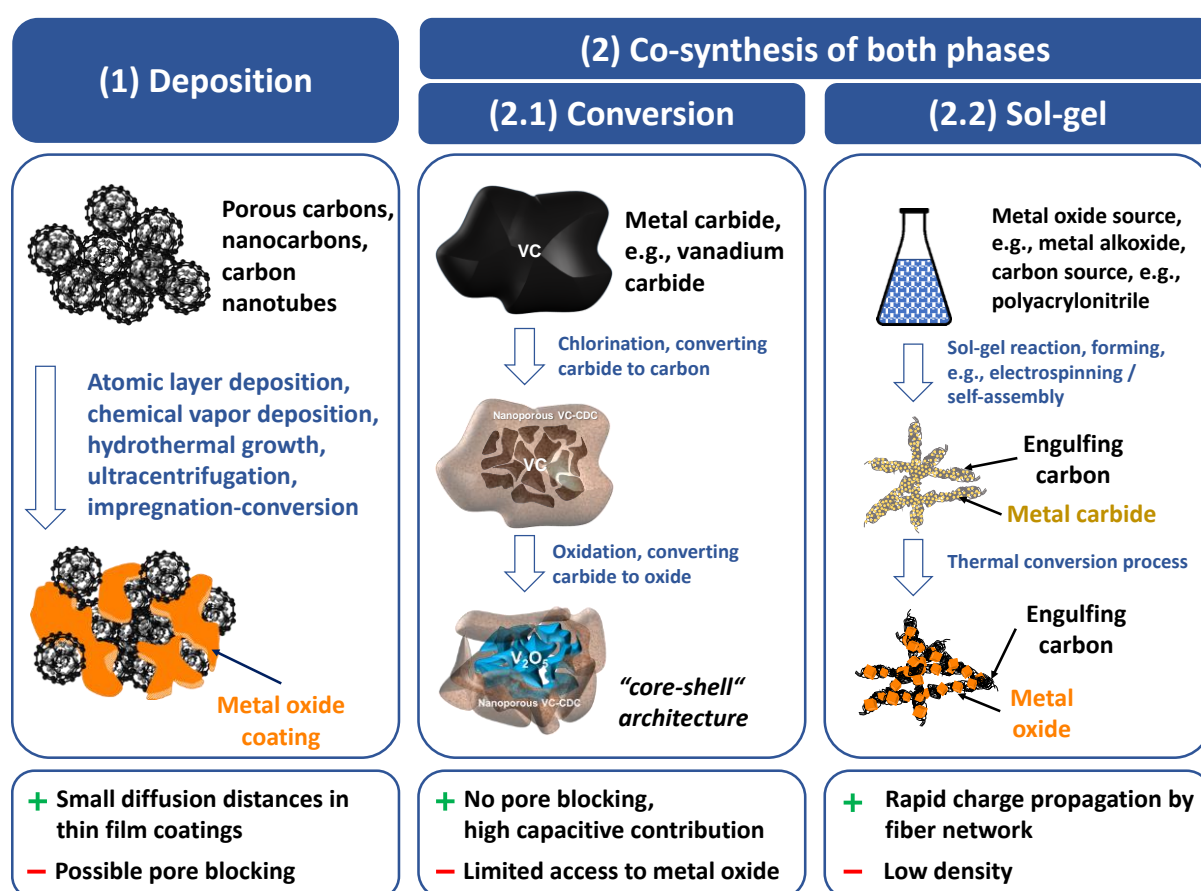


Fig. 8: Schematic illustration of different synthesis strategies for material hybridization. Reproduced from Ref. ¹⁵ with permission from John Wiley and Sons.

2.5.2 Hybrid supercapacitor devices

The merging of EDLC and battery technology on a device level can be achieved by combining two electrodes with different charge storage mechanisms: One electrode facilitating EDL formation and one electrode being capable of Faradaic reactions. These **hybrid**

supercapacitors (HSCs) or asymmetric supercapacitors can achieve a specific energy greater than EDLCs and higher specific power and cycling stability compared to LIBs.¹² The most common type of HSC uses a capacitive activated carbon positive electrode (cathode) and a lithium intercalation host as negative electrode (anode), with LIB materials like graphite and LTO being a common choice.^{111, 112} This kind of hybrid supercapacitor has also become known as a lithium-ion capacitor (LIC).¹¹³ LICs use an organic electrolyte with a dissolved lithium salt that provides lithium ions for intercalation at the anode and anions like PF_6^- or ClO_4^- for EDL formation at the cathode. Apart from these LIC cells, a vast number of different HSC materials and combinations can be found in the literature, such as aqueous manganese oxide/activated carbon cells¹¹⁴ or aqueous nickel hydroxide/porous graphene cells.¹¹⁵ This thesis will focus on the above described LIC type using ion intercalation at the anode, as it appears to be the most promising HSC toward application and has already been commercialized by the company JM Energy.

In an LIC cell, the **anode** operates at a relatively constant intercalation potential, whereas the cathode exhibits a linear potential development. Consequently, the maximum cell voltage that can be achieved is given by the difference between intercalation potential and stability limit of the electrolyte at the activated carbon cathode.⁴³ To maximize the voltage and corresponding energy of the LIC, an anode with a low intercalation potential is beneficial and graphite anodes (intercalation below ca. +0.2 V vs. Li^+/Li) are a common choice.¹² Considering an average potential limit around +4.0 V to +4.2 V vs. Li^+/Li for organic electrolytes at the cathode, LIC cell voltages up to 4 V are feasible for the graphite/AC electrode pair. Like in a LIB, the SEI is formed at the graphite anode during the first cycle consuming lithium ions. In absence of a lithium-containing compound cathode as the lithium source, lithium ions are consumed from the electrolyte, effectively reducing its lithium concentration and decreasing its lithium ion conductivity. To avoid this detrimental effect in an LIC, the graphite anode has to be prelithiated, for example, by using a sacrificial lithium metal electrode in the cell.^{12, 116} This step significantly complicates cell design and research is directed towards facilitating the prelithiation process. Jeżowski et al. recently reported on the use of a sacrificial organic lithium salt (3,4-dihydroxybenzointrile dilithium) that can deliver an appropriate amount of lithium ions in operando during the first charging step, without negatively impacting on the LIC performance.¹¹⁷

Besides the issue of prelithiation, the presence of the SEI at the graphite anode brings the same issues as for LIBs, namely, a reduced power handling ability because of low lithium mobility through the SEI and safety concerns at high rates and low temperatures.⁷⁰ Using LTO is a viable alternative to increase LIC power and safety but its use comes at the cost of reduced cell voltages to around 2.5 V to 3 V in organic electrolytes. A typical voltage profile of an LIC cell using LTO and activated carbon is shown in **Fig. 9**, including the different characteristic potential developments of each electrode upon charging and discharging.

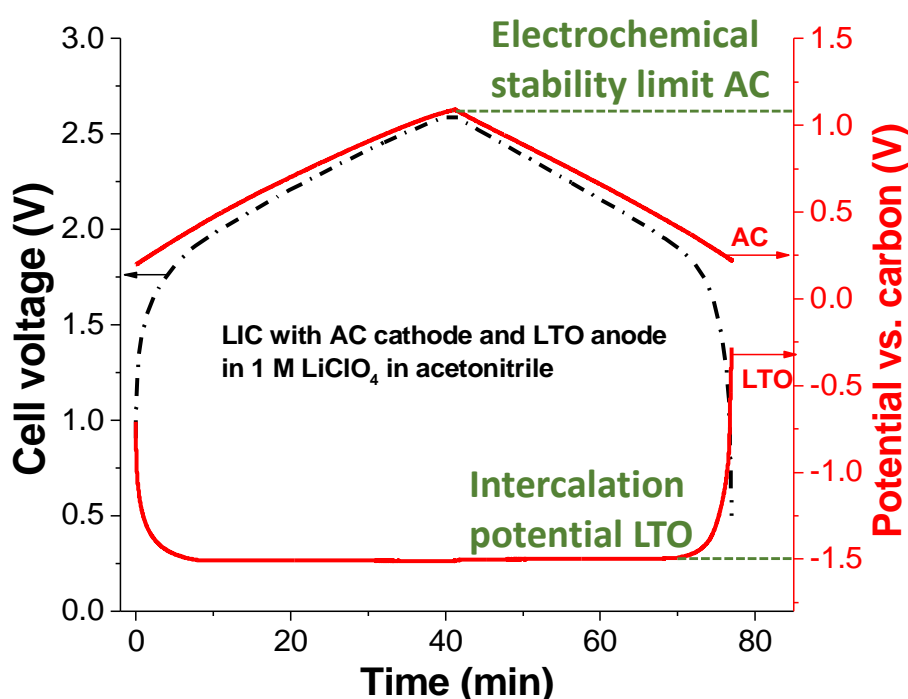


Fig. 9: Voltage profile of LIC using LTO and activated carbon (electrolyte: 1 M LiClO₄ in acetonitrile).

The potential development of each individual electrode is monitored via a spectator reference electrode. Data adapted from Ref. ⁴³.

To determine the maximum possible cell voltage, the electrochemical stability limit of the used electrolyte at the activated carbon **cathode** must be evaluated. A suitable method is the so-called R-value or S-value test (R stands for reversibility, S for stability), as proposed by Xu et al. and Weingarth et al., which is a mathematical tool to determine irreversible currents from parasitic Faradaic contributions during cyclic voltammetry experiments that indicate electrolyte decomposition.^{118, 119} For that purpose, the charge Q_i from the positive and negative currents during sweeping to a certain vertex potential are calculated. To evaluate the positive and negative potential stability limits, the values S_{pos} and S_{neg} are calculated as:

$$S_{pos} = \frac{Q_{pos}}{Q_{neg}} - 1; S_{neg} = \frac{Q_{neg}}{Q_{pos}} - 1 \quad (2.11)$$

According to Xu's criterion, the stability limit is reached at the vertex potential, where this S value is greater than 10%, which indicates Faradaic contributions above 10%.¹¹⁸ Weingarth modified the accuracy of the method by calculating the second derivative of S with the change in vertex potential d^2S/dU^2 .¹¹⁹ By this way, constant background currents that occur at all potentials and leakage currents that linearly increase with the potential are removed from the analysis and the onset of Faradaic decomposition of the electrolyte is detected more precisely.¹¹⁹ The proposed stability criterion is when the S -value surpasses 5%.¹¹⁹

The optimized design of an LIC cell must consider the individual properties of each electrode to synergistically combine them into one device. When current is applied to the cell, the charge is equally distributed among both electrodes; yet, only when both electrodes have the same total capacity, they can both reach a state-of-charge of 100% at the maximum cell voltage. Unequal distribution of electrode capacities leads to reduced maximum cell voltages at which the electrochemical stability limit at either anode or cathode is reached or exceeded. The capacity of the anode (Faradaic) is usually higher than of the cathode (capacitive). Therefore, balancing is achieved by adjusting the masses of both electrodes, usually by "oversizing" the AC cathode mass.¹¹⁴ The optimum mass ratio between cathode mass m_+ and anode mass m_- is:

$$\frac{m_+}{m_-} = \frac{C_-}{C_+} \quad (2.12)$$

with C_- and C_+ being the maximum specific capacity of the anode and cathode, respectively.¹¹⁴

Adjusting the electrode mass ratio according to the maximum specific capacities of each electrode neglects kinetic disparities between the electrodes: The capacitive electrode is characterized by high power capability, whereas the intercalation electrode often shows kinetic limitations at high charge/discharge rates. At increased LIC cycling rates, the capacity retention of the cathode will be higher than of the anode, effectively decreasing the potential window in which the cathode operates and possibly leading the anode to shift outside of its stable potential window if the maximum cell voltage is not properly adjusted. This effect is caused by the different kinetic properties of both charge storage mechanisms and cannot be fully avoided. The effect is showcased for an LIC with activated carbon and LTO electrodes that

is cycled at a slow rate (**Fig. 10A**) and a high rate (**Fig. 10B**). The working potential windows of anode and cathode drastically change as a function of the cycling rate.

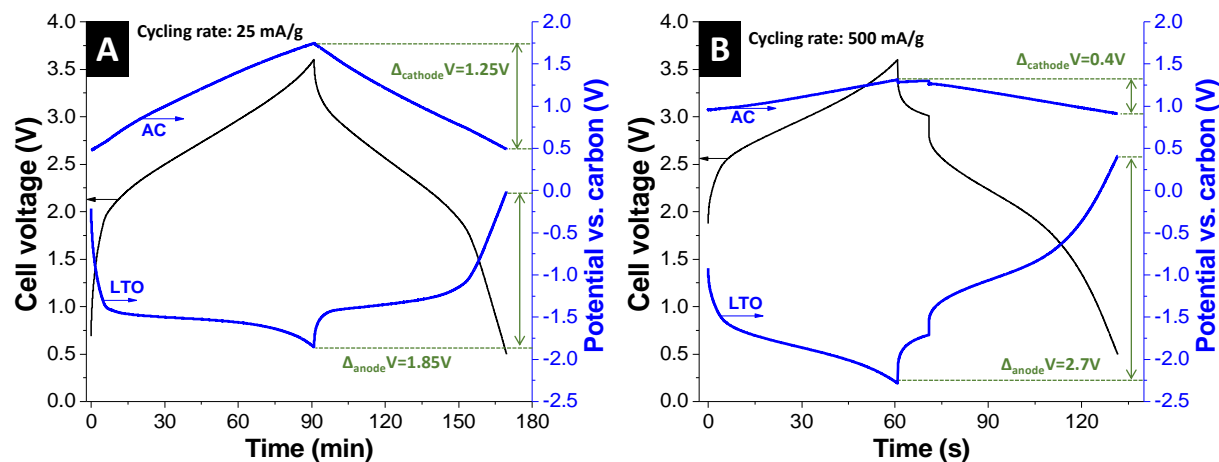


Figure 10: Voltage profile of an LIC with LTO anode and activated carbon cathode (electrolyte: 1 M Li-TFSI in propylpyrrolidinium bis(trifluoromethylsulfonyl)imide) cycled at 25 mA/g (A) and at 500 mA/g (B). The operating potential window of the LTO anode drastically increases at a higher rate because of the kinetic imbalance between the electrodes. Data adapted from Ref.⁴³.

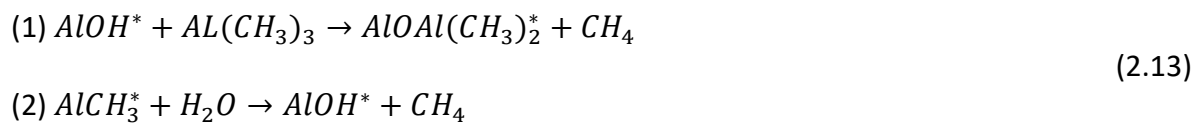
For fundamental research on LICs, the use of a third electrode as a reference is recommended, so that the potential development at anode and cathode can be monitored individually.¹²⁰ In principle, maximization of the usable capacity of the LIC electrodes can only be achieved for one certain cycling current, at which the mass adjustment calculation was conducted. For this reason, large disparities in rate handling ability of anode and cathode should be avoided in LICs; and anode materials with high power capability are in particular demand.¹²¹ Materials exhibiting pseudocapacitive intercalation characteristics with high rate handling behavior are attractive candidates for LIC anodes. As such, hybrid materials have moved in the focus for use as LIC anodes, with niobium pentoxide/porous carbon fiber, molybdenum dioxide/carbon nanotubes, and LTO/porous carbon showing particularly attractive electrochemical performances.^{72, 88, 122}

2.6 Atomic layer deposition

2.6.1 Working principle

Atomic layer deposition (ALD) is a vapor phase coating technology that enables thin film deposition of various materials, including metal oxides,^{123, 124} metal nitrides,^{125, 126} transition or noble metals,^{127, 128} and most recently metal sulfides.¹²⁹⁻¹³¹ It became first known as atomic

layer epitaxy (ALE) and was introduced by Tuomo Suntola in 1974.¹³² ALD is characterized by precise control over film thickness on an Ångström level and high film conformity, owing to its binary, self-limiting reaction cycles.^{133, 134} Every ALD reaction cycle (=ALD-cycle) is divided into two half-cycles. During the **first half-cycle**, a precursor is pulsed into the evacuated reactor and given a certain time to fully adsorb onto the sample surface, forming a self-limiting monolayer, before the reactor is purged with inert gas.¹³⁴ The most common ALD precursors are metal-organic compounds (desired metal with organic ligands) or metal tetrachlorides. The pulse time required for full adsorption and monolayer formation mainly depends on the surface area of the sample. It can range from below one second for flat surfaces to about 20 s on highly porous samples, as is later demonstrated in this thesis. In the **second half-cycle**, a counter-reactant is introduced to the chamber, reacting with the precursor and forming a monolayer of the desired material (**Fig. 11A**).¹³⁴ One of the most frequently studied ALD systems is the deposition of alumina (Al₂O₃), which is considered a model system sharing close similarity to the reaction mechanisms of ALD for other metal oxides.^{123, 133} The surface reactions using metal-organic trimethylaluminum (Al(CH₃)₃) and water take place according to the following mechanism, with the asterisks indicating a surface species:¹³³



Adjusting the number of ALD-cycles will precisely control the film thickness. To ensure the formation of a uniform monolayer on the substrate, the availability of anchoring sites on the substrate surface is critical. Precursor molecules usually adsorb on functional groups or defects, whereas, for example, the inert surface of a graphene layer or carbon nanotube surface is inaccessible for adsorption.^{135, 136} In this case, a pre-functionalization of the substrate must be carried out,¹³⁷ for example, by treatment in acidic media.⁹⁹

In many cases, thin films deposited by ALD exhibit an amorphous structure. When depositing vanadium oxide on carbon nanotubes, Boukhalifa et al. found vanadium present in several oxidation states.⁹⁹ When a certain crystal phase is desired, a post-deposition annealing step may be necessary. For metal oxides, higher oxidation states can be achieved by annealing in oxygen or carbon dioxide atmospheres, whereas argon and hydrogen annealing can lead to a reduction in oxidation state.¹²² Mixed ALD systems containing several metal oxides can form

solid solutions after post-deposition annealing.¹³⁸ A detrimental effect of the annealing step is crystal growth that may cause drastic changes to the film morphology.¹²²

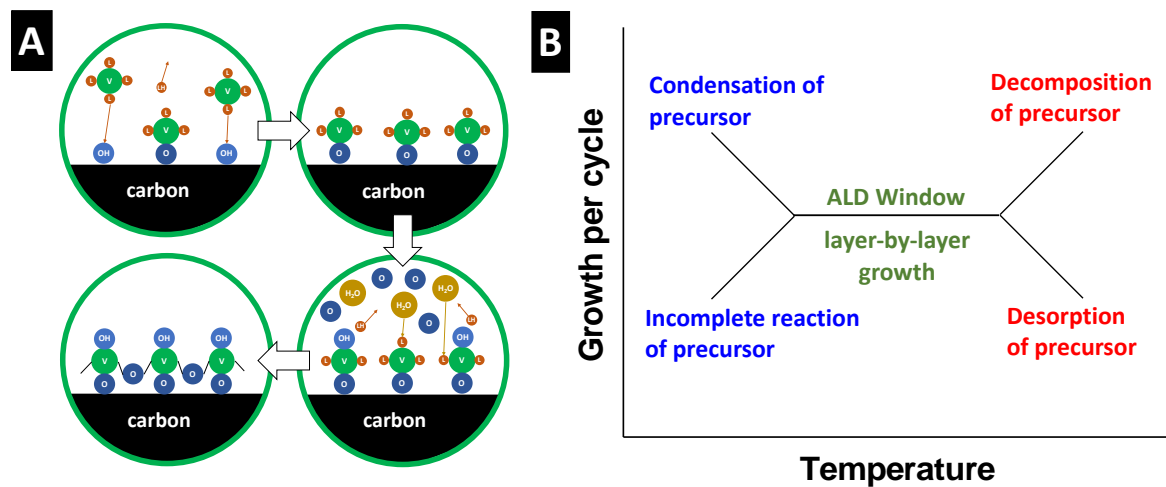


Figure 11: Reaction mechanism of one ALD-cycle for vanadium oxide deposition from vanadium(V)-oxytriisopropoxide precursor and water counter-reactant on carbon substrate (A). ALD window with ideal layer-by-layer growth, non-ideal growth conditions (B, inspired by Ref. ^{133, 139}).

An ideal ALD behavior shows a linear relation between film thickness and number of ALD-cycles. It is only achieved in a certain deposition temperature window, which is mostly found between 50-350 °C, depending on the used precursors (=ALD window). This ALD window must be determined for each pair of precursor and counter-reactant. For that purpose, ALD experiments with in situ quartz crystal microbalance measurements are employed, monitoring the growth per ALD-cycle (GPC, in Å/cycle) in real time.^{140, 141} At temperatures outside the ALD window, unwanted effects like poor reaction kinetics, precursor condensation, precursor desorption, or precursor decomposition impede film growth or lead to non-conformal gas phase deposition (**Fig. 11B**).¹³⁴

ALD processes can be classified depending on the used counter-reactant as thermal ALD or plasma-enhanced ALD (PEALD). Thermal ALD reactions are closely related to chemical vapor deposition (CVD) chemistries but instead of gas phase reactions of the two reactants in CVD, ALD uses the sequential application of the reactants.¹³³ Thereby, the reaction becomes self-limited. For deposition of metal oxides, oxygen sources like H₂O, O₃, O₂, or H₂O₂ are often used as counter-reactants. For metal nitride deposition, NH₃ is most commonly found, and for metal sulfide deposition, H₂S or dimethyl disulfide (CH₃S₂CH₃) have been used.^{129, 130, 133, 134} PEALD is mostly used to produce pure metal coatings. In this case, hydrogen plasma is employed to fully reduce the precursors.¹³³ Oxygen and nitrogen plasma can also be used to

synthesize metal oxides and nitrides, respectively. In most cases, thermal ALD methods are preferred because of less harsh effects on the sample surfaces.¹³⁴

Other thin film coating techniques related to ALD are CVD and physical vapor deposition (PVD). ALD and CVD share many similarities: both are non-line-of-sight deposition techniques that allow for deposition on high aspect ratio and/or porous samples. The main difference between them lies in the sequential character and lower deposition temperature of ALD, offering higher conformality, enhanced access to high aspect ratio structures, and milder sample conditions.¹³⁴ Contrarily, PVD is a line-of-sight deposition technique that vaporizes precursors from a solid or liquid source (=target) by evaporation or sputtering and transports the atoms or molecules on a direct pathway to the substrate via vacuum or plasma streams.¹⁴² Some characteristics of the different deposition techniques are summarized in **Table 2**.

Table 2: Summary of typical synthesis parameters of ALD, CVD, and PVD.^{110, 142-144}

	ALD	CVD	PVD
Deposition type	non-line-of-sight	non-line-of-sight	line-of-sight
Deposition temperature	50-350 °C	≤1200 °C	150-500 °C
Deposition rate	0.1-1 nm/min	1-100 nm/min	50-500 nm/min
Coating of porous substrates	yes	limited	no

2.6.2 Applications

ALD is employed in a variety of fields today, both in research and in industrial applications. Owing to its unique features, ALD can increase both the fundamental understanding of many technologies and further push their performance.¹³⁴ With increasing miniaturization in electronics, the demand for high precision coating techniques is steadily growing. Materials synthesized via ALD are attractive for applications in the fields of energy conversion¹⁴⁵ and energy storage.¹⁴⁴ In photovoltaics, ALD is employed for synthesizing a wide range of cell elements, including absorber materials, buffer layers, or passivating films. Recently, Bush et al. demonstrated a 23.6%-efficient monolithic perovskite/silicon tandem solar cell owing to a tin oxide buffer layer synthesized by ALD. A similar approach was also used by Baena et al.¹⁴⁶ and Albrecht et al.¹⁴⁷, who benefited from the low deposition temperature of ALD to produce

a planar electron selective layer of tin oxide. For fuel cells, ALD is particularly interesting to deposit the electrolyte in solid oxide fuel cells (SOFCs). Shim et al. demonstrate the synthesis of yttria stabilized zirconia (YSZ) by deposition of zirconia and yttria, where adjusting the pulse ratio of Y and Zr precursors allowed to precisely tune the final stoichiometry of the solid electrolyte layer.¹⁴⁸ Especially thin solid electrolyte layers with controlled composition are important to reduce the resistance and therefore allow lower operation temperatures of the SOFC.¹³⁴ In the area of electrochemical energy storage, ALD has been shown to be an effective protective coating for active materials. Jung et al. showed that the deposition of protective alumina coatings on graphite anodes in LIBs significantly improved the performance stability, especially at an elevated temperature of 50 °C.¹⁴⁹ Kozen et al. used ALD to stabilize lithium metal anodes in LIBs by applying a 14 nm protective coating that prevented surface corrosion of lithium.¹⁵⁰ Lithium-sulfur battery technology suffers from low stability and efficiency arising from polysulfide formation at the cathode and their shuttling to the anode during cycling.¹⁵¹ Yu et al. demonstrated that thin protective layers ZnO or MgO on the active sulfur material deposited via ALD can significantly enhance the stability and efficiency by isolating polysulfides within the cathode region.¹⁵¹

ALD is also an attractive tool for the synthesis of hybrid materials, where thin layers of Faradaic material are deposited on a high surface area conductive carbon substrate. That way, a large interface between electrode and electrolyte can be realized, leading to enhanced kinetics. The main challenge is the high aspect ratio of the substrate in form of the carbon porosity, which can lead to the blocking of pores at an increased number of ALD-cycles. Therefore, most literature focusses on ALD coating of carbons with an open porosity and external surfaces, such as carbon nanotubes.⁹⁹ Carbons with internal porosity, like activated carbon or mesoporous carbon, however, offer higher specific surface areas, potentially leading to even larger electrode-electrolyte interfaces.

Within this thesis, the suitability of different forms of carbon with drastically different pore structures will be analyzed. Moreover, ALD of different Faradaic materials (vanadium oxide, titanium oxide, and molybdenum oxide), as well as mixed oxide systems (vanadium-titanium oxide), and different post-deposition thermal treatments will be explored.

3 Outline

The current state-of-the-art in electrochemical energy storage is very advanced concerning electrical double-layer capacitors and rocking-chair lithium-ion batteries. Yet, a combination between both technologies, combining the desired properties of high specific energy, high specific power, and long cyclability remains to be fully realized.

Materials hybridization to combine a high surface area, conductive carbon with a Faradaic material enabling redox reactions, is being heavily explored. Atomic layer deposition is a very promising approach to introduce thin films of metal oxides onto high surface area carbons. That way, large electrode-electrolyte interfaces can be combined with electric conductivity. The state-of-the-art research on ALD hybrid materials focusses on substrates with outer surfaces, such as carbon nanotubes. Carbon nanotubes only offer a comparatively small specific surface area and cannot prevent sintering of the Faradaic material during post-deposition thermal annealing. In the first study (**Chapter 4.1**), carbon substrates with a high internal surface area will be explored by using representatives of carbons with large internal porosity (activated carbon) and carbons with only outer surface (carbon onions) to deposit varying amounts of vanadium oxide via ALD. Based on the gathered knowledge, in a second study (**Chapter 4.2**), a mesoporous carbon substrate will be tailored that combines a large internal surface area with sufficiently large pores for deposition, showing optimized properties when being coated via ALD. Benchmarking of all hybrid materials as LIB electrodes will investigate the impact of carbon substrate porosity on the resulting electrochemical performance (**Fig. 12A**)

In a third study (**Chapter 4.3**), hybrid electrodes of carbon and metal oxides are compared to composite electrodes of the same materials that have been mechanically mixed. Our data provide direct comparison between hybrid materials and comparable, conventionally synthesized electrodes. The influence of hybridization on electrochemical kinetics, voltage profiles, and expansion behavior of the electrodes during electrochemical cycling will be investigated (**Fig. 12B**).

After thoroughly analyzing the impact of carbon porosity on the resulting hybrid material properties, the carbon / metal oxide hybridization approach is conceptualized and set into broader context of literature (**Chapter 4.4**). This study discusses the advances in the field of carbon/metal oxide hybrid materials for electrochemical energy storage applications and is focused on the role of the carbon phase. Different synthesis strategies for the combination of

the components on a nanoscopic scale are presented and the importance of a carefully designed carbon phase is highlighted. The advantages and disadvantages of the synthesis paths are evaluated and possibilities to overcome the latter are proposed (**Fig. 12C**).

In the field of solid oxide fuel cells, it has been shown that ALD is a powerful tool to create mixed metal oxides with a defined composition. However, this approach has never been transferred to the field of electrochemical energy storage. In a further study (**Chapter 4.5**), we will employ this approach to create different mixtures of vanadium oxide and titanium oxide that were stacked in a layer-by-layer manner. By post-deposition annealing, titanium will be built into the vanadium oxide structure, manipulating the lattice spacing and offering changes in lithium intercalation capacity (**Fig. 12D**).

In the next part of the thesis (**Chapter 4.6**), the compilation of hybrid supercapacitor cells will be thoroughly investigated. Molybdenum oxide will be explored as an anode material for lithium-ion capacitors for the first time. Using ALD, carbon nanotube/molybdenum oxide hybrid materials will be synthesized, and different crystal structures of molybdenum oxide will be obtained by post-deposition thermal annealing in different gas atmospheres. Employing different hybrid materials as anodes in LICs will provide insights into the required properties to obtain high device-level performance, which we will be linked conclusively to crystal structure and electrochemical half-cell properties (**Fig. 12E**).

After having thoroughly optimized the electrode materials, an especially formulated electrolyte will be employed to further enhance the performance of hybrid supercapacitor cells (**Chapter 4.7**). We will use ionic liquid electrolytes with dissolved lithium and sodium salts in a hybrid cell with an LTO anode and activated carbon cathode for the first time. Our approach holds promise, as it is aimed to enable a widened stable electrochemical potential window for the cathode, effectively increasing the cell voltage and thereby the energy of the device. Also, the operation temperature window of the hybrid supercapacitor cell can be increased (**Fig. 12F**).

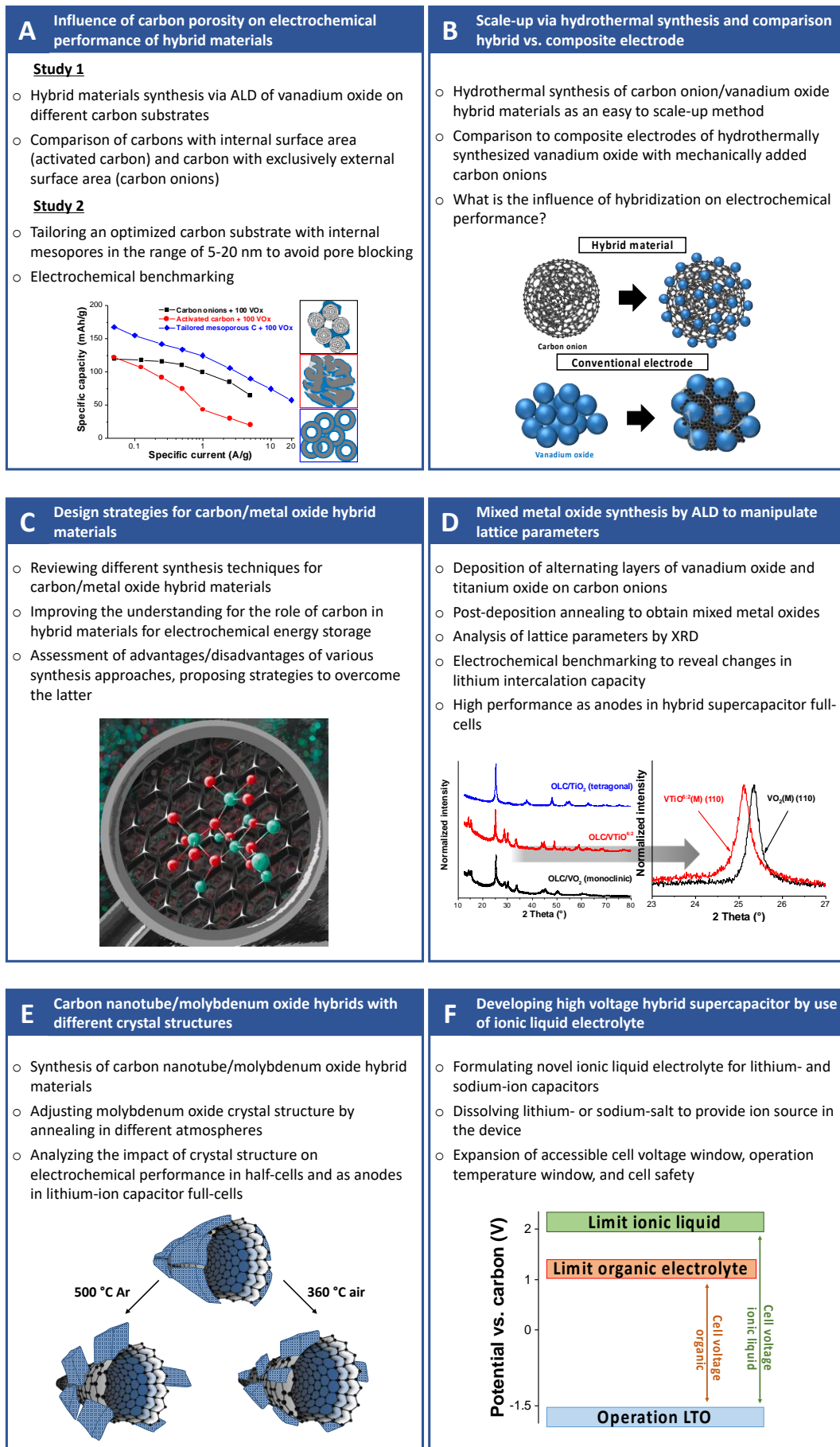


Fig. 12: Chapter overview.

4 Results and Discussion

4.1 Enhanced electrochemical energy storage by nanoscopic decoration of endohedral and exohedral carbon with vanadium oxide via atomic layer deposition

4.2 Tailored mesoporous carbon/vanadium pentoxide hybrid electrodes for high power pseudocapacitive lithium and sodium intercalation

4.3 Tuning pseudocapacitive and battery-like lithium intercalation in vanadium dioxide/carbon onion hybrids for asymmetric supercapacitor anodes

4.4 Design of carbon/metal oxide hybrids for electrochemical energy storage

4.5 Vanadia–titania multilayer nanodecoration of carbon onions via atomic layer deposition for high performance electrochemical energy storage

4.6 Atomic layer deposited molybdenum oxide/carbon nanotube hybrid electrodes: Influence of crystal structure on lithium-ion capacitor performance

4.7 High voltage asymmetric hybrid supercapacitors using lithium- and sodium-containing ionic liquids

4.1 Enhanced electrochemical energy storage by nanoscopic decoration of endohedral and exohedral carbon with vanadium oxide via atomic layer deposition

Simon Fleischmann,^{1,2} Nicolas Jäckel,^{1,2} Marco Zeiger,^{1,2}
Benjamin Krüner,^{1,2} Ingrid Grobelsek,¹ Petr Formanek,³
Soumyadip Choudhury,^{1,3} Daniel Weingarth,¹ Volker Presser^{1,2}

¹ INM - Leibniz Institute for New Materials, 66123 Saarbrücken, Germany

² Department of Materials Science and Engineering, Saarland University, 66123 Saarbrücken, Germany

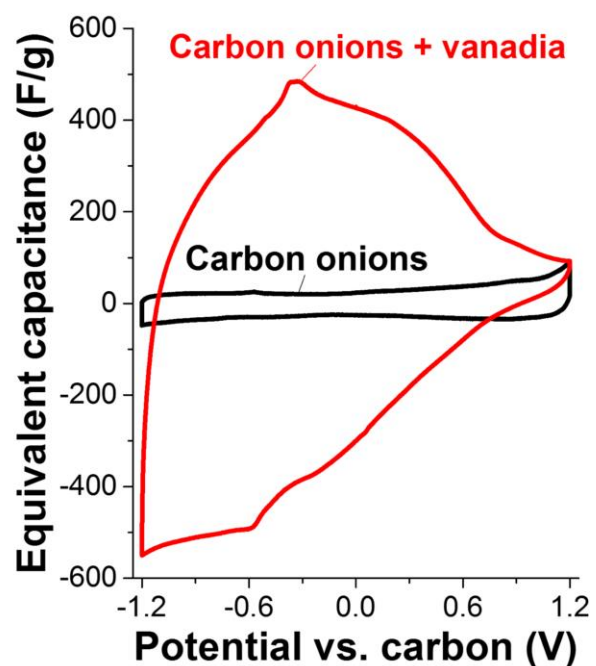
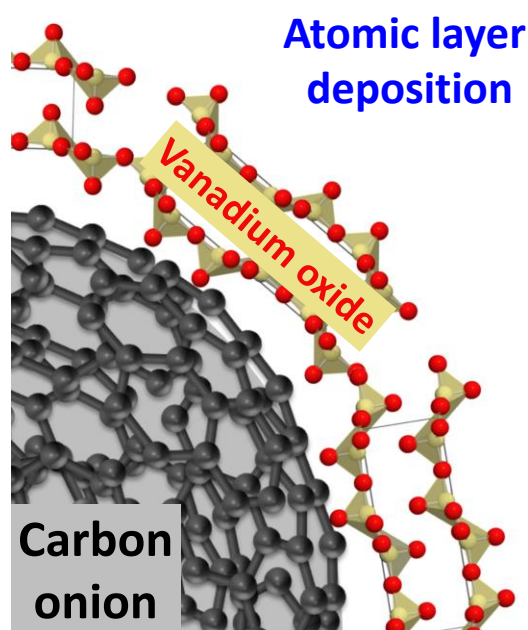
³ Leibniz-Institut für Polymerforschung Dresden e. V., 01069 Dresden, Germany

Citation:

S. Fleischmann, N. Jäckel, M. Zeiger, B. Krüner, I. Grobelsek, P. Formanek, S. Choudhury, D. Weingarth and V. Presser, *Enhanced electrochemical energy storage by nanoscopic decoration of endohedral and exohedral carbon with vanadium oxide via atomic layer deposition*, *Chem. Mater.*, **2016**, 28, 2802-2813. (DOI: 10.1021/acs.chemmater.6b00738)

Own contributions:

Planning, ALD synthesis, X-ray diffraction measurements, Raman measurements, electrochemical measurements, writing.



Enhanced Electrochemical Energy Storage by Nanoscopic Decoration of Endohedral and Exohedral Carbon with Vanadium Oxide via Atomic Layer Deposition

Simon Fleischmann,^{†,‡} Nicolas Jäckel,^{†,‡} Marco Zeiger,^{†,‡} Benjamin Krüner,^{†,‡} Ingrid Grobelsek,[†] Petr Formanek,[§] Soumyadip Choudhury,^{†,§} Daniel Weingarth,[†] and Volker Presser^{*,†,‡}

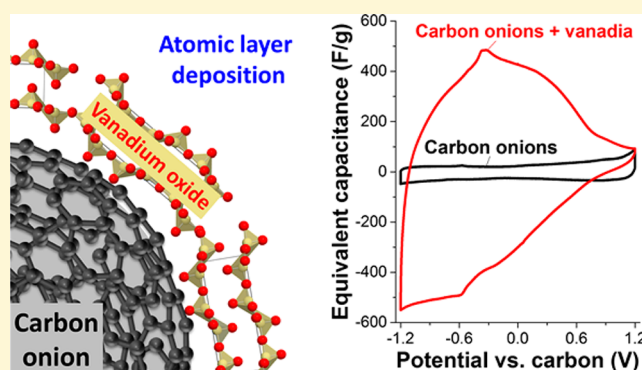
[†]INM - Leibniz Institute for New Materials, 66123 Saarbrücken, Germany

[‡]Department of Materials Science and Engineering, Saarland University, 66123 Saarbrücken, Germany

[§]Leibniz-Institut für Polymerforschung Dresden e. V., 01069 Dresden, Germany

Supporting Information

ABSTRACT: Atomic layer deposition (ALD) is a facile process to decorate carbon surfaces with redox-active nanolayers. This is a particularly attractive route to obtain hybrid electrode materials for high performance electrochemical energy storage applications. Using activated carbon and carbon onions as representatives of substrate materials with large internal or external surface area, respectively, we have studied the enhanced energy storage capacity of vanadium oxide coatings. While the internal porosity of activated carbon readily becomes blocked by obstructing nanopores, carbon onions enable the continued deposition of vanadia within their large interparticle voids. Electrochemical benchmarking in lithium perchlorate in acetonitrile (1 M LiClO₄) showed a maximum capacity of 122 mAh/g when using vanadia coated activated carbon and 129 mAh/g for vanadia coated carbon onions. There is an optimum amount of vanadia between 50 and 65 wt % for both substrates that results in an ideal balance between redox-activity and electrical conductivity of the hybrid electrode. Assembling asymmetric (charge balanced) full-cells, a maximum specific energy of 38 Wh/kg and 29 Wh/kg was found for carbon onions and activated carbon, respectively. The stability of both systems is promising, with a capacity retention of ~85–91% after 7000 cycles for full-cell measurements.



1. INTRODUCTION

Supercapacitors are devices for rapid and efficient electrochemical energy storage,¹ distinguished by high specific power, fast charge and discharge, and long lifetimes. However, supercapacitors suffer from an energy density significantly below state-of-the-art lithium-ion batteries, commonly by an order of magnitude.² The most common variety of supercapacitors, so-called electrical double-layer capacitors (EDLCs), store energy via reversible ion electroadsorption at electrically charged fluid/solid interfaces of high surface area carbon electrodes.³ So far, various carbons and carbon nanomaterials have been extensively studied including activated carbons (ACs),^{4,5} carbon onions (or onion-like carbon, OLC),^{6,7} carbon nanotubes,^{8,9} graphene,^{10,11} carbon nanofibers,^{12,13} and carbon aerogels.¹⁴ The most common group of electrode materials is ACs because of their low cost and high specific surface area (SSA), which can reach up to about 3000 m²/g,^{15,16} enabling specific double-layer capacitances of typically 100–200 F/g (equal to 33–66 mAh/g) in aqueous electrolytes.²

With a common diameter in the micrometer range, the high intraparticle porosity (inner porosity) of AC particles may reduce the high power performance of AC-based supercapacitors due to ion transport limitations.¹⁷ Thus, materials with a large interparticle porosity (outer porosity originating from a nanoscopic primary particle size) are highly attractive, for example, carbon nanotubes, graphene, or carbon onions.^{2,6,18} In particular, carbon onions have been found as promising candidates for high power supercapacitor electrodes. Structurally, carbon onions are small carbon quasi-nanospheres composed of concentrically stacked graphitic shells,¹⁹ usually without inner porosity and surface area values in the range of 200–600 m²/g.²⁰ A facile and scalable synthesis route for carbon onions is the thermal annealing of nanodiamond powders in inert atmosphere or vacuum.²¹ During the annealing process, sp³-hybridized nanodiamond is progressively converted to quasi-spherical sp²-carbon onions, yielding

Received: February 20, 2016

Revised: March 27, 2016

Published: March 28, 2016

particles of about 5–10 nm in diameter.¹⁹ Given the moderate surface area (typically four-times smaller than activated carbon), carbon onions themselves only provide a specific capacitance of about 20–40 F/g (= 7–14 mAh/g) in aqueous electrolytes.⁷ Yet, their electrical conductivity is about one order of magnitude higher than for AC,²² which makes them attractive as electrode materials for high-rate supercapacitors,^{18,22} conductive additive,²³ or substrate for hybrid electrodes employing redox-active materials such as metal oxides,²⁴ electroactive polymers,²⁵ or surface functional groups.²⁶

With the limitation of double-layer capacitance to around 0.1 F/m² (normalized to electrode surface area), the energy storage capacity can be severely enhanced by use of redox-active materials.^{6,27} The resulting devices benefit from fast and reversible redox reactions or intercalation processes between the ions and the surface of the electrode.²⁸ Depending on the charge-vs-voltage profile, redox-active media can be separated in capacitor-like systems (also known as pseudocapacitors; e.g., MnO₂, RuO₂, or MXene)^{29–31} and battery-like systems (with clearly visible redox peaks; e.g., Co(OH)₂, polyaniline, or quinones).^{25,32} Materials enabling Li⁺ intercalation commonly belong to the latter group, for example, vanadium pentoxide (V₂O₅).^{33–35} The distinction between capacitor- or battery-like behavior determines the choice of the most suitable performance metrics; while capacitors and intrinsic pseudocapacitive materials can be characterized by their specific capacitance (unit: F/g), the performance of battery-like devices should be described by means of specific capacity (unit: mAh/g) because of the nonconstant charge-vs-potential relation. For comparison between the two, the use of specific energy (Wh/kg) is preferred.^{36,37}

The implementation of redox-active media to carbon electrodes faces many challenges. The direct use of most redox-active materials is not favorable given their poor electrical conductivity and low charge propagation.^{2,38} Mixtures of conductive materials and redox-active materials, such as metal oxides, are often complicated by the need for small particle sizes and highly homogeneous phase distribution for optimized performance. The final goal is a hybrid electrode of highly conductive substrates decorated with thin layers or small particles of redox-active materials.^{2,39} By this way, the high specific energy of battery-like devices may be matched with a rate handling performance known from capacitor-like systems. For that purpose, carbon nanotubes,^{40–42} carbon onions,^{24,43} and metal nanowires^{44,45} have been investigated, among others, as substrate materials. The outer surface of these materials can be effectively decorated with redox-active materials by vapor deposition techniques like chemical vapor deposition and atomic layer deposition (ALD),^{41,46,47} hydrothermal synthesis,^{24,48} or drop-casting methods.⁴³

ALD is a very versatile method to deposit nanoscale films of metal oxides on substrate surfaces. The process exhibits enhanced control over thickness and conformity of the fabricated coating due to its cyclic and self-limiting character.⁴⁹ Therefore, ALD has emerged as a promising tool to improve the performance of electrochemical devices, especially by decorating carbons with redox-active material, where a so-called nonline-of-sight deposition technique is required.⁵⁰ For example, Boukhalifa et al. coated carbon nanotubes with vanadium oxide via ALD and showed a linear increase in the tube diameter with increasing number of ALD cycles, thereby demonstrating the high conformity of the layer and high controllability of the thickness.⁴¹ The amount of deposited

vanadia strongly influenced the electrochemical performance of the hybrid electrode: for 100 ALD cycles, which corresponded to a layer thickness of about 10 nm, a specific capacitance of 530 F/g (177 mAh/g) in aqueous LiCl electrolyte was measured at a scan rate of 5 mV/s. Yet, for 500 ALD cycles, this value dropped by nearly 90% to about 60 F/g (20 mAh/g). The authors explained this behavior with the limited access of the electrolyte ions to the bulk of the coating and the drop in electrical conductivity with increasing metal oxide content.

Our work has been sparked by the pioneering work, among others, from the Yushin group⁴¹ regarding the highly promising enhancement of electrochemical energy storage capacity by ALD decoration on carbon nanotubes as well as by the most recent work of Daubert et al.,⁴⁷ employing ALD on nanoporous carbons. Here, we present for the first time a comprehensive study on the impact of endohedral (AC) and exohedral (OLC) surface morphology on the ALD growth mechanism and the resulting electrochemical performance. Especially decorating directly free-standing polymer-bound electrodes is highly attractive because of beneficial electrical contacting between the carbon particles and the enhanced creation of an electrically conductive network. For contrast: metal oxide coated particles may increase the electrode resistance because of the high resistance of many redox active materials. Furthermore, vanadia nanocoatings are not fully stable in solvents used for electrode production, which is of no concern when already assembled electrodes are subject to the ALD process. The main issue with employing materials like activated carbon is related to clogging nanopores⁴⁷ in micrometer-sized particles, which may drastically reduce the energy storage capacity and even more severely limit the power performance. Also, it has not yet been established what the actual performance difference will be when comparing materials with high intraparticle porosity versus materials with just external surface area to survey competing effects of number of active sites versus ion transport.

2. EXPERIMENTAL SECTION

2.1. Preparation of Carbon Substrate Electrodes. OLCs were synthesized by thermal annealing of detonation nanodiamond with a diameter of 4–6 nm (NaBond Technologies), as described elsewhere.²⁰ The annealing process of the nanodiamond powder was carried out in a graphite crucible using a water cooled high temperature furnace with tungsten heater (Thermal Technology Inc.) in argon atmosphere at 1700 °C for 1 h (heating/cooling rate: 20 °C/min). Commercial YP-80F (Kuraray Chemicals Co.) was chosen as activated carbon (AC).

To fabricate free-standing carbon electrodes, carbon powder was mixed with 5 wt % (AC) or 10 wt % (carbon onions) of polytetrafluoroethylene binder (PTFE, 60 wt % solution in water, Sigma-Aldrich) and ethanol. The obtained slurry was then rolled to a 50–60 μm thick electrode. Electrodes were dried in a vacuum oven (2 × 10³ Pa) for about 6 h at 120 °C prior to further use. Further information on the electrode fabrication procedure is found in ref 51.

2.2. ALD of Redox-Active Material on Carbon Substrate Electrodes. The coating process was performed with an open-load ALD system (OpAL; Oxford Instruments). The reactor is surrounded by a custom-made inert gas glovebox (M. Braun Inertgas-Systeme) to ensure dry loading of the samples. Vanadium oxide layers were synthesized from vanadium(V)-oxytriisopropoxide (VOTIP; SAFC Hitech) as metalorganic precursor and deionized water vapor (Milli-Q, Merck) as reactant gas. The VOTIP pot was heated to 45 °C, and the gases entered the ALD reactor during successive 20 s dosage steps. After each dosage step, argon was used to purge the reactor for 10 s. At the end of each cycle, the reactor was evacuated for 8 s. The table temperature inside the reactor was kept at 180 °C. The PTFE-bound carbon electrodes were mounted vertically on the heated table so that

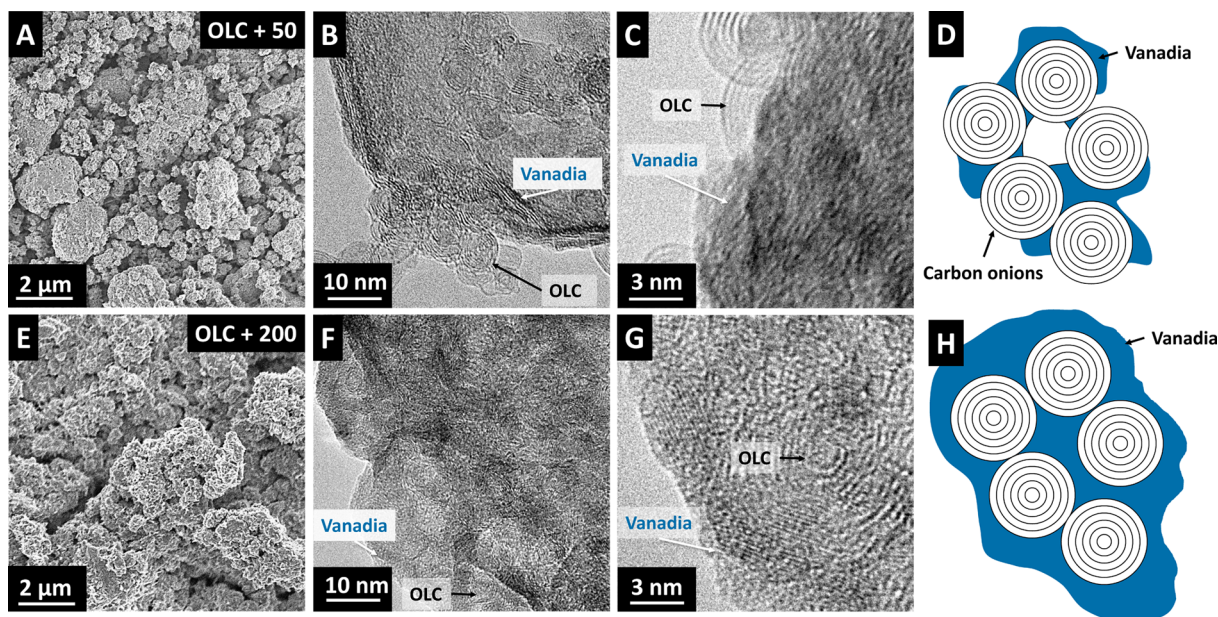


Figure 1. Scanning and transmission electron micrographs of carbon onion hybrid electrodes coated with (A, B, C) 50 ALD cycles and (E, F, G) 200 ALD-cycles as well as (D, H) schematic illustrations of the respective coating structures.

the precursor and reactant gas were able to penetrate the electrodes from both sides. Before the deposition process, the electrodes were treated with oxygen plasma for 5 min to enrich their surfaces in functional groups. By that way, the homogeneity of VOTIP adsorption on the carbon substrate in the first ALD cycle was enhanced. The resulting vanadium oxide coated electrodes are further referred to as carbon/vanadia hybrids. The nomenclature of samples (e.g., OLC +100) means the carbon substrate coated with 100 ALD cycles of vanadia.

In preliminary tests, instead of coating PTFE-bound electrodes, we also surveyed to coat carbon particles instead. However, the metal oxide coatings were not stable when exposed to the ethanol-based electrode preparation. Use of PTFE-bound electrodes was also more beneficial since carbon–carbon contacts were not negatively affected by the coating process and improved scalability was ensured.

2.3. Structural Characterization. Scanning electron microscopy (SEM) was carried out employing a JSM-7500F (JEOL) operating at 3 kV. Electrodes were cut with a razor blade and attached to a steel sample holder by carbon tape to take cross-sectional images. Energy dispersive X-ray (EDX) spectra were recorded at 15 kV with an X-Max-150 (Oxford Instruments) attached to the SEM. Transmission electron microscopy (TEM) was performed with a 2100F system (JEOL) at 200 kV. The samples were prepared by dispersing and sonicating the electrodes in isopropanol and placed on a copper grid with a lacey carbon film (Gatan Inc.).

For X-ray diffraction (XRD) experiments, a D8 Advance XRD (Bruker AXS) diffractometer with a copper X-ray source ($\text{Cu}_{K\alpha}$, 40 kV, 40 mA) and a nickel filter was used. All measurements were performed in a range from 10 – 60° 2θ with a step width of 0.02° 2θ .

Raman spectra were recorded by a Renishaw inVia Raman Microscope employing an Nd:YAG laser with an excitation wavelength of 532 nm. A grating with 2400 lines/mm and a $50\times$ objective were used to reach a spectral resolution of about 1.2 cm^{-1} . The laser spot on the sample was about $1\ \mu\text{m}$ in diameter at a power of 2.5 mW. The acquisition time of each spectrum was 30 s, and 10 accumulations were applied.

Nitrogen gas sorption analysis (GSA) was performed with an Autosorb iQ System (Quantachrome). The PTFE-bound electrodes and the carbon/vanadia hybrid electrodes were degassed at 150°C for 10 h under vacuum (100 Pa) to remove adsorbed water and gas molecules. For the GSA, the variation of relative pressure of liquid nitrogen (-196°C) from 5×10^{-7} to 1.0 occurred in 68 steps. The SSA was calculated with the Brunauer–Emmett–Teller (BET)

equation⁵² in the linear range of the relative pressure between 0.01 and 0.20 using the ASQwin-software. The pore size distribution (PSD), as well as the total pore volume, was calculated by quenched-solid density functional theory (QSDFT).⁵³ A model for slit-shaped pores between 0.56 and 37.5 nm was employed.

Energy filtered imaging (EFTEM) was conducted on Libra 120 transmission electron microscope (Carl Zeiss AG) operated at 120 keV. The specimen was prepared by dispersing vanadium oxide coated carbon onion powder in tetrahydrofuran (THF) followed by placing a drop on a lacey carbon film TEM grid. The TEM grid was dried at 50°C to remove traces of THF before inserting into the TEM instrument.

2.4. Electrochemical Characterization. The electrochemical performance was characterized using a three-electrode setup (half-cell) outlined in more detail in ref 54. The carbon/vanadia hybrids with different vanadia-loadings were employed as working electrodes. The mass of the working electrodes was between 1 and 2 mg. The oversized counter electrode was PTFE-bound AC (YP-80F, Kuraray) with a mass of about 15 mg. As reference electrode, PTFE-bound activated carbon (YP-50F, Kuraray) was chosen.⁵⁵ The current collectors consisted of carbon-coated, 12 mm diameter aluminum foil (Zflo 2653, Exopack Technologies) and 13 mm glass fiber mat as separator (GF/D, Whatman). After assembly, the cells were dried at 120°C in a vacuum oven overnight to remove any moisture. The cells were then electrolyte filled in an inert gas glovebox (MBraun Labmaster 130, O_2 and $\text{H}_2\text{O} < 1\text{ ppm}$) with 1 M LiClO_4 (battery grade, Sigma-Aldrich) in acetonitrile (battery grade, BASF). A two-electrode setup (full-cell) was employed to further characterize hybrid electrodes with 100 ALD cycles. Therefore, both a charge balanced, asymmetric setup with carbon/vanadia and activated carbon (YP-80F, Kuraray) and a symmetric setup with two carbon/vanadia electrodes of the same mass were utilized. In the charge balanced setup, the mass of the activated carbon electrode was chosen as three-fold the mass of carbon/vanadia electrodes. All other assembly steps were chosen equivalently to the three-electrode setup described above.

The electrochemical measurements were carried out with a potentiostat/galvanostat (VSP300, Bio-Logic) and included cyclic voltammetry (CV) and galvanostatic charge/discharge with potential limitation (GCPL). Cyclic voltammograms were recorded in a potential window from -1.2 V to $+1.2\text{ V}$ versus YP-50F reference for half-cells and 0 V to $+2.5\text{ V}$ for full-cells, respectively, with scanning rates of 1 mV/s and 10 mV/s . For half-cells, galvanostatic charge/discharge cycling was carried out by between 0 and -1.2 V , for full-

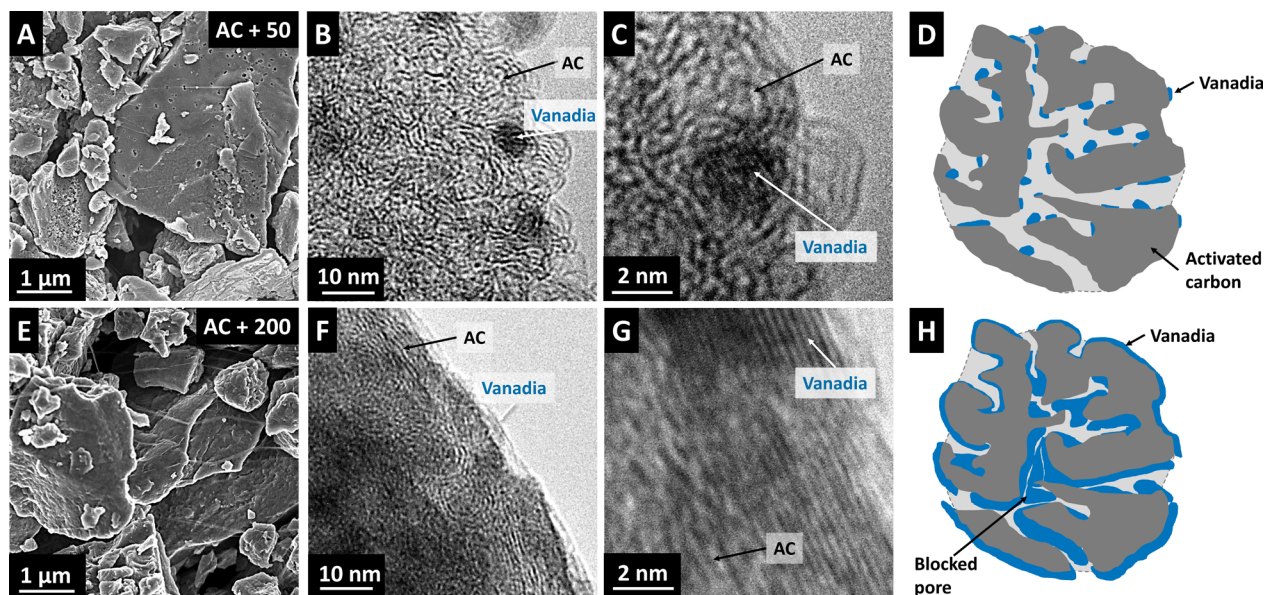


Figure 2. Scanning and transmission electron micrographs of activated carbon hybrid electrodes coated with (A, B, C) 50 ALD cycles and (E, F, G) 200 ALD-cycles as well as (D, H) schematic illustrations of the respective coating structures.

cells between 0 and +2.5 V. The applied specific currents ranged from 0.05–10 A/g, with respect to the active mass of the working electrode in half-cells, or to the active mass of both electrodes in full-cells, respectively (excluding the mass of the PTFE-binder, which differs for AC and carbon onion electrodes). The specific (gravimetric) capacity C_{sp} was calculated from the GCPL data by integration of the discharge current over the discharge time according to eq 1:

$$C_{sp} = \frac{\int_{t_0}^t I dt}{m} \quad (1)$$

where I is the current, t the discharge time, and m the total mass of the working electrode (half-cells) or the total mass of both electrodes (full-cells), respectively.

The specific energy E_{sp} of full-cells was calculated by integration of the voltage over the discharge time by employing eq 2:

$$E_{sp} = \frac{I \int_{t(U_{max})}^{t(U_{min})} U(t) dt}{m} \quad (2)$$

where $U(t)$ is the time-dependent voltage and m the total mass of both electrodes. Long-term stability tests were performed in half-cells by charge/discharge from −1.2 to 0 V with a specific current of 1.0 A/g.

3. RESULTS AND DISCUSSION

3.1. Structural Characterization. Carbon onions were derived from detonation nanodiamond (ND) powder by thermal annealing at 1700 °C (see Supporting Information, Figure S1), which caused transformation of the diamond core and amorphous layers of ND to graphitic carbon shells, resulting in carbon onion particles. These particles form agglomerates of up to 2 μm, which are built up by primary aggregates ranging from 10–100 nm in size (see Supporting Information, Figure S2), as has been demonstrated before.²³ The agglomeration of carbon onions during the synthesis is resulting from agglomeration of the precursor, high temperature treatment induced particle–particle sintering, and carbon redistribution processes.⁵⁶ Carbon onion electrodes have been coated with different mass loadings of vanadium oxide, and their surface morphology has been studied via SEM and TEM and is shown in Figure 1. From a macroscopic point of view, no

major structural changes were detected after the ALD process using SEM (Figure 1A,E). As seen from the TEM images in Figure 1, panels B and C and as schematically exemplified in Figure 1, panel D, a partial coverage of carbon onion surfaces with vanadia layers was obtained at a low mass loading after 50 ALD cycles. Sample OLC + 200 (Figure 1F–H) shows a dense particle coating, which exhibits a mixture of crystalline and amorphous vanadia structures. The interparticle space is fully covered by the vanadia coating; hence, there is no observable pore space inside the carbon onion agglomerates. The TEM micrographs show that the growth of vanadia layers on carbon onion particles does not occur in a completely continuous manner on a nanoscopic level. After 50 ALD cycles, the carbon onion particles were only partially coated. This can be explained by the lack of initial adsorption sites for the VOTIP precursor molecules.⁵⁷ As a consequence, small domains of vanadia nucleate distributed over the carbon onion surfaces and start growing. After 200 ALD cycles, these vanadia domains merged, and the surface is more continuously coated. Crystalline vanadia is preferentially found on the outside of agglomerates, while interparticle space inside the agglomerates mostly consists of amorphous vanadia in absence of required space for crystal growth. The distribution of vanadia within the primary particles was evaluated using EFTEM and was found to be relatively homogeneous (Supporting Information, Figure S3). It is demonstrated that vanadia growth occurred mostly inside the agglomerates, filling interparticle space, rather than forming thick layers on the outer surface of carbon onion primary particles.

AC consists of porous and incompletely graphitic carbon particles (Figure 2) with a size distribution between 1 and 5 μm, which is in accordance with data from sedimentation analysis (Supporting Information, Figure S2). The shape of the particles is not uniform and more polygonal compared to the highly spherical and isometric carbon onions. Large macropores of different sizes are readily seen on the surfaces of the particles with electron microscopy (Figure 2A,E). AC exhibits few interparticle contacts, and connections are mainly formed by PTFE-fibers in the electrode. Inside the AC particles that were

coated with 50 ALD cycles, several vanadia domains with a diameter of about 1 nm were detected by TEM (Figure 2B,C), while no vanadia is present outside of these spots. Also, on the outer surface of AC particles, only little coating is visible, indicating a preferential initial adsorption of VOTIP precursor inside the nanopores. These domains inside the AC particles grow with an increasing number of ALD cycles. At higher mass loadings, a rather homogeneous distribution of vanadia in the intraparticle space (Figure 2F,G) is observed. The dense filling is a result of the merging of growing domains.

To examine the coating arrangement fabricated via ALD in the cross-section of the about 50 μm thick, free-standing electrodes, energy dispersive X-ray spectroscopy (EDX) was carried out. As indicated by the homogeneous intensity of oxygen and vanadium element mappings (Supporting Information, Figure S4), a highly uniform distribution of vanadia through the entire electrode thickness was achieved by choosing suitable ALD parameters.

The vanadia loading in the hybrid electrodes was determined by weighing the electrodes prior to and after the ALD process. The relation between the number of ALD cycles and the relative mass gain is illustrated in Figure 3. It is demonstrated

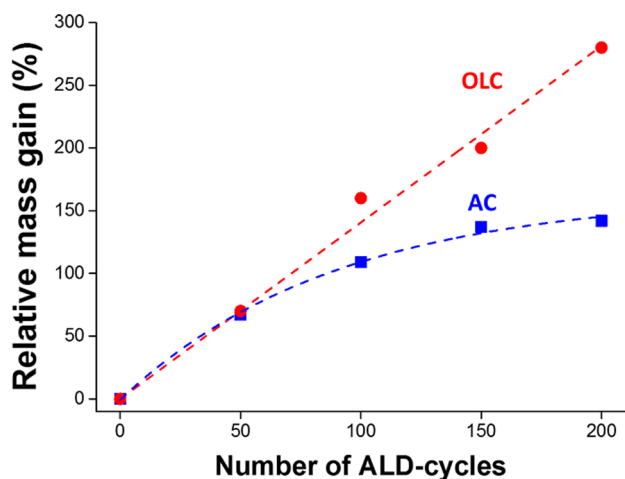


Figure 3. Relative mass gain of OLC and AC hybrid electrodes after the ALD process, with respect to the initial mass.

that the vanadia loading increases linearly with the number of ALD cycles for carbon onion electrodes, with an average mass gain of about 1.4% per cycle, with respect to the initial mass. This linearity demonstrates the highly conformal ALD deposition enabled by choosing a suitable dosage time of 20 s for sufficient diffusion of VOTIP precursor and reaction gas molecules to all available adsorption sites in the OLC electrode and for complete reaction during each ALD cycle. The mass gain for AC converges to a saturation for higher numbers of ALD cycles. The nonlinear mass gain behavior is a consequence of the high inner porosity of AC. With increasing vanadia loading, blocking of subnanometer pores in the micrometer-sized particles reduces the accessible surface area for VOTIP molecules on which to adsorb. Consequently, the mass increase for one ALD cycle decreases from a 1.3% after 50 cycles to 0.7% after 200 cycles.

X-ray diffractograms of the hybrid electrodes (Supporting Information, Figure S5) exhibited very low peak intensities for vanadia, which make the data insufficient for a detailed description of the crystal structure. It can rather be regarded

as an indication for a predominately amorphous/nanocrystalline vanadia of vanadia. To provide a more detailed structural characterization of the coating material, Raman spectroscopy was carried out.

The Raman spectrum of carbon onion hybrid electrodes contains several characteristic vanadia peaks (Figure 4A). The peak corresponding to the relative motions of two V_2O_5 unit cells is located at 142 cm^{-1} ^{58–60} and can be found for sample OLC+50, but for the other three mass loadings of vanadia, the corresponding peak is shifted to 158 cm^{-1} . Similarly, the peak attributed to the $\text{V}=\text{O}$ stretching mode, found in V_2O_5 , V_2O_3 , and VO_2 , is reported at 992 cm^{-1} in literature,^{58–60} which is in accordance to the peak observed for OLC+50. For the other three samples, the peak is shifted to a value of 1024 cm^{-1} . The two peaks at 267 and 406 cm^{-1} , also characteristic for the $\text{V}=\text{O}$ bond,^{58–60} are found in all recorded spectra, with the latter only exhibiting a sharp shape for the OLC+50 sample. The peak occurring at 516 cm^{-1} represents a triply coordinated oxygen bond (present in V_2O_5), and the peak at 704 cm^{-1} a doubly coordinated oxygen bond (present in VO_2 and V_2O_3).^{58–60} The results suggest the presence of vanadia in three oxidation states (III–V), with the fully oxidized and V_2O_5 being the predominant phase, indicated by the peaks with most intensity at 142 , 158 , and 516 cm^{-1} . The spectrum of OLC + 50 is in best accordance with the literature values. For higher vanadia loadings, the peak shifting suggests distortions of the $\text{V}=\text{O}$ bond, as have been described in literature for V_2O_5 .^{58,61}

The Raman spectrum of AC hybrid electrodes only exhibits a very low intensity of the characteristic V_2O_5 peak at 142 or 158 cm^{-1} (Figure 4B) as a consequence of the growth of mostly amorphous vanadia in the intraparticle space. The exclusively external surface area of carbon onions provides favorable conditions for crystalline growth of vanadia layers, contrary to the microporous internal surface area of AC particles. Consequently, OLC/vanadia electrodes contain proportionally more crystalline vanadia, therefore showing higher Raman signal intensities.

An analysis of the D- and G-peaks is conducted with baseline-subtracted and D-peak normalized spectra, given in Figure 4, panels C and D. For both carbon materials after coating, a shift of D- and G-peak position to higher vibration frequencies is clearly visible compared to the uncoated carbon materials. Furthermore, the full width at half-maximum (FWHM) of the D-peaks increases by about 20% for all coated electrodes, while the FWHM of G-peaks remains roughly constant (Figure 4E). A decreasing areal intensity ratio of the D- and G-peak (I_D/I_G) is detected for coated carbon onion electrodes, while I_D/I_G increases with higher ALD cycle numbers for coated activated carbon (Figure 4F). The changes in peak position, FWHM, and areal intensity ratio appear to be irrespective of the vanadia loading, as the spectra of all coated electrodes are virtually identical. Thus, we can see that some initial change of the carbon structure of AC and OLC takes place after a few ALD cycles without significant further changes. The reason for this behavior is the formation of the vanadia/carbon interface during the beginning of the coating process. With a higher number of ALD cycles, the layer growth is mostly realized by vanadia/vanadia reactions, which have no impact on the carbon structure. The peak shifting has been described for the G-peak of disordered graphite in literature.^{62,63} While the effect is not observable for pure graphite, the introduction of disorder is linked with a proportionally growing G-peak shifting.⁶² We suspect the observed carbon disordering of

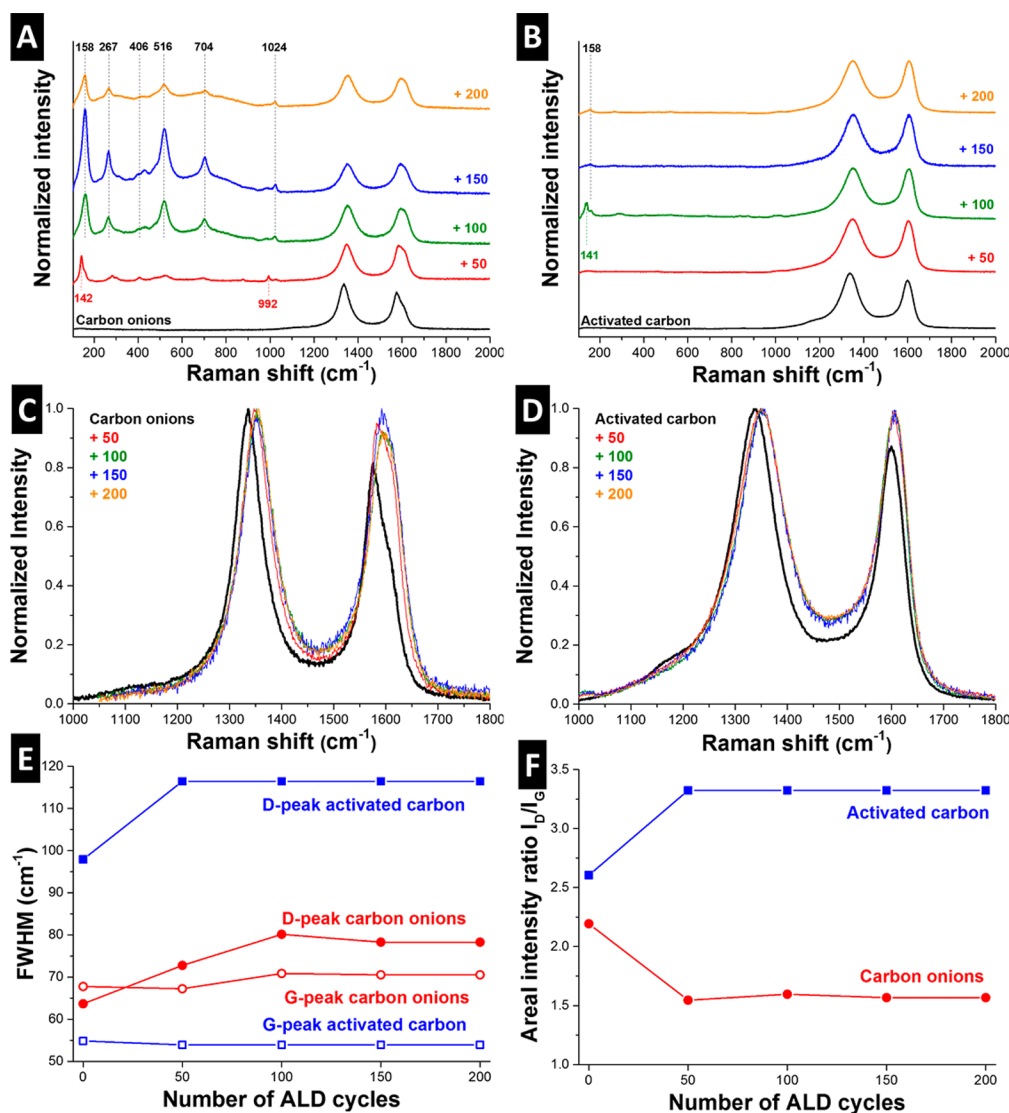


Figure 4. Raman spectra (overview) of (A) carbon onion and (B) activated carbon hybrid electrodes, characteristic vanadia peaks are labeled accordingly. Detailed spectra of D- and G-peaks for (C) carbon onion and (D) activated carbon hybrid electrodes as well as (E) the full width at half-maximum (FWHM) and (F) the areal intensity ratio as a function of coating thickness highlight the changes in carbon structure introduced by vanadia coatings.

coated electrodes to be the consequence of surface stresses induced by a nonepitaxial growth of vanadia layers. Thereby, we introduce external stresses to the hexagonal arrays of sp^2 -carbon that cause a change in vibrational modes of in-plane bond-stretching motions.⁶³ This analysis is in conclusion with the increasing FWHM of the D-peak for both carbons, which is indicative for a reduction in long-range ordering of graphitic carbon.²⁰

An increasing I_D/I_G ratio is generally associated with structural disorder and the introduction of defects in carbon.⁶⁴ The increasing I_D/I_G ratio for coated activated carbons supports the former observations, whereas the decreasing I_D/I_G ratio for carbon onions can be explained by the model of Ferrari and Robertson.⁶³ For crystalline domain sizes below a diameter of about 2 nm, I_D is considered to be proportional to the probability of finding sp^2 -hybridized carbon rings,⁶³ and consequently, a decreasing I_D/I_G ratio suggests a higher degree of disorder. In the case of carbon onions, the domain size of hexagonal sp^2 -carbon rings is further reduced under the influence of external stresses. Thus, a drop to or below 2 nm

of the remaining crystalline clusters can be assumed, and therefore, the drop in I_D/I_G is in agreement with the findings for peak shifting and FWHM.

The impact of the ALD coating on porosity and pore size distribution of the carbon electrodes is evaluated by nitrogen gas sorption analysis. The isotherms of carbon onion hybrid electrodes, as shown in Figure 5, panel A, exhibit a typical type II shape with H3 hysteresis of the most recent 2015 IUPAC classification,⁶⁵ which is evident for a nonporous nanoparticle structure. With increasing vanadia loading, the specific volume of adsorbed nitrogen decreases due to the density increase of the hybrid electrode and partial filling of interparticle space. The isotherm shape of AC-based hybrid electrodes up to 100 ALD cycles correspond to type I(b), as seen from Figure 5, panel B. These electrodes exhibit a steep increase in adsorbed nitrogen at low pressures, which is associated with the filling of micropores. The hysteresis loops are smaller than for carbon onion electrodes and match with type H4, which is correlated with a micro- and mesoporous carbon structure. Only a very small amount of nitrogen was adsorbed on samples AC+150

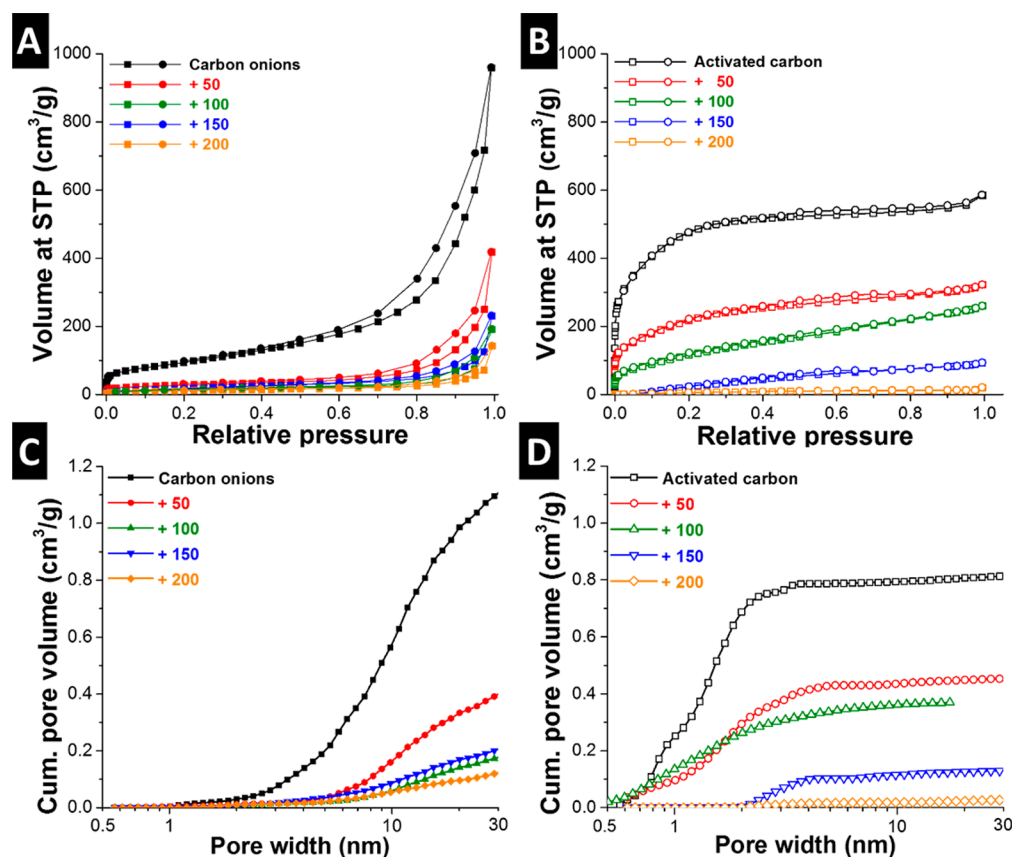


Figure 5. Nitrogen sorption isotherms at standard temperature and pressure (STP) and specific cumulative pore volume of (A, C) carbon onion and (B, D) activated carbon hybrid electrodes.

and AC+200. Their isotherm shape is best described as type-III-like, corresponding to nonporous or macroporous materials with weak adsorbent–adsorbate interactions.⁶⁵ The reason for this is the extensive micro- and mesopore blocking for higher amounts of vanadia coating. These observations are corroborated by the calculated SSAs (BET), which are listed in Table 1.

Table 1. Comparison of SSA_{BET} , SSA_{DFT} , and Pore Volume of Carbon Onion and Activated Carbon Hybrid Electrodes

material	SSA_{BET} (m^2/g)	SSA_{DFT} (m^2/g)	pore volume (cm^3/g)
carbon onions	352	311	0.93
+ 50	98	98	0.31
+ 100	50	44	0.12
+ 150	69	53	0.15
+ 200	42	33	0.09
activated carbon	1759	1289	0.86
+ 50	800	643	0.48
+ 100	458	323	0.38
+ 150	237	77	0.13
+ 200	28	13	0.02

With increasing vanadia loading, SSA_{BET} and pore volume decreased for both types of hybrid electrodes. This decrease is mainly caused by two factors. First, the skeletal and geometric density of the hybrid electrode increases with a growing amount of comparably high density vanadia (V_2O_5 , 3.36 g/cm^3 ; VO_2 , 4.34 g/cm^3) that is primarily occupying internal pore volume and interparticle voids. The second factor is attributed to pore blocking by the vanadia coating, which makes surface

area inside micropores inaccessible, as it is mainly observed for AC hybrid electrodes.

The pore size distribution (PSD) of carbon onion electrodes is characterized by micropores around 1 nm, formed by direct particle contacts, and a high amount of mesopores, formed by intercluster voids between the nanoscopic primary particles (Figure 5C).²⁰ Uncoated OLCs are dominated by mesopores starting at about 2 nm, while pores of coated samples are mostly above 6 nm in size. The general shape of all OLC pore size distribution curves is similar, only shifted toward larger pore widths and smaller total volume with increasing number of ALD cycles. Therefore, it can be assumed that mostly small mesopores between the primary particles in the range of about 2–6 nm were filled by vanadia during the ALD process. The pore structure of AC electrodes (Figure 5D) for samples AC+50 and AC+100 shares many similarities with uncoated AC. The amount of micropores up to 0.8 nm is roughly equal (ca. $0.1\text{ cm}^3/g$), and a decrease in pore volume is found for pores starting at a width of about 1 nm up to 100 ALD cycles. These findings show that vanadia growth preferentially occurs in pores above 1 nm since there is insufficient space for initial VOTIP adsorption inside subnanometer micropores, as confirmed in a previous study.⁴⁷ Complete blocking of these micropores is observed in advanced growth stages of vanadia, for samples AC+150 and AC+200, which is caused by layers covering the micropore necks.

3.2. Electrochemical Characterization. CV for carbon onion electrodes was carried out in half-cells (i.e., three electrode setup) to first characterize the performance of hybrid electrodes with respect to the coating thickness. The CVs of

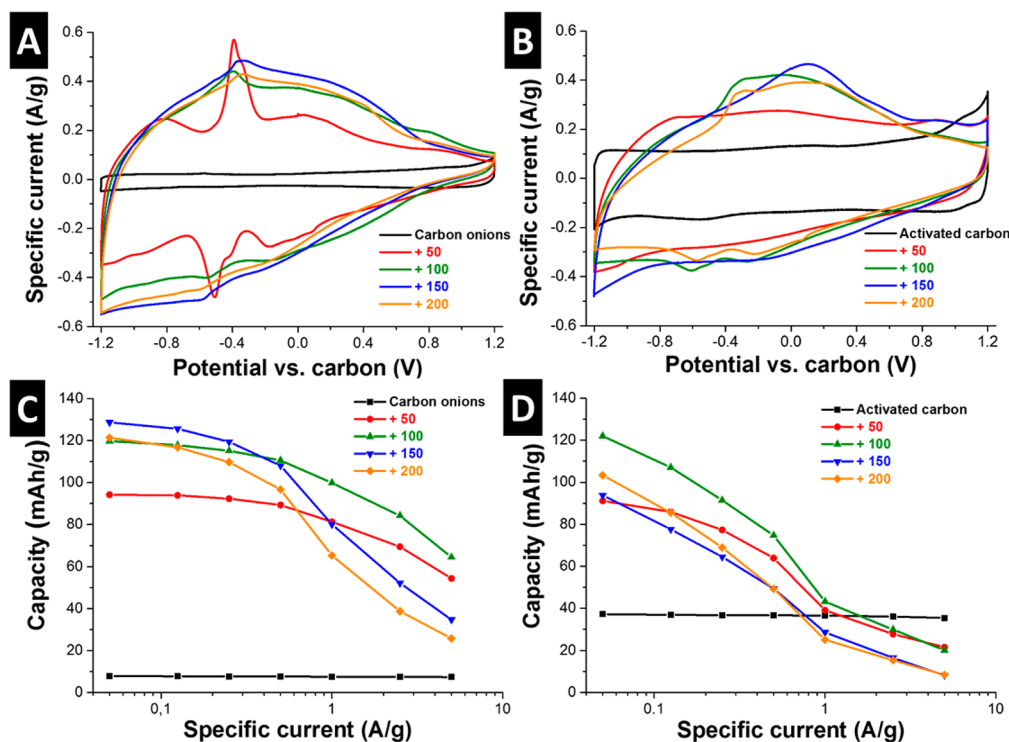


Figure 6. Cyclic voltammograms measured at 1 mV/s and specific capacity values derived from integrating galvanostatic discharge curves for (A, C) carbon onion and (B, D) activated carbon hybrid electrodes.

uncoated carbon onion electrodes exhibit a rectangular shape (Figure 6A), which is indicative of a nearly ideal capacitive behavior.^{36,66} The symmetric, slight current increase observed at higher voltages is not related to noncapacitive reactions but is rather caused by an increase in the density of states of charge carriers for highly graphitized carbon electrodes at high potentials (“butterfly-effect”) and has been discussed elsewhere in more detail.^{54,67} The specific current of OLC/vanadia hybrid electrodes at 1 mV/s significantly increased compared to uncoated carbon onions, particularly for negative potentials (Figure 6A). The current increase can be distinguished as either an amplification of the rectangular signal, which is typical for pseudocapacitors, or as formation of two peaks, characteristic for battery-like devices.²⁸ These findings are similar to other carbon/vanadia systems that have been investigated before such as CNT/vanadia⁴¹ or nanoporous carbon/vanadia.⁴⁷ It can be assumed that Faradaic reactions at the electrode/electrolyte interface and intercalation reactions of lithium-ions in the coating both contribute to the current increase. For sample OLC+50, two redox peaks are clearly visible at -0.4 V versus carbon for charging and -0.5 V versus carbon for discharging, indicating a potential-dependent reaction, which is in alignment with peak positions for lithium intercalation.^{68,69} With an increasing number of ALD cycles, the peaks are less pronounced and the current increase associated with the potential dependent reaction is stretched over a larger potential range.³⁸ The change of the CV shape for different coating thicknesses gives information about the kinetics of the reactions. The pronounced peaks for OLC+50 are the result of a high reaction rate of lithium intercalation in V_2O_5 , whereas the peak stretching for higher numbers of ALD cycles is caused by slower reaction kinetics. The main reason is the growing coating thickness that results in a decrease in electrical conductivity due to the less conductive vanadia^{42,70} and longer

diffusion paths for lithium ions to the reaction sites,⁷¹ both inhibiting high reaction rates. Also, as discussed in the Raman data section, OLC+50 exhibited the highest degree of structural V_2O_5 ordering, which contributes to enhanced intercalation kinetics.

The CVs of AC/vanadia hybrid electrodes (Figure 6B) reveal a higher charge storage capacity compared to uncoated AC. The shape of the CV curves reveals similarities with OLC/vanadia, except for the sample AC+50. Here, in contrast to OLC+50, no typical battery-like redox peaks can be observed, and a mostly (pseudo)capacitive behavior is exhibited. Vanadia growth on AC surfaces is initiated by the formation of few nanodomains, mostly inside the porous AC particles, which are about 1 nm in size after 50 ALD cycles (Figure 2B,C). From the Raman data, it was concluded that these domains do not exhibit a crystalline structure (Figure 4B), and therefore, no high intercalation capacity for lithium ions is expected. Thus, the increase in specific capacity for AC+50 is mainly attributed to Faradaic (surface) reactions. The emergence of highly broad and ill-contoured redox peaks at a higher number of ALD cycles is resulting from the converging vanadia nuclei, which begin to form crystalline structures that mostly consist of V_2O_5 and promote lithium intercalation.³⁴

Galvanostatic charge/discharge measurements were carried out by applying a negative potential to the working electrode versus carbon in anticipation of redox reactions of Li^+ with the vanadia layers of the hybrid electrodes (Figure 6C,D). It can be seen that the discharge capacity of the OLC/vanadia electrodes was about one order of magnitude above uncoated carbon onion electrodes at low specific currents (Figure 6C). With increasing specific current, the specific capacity of the hybrid electrodes decreased, while carbon onion electrodes performed on a relatively constant level. It can be observed that higher coating thickness results in less capacity retention at high

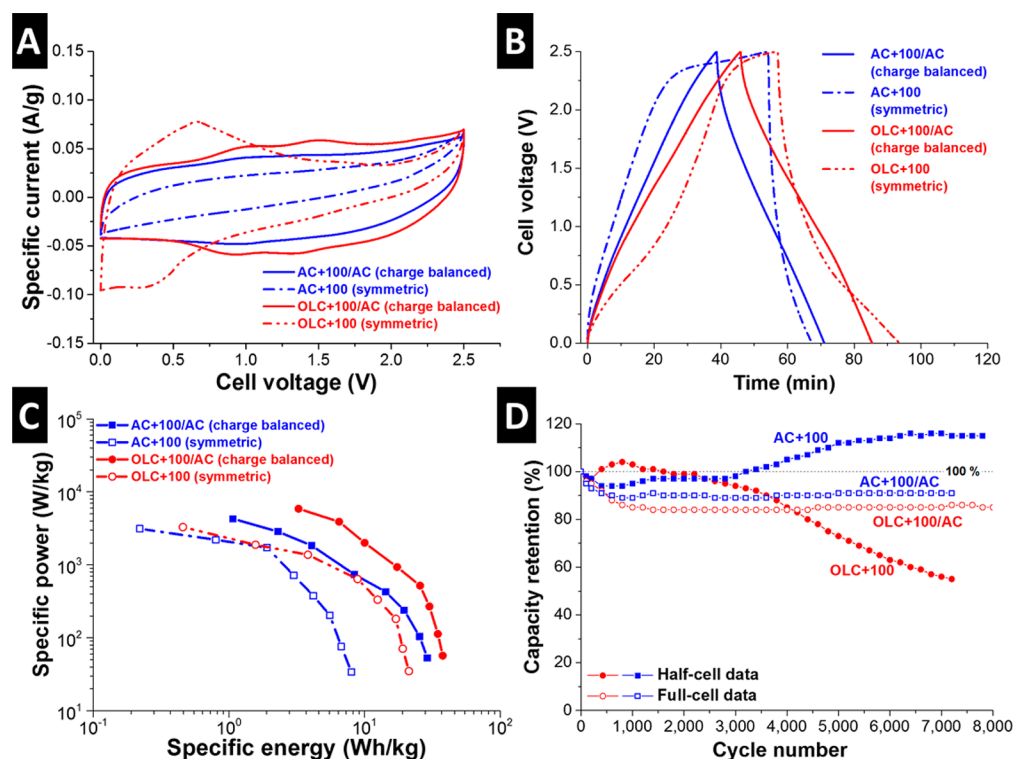


Figure 7. (A) Cyclic voltammograms measured at 1 mV/s, (B) galvanostatic charge–discharge profiles measured at 0.05 A/g, and (C) Ragone plot for charge balanced (against activated carbon, YP-80F) and symmetrical full-cells of OLC+100 and AC+100 hybrid electrodes. (D) Cycling stability test of AC+100 and OLC+100 in half cells, and AC+100/AC and OLC+100/AC in charge balanced full-cells at a specific current of 1 A/g.

specific currents. The performance decline for thicker coatings is a result of longer diffusion paths and the insulating effect of vanadia, which leads to charge limitations particularly at high sweeping rates. At a low specific current of 0.05 A/g, OLC+150 exhibited with 129 mAh/g the highest capacity of all studied hybrid electrodes (to provide a better comparability: when (incorrectly) expressed as capacitance, this value would correspond to 387 F/g). The value dropped with an increasing specific current, and a capacity retention of about 27% was observed at 5 A/g. In comparison, OLC+100 showed a comparably high capacity of 120 mAh/g at 0.05 A/g while still retaining 53% of its initial capacity at 5 A/g. The rate handling performance of OLC+50 and OLC+100 is similar and comparable to uncoated carbon onions below a current density of 1 A/g. The capacity of the electrode with 150 ALD cycles is only marginally superior to 100 ALD cycles at a very low specific current. This suggests that most reactions take place at the coating surface, while only little lithium intercalation into the “bulk” of the coating takes place as supported by the lower initial capacity of OLC+200. This electrochemically inactive vanadia can be considered as dead mass, decreasing the specific performance values of the electrode. A reason for this behavior is that the vanadia coatings exhibit only partial crystallinity, while substantial amounts of the coating show a distorted or amorphous structure, which is not favorable for lithium intercalation.³⁴ Overall, the hybrid electrode with 100 ALD cycles showed the most attractive electrochemical properties, with a good compromise between high initial capacity and good rate handling performance.

The discharge capacity of AC/vanadia hybrid electrodes at a low current density was about 2–3-times higher than that of uncoated AC. With higher current densities, the capacity values dropped increasingly with a higher coating thickness, exhibiting

retentions between 24% (for 50 ALD-cycles) and 8% (for 200 ALD-cycles) at 5 A/g. At a low current density of 0.05 A/g, AC+100 showed the highest capacity of all AC/vanadia electrodes with 122 mAh/g, which is comparable to OLC+100. Yet, with increasing current densities, the observed drop in capacity was more severe as for carbon onion electrodes. Above specific currents of 1 A/g, all AC/vanadia electrodes showed less capacity than uncoated AC. Besides the aforementioned insulating effect of vanadia, the inferior electrical conductivity of AC, which is about one order of magnitude lower than for carbon onions,²³ is another reason for the more severe decline in performance at higher scanning rates. Furthermore, this behavior can be related to the microporous structure of AC. The vanadia coating is responsible for micropore blocking inside the AC particles and causing a large reduction in accessible SSA,⁴⁷ as observed by GSA (Figure 5B). Also, diffusion paths in the porous network of AC become narrower, thus increasing the diffusion resistance for ions. Obviously, a high electrical conductivity of the carbon substrate material is a requirement for good rate handling characteristics of hybrid electrodes. Vanadia coatings introduced to AC electrodes are only desirable for low rate applications, and a coating thickness, equivalent to 100 ALD cycles in this work, should not be exceeded to avoid extensive pore blocking and insulating phenomena.

It was demonstrated that both hybrid electrodes exhibited the best performance when loaded with 100 ALD cycles of vanadia. Therefore, the electrochemical performance of these hybrid electrodes is further investigated both in charge balanced full-cells against activated carbon and in symmetrical full-cells. The CV (Figure 7A) of charge balanced OLC+100/AC exhibits a slightly higher specific current than AC+100/AC as a result of small redox peaks at cell voltages of around +1.0 V and +1.3 V

cell voltage. At a cell voltage of +1.0 V, the applied potential at the OLC+100 electrode in the charge balanced system is at about -0.5 V, which is in alignment with the redox peaks observed in half-cells. In comparison, the specific current of symmetrical full-cells is extensively reduced, especially at higher cell voltages. This behavior is explained by charge limitations caused at the positive electrode, which are a consequence of the inferior performance of the hybrid electrodes in the positive potential area, as has been demonstrated by the CVs of half-cells (Figure 6A,B).

Galvanostatic charge–discharge profiles (Figure 7B) were used to calculate the specific energy and specific power as used for a Ragone plot (Figure 7C). The performance of charge balanced full-cells is superior compared to symmetrical full-cells in both specific energy and specific power. OLC+100/AC exhibits specific energies of 38 Wh/kg and 3.3 Wh/kg at specific powers of 57 W/kg and 5.9 kW/kg, respectively. In comparison, AC+100/AC shows a performance of 29 Wh/kg (1.1 Wh/kg) at 53 W/kg (4.3 kW/kg). The low performance of symmetrical cells is effected by the rapid voltage drop in the discharge cycle (Figure 7B). This low cycle efficiency is explained by the disparate electrochemical behavior of the carbon/vanadia hybrid electrodes in the positive and negative potential window. Therefore, the two electrodes are disproportionately charged, and the resulting potential at the positive electrode exceeds the stability window of the electrolyte. Superior performance can only be found for asymmetrical cells, where the carbon/vanadia hybrid material is used as a negative electrode.

Stability testing was carried out in both a half-cell setup with AC+100 and OLC+100 hybrid electrodes, and in charge balanced full-cells (AC+100/AC and OLC+100/AC) via galvanostatic charge–discharge at 1 A/g (Figure 7D). Both half-cells retained about 95% of their initial discharge capacity up to 3000 cycles. Afterward, OLC+100 exhibited a steady capacity fading of about 1% every 100 cycles, while the capacity of AC+100 increased to about 115% of the initial value after 8000 cycles. Long-term cycling leads to electrochemical degradation of vanadia, which causes a reduced redox activity and therefore a decrease in performance of the OLC+100 hybrid electrodes. For the AC+100 hybrid electrodes, though, the electrochemical degradation of vanadia gave rise to a partial clearance of blocked channels inside the microporous AC particles, which benefited the ion mobility and thereby decreased the electrodes resistivity, as seen from the reduction of the IR drop (Supporting Information, Figure S6). The result is a slight increase in capacity after 3000 cycles. The charge balanced full-cells exhibited a minor drop in discharge capacity after a few hundred cycles but then remained highly stable at 91% (AC+100/AC) and 85% (OLC+100/AC) of their initial value, respectively, up to 8000 cycles.

4. CONCLUSIONS

It was demonstrated that ALD allows the deposition of vanadia on free-standing, porous carbon electrodes. Exohedral carbon onions were uniformly coated, while for endohedral AC, micropores were blocked, and the accessible surface area declined extensively at high vanadia loadings. The growth mechanism of vanadia on carbon substrates was characterized by an initial island growth, which began to form a more continuous layer after a sufficient number of ALD cycles. The pore structure proved to have a severe impact on the crystallinity of the resulting vanadia layers. The external surface

area of carbon onions provided favorable conditions for crystalline growth, contrarily to the microporous internal surface area of activated carbon, where mostly amorphous vanadia was formed.

The electrochemical performance of the hybrid electrodes was enhanced by the vanadia coating on carbon onions and AC at low specific currents. Yet, only carbon onions as substrate material provided a sufficient electrical conductivity for superior capacity at high rates, while the performance of AC/vanadia electrodes dropped at high charging and discharging rates. Consequently, highly conductive carbons with exohedral surfaces are found to be the superior substrate material for hybrid electrodes. It was found that there is an optimum amount of vanadia that results in an ideal balance between redox-activity and electrical conductivity of the hybrid electrode. In this work, the optimum amount of vanadia was around 50 wt % for activated carbon and 65 wt % for carbon onions. Furthermore, the performance of activated carbon hybrid electrodes dropped drastically due to blocking of internal surface area when exceeding 65 wt % of vanadia. In full-cells, the fabricated carbon/vanadia hybrid electrodes exhibit superior performance only when employed as negative electrodes in an asymmetrical cell.

■ ASSOCIATED CONTENT

Supporting Information

The Supporting Information is available free of charge on the ACS Publications website at DOI: [10.1021/acs.chemmater.6b00738](https://doi.org/10.1021/acs.chemmater.6b00738).

TEM of nanodiamond precursor and resulting carbon onions, sedimentation analysis of carbon onions and activated carbon, EFTEM mappings of OLC+100, cross-sectional EDX mappings of all electrodes, XRD of all samples, and galvanostatic charge–discharge profiles of AC+100 during stability testing (PDF)

■ AUTHOR INFORMATION

Corresponding Author

*E-mail: volker.presser@leibniz-inm.de.

Notes

The authors declare no competing financial interest.

■ ACKNOWLEDGMENTS

This work is part of the strategic Leibniz partnership between IPF and INM. We acknowledge funding from the German Federal Ministry for Research and Education (BMBF) in support of the nanoEES^{3D} project (Award No. 03EK3013) as part of the strategic funding initiative energy storage framework. This work is part of the CREATE-Network Project, Horizon 2020 of the European Commission (RISE Project No. 644013). We thank Prof. Arzt (INM) for the continuing support.

■ REFERENCES

- (1) Béguin, F.; Presser, V.; Balducci, A.; Frackowiak, E. Carbons and electrolytes for advanced supercapacitors. *Adv. Mater.* **2014**, *26*, 2219–2251.
- (2) Simon, P.; Gogotsi, Y. Materials for electrochemical capacitors. *Nat. Mater.* **2008**, *7*, 845–854.
- (3) Conway, B. E. *Electrochemical Supercapacitors: Scientific Fundamentals and Technological Applications*; Springer Science & Business Media, 2013.

- (4) Qu, D.; Shi, H. Studies of activated carbons used in double-layer capacitors. *J. Power Sources* **1998**, *74*, 99–107.
- (5) Shi, H. Activated carbons and double layer capacitance. *Electrochim. Acta* **1996**, *41*, 1633–1639.
- (6) Zeiger, M.; Jäckel, N.; Mochalin, V. N.; Presser, V. Review: Carbon onions for electrochemical energy storage. *J. Mater. Chem. A* **2016**, *4*, 3172–3196.
- (7) Bushueva, E.; Galkin, P.; Okotrub, A.; Bulusheva, L.; Gavrilov, N.; Kuznetsov, V.; Moiseev, S. Double layer supercapacitor properties of onion-like carbon materials. *Phys. Status Solidi B* **2008**, *245*, 2296–2299.
- (8) Frackowiak, E.; Jurewicz, K.; Delpoux, S.; Beguin, F. Nanotubular materials for supercapacitors. *J. Power Sources* **2001**, *97-98*, 822–825.
- (9) Frackowiak, E.; Metenier, K.; Bertagna, V.; Beguin, F. Supercapacitor electrodes from multiwalled carbon nanotubes. *Appl. Phys. Lett.* **2000**, *77*, 2421–2423.
- (10) Zhang, L. L.; Zhou, R.; Zhao, X. Graphene-based materials as supercapacitor electrodes. *J. Mater. Chem.* **2010**, *20*, 5983–5992.
- (11) Jo, K.; Gu, M.; Kim, B.-S. Ultrathin Supercapacitor Electrode Based on Reduced Graphene Oxide Nanosheets Assembled with Photo-Cross-Linkable Polymer: Conversion of Electrochemical Kinetics in Ultrathin Films. *Chem. Mater.* **2015**, *27*, 7982–7989.
- (12) Atchison, J. S.; Zeiger, M.; Tolosa, A.; Funke, L. M.; Jäckel, N.; Presser, V. Electrospinning of ultrafine metal oxide/carbon and metal carbide/carbon nanocomposite fibers. *RSC Adv.* **2015**, *5*, 35683–35692.
- (13) Ra, E.; Raymundo-Piñero, E.; Lee, Y.; Béguin, F. High power supercapacitors using polyacrylonitrile-based carbon nanofiber paper. *Carbon* **2009**, *47*, 2984–2992.
- (14) Fischer, U.; Saliger, R.; Bock, V.; Petricevic, R.; Fricke, J. Carbon aerogels as electrode material in supercapacitors. *J. Porous Mater.* **1997**, *4*, 281–285.
- (15) Lozano-Castello, D.; Cazorla-Amorós, D.; Linares-Solano, A.; Shiraiishi, S.; Kurihara, H.; Oya, A. Influence of pore structure and surface chemistry on electric double layer capacitance in non-aqueous electrolyte. *Carbon* **2003**, *41*, 1765–1775.
- (16) Marsh, H.; Reinoso, F. R. *Activated Carbon*; Elsevier, 2006.
- (17) Pérez, C. R.; Yeon, S. H.; Ségalini, J.; Presser, V.; Taberna, P. L.; Simon, P.; Gogotsi, Y. Structure and Electrochemical Performance of Carbide-Derived Carbon Nanopowders. *Adv. Funct. Mater.* **2013**, *23*, 1081–1089.
- (18) Portet, C.; Yushin, G.; Gogotsi, Y. Electrochemical performance of carbon onions, nanodiamonds, carbon black and multiwalled nanotubes in electrical double layer capacitors. *Carbon* **2007**, *45*, 2511–2518.
- (19) Kuznetsov, V. L.; Chuvilin, A. L.; Butenko, Y. V.; Mal'kov, I. Y.; Titov, V. M. Onion-like carbon from ultra-disperse diamond. *Chem. Phys. Lett.* **1994**, *222*, 343–348.
- (20) Zeiger, M.; Jäckel, N.; Aslan, M.; Weingarth, D.; Presser, V. Understanding structure and porosity of nanodiamond-derived carbon onions. *Carbon* **2015**, *84*, 584–598.
- (21) Zeiger, M.; Jäckel, N.; Weingarth, D.; Presser, V. Vacuum or flowing argon: What is the best synthesis atmosphere for nanodiamond-derived carbon onions for supercapacitor electrodes? *Carbon* **2015**, *94*, 507–517.
- (22) McDonough, J. K.; Frolov, A. I.; Presser, V.; Niu, J.; Miller, C. H.; Ubiato, T.; Fedorov, M. V.; Gogotsi, Y. Influence of the structure of carbon onions on their electrochemical performance in supercapacitor electrodes. *Carbon* **2012**, *50*, 3298–3309.
- (23) Jäckel, N.; Weingarth, D.; Zeiger, M.; Aslan, M.; Grobelsek, I.; Presser, V. Comparison of carbon onions and carbon blacks as conductive additives for carbon supercapacitors in organic electrolytes. *J. Power Sources* **2014**, *272*, 1122–1133.
- (24) Makgopa, K.; Ejikeme, P. M.; Jafta, C. J.; Raju, K.; Zeiger, M.; Presser, V.; Ozoemena, K. I. A high-rate aqueous symmetric pseudocapacitor based on highly graphitized onion-like carbon/birnessite-type manganese oxide nanohybrids. *J. Mater. Chem. A* **2015**, *3*, 3480–3490.
- (25) Kovalenko, I.; Bucknall, D. G.; Yushin, G. Detonation Nanodiamond and Onion-Like-Carbon-Embedded Polyaniline for Supercapacitors. *Adv. Funct. Mater.* **2010**, *20*, 3979–3986.
- (26) Anjos, D. M.; McDonough, J. K.; Perre, E.; Brown, G. M.; Overbury, S. H.; Gogotsi, Y.; Presser, V. Pseudocapacitance and performance stability of quinone-coated carbon onions. *Nano Energy* **2013**, *2*, 702–712.
- (27) Zhang, Y.; Feng, H.; Wu, X.; Wang, L.; Zhang, A.; Xia, T.; Dong, H.; Li, X.; Zhang, L. Progress of electrochemical capacitor electrode materials: A review. *Int. J. Hydrogen Energy* **2009**, *34*, 4889–4899.
- (28) Simon, P.; Gogotsi, Y.; Dunn, B. Where do batteries end and supercapacitors begin? *Science* **2014**, *343*, 1210–1211.
- (29) Rakhi, R.; Ahmed, B.; Hedhili, M.; Anjum, D. H.; Alshareef, H. N. Effect of Postetch Annealing Gas Composition on the Structural and Electrochemical Properties of Ti₂CT_x MXene Electrodes for Supercapacitor Applications. *Chem. Mater.* **2015**, *27*, 5314–5323.
- (30) Liu, J.; Essner, J.; Li, J. Hybrid supercapacitor based on coaxially coated manganese oxide on vertically aligned carbon nanofiber arrays. *Chem. Mater.* **2010**, *22*, 5022–5030.
- (31) Levi, M. D.; Lukatskaya, M. R.; Sigalov, S.; Beidaghi, M.; Shpigel, N.; Daikhin, L.; Aurbach, D.; Barsoum, M. W.; Gogotsi, Y. Solving the Capacitive Paradox of 2D MXene using Electrochemical Quartz-Crystal Admittance and In Situ Electronic Conductance Measurements. *Adv. Energy Mater.* **2015**, *5*, 1400815.
- (32) Zhang, K.; Zhang, L. L.; Zhao, X.; Wu, J. Graphene/polyaniline nanofiber composites as supercapacitor electrodes. *Chem. Mater.* **2010**, *22*, 1392–1401.
- (33) Salloux, K.; Chaput, F.; Wong, H.; Dunn, B.; Breiter, M. Lithium intercalation in vanadium pentoxide aerogels. *J. Electrochem. Soc.* **1995**, *142*, L191–L192.
- (34) Takahashi, K.; Limmer, S. J.; Wang, Y.; Cao, G. Synthesis and electrochemical properties of single-crystal V₂O₅ nanorod arrays by template-based electrodeposition. *J. Phys. Chem. B* **2004**, *108*, 9795–9800.
- (35) Wang, Y.; Takahashi, K.; Lee, K.; Cao, G. Nanostructured vanadium oxide electrodes for enhanced lithium-ion intercalation. *Adv. Funct. Mater.* **2006**, *16*, 1133.
- (36) Laheäär, A.; Przygocki, P.; Abbas, Q.; Béguin, F. Appropriate methods for evaluating the efficiency and capacitive behavior of different types of supercapacitors. *Electrochem. Commun.* **2015**, *60*, 21–25.
- (37) Brousse, T.; Bélanger, D.; Long, J. W. To be or not to be pseudocapacitive? *J. Electrochem. Soc.* **2015**, *162*, A5185–A5189.
- (38) Bandaru, P.; Yamada, H.; Narayanan, R.; Hofer, M. Charge transfer and storage in nanostructures. *Mater. Sci. Eng., R* **2015**, *96*, 1–69.
- (39) Gu, W.; Yushin, G. Review of nanostructured carbon materials for electrochemical capacitor applications: advantages and limitations of activated carbon, carbide-derived carbon, zeolite-templated carbon, carbon aerogels, carbon nanotubes, onion-like carbon, and graphene. *Wiley Interdiscip. Rev.: Energy Environ.* **2014**, *3*, 424–473.
- (40) Yilmaz, G.; Guo, C. X.; Lu, X. High Performance Solid-State Supercapacitors Based on V₂O₅/Carbon Nanotube Composites. *ChemElectroChem* **2016**, *3*, 158–164.
- (41) Boukhalfa, S.; Evanoff, K.; Yushin, G. Atomic layer deposition of vanadium oxide on carbon nanotubes for high-power supercapacitor electrodes. *Energy Environ. Sci.* **2012**, *5*, 6872–6879.
- (42) Chen, Z.; Augustyn, V.; Wen, J.; Zhang, Y.; Shen, M.; Dunn, B.; Lu, Y. High-Performance Supercapacitors Based on Intertwined CNT/V₂O₅ Nanowire Nanocomposites. *Adv. Mater.* **2011**, *23*, 791–795.
- (43) Zeiger, M.; Weingarth, D.; Presser, V. Quinone-Decorated Onion-Like Carbon/Carbon Fiber Hybrid Electrodes for High-Rate Supercapacitor Applications. *ChemElectroChem* **2015**, *2*, 1117–1127.
- (44) Benson, J.; Boukhalfa, S.; Magasinski, A.; Kvit, A.; Yushin, G. Chemical vapor deposition of aluminum nanowires on metal substrates for electrical energy storage applications. *ACS Nano* **2012**, *6*, 118–125.

- (45) Luo, J.; Xia, X.; Luo, Y.; Guan, C.; Liu, J.; Qi, X.; Ng, C. F.; Yu, T.; Zhang, H.; Fan, H. J. Rationally designed hierarchical $\text{TiO}_2@\text{Fe}_2\text{O}_3$ hollow nanostructures for improved lithium ion storage. *Adv. Energy Mater.* **2013**, *3*, 737–743.
- (46) Chen, X.; Pomerantseva, E.; Banerjee, P.; Gregorczyk, K.; Ghodssi, R.; Rubloff, G. Ozone-Based Atomic Layer Deposition of Crystalline V_2O_5 Films for High Performance Electrochemical Energy Storage. *Chem. Mater.* **2012**, *24*, 1255–1261.
- (47) Daubert, J. S.; Lewis, N. P.; Gotsch, H. N.; Mundy, J. Z.; Monroe, D. N.; Dickey, E. C.; Losego, M. D.; Parsons, G. N. Effect of Meso- and Micro-Porosity in Carbon Electrodes on Atomic Layer Deposition of Pseudocapacitive V_2O_5 for High Performance Supercapacitors. *Chem. Mater.* **2015**, *27*, 6524–6534.
- (48) Azhagan, M. V. K.; Vaishampayan, M. V.; Shelke, M. V. Synthesis and electrochemistry of pseudocapacitive multilayer fullerenes and MnO_2 nanocomposites. *J. Mater. Chem. A* **2014**, *2*, 2152–2159.
- (49) George, S. M. Atomic layer deposition: an overview. *Chem. Rev.* **2010**, *110*, 111–131.
- (50) Wang, X.; Yushin, G. Chemical vapor deposition and atomic layer deposition for advanced lithium ion batteries and supercapacitors. *Energy Environ. Sci.* **2015**, *8*, 1889–1904.
- (51) Jäckel, N.; Weingarth, D.; Schreiber, A.; Krüner, B.; Zeiger, M.; Tolosa, A.; Aslan, M.; Presser, V. Performance evaluation of conductive additives for activated carbon supercapacitors in organic electrolyte. *Electrochim. Acta* **2016**, *191*, 284–298.
- (52) Brunauer, S.; Emmett, P. H.; Teller, E. Adsorption of gases in multimolecular layers. *J. Am. Chem. Soc.* **1938**, *60*, 309–319.
- (53) Gor, G. Y.; Thommes, M.; Cychosz, K. A.; Neimark, A. V. Quenched solid density functional theory method for characterization of mesoporous carbons by nitrogen adsorption. *Carbon* **2012**, *50*, 1583–1590.
- (54) Weingarth, D.; Zeiger, M.; Jäckel, N.; Aslan, M.; Feng, G.; Presser, V. Graphitization as a Universal Tool to Tailor the Potential-Dependent Capacitance of Carbon Supercapacitors. *Adv. Energy Mater.* **2014**, *4*, 1400316.
- (55) Ruch, P.; Cericola, D.; Hahn, M.; Kötz, R.; Wokaun, A. On the use of activated carbon as a quasi-reference electrode in non-aqueous electrolyte solutions. *J. Electroanal. Chem.* **2009**, *636*, 128–131.
- (56) Kuznetsov, V.; Butenko, Y. V.; Zaikovskii, V.; Chuvilin, A. Carbon redistribution processes in nanocarbons. *Carbon* **2004**, *42*, 1057–1061.
- (57) Yanguas-Gil, A.; Libera, J. A.; Elam, J. W. Modulation of the Growth Per Cycle in Atomic Layer Deposition Using Reversible Surface Functionalization. *Chem. Mater.* **2013**, *25*, 4849–4860.
- (58) Baddour-Hadjean, R.; Golabkan, V.; Pereira-Ramos, J.; Mantoux, A.; Lincot, D. A Raman study of the lithium insertion process in vanadium pentoxide thin films deposited by atomic layer deposition. *J. Raman Spectrosc.* **2002**, *33*, 631–638.
- (59) Lee, S.-H.; Cheong, H. M.; Seong, M. J.; Liu, P.; Tracy, C. E.; Mascarenhas, A.; Pitts, J. R.; Deb, S. K. Raman spectroscopic studies of amorphous vanadium oxide thin films. *Solid State Ionics* **2003**, *165*, 111–116.
- (60) Wang, X.; Li, H.; Fei, Y.; Wang, X.; Xiong, Y.; Nie, Y.; Feng, K. XRD and Raman study of vanadium oxide thin films deposited on fused silica substrates by RF magnetron sputtering. *Appl. Surf. Sci.* **2001**, *177*, 8–14.
- (61) Julien, C.; Ivanov, I.; Gorenstein, A. Vibrational modifications on lithium intercalation in V_2O_5 films. *Mater. Sci. Eng., B* **1995**, *33*, 168–172.
- (62) Ferrari, A. C. *Mater. Res. Soc. Symp. Proc.* **2001**, W11.15.11.
- (63) Ferrari, A. C.; Robertson, J. Interpretation of Raman spectra of disordered and amorphous carbon. *Phys. Rev. B: Condens. Matter Mater. Phys.* **2000**, *61*, 14095.
- (64) Cebik, J.; McDonough, J. K.; Peerally, F.; Medrano, R.; Neitzel, I.; Gogotsi, Y.; Osswald, S. Raman spectroscopy study of the nanodiamond-to-carbon onion transformation. *Nanotechnology* **2013**, *24*, 205703.
- (65) Thommes, M.; Kaneko, K.; Neimark, A. V.; Olivier, J. P.; Rodriguez-Reinoso, F.; Rouquerol, J.; Sing, K. S. Physisorption of gases, with special reference to the evaluation of surface area and pore size distribution (IUPAC Technical Report). *Pure Appl. Chem.* **2015**, *87*, 1051–1069.
- (66) Zhang, S.; Pan, N. Supercapacitors performance evaluation. *Adv. Energy Mater.* **2015**, *5*, 1401401.
- (67) Xia, J.; Chen, F.; Li, J.; Tao, N. Measurement of the quantum capacitance of graphene. *Nat. Nanotechnol.* **2009**, *4*, 505–509.
- (68) Liu, H.; Yang, W. Ultralong single crystalline V_2O_5 nanowire/graphene composite fabricated by a facile green approach and its lithium storage behavior. *Energy Environ. Sci.* **2011**, *4*, 4000–4008.
- (69) Coustier, F.; Lee, J.-M.; Passerini, S.; Smyrl, W. H. V_2O_5 aerogel-like lithium intercalation host. *Solid State Ionics* **1999**, *116*, 279–291.
- (70) Hu, Y. S.; Liu, X.; Müller, J. O.; Schlögl, R.; Maier, J.; Su, D. S. Synthesis and Electrode Performance of Nanostructured V_2O_5 by Using a Carbon Tube-in-Tube as a Nanoreactor and an Efficient Mixed-Conducting Network. *Angew. Chem., Int. Ed.* **2009**, *48*, 210–214.
- (71) Cao, A. M.; Hu, J. S.; Liang, H. P.; Wan, L. J. Self-assembled vanadium pentoxide (V_2O_5) hollow microspheres from nanorods and their application in lithium-ion batteries. *Angew. Chem., Int. Ed.* **2005**, *44*, 4391–4395.

Supporting Information

ENHANCED ELECTROCHEMICAL ENERGY STORAGE BY NANOSCOPIC DECORATION OF ENDOHEDRAL AND EXOHEDRAL CARBON WITH VANADIUM OXIDE VIA ATOMIC LAYER DEPOSITION

Simon Fleischmann,^{1,2} Nicolas Jäckel,^{1,2} Marco Zeiger,^{1,2}

Benjamin Krüner,^{1,2} Ingrid Grobelsek,¹ Petr Formanek,³

Soumyadip Choudhury,^{1,3} Daniel Weingarh,¹ Volker Presser^{1,2,*}

¹ INM - Leibniz Institute for New Materials, 66123 Saarbrücken, Germany

² Department of Materials Science and Engineering, Saarland University, 66123 Saarbrücken, Germany

³ Leibniz-Institut für Polymerforschung Dresden e. V., 01069 Dresden, Germany

* Corresponding author's eMail: volker.presser@leibniz-inm.de

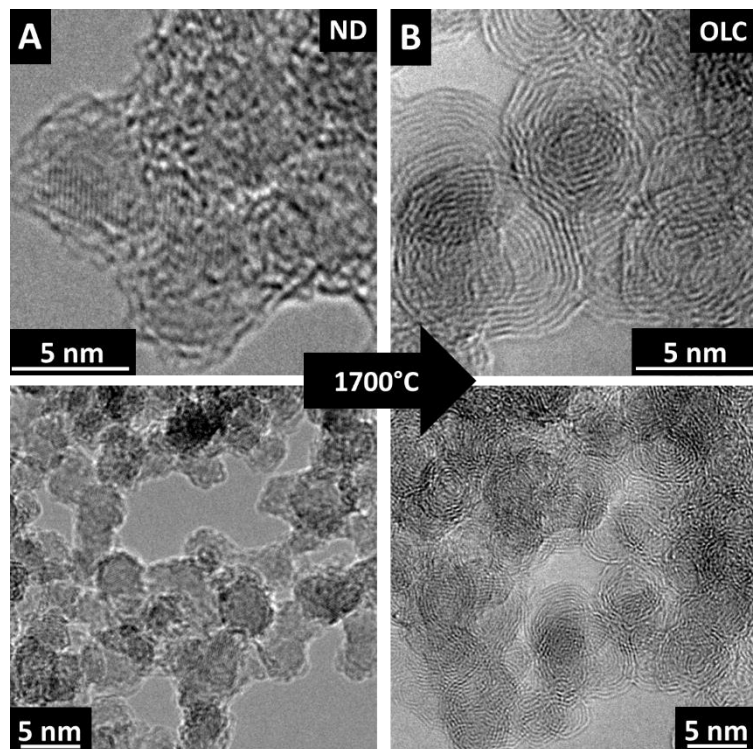


Fig. S1: Transmission electron micrographs of nanodiamond precursor (ND) (A) and the resulting carbon onions (B) after thermal annealing in argon atmosphere at 1700 °C for 1 h. The top and bottom rows show different magnifications.

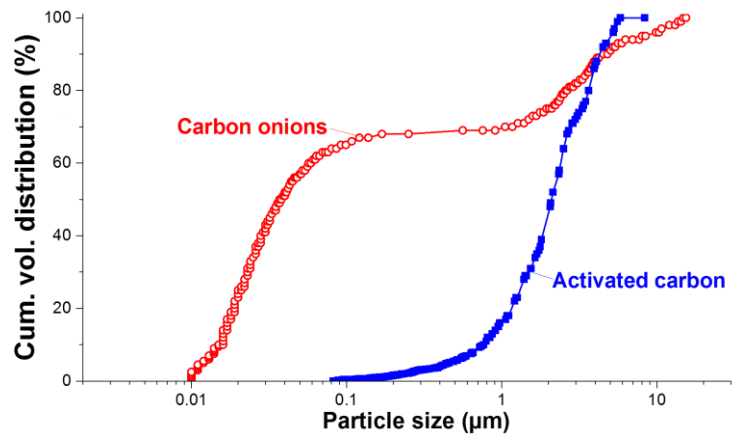


Fig. S2: Cumulative volume distribution of carbon onions and activated carbon particles plotted against the particle size. Measured by centrifugal sedimentation analysis in ethanol, adapted from Ref. ²³.

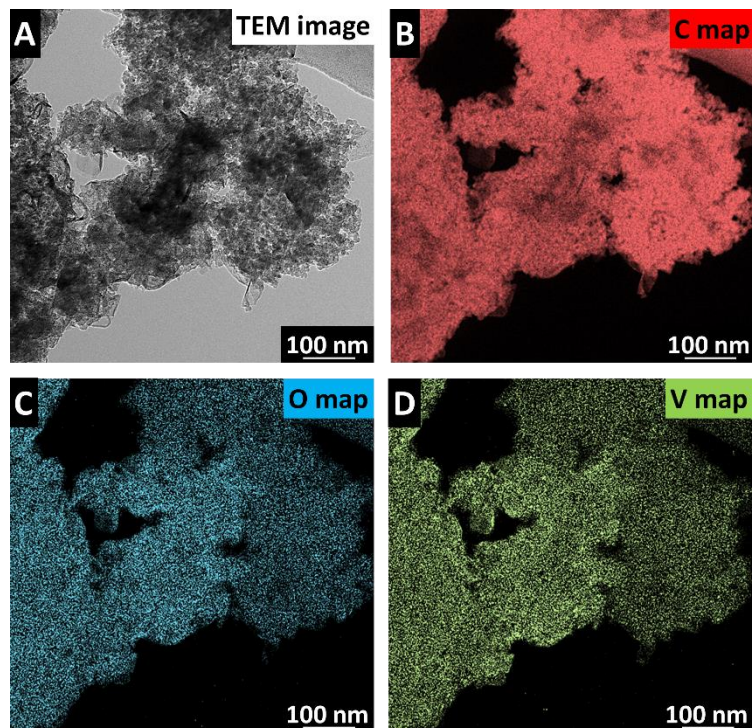


Fig. S3: Transmission electron micrograph of carbon onion particles coated with 100 ALD cycles (A), and the corresponding EFTEM maps of carbon (B), oxygen (C), and vanadium (D).

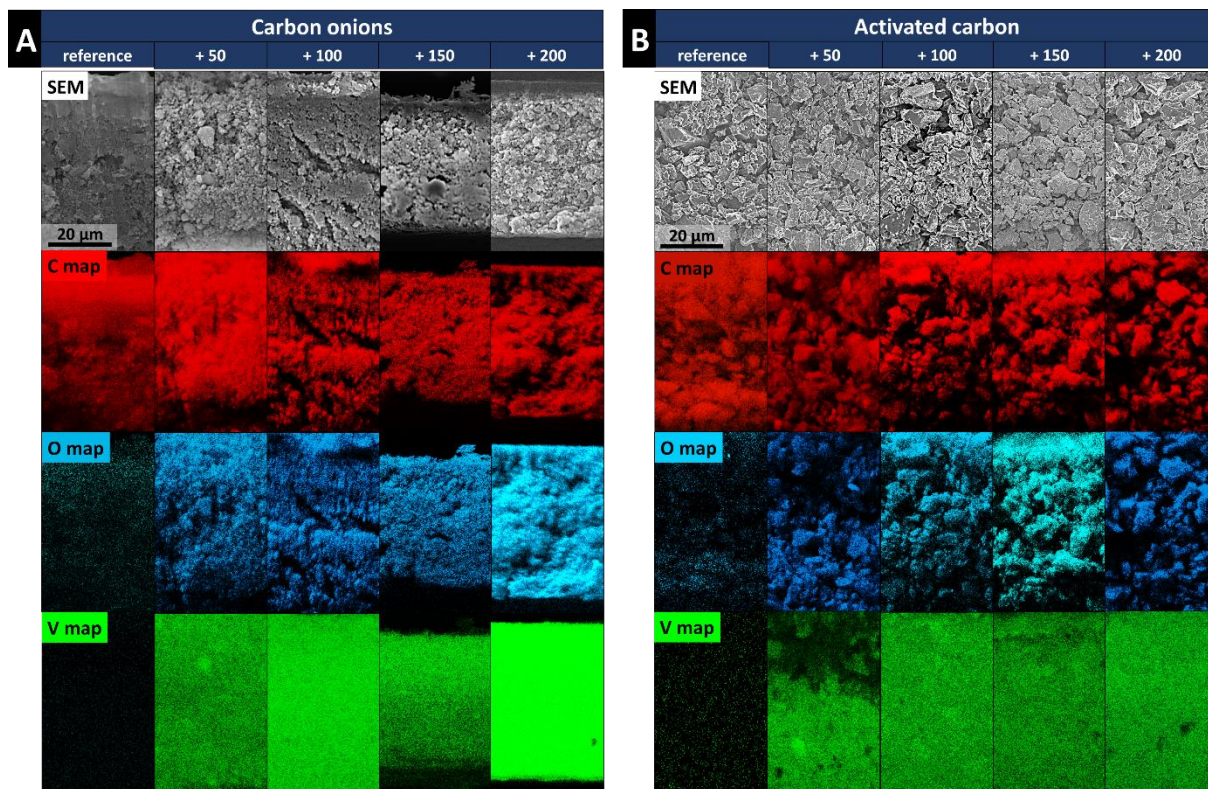


Fig. S4: Cross sectional EDX mappings of carbon onion (A) and activated carbon (B) hybrid electrodes. The element distribution of carbon (C map), oxygen (O map), and vanadium (V map) is illustrated across the whole electrode cross section, including the original SEM image in the top row. For the analysis, the $C_{K\alpha}$, $O_{K\alpha}$, and $V_{L\alpha}$ -lines were employed.

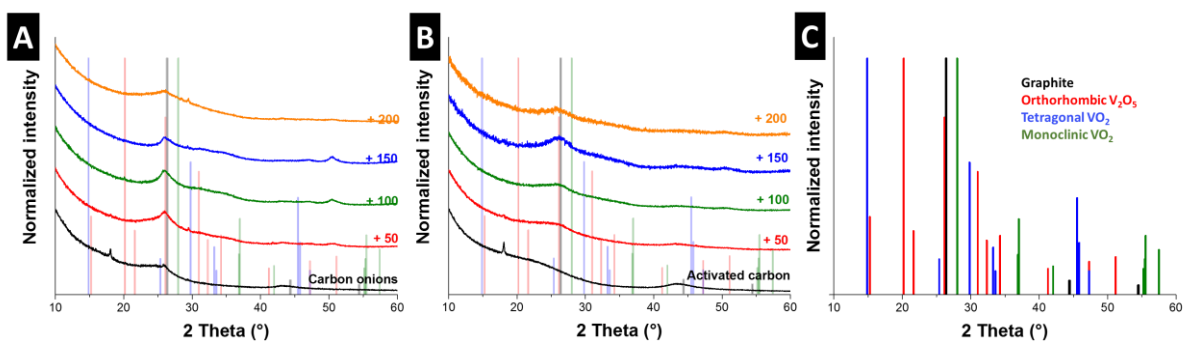


Fig. S5: X-ray diffractograms of carbon onion (A) and activated carbon (B) hybrid electrodes. The ideal peak positions from the powder diffraction files for orthorhombic V_2O_5 (PDF 41-1426), tetragonal VO_2 (PDF 42-0876), monoclinic VO_2 (PDF 44-0353), and graphite (PDF 41-1487) are given in (C) and, with transparency, visible in the background of (A) and (B). The small sharp peaks for carbon onions and activated carbons at $18^\circ 2\theta$ is associated with PTFE (which is the polymer binder used for electrode manufacturing).

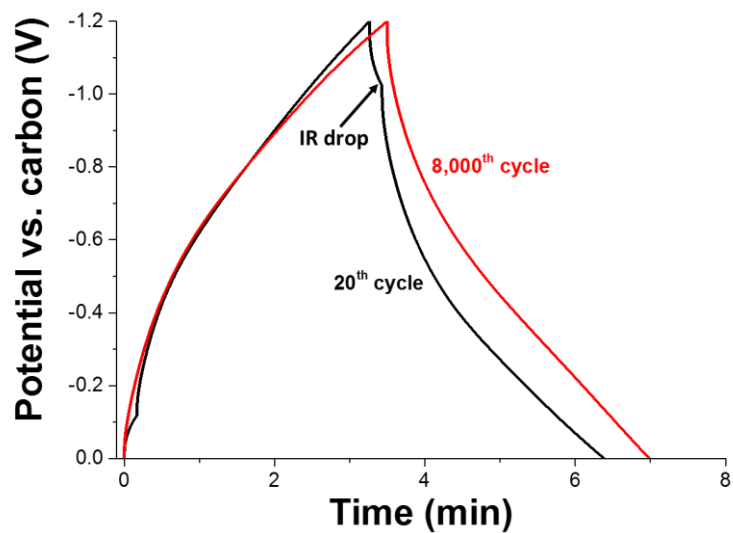


Fig. S6: Galvanostatic charge-discharge profiles of AC + 100 during stability testing. The black line shows the presence of an IR drop in the beginning of the stability test (20th cycle), while the red line (8,000th cycle) shows no IR drop.

4.2 Tailored mesoporous carbon/vanadium pentoxide hybrid electrodes for high power pseudocapacitive lithium and sodium intercalation

Simon Fleischmann,^{1,2} Desirée Leistenschneider,³ Valeria Lemkova,^{1,2}
Benjamin Krüner,^{1,2} Marco Zeiger,^{1,2} Lars Borchardt,³ and Volker Presser^{1,2}

¹ INM - Leibniz Institute for New Materials, 66123 Saarbrücken, Germany

² Department of Materials Science and Engineering, Saarland University, 66123 Saarbrücken, Germany

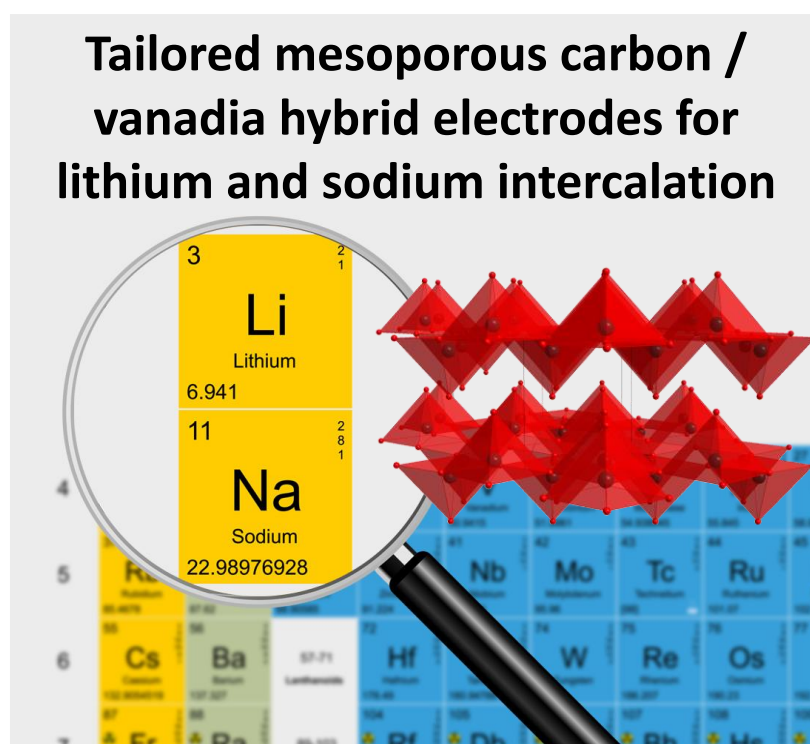
³ Department of Inorganic Chemistry, Technische Universität Dresden, 01062 Dresden, Germany

Citation:

S. Fleischmann, D. Leistenschneider, V. Lemkova, B. Krüner, M. Zeiger, L. Borchardt and V. Presser, *Tailored mesoporous carbon/vanadium pentoxide hybrid electrodes for high power pseudocapacitive lithium and sodium intercalation*, Chem. Mater., **2017**, 29, 8653-8662. (DOI: 10.1021/acs.chemmater.7b02533)

Own contribution:

Planning, ALD synthesis, X-ray diffraction measurements, Raman measurements, thermogravimetric analysis, scanning electron microscopy, electrochemical measurements, writing.



Tailored Mesoporous Carbon/Vanadium Pentoxide Hybrid Electrodes for High Power Pseudocapacitive Lithium and Sodium Intercalation

Simon Fleischmann,^{†,‡} Desirée Leistenschneider,[§] Valeria Lemkova,^{†,‡} Benjamin Krüner,^{†,‡} Marco Zeiger,^{†,‡} Lars Borchardt,^{*,§} and Volker Presser^{*,†,‡}

[†]INM - Leibniz Institute for New Materials, 66123 Saarbrücken, Germany

[‡]Department of Materials Science and Engineering, Saarland University, 66123 Saarbrücken, Germany

[§]Department of Inorganic Chemistry, Technische Universität Dresden, Bergstraße 66, 01062 Dresden, Germany

Supporting Information

ABSTRACT: In this study, atomic layer deposition (ALD) is employed to synthesize hybrid electrode materials of especially tailored mesoporous carbon and vanadium oxide. The highly conformal and precise character of ALD allowed for depositing up to 65 mass % of vanadium oxide inside the 5–20 nm mesopores of the carbon particles, without substantially obstructing internal surface area. The deposited phase was identified as orthorhombic V_2O_5 , and an increasing crystalline order was detected for higher mass loadings. Employing the hybrid material as lithium and sodium intercalation hosts at a rate of 0.5C yielded specific capacities of 310 and 250 mAh/g per V_2O_5 , respectively, while showing predominantly pseudocapacitive behavior, that is, capacitor-like voltage profiles. C-rate benchmarking revealed a retention of about 50% of the maximum capacity for both lithium and sodium at a high rate of 100C. When testing for longevity in lithium-containing electrolyte, a steadily increasing capacity was observed to 116% of the initial value after 2000 cycles. In sodium electrolyte, the capacity faded to 75% after 2000 cycles, which represents one of the most stable performances for sodium intercalation in the literature. Homogeneously distributed vanadium oxide that is locally confined in the tailored carbon mesopores was identified as the reason for enhanced cyclability and rate behavior of the hybrid material.

Tailored mesoporous carbon / vanadia hybrid electrodes for lithium and sodium intercalation



1. INTRODUCTION

Fast-responding electrochemical energy storage (EES) is a key enabling technology for the transition from fossil to renewable energy sources.¹ Electrical double-layer capacitors (EDLCs) rapidly store energy via electrical double-layer formation at the charged interface of high surface area carbon electrodes and the electrolyte.² They provide high specific power, charge efficiency, and stable cycling behavior over many thousands of cycles owing to their purely physical charge storage mechanism of electrosorption.³ However, the specific capacitance of EDLCs is intrinsically limited to about 0.1 F/m² because of a minimum pore size accessible to the electrolyte ions.^{4,5} Among the best known electrode materials for EDLCs are activated carbons (ACs) and carbide-derived carbons (CDCs), which offer a high specific surface area (SSA) of over 2000 m²/g, related to their intraparticle microporosity.^{6,7} Carbon nanomaterials such as carbon nanotubes (CNTs)⁸ or carbon onions^{9,10} can offer even higher specific power, as their exclusively external surface area provides easier access for the electrolyte ions.¹¹

A promising route to enhance the specific energy of EDLCs is the hybridization of carbon electrodes with Faradaic materials.^{12,13} Most prominently, layered metal oxides such as V_2O_5 ,^{14–17} $V_xTi_{1-x}O_2$,^{18,19} Nb_2O_5 ,^{20,21} or MnO_2 ^{22,23} have been

employed, but also sulfur^{24,25} and transition metal dichalcogenides²⁶ recently found application in hybrid electrodes. Layered electrode materials typically store energy via ion intercalation reactions in the interlayer space. In recent years, sodium intercalation hosts for batteries and hybrid supercapacitor devices are explored as an alternative to lithium, because of the lower cost and natural abundance of sodium.^{27,28} The substitution with sodium is a crucial requisite on the path toward more sustainable energy storage systems, as the availability of lithium is geographically limited to few local monopolies.²⁹ Vanadium pentoxide has been widely studied as an intercalation host for lithium ions;^{30–32} however, only few studies were conducted on the intercalation behavior of sodium ions.^{33–35} Moretti et al. employed V_2O_5 aerogel as cathode³⁶ and anode³⁷ material in sodium batteries, yielding performances of about 150 and 200 mAh/g, respectively, at low rates of C/10 and stable cycling over 200 cycles. Hybridizing carbon with vanadium oxide brings synergistic effects concerning rate handling and longevity of the material,^{2,38} but so far, to the best of our knowledge, only one study exists on V_2O_5 /carbon

Received: June 19, 2017

Revised: August 9, 2017

Published: September 27, 2017

hybrids as sodium intercalation hosts. Chen et al. studied layer-structured V_2O_5 /CNT hybrids mixed with conductive additive and demonstrated pseudocapacitive charge storage behavior in sodium-containing electrolyte.³⁹ However, neither the influence of vanadium oxide loading nor half-cell stability was investigated, creating the need for more thorough studies on high power sodium intercalation electrodes.

By implementing nanoscopic layers or clusters of ion intercalation materials into the conductive carbon network, a high power handling can be maintained owing to rapid electron transport and short diffusion paths for the ions to the reactive sites.⁴⁰ A major challenge for the synthesis of hybrid electrodes is achieving a homogeneous distribution of the Faradaic material throughout the carbon matrix.⁴¹ Therefore, appropriate synthesis techniques for metal oxide decoration have to be employed, which include atomic layer deposition (ALD),^{18,42,43} wet-chemical approaches,^{44,45} or vacuum infiltration.⁴⁶ ALD is a vapor phase deposition technique with enhanced thickness control and layer conformity due to its cyclic and self-limiting characteristics.⁴⁷ It has emerged as an advanced method to decorate nanomaterials with metal oxides at molecular precision.⁴⁸ To ensure complete accessibility for the metal oxide coating, carbons with exclusively external surface area such as CNTs, graphene, or carbon onions are preferred as substrates,^{32,49} even though their SSA is inferior to activated carbons with internal porosity. In theory, high SSA porous carbons as substrates would allow for creating larger interfaces between the redox active coating and the electrolyte. However, several studies hybridized microporous carbon with metal oxides, but the attempts were unsuccessful due to pore blocking,²² or showed only little effect because micropores were inaccessible to the metal oxide precursors.⁵⁰

In a recent study, we compared the suitability of carbons with external (carbon onions) and internal surface area (AC) as substrates for atomic layer deposited vanadium oxide.¹⁴ Our data showed that AC can accommodate small mass loadings of vanadium oxide, but loadings that exceed about 50 mass % lead to an obstruction of micropores below 1 nm, leading to inaccessibility of internal surface area to the electrolyte.¹⁴ Our present study explores for the first time a tailored mesoporous carbon (TMC) as an advanced nanoporous carbon substrate that combines high internal surface area with pore volume accessible for ALD.⁵¹ The spherical pores are interconnected, uniform in size, and allow for a homogeneous precursor adsorption during the ALD process and a high accessibility during electrochemical cycling. TMC is synthesized via hard-templating using SiO_2 nanoparticles, which are removed by hydrofluoric acid, leaving spherical mesopores in the size of the former nanoparticles. Herein, we employ TMC for hybridization with a metal oxide, namely, vanadium oxide, via atomic layer deposition. The resulting hybrid electrode will be structurally analyzed and comparatively benchmarked for rate behavior and longevity as lithium and sodium intercalation hosts by electrochemical half-cell experiments.

2. EXPERIMENTAL SECTION

2.1. Preparation of Carbon Substrate Electrodes. First, 10 nm SiO_2 nanoparticles have been synthesized by a modified Stöber method of Watanabe et al.⁵² Therefore, 0.4 g of L-arginine (Roth) has been dissolved in 400 g of deionized water. After adding 23.94 g of tetraethylorthosilicate (TEOS, Sigma-Aldrich), the mixture was stirred at 1000 rpm for 24 h at 70 °C. After cooling down and solvent removal, the nanoparticles were calcinated in air at 550 °C for 3 h.

Then, to obtain the mesoporous carbon, 3.0 g of the SiO_2 nanoparticles were dispersed in a solution of 1.5 g of sucrose (Roth) in 10 mL of water and 0.3 g of H_2SO_4 (95 mass % aqueous solution, Fischer Scientific) was added as a catalyst for the polymerization of the carbon precursor. The dispersion was kept at 100 °C for 3 h and at 160 °C for another 3 h. The obtained polymer- SiO_2 composite was carbonized under an argon atmosphere (flow rate 150 mL/min) at 900 °C for 2 h with a heating rate of 150 °C/min. In the last step, the SiO_2 nanoparticles have been removed by a treatment with hydrofluoric acid (38–40 mass %, Merck) in ethanol and water (volume ratio: 1:1:1) for 24 h. After washing three times with water, the mesoporous carbon was received.

Free-standing TMC electrodes were prepared by dispersion of the carbon powder in ethanol and admixing of 10 mass % polytetrafluoroethylene (PTFE, 60 mass % aqueous solution, Sigma-Aldrich) in a mortar. After thorough mixing, a dough-like mass was obtained and rolled to ca. 50 μm thick electrodes, which were dried in a vacuum oven (2×10^3 Pa) at 120 °C overnight prior to further use. A more detailed description of the electrode preparation procedure can be found in ref 53.

2.2. Plasma-Enhanced Atomic Layer Deposition of Vanadium Oxide. Plasma-enhanced atomic layer deposition (PEALD) was performed directly onto the free-standing TMC electrodes with an open-load atomic layer deposition system (OpAL; Oxford Instruments). Vanadium oxide was synthesized from vanadium(V)-oxy-triisopropoxide (VOTIP; SAFC Hitech) as metalorganic precursor and oxygen plasma as reactant gas. The VOTIP pot was preheated to 45 °C and bubbled by argon carrier gas to deliver the precursor to the reaction chamber. In a typical PEALD cycle, VOTIP was dosed for 20 s and the chamber pressure was set to 66.7 kPa, before argon was used to purge the reactor for 10 s. Then, oxygen was introduced to the chamber and the pressure was set to 21.3 kPa, before remote plasma with a power of 300 W was ignited and applied for 60 s. At the end of each cycle, the reactor was evacuated for 8 s. Prior to the coating process, oxygen plasma was applied for 10 min to the electrodes to create suitable surface functionalities, yielding a more homogeneous precursor adsorption during the first PEALD cycle. The table temperature inside the reactor was kept at 180 °C. The free-standing electrodes were arranged on a sample holder that allows precursor penetration from both sides. This way, a homogeneous precursor penetration along the entire thickness of the electrodes is ensured. The nomenclature of the samples indicates the number of PEALD cycles applied; for example, sample TMC+100VOx was coated with 100 PEALD cycles of vanadium oxide.

2.3. Structural Characterization. Scanning electron microscopy (SEM) was conducted using a JSM-7500F (JEOL) with an operating voltage of 3 kV. Energy dispersive X-ray spectroscopy (EDX) was used to determine the elemental composition with an X-Max-150 (Oxford Instruments) attached to the SEM chamber. The spectra were recorded at 10 kV.

Transmission electron microscopy (TEM) was carried out using a 2100F system (JEOL) at an operating voltage of 200 kV. For sample preparation, electrodes were dispersed in isopropanol by tip sonication and placed on a copper grid with lacey carbon film (Gatan Inc.).

For thermogravimetric analysis (TGA), a TG 209 F1 Libra system (Netzsch) was used. Samples with masses of around 10 mg were heated in alumina crucibles in a synthetic air atmosphere (flow rate: 20 sccm) to 650 °C with a heating rate of 5 °C/min. The mass retention was used to derive the metal oxide content of the samples. The relative mass gain was calculated by dividing the metal oxide mass by the mass of the electrode prior to PEALD.

For X-ray diffraction (XRD) measurements, a D8 Advance XRD (Bruker AXS) diffractometer, calibrated with a corundum standard, was used. It employed a copper X-ray source (Cu $K\alpha$, 40 kV, 40 mA), a Göbel mirror, a 0.5 mm point focus, and a two-dimensional detector (VANTEC-500). The detector covered a 2θ range of about 20° and was positioned at 20°, 40°, and 60° 2θ for 17 min measurement steps. The diffractograms were derived by integration of the areal intensities with a step width of 0.02° 2θ .

Raman measurements were performed with a Renishaw inVia Raman Microscope employing a Nd:YAG laser with an excitation wavelength of 532 nm. A grating with 2400 lines/mm and a 50 \times objective (numeric aperture: 0.9) were used to reach a spectral resolution of about 1.2 cm⁻¹. The laser spot on the sample was about 1 μ m in diameter at a power of 0.05 mW. Spectra were recorded with 10 accumulations and 30 s acquisition time.

An Autosorb iQ System from Quantachrome was used for nitrogen gas sorption analysis (GSA) on free-standing electrode samples with masses of ca. 20 mg. Electrodes were degassed at 150 $^{\circ}$ C for 10 h at 100 Pa, before being measured with liquid nitrogen (-196 $^{\circ}$ C) in a relative pressure range from 5×10^{-7} to 1.0 in 68 steps. The SSA was calculated via the Brunauer–Emmett–Teller (BET) equation⁵⁴ in the linear pressure range using ASQwin software. Quenched-solid density functional theory (QSDFT)⁵⁵ with a slit-cylindrical-spherical pore model was employed to derive the pore size distribution (PSD) and the total pore volume.

2.4. Electrochemical Characterization. The electrochemical characterization was performed in a custom-built three-electrode setup (half-cell), as it has been described in ref 56. In short, TMC/vanadium oxide hybrids with a mass of 1.5–2 mg were employed as working electrodes and an oversized PTFE-bound AC electrode (type YP-80F, Kuraray, 5 mass % PTFE, total mass ca. 15 mg) was used as counter electrode, separated by a 13 mm glass fiber disc (GF/A, Whatman). As current collectors, 12 mm diameter carbon-coated aluminum foil (Zflo 2653, Exopack Technologies) was employed. Instead of the conventionally used lithium reference in carbonate-based electrolytes, AC (type YP-50F, Kuraray) was employed as a quasi-reference electrode⁵⁷ because of the instability of acetonitrile in the presence of metallic lithium.⁵⁸ The cells were dried in a vacuum oven (2×10^3 Pa) prior to electrolyte filling at 120 $^{\circ}$ C overnight, before being transferred to an argon filled glovebox (MBraun Labmaster 130, O₂ and H₂O < 1 ppm) and being vacuum-backfilled with 1 M LiClO₄ and 1 M NaClO₄ in acetonitrile (Sigma-Aldrich) as electrolytes. Acetonitrile was chosen as a solvent because of its increased ionic conductivity as compared to carbonate-based electrolytes, making it more attractive for high-power applications.⁵⁸

For electrochemical measurements, cyclic voltammetry (CV) and galvanostatic cycling with potential limitation (GCPL) were carried out with a potentiostat/galvanostat (VSP300, Bio-Logic). CVs were recorded in a potential range from -1.2 to $+1.0$ V vs. carbon at a scan rate of 1 mV/s. Galvanostatic cycling was performed in the same potential range with specific currents between 0.05 and 20 A/g and C-rates between 0.5C and 50C (for LiClO₄ electrolyte: 1C = 0.167 A/g, for NaClO₄ electrolyte: 1C = 0.107 A/g), respectively, all normalized to the mass of the working electrodes including carbon and vanadium oxide, but excluding PTFE binder. The specific (gravimetric) capacity C_{sp} was calculated from the GCPL data by integration of the cathodic current over the time by eq 1

$$C_{sp} = \frac{\int_{t_0}^t I dt}{m} \quad (1)$$

where I is the cathodic current, t the step time, and m the mass of the working electrode including carbon and vanadium oxide, but excluding PTFE binder.

3. RESULTS AND DISCUSSION

3.1. Structural Characterization. The synthesis process of the TMC/vanadia hybrids is illustrated in Figure 1A. In a first step, the sucrose matrix surrounding the spherical SiO₂ particles is carbonized, before the silica particles are removed from the carbon matrix via hydrofluoric acid treatment. Porous carbon is formed with primary particle sizes between 0.5 and 2.0 μ m (Figure 1B). The carbon particles show a high inner porosity with a uniform distribution of mesopores in the size range of the former silica particles that are engulfed by microporous carbon shells, as can be seen by TEM in Figure 1C. When

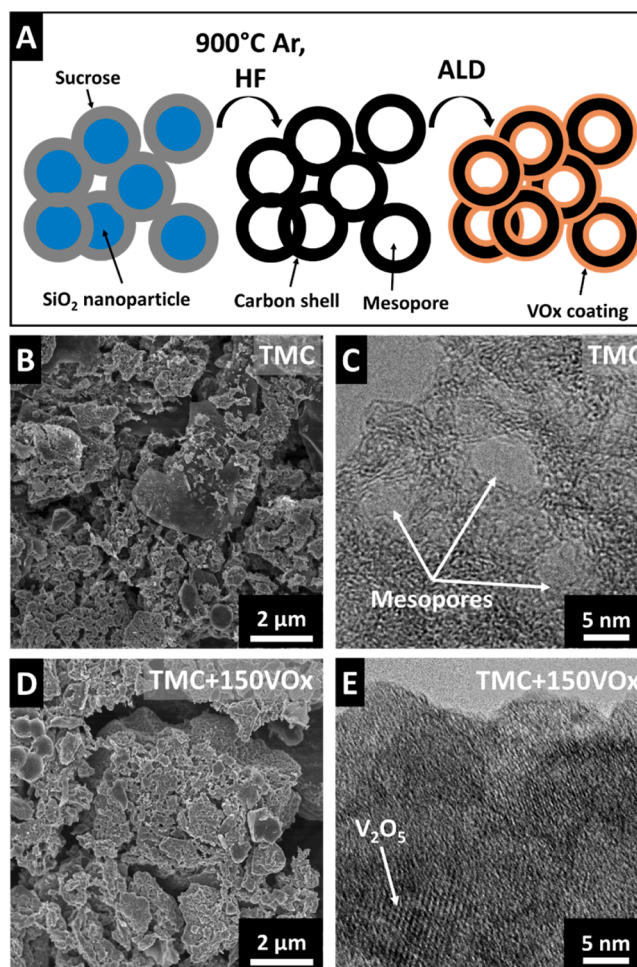


Figure 1. Schematic illustration of the TMC/vanadium oxide synthesis process (A). Scanning and transmission electron micrographs of uncoated TMC electrodes (B, C) and TMC/vanadium oxide hybrid electrodes coated with 150 ALD cycles (D, E).

applying PEALD coating to TMC, no direct changes to the primary particles are visible by SEM (Figure 1D), but vanadium oxide mainly forms in the mesopore volume inside the TMC particles, as can be observed in the TEM image in Figure 1E (exemplified for TMC+150VOx, images of the remaining hybrid samples are found in Figure S1A–C). This confirms the original assumption that mesopores of this size are well accessible to the PEALD process.

To determine the vanadium oxide mass in the hybrid electrodes, thermogravimetric analysis is conducted, and the results are shown in Figure 2A. By heating in synthetic air up to 650 $^{\circ}$ C, all non-vanadia species, that is, carbon and PTFE binder, are burned off. The observed mass loss up to a temperature of about 120 $^{\circ}$ C is caused by evaporation of adsorbed surface water⁵⁹ and has to be considered when calculating the composition of the electrode. The mass retentions are determined to 23, 48, 52, and 64 mass %, leading to dry electrode vanadium oxide contents of 24, 51, 56, and 65 mass % for samples coated with 50, 100, 150, and 200 PEALD cycles, respectively. The electrode composition has to be calculated in the dry state that is representative of the electrodes' electrochemical testing conditions. The mass increase due to vanadium oxide coating increases linearly per PEALD cycle number, as can be seen in Figure 2B. This behavior corresponds with an ideal PEALD process and is

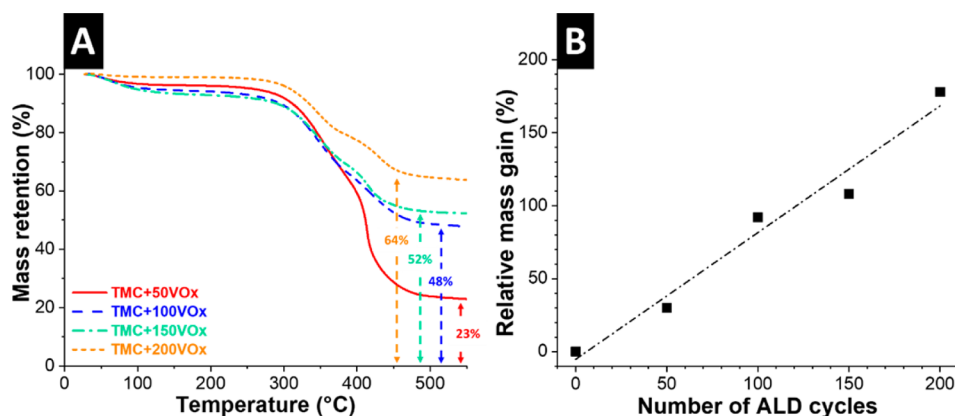


Figure 2. Mass retention of TMC/vanadium oxide hybrid electrode samples measured via thermogravimetric analysis to 650 °C in synthetic air at a heating rate of 5 °C/min (A). Relative mass gain of TMC electrodes coated with vanadium oxide via 50, 100, 150, and 200 ALD cycles (B).

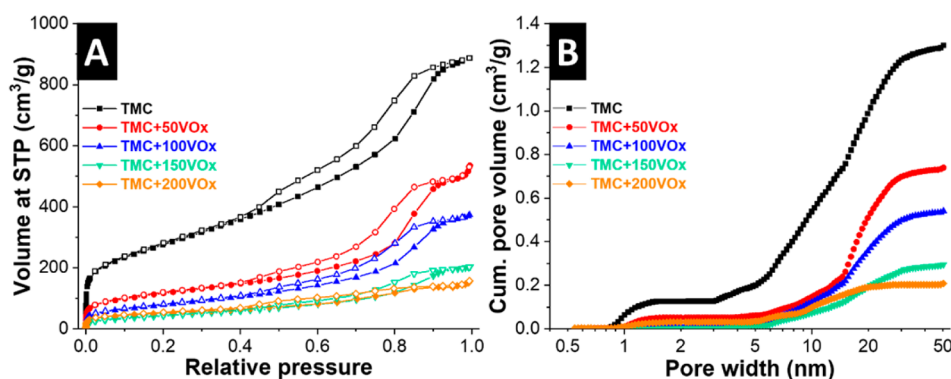


Figure 3. Nitrogen gas sorption isotherms measured at standard temperature and pressure (A), and cumulative pore volume of the TMC and TMC/vanadium oxide hybrid electrodes (B). STP: standard temperature and pressure.

typical for coating exohedral carbon substrates,⁴⁹ that is, carbons with exclusively external surface area.⁶⁰ In contrast, when coating carbons with high inner particle porosity (such as activated carbon),⁶⁰ we would expect to observe a saturation in mass gain with increased number of PEALD cycles.¹⁴ This saturation is related to blocking of internal surface area by growing layers of the coating, making less surface area accessible for further ALD precursor adsorption.¹⁴ The fact that no saturation in mass gain is observed clearly shows that the pore volume remains highly accessible to the reagents and substantial blocking of the internal surface area is avoided when coating TMC via PEALD.

A quantitative examination of the porosity and pore size distribution of TMC and TMC/vanadium oxide hybrids is carried out via nitrogen gas sorption analysis (GSA). The adsorption/desorption isotherms of all samples are shown in Figure 3A. As-synthesized TMC shows an isotherm shape of type IV(a), with an additional step increase of adsorbed volume in the low pressure range resembling a type I(b) shape, according to the 2015 IUPAC classification.⁶¹ The steep increase at low relative pressure is associated with micropores and small mesopores below 2.5 nm, which are found in the microporous carbon shells surrounding the mesopores. The remaining isotherm shows a distinct hysteresis loop that is associated with well-defined mesoporosity. The TMC/vanadium oxide hybrid samples show the same isotherm shape, except for the steep increase at low pressure, which indicates the occupation of small micropores by the coating. This, though, does not obstruct the accessibility of mesopores, as

evidenced by hysteresis loops observed for all coated samples. The hysteresis shape can best be described by type H1, characteristic for ordered mesoporous materials. Additional contribution of H2 is present, typical for cavitation-like mesopores in the structure⁶¹ related to spherical pores with narrow pore necks. Even though the shape of the isotherms is similar for all samples, the magnitude of specific adsorbed volume decreases for higher coating thicknesses. The reasons for this behavior are (1) the growing electrode density with higher mass loadings of vanadium oxide that is heavier than carbon and (2) the decreasing total pore volume associated with gradual vanadium oxide filling.

These qualitative observations are confirmed by quantitative SSA values derived from both BET and QSDFT models, as well as the specific pore volume calculated by QSDFT (Table 1). The SSA_{BET} of TMC electrodes is around 1000 m²/g and decreases to 421, 290, 164, and 186 m²/g for 50, 100, 150, and

Table 1. Comparison of SSA_{BET} , SSA_{DFT} , and Total Pore Volume of TMC and TMC/Vanadium Oxide Hybrid Electrodes

material	SSA_{BET} (m ² /g)	SSA_{DFT} (m ² /g)	pore volume (cm ³ /g)
TMC	999	856	1.30
TMC+50VOx	421	367	0.74
TMC+100VOx	290	247	0.54
TMC+150VOx	164	133	0.30
TMC+200VOx	186	162	0.21

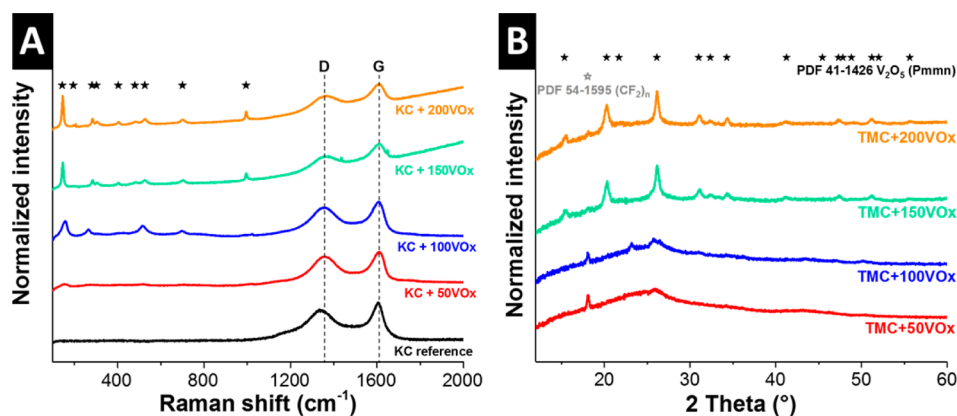


Figure 4. Raman spectra of TMC and TMC/vanadium oxide hybrid electrode samples with stars indicating the ideal peak positions of V_2O_5 (ref ⁶³) and dashed lines indicating the positions of D- and G-peaks (A), as well as X-ray diffractograms of TMC/vanadium oxide hybrid electrode samples including the ideal peak positions of V_2O_5 and PTFE (electrode binder) according to PDF 41-1426 and PDF 54-1595, respectively (B).

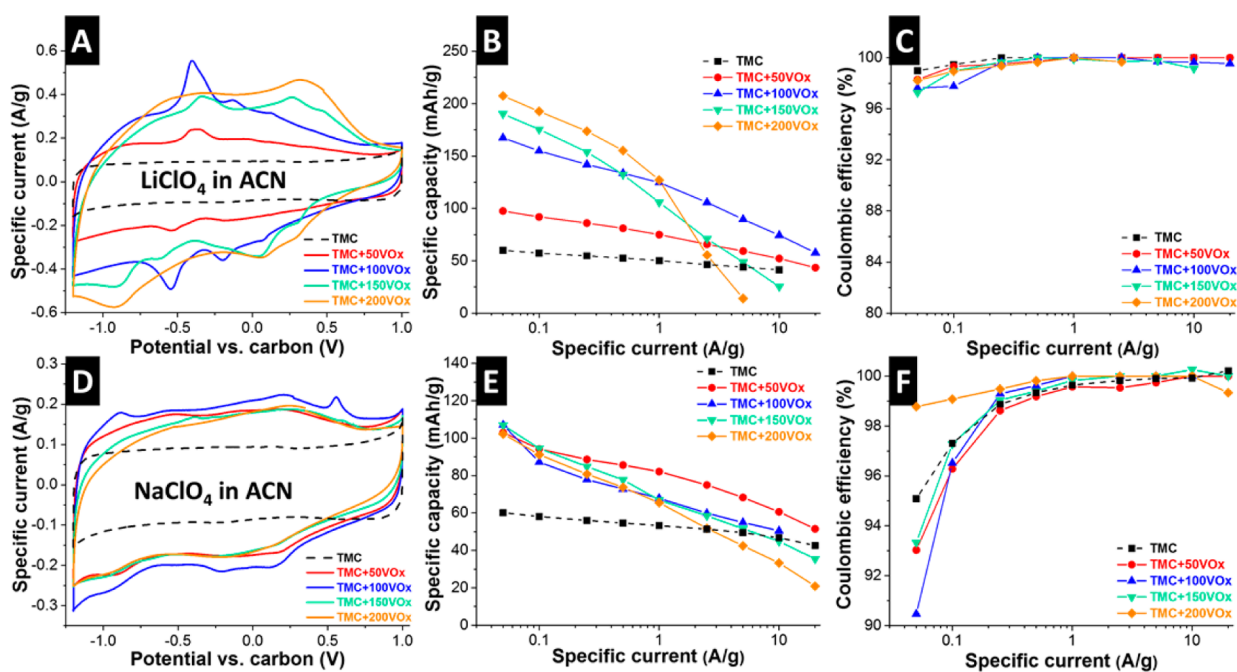


Figure 5. Cyclic voltammograms of all samples measured at 1 mV/s in $LiClO_4$ in ACN (A) and $NaClO_4$ in ACN (D). Specific capacity of all samples including the Coulombic efficiency derived from the cathodic scan of galvanostatic measurements with specific currents ranging from 0.05 to 20 A/g in $LiClO_4$ in ACN (B, C) and $NaClO_4$ in ACN (E, F).

200 ALD cycles of vanadium oxide coating, respectively. The decrease of SSA is, on the one hand, related to the additional mass of vanadium oxide that does not bring any additional surface area and, on the other hand, to the blocking of micropores that can already be observed after 50 ALD cycles. The cumulative pore volume as a function of the pore width derived by QSDFT (Figure 3B) shows a micropore volume of about $0.13 \text{ cm}^3/\text{g}$ for uncoated TMC (that is about 10% of the total pore volume) and significantly smaller values for all coated TMC/vanadium oxide hybrid samples. The largest fraction of pore volume is formed by mesopores in the range of about 6–25 nm for uncoated TMC up to a pore volume of about $1.3 \text{ cm}^3/\text{g}$. The specific pore volume of hybrid samples decreases to 0.74, 0.54, 0.3, and $0.21 \text{ cm}^3/\text{g}$ for 50, 100, 150, and 200 ALD cycles, respectively, because of additional mass and gradual filling of the pore volume with vanadium oxide.

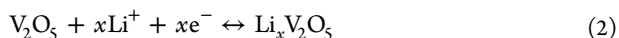
Raman spectra of TMC and TMC/vanadium oxide samples are recorded and given in Figure 4A. All spectra exhibit the characteristic D- and G-peaks of carbon; however, a clear shift to higher vibration frequencies is observed for the D-peak ($1336\text{--}1360 \text{ cm}^{-1}$) and to a smaller extent for the G-peak ($1605\text{--}1610 \text{ cm}^{-1}$) when comparing uncoated to coated samples (dashed line in Figure 4A). This blue shift has been described by Ferrari et al. for disordered graphite⁶² and was recently traced back to surface stresses introduced by nonepitaxially grown ALD layers on the carbon substrate.¹⁴ Furthermore, TMC/vanadium oxide hybrid electrodes exhibit several peaks characteristic for vanadium oxide. Depending on the coating thickness, the observed peaks vary in position and shape. Samples TMC+150VOx and TMC+200VOx show typical sharp signals of V_2O_5 ,⁶³ which broaden and shift significantly for TMC+50VOx and TMC+100VOx. Peak broadening as well as wavenumber shifting is an indication

for smaller domain sizes of vanadium oxide in these samples, in agreement with the literature for nanometer-sized metal oxide structures because of phonon confinement.^{64,65}

X-ray diffraction was carried out for a complementary confirmation of the vanadium oxide oxidation state (Figure 4B). All diffractograms exhibit a peak at $18.5^\circ 2\theta$ associated with the PTFE binder according to PDF 54-1595 and a broad shoulder around $25.5^\circ 2\theta$ from amorphous carbon. The relative intensity of this shoulder decreases for higher coating thicknesses because of the decreasing carbon content of the samples. The vanadium oxide phase of TMC+150VOx and TMC+200VOx is clearly found to be orthorhombic V_2O_5 in *Pmmn* space group, according to PDF 41-1426. Like the observations made in the Raman section, these peaks broaden and decrease in intensity for TMC+50VOx and TMC+100VOx because of nanoscopic domain sizes in the confined mesopore space.

3.2. Electrochemical Characterization. Electrochemical measurements of TMC/vanadium oxide hybrid electrodes were carried out in both lithium- and sodium-containing electrolytes, namely, 1 M $LiClO_4$ and 1 M $NaClO_4$ both dissolved in ACN. Cyclic voltammetry (CV) in lithium electrolyte was performed using TMC and TMC/vanadium oxide electrodes as working electrodes in a half-cell setup (Figure 5A). Uncoated TMC electrodes exhibit a rectangular CV signal characteristic for the purely capacitive charge storage mechanism of porous carbon materials.³

TMC coated with vanadium oxide shows significantly enhanced charge storage capacity, specifically in the negative potential range, where several mechanisms are contributing to the overall charge storage. The enhanced current signal can be divided into two contributions: (1) An enlarged rectangular signal and (2) two small pairs of redox peaks that become more stretched out and show larger potential gaps between cathodic and anodic scan with increasing coating thickness. The rectangular signal originates, for the most part (besides a small capacitive contribution from the carbon substrate), from pseudocapacitive lithium intercalation reactions that have been described for nanocrystalline V_2O_5 in the literature.⁴⁰ Pseudocapacitance describes Faradaic charge storage exhibiting a capacitor-like electrical response in the form of a rectangular CV signal and a sloping voltage profile.⁶⁶ Pseudocapacitive intercalation causes no phase transformation to the host lattice and can occur in parts of the nanometer-sized V_2O_5 coatings where intercalation kinetics are no longer limited by solid-state diffusion.⁴⁰ Diffusion-limited, battery-like lithium intercalation, that is, Faradaic charge storage exhibiting a plateau in the voltage profile,⁶⁶ is observed to a smaller extent and occurs with a redox peak at around -0.6 V vs carbon in the cathodic scan for samples TMC+50VOx and TMC+100VOx. This peak becomes broader and is shifted toward lower potentials for samples TMC+150VOx and TMC+200VOx as a result of decreased electrical conductivity and longer diffusion paths for lithium ions caused by higher coating thicknesses. The reaction mechanism of lithium intercalation in vanadium pentoxide is typically described by eq 2⁶⁷

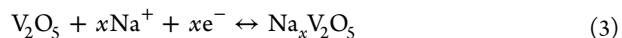


with x representing the mole fraction of intercalated lithium ions.

A quantitative assessment of the specific capacity and rate handling was conducted by galvanostatic cycling at various currents (Figure 5B). It should be noted that all capacity values

are given with respect to the combined mass of carbon and vanadium oxide. While uncoated TMC exhibits a maximum specific capacity of 60 mAh/g, ALD coating with 50 cycles already increased the maximum capacity to 100 mAh/g. For higher mass loadings of vanadium oxide, the capacity increased up to a maximum value of about 210 mAh/g for TMC+200VOx. When analyzing the rate behavior, it is evident that higher vanadium oxide loadings lead to quicker capacity fading at higher rates. The reason for this behavior is the decreasing electrode conductivity as well as longer diffusion paths for lithium ions to the reactive sites. The specific capacity of TMC+150VOx drops to 25 mAh/g at 10 A/g, whereas TMC+200VOx drops to 14 mAh/g already when cycling at 5 A/g. Sample TMC+100VOx offers a good compromise of capacity and rate handling by showing a maximum of about 170 mAh/g with a retention of almost 60 mAh/g at a high rate of 20 A/g (corresponding to a rate of 118C). Consequently, depending on the application, the desired properties in terms of maximum capacity or high rate behavior can be tailored by adjusting the number of ALD cycles. The Coulombic efficiency of all samples is above 97% at low rates and 100% at high rates (Figure 5C).

Cyclic voltammetry of TMC/vanadium oxide electrodes was further carried out in sodium-containing electrolyte (Figure 5D). All CVs are found to exhibit a rather rectangular signal with a slightly increasing current in the negative potential range during the cathodic scan. No major differences in shape or magnitude are visible between all coated samples, except for a more pronounced resistive knee during polarization change for higher vanadium oxide loadings, which is a consequence of higher electrode resistivity. The absence of any distinct redox peak indicates exclusively pseudocapacitive sodium intercalation in TMC/vanadium oxide hybrid electrodes, which aligns with previous reports on bilayered V_2O_5 .^{36,39} This study demonstrates stable pseudocapacitive sodium intercalation behavior for the first time in an orthorhombic V_2O_5 host lattice. The intercalation of sodium in the vanadium oxide structure is described by eq 3:³⁹



The specific capacity of TMC/vanadium oxide electrodes is analyzed by galvanostatic cycling (Figure 5E); the associated Coulombic efficiencies are well above 90% and given in Figure 5F. The maximum capacity for all hybrid electrodes, independent of the vanadium oxide loading, is almost identical with values between 102 and 107 mAh/g. This is in clear contrast to the behavior in lithium-containing electrolyte, where the maximum capacity scales with the vanadium oxide content of the hybrid electrode. The observation can be attributed to two reasons: (1) To a small extent, there is a higher double-layer contribution to the overall capacity of hybrid electrodes with smaller vanadium oxide loadings, since they exhibit slightly higher specific surface areas. However, considering the rapid decrease of micropore volume already seen for TMC+50VOx, this contribution is relatively low. (2) To a larger extent, not the entire volume of the vanadium oxide coating contributes toward charge storage: sodium appears not to reach all possible reactive sites but only intercalates to a certain extent into thicker orthorhombic V_2O_5 structures. This can be understood by considering the larger ionic radius of sodium with 1.02 Å compared to 0.76 Å for lithium.³⁴ When cycling at higher rates, the capacity decreases most rapidly for TMC+200VOx; the highest retention is observed for TMC+50VOx with 51 mAh/g at 20 A/g (corresponds to 187C). Qualitatively, this is the same

Table 2. Literature Overview of V₂O₅-Based Lithium and Sodium Intercalation Electrodes^a

electrode material	electrolyte	max. capacity (mAh/g)	capacity (mAh/g) at maximum rate	cycling stability	reference
OLC/V ₂ O ₅	1 M LiClO ₄ in ACN	129	68 @ 5 A/g	4000	14
AC/V ₂ O ₅	1 M LiClO ₄ in ACN	122	21 @ 5 A/g	8000	14
V ₂ O ₅ nanosheets (+ 20 mass % CB)	1 M LiPF ₆ in EC/DMC	141	80 @ 8C or 1.2 A/g	50	72
porous C/V ₂ O ₅ (+ 20 mass % CB)	1 M LiPF ₆ in EC/DMC	140	118 @ 64C or 9.4 A/g	800	31
graphene/V ₂ O ₅ (+ 15 mass % CB)	1 M LiPF ₆ in EC/DMC	280	210 @ 4C or 1.6 A/g	100	32
TMC/V ₂ O ₅	1 M LiClO ₄ in ACN	170	60 @ 118C or 20 A/g	2000	this work
CNT/V ₂ O ₅ (+ 10 mass % CB)	1 M NaPF ₆ in PC	110	67 @ 72C	no half-cell data	39
V ₂ O ₅ aerogel (+ 20 mass % CB)	1 M NaPF ₆ in PC	150	50 @ 4C or 2.24 A/g	100	36
V ₂ O ₅ nanobelts (+ 20 mass % CB)	1 M NaPF ₆ in EC/DMC	231	134 @ 0.64 A/g	100	33
amorphous V ₂ O ₅	1 M NaPF ₆ in PC	170	80 @ 5C or 1.17 A/g	100	35
TMC/V ₂ O ₅	1 M NaClO ₄ in ACN	107	51 @ 187C or 20 A/g	2000	this work

^aThe specific capacity values are normalized to the “active material”, that means, neglecting the addition of CB as indicated with parentheses. Abbreviations: onion-like carbon (OLC), activated carbon (AC), carbon black (CB), acetonitrile (ACN), ethylene carbonate (EC), dimethyl carbonate (DMC), carbon nanotubes (CNT), propylene carbonate (PC).

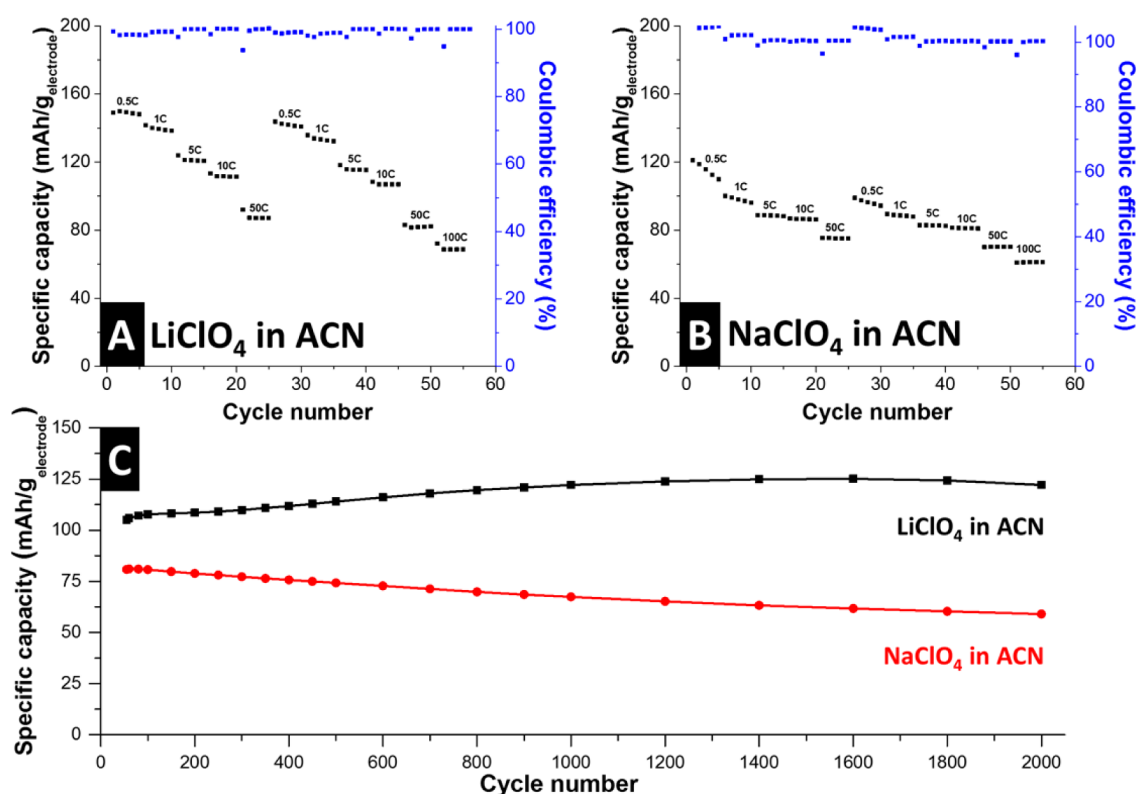


Figure 6. C-rate tests from 0.5C to 100C of sample TMC+100VOx in LiClO₄ in ACN (A), NaClO₄ in ACN (B), and cycling stability in both electrolytes at a rate of 10C (C). The rate of 1C was equivalent to 167 mA/g for Li-containing electrolyte and to 107 mA/g for Na-containing electrolyte.

trend as in lithium electrolyte and a consequence of increasing electrode resistivity with higher vanadium oxide loading. It should be noted that the specific capacities in sodium electrolyte at high rates are on the same level as in lithium electrolyte, despite the larger ionic radius of Na⁺. The reason is the exclusively pseudocapacitive intercalation mechanism of sodium, which is not limited by solid-state diffusion.

To quantitatively separate pseudocapacitive and battery-like intercalation for both electrolyte systems, a kinetic analysis as proposed by Dunn et al. is carried out.⁶⁸ Therefore, CVs of TMC+100VOx samples are recorded in both lithium- and sodium-containing electrolytes at scanning rates between 10 and 500 mV/s (Supporting Information, Figure S2A,B) and the

cathodic current at a fixed potential of -0.75 V vs carbon is traced at every scan rate. By logarithmic plotting of the current over the logarithmic scan rate, a linear relation is observed (Supporting Information, Figure S2C). A slope of 0.5 is typically associated with ideal battery-like, solid-state diffusion limited charge transfer, whereas a slope of 1.0 corresponds to an ideal capacitive behavior that is not diffusion limited.^{69,70} In lithium electrolyte, a slope of 0.62 is calculated, being in line with a mixed battery-like and pseudocapacitive behavior. Contrarily, in sodium electrolyte, a slope of 0.92 corresponds to an almost ideal (pseudo-)capacitive behavior, thereby underlining the reasoning for the good rate behavior of larger Na⁺.

Finally, TMC+100VO_x hybrid electrodes will be subjected to C-rate and stability benchmarking to provide a better comparability to state-of-the-art literature (Table 2). When considering the performance with a lithium electrolyte, a maximum capacity of about 150 mAh/g at a rate of 0.5C is observed (310 mAh/g when normalizing to the vanadium oxide content of the electrode) (Figure 6A). This value is in the range of other state-of-the-art V₂O₅ cathode materials. When increasing the cycling rate up to 100C, TMC+100VO_x shows a capacity retention of 46% compared to the initial value. In the sodium electrolyte, a maximum specific capacity of 120 mAh/g is measured at 0.5C (250 mAh/g normalized to V₂O₅ content) (Figure 6B), which is already among the highest reported for V₂O₅-based cathodes in the literature. In addition, an attractive 51% capacity retention of the maximum value is observed when cycling at 100C. The good rate behavior in both electrolytes is caused by the homogeneously distributed, nanoscopic V₂O₅ clusters and the consequential large interface to the electrolyte, owing to the TMC substrate that additionally provides a superior electric conductivity.

The longevity of the electrodes is monitored by cycling TMC+100VO_x electrodes in lithium- and sodium-containing electrolytes at a rate of 10C (Figure 6C). In lithium electrolyte, no capacity fading is observed after 2000 charge/discharge cycles. Contrarily, the capacity even increased slightly to 116% of the initial value. A similar behavior was observed in a previous study on vanadium oxide/activated carbon hybrid electrodes, where a rising capacity after several thousand cycles was linked to a partial clearance of previously blocked micropores,¹⁴ and the present study confirms this trend for hybrid materials employing endohedral, porous carbon. For sodium-containing electrolyte, very small, constant capacity fading is observed over 2000 cycles to a retention of about 75% of the initial value, related to the higher lattice expansions upon intercalation of larger Na⁺ compared to Li⁺. This is, to the best of our knowledge, the most stable sodium intercalation behavior reported so far for V₂O₅-based electrodes. Interestingly, orthorhombic V₂O₅ was previously reported unsuitable for sodium intercalation because of rapid capacity fading.⁷¹ The reason for the enhanced stability of the TMC/vanadium oxide electrodes appears to result from (1) the nanoscopic vanadium oxide layer size and (2) the confinement of vanadium oxide in spherical mesopores. The nanometer-sized dimensions of the ALD coating are enabled by the homogeneous distribution of TMC pores and contribute toward a significantly reduced strain formation in the vanadium oxide structure upon intercalation of large sodium ions. Further, by locally confining vanadium oxide in the mesopore space, disintegration and the consequential loss of contact with the conductive carbon matrix can be effectively prevented.

4. CONCLUSIONS

We demonstrated the synthesis of tailored mesoporous carbon/vanadium oxide hybrid electrodes via atomic layer deposition with varying metal oxide loadings between 24 and 65 mass %, without observing substantial pore blocking of the carbon substrate. The coating was identified as orthorhombic V₂O₅, and an increasing crystalline ordering was detected for higher vanadium oxide loadings. When employing the hybrid electrodes as lithium and sodium hosts, intercalation was found to be predominantly pseudocapacitive and maximum capacities of 200 mAh/g for lithium and 110 mAh/g for sodium were measured (per electrode mass). Kinetic analysis revealed

that sodium intercalation was less limited by solid-state diffusion than lithium, which resulted in an impressive rate behavior for Na⁺, with 51% retention of the maximum capacity at an ultrahigh rate of 100C. Stability testing showed superior longevity over more than 2000 charge/discharge cycles, which was attributed to reduced strain formation in the nanometer-sized ALD coating in the tailored mesopores and an effective prevention of vanadium oxide disintegration in the confined pore space.

■ ASSOCIATED CONTENT

Supporting Information

The Supporting Information is available free of charge on the ACS Publications website at DOI: 10.1021/acs.chemmater.7b02533.

Transmission electron micrographs and cyclic voltammograms (PDF)

■ AUTHOR INFORMATION

Corresponding Authors

*E-mail: lars.borchardt@tu-dresden.de (L.B.).

*E-mail: volker.presser@leibniz-inm.de (V.P.).

ORCID

Volker Presser: 0000-0003-2181-0590

Notes

The authors declare no competing financial interest.

■ ACKNOWLEDGMENTS

The work at INM was part of the Carbon Metal Oxide Nanohybrid project (CarMON) supported by the Leibniz Association (SAW-2017). V.P. acknowledges funding from the German Federal Ministry for Economic Affairs and Energy (BMW) in support of the HyBaCap project (award number 03ET6113C). We thank Prof. Arzt (INM) for his continuing support. Financial support from the German Federal Ministry of Education and Research (BMBF) within the Mechanocarb project (award number 03SF0498) is gratefully acknowledged by L.B. and D.L.

■ REFERENCES

- (1) Yang, Z.; Zhang, J.; Kintner-Meyer, M. C.; Lu, X.; Choi, D.; Lemmon, J. P.; Liu, J. Electrochemical Energy Storage for Green Grid. *Chem. Rev.* **2011**, *111*, 3577–3613.
- (2) Simon, P.; Gogotsi, Y. Materials for Electrochemical Capacitors. *Nat. Mater.* **2008**, *7*, 845–854.
- (3) Béguin, F.; Presser, V.; Balducci, A.; Frackowiak, E. Carbons and Electrolytes for Advanced Supercapacitors. *Adv. Mater.* **2014**, *26*, 2219–2251.
- (4) Centeno, T. A.; Sereda, O.; Stoeckli, F. Capacitance in Carbon Pores of 0.7 to 15 nm: A Regular Pattern. *Phys. Chem. Chem. Phys.* **2011**, *13*, 12403–12406.
- (5) Jäckel, N.; Rodner, M.; Schreiber, A.; Jeongwook, J.; Zeiger, M.; Aslan, M.; Weingarh, D.; Presser, V. Anomalous or Regular Capacitance? The Influence of Pore Size Dispersity on Double-Layer Formation. *J. Power Sources* **2016**, *326*, 660–671.
- (6) Frackowiak, E.; Béguin, F. Carbon Materials for the Electrochemical Storage of Energy in Capacitors. *Carbon* **2001**, *39*, 937–950.
- (7) Presser, V.; Heon, M.; Gogotsi, Y. Carbide-Derived Carbons—From Porous Networks to Nanotubes and Graphene. *Adv. Funct. Mater.* **2011**, *21*, 810–833.
- (8) Frackowiak, E.; Jurewicz, K.; Delpoux, S.; Béguin, F. Nanotubular Materials for Supercapacitors. *J. Power Sources* **2001**, *97–98*, 822–825.

- (9) Zeiger, M.; Jäckel, N.; Mochalin, V. N.; Presser, V. Review: Carbon Onions for Electrochemical Energy Storage. *J. Mater. Chem. A* **2016**, *4*, 3172–3196.
- (10) Zeiger, M.; Jäckel, N.; Weingarh, D.; Presser, V. Vacuum or Flowing Argon: What is the Best Synthesis Atmosphere for Nanodiamond-Derived Carbon Onions for Supercapacitor Electrodes? *Carbon* **2015**, *94*, 507–517.
- (11) Pech, D.; Brunet, M.; Durou, H.; Huang, P.; Mochalin, V.; Gogotsi, Y.; Taberna, P.-L.; Simon, P. Ultrahigh-Power Micrometre-Sized Supercapacitors Based on Onion-Like Carbon. *Nat. Nanotechnol.* **2010**, *5*, 651–654.
- (12) Zhi, M.; Xiang, C.; Li, J.; Li, M.; Wu, N. Nanostructured Carbon–Metal Oxide Composite Electrodes for Supercapacitors: A Review. *Nanoscale* **2013**, *5*, 72–88.
- (13) Lim, E.; Jo, C.; Lee, J. A Mini Review of Designed Mesoporous Materials for Energy-Storage Applications: From Electric Double-Layer Capacitors to Hybrid Supercapacitors. *Nanoscale* **2016**, *8*, 7827–7833.
- (14) Fleischmann, S.; Jäckel, N.; Zeiger, M.; Krüner, B.; Grobelsek, I.; Formanek, P.; Choudhury, S.; Weingarh, D.; Presser, V. Enhanced Electrochemical Energy Storage by Nanoscopic Decoration of Endohedral and Exohedral Carbon with Vanadium Oxide via Atomic Layer Deposition. *Chem. Mater.* **2016**, *28*, 2802–2813.
- (15) Zeiger, M.; Ariyanto, T.; Krüner, B.; Peter, N. J.; Fleischmann, S.; Etzold, B. J. M.; Presser, V. Vanadium Pentoxide/Carbide-Derived Carbon Core–Shell Hybrid Particles for High Performance Electrochemical Energy Storage. *J. Mater. Chem. A* **2016**, *4*, 18899–18909.
- (16) Yue, Y.; Liang, H. Micro- and Nano-Structured Vanadium Pentoxide (V_2O_5) for Electrodes of Lithium-Ion Batteries. *Adv. Energy Mater.* **2017**, *7*, 1602545.
- (17) An, Q.; Li, Y.; Yoo, H. D.; Chen, S.; Ru, Q.; Mai, L.; Yao, Y. Graphene decorated vanadium oxide nanowire aerogel for long-cycle-life magnesium battery cathodes. *Nano Energy* **2015**, *18*, 265–272.
- (18) Fleischmann, S.; Tolosa, A.; Zeiger, M.; Krüner, B.; Peter, N. J.; Grobelsek, I.; Quade, A.; Kruth, A.; Presser, V. Vanadia–Titania Multilayer Nanodecoration of Carbon Onions via Atomic Layer Deposition for High Performance Electrochemical Energy Storage. *J. Mater. Chem. A* **2017**, *5*, 2792–2801.
- (19) Jampani, P. H.; Velikokhatnyi, O.; Kadakia, K.; Hong, D. H.; Damle, S. S.; Poston, J. A.; Manivannan, A.; Kumta, P. N. High Energy Density Titanium Doped-Vanadium Oxide-Vertically Aligned CNT Composite Electrodes for Supercapacitor Applications. *J. Mater. Chem. A* **2015**, *3*, 8413–8432.
- (20) Tolosa, A.; Krüner, B.; Fleischmann, S.; Jäckel, N.; Zeiger, M.; Aslan, M.; Grobelsek, I.; Presser, V. Niobium Carbide Nanofibers as a Versatile Precursor for High Power Supercapacitor and High Energy Battery Electrodes. *J. Mater. Chem. A* **2016**, *4*, 16003–16016.
- (21) Lim, E.; Kim, H.; Jo, C.; Chun, J.; Ku, K.; Kim, S.; Lee, H. I.; Nam, I.-S.; Yoon, S.; Kang, K.; Lee, J. Advanced Hybrid Supercapacitor Based on a Mesoporous Niobium Pentoxide/Carbon as High-Performance Anode. *ACS Nano* **2014**, *8*, 8968–8978.
- (22) Zeiger, M.; Fleischmann, S.; Krüner, B.; Tolosa, A.; Bechtel, S.; Baltes, M.; Schreiber, A.; Moroni, R.; Vierrath, S.; Thiele, S.; Presser, V. Influence of Carbon Substrate on the Electrochemical Performance of Carbon/Manganese Oxide Hybrids in Aqueous and Organic Electrolytes. *RSC Adv.* **2016**, *6*, 107163–107179.
- (23) Wang, Y.; Lai, W.; Wang, N.; Jiang, Z.; Wang, X.; Zou, P.; Lin, Z.; Fan, H. J.; Kang, F.; Wong, C.-P.; Yang, C. A Reduced Graphene Oxide/Mixed-Valence Manganese Oxide Composite Electrode for Tailorable and Surface Mountable Supercapacitors with High Capacitance and Super-Long Life. *Energy Environ. Sci.* **2017**, *10*, 941–949.
- (24) Borchardt, L.; Oschatz, M.; Kaskel, S. Carbon Materials for Lithium Sulfur Batteries—Ten Critical Questions. *Chem. - Eur. J.* **2016**, *22*, 7324–7351.
- (25) Choudhury, S.; Zeiger, M.; Massuti-Ballester, P.; Fleischmann, S.; Formanek, P.; Borchardt, L.; Presser, V. Carbon Onion-Sulfur Hybrid Cathodes for Lithium-Sulfur Batteries. *Sustainable Energy Fuels* **2017**, *1*, 84–94.
- (26) Stephenson, T.; Li, Z.; Olsen, B.; Mitlin, D. Lithium Ion Battery Applications of Molybdenum Disulfide (MoS_2) Nanocomposites. *Energy Environ. Sci.* **2014**, *7*, 209–231.
- (27) Slater, M. D.; Kim, D.; Lee, E.; Johnson, C. S. Sodium-Ion Batteries. *Adv. Funct. Mater.* **2013**, *23*, 947–958.
- (28) Lim, E.; Jo, C.; Kim, M. S.; Kim, M. H.; Chun, J.; Kim, H.; Park, J.; Roh, K. C.; Kang, K.; Yoon, S.; Lee, J. High-Performance Sodium-Ion Hybrid Supercapacitor Based on Nb_2O_5 @Carbon Core–Shell Nanoparticles and Reduced Graphene Oxide Nanocomposites. *Adv. Funct. Mater.* **2016**, *26*, 3711–3719.
- (29) Ortiz-Vitoriano, N.; Drewett, N. E.; Gonzalo, E.; Rojo, T. High Performance Manganese-Based Layered Oxide Cathodes: Overcoming the Challenges of Sodium Ion Batteries. *Energy Environ. Sci.* **2017**, *10*, 1051–1074.
- (30) Chen, Z.; Augustyn, V.; Wen, J.; Zhang, Y.; Shen, M.; Dunn, B.; Lu, Y. High-Performance Supercapacitors Based on Intertwined CNT/ V_2O_5 Nanowire Nanocomposites. *Adv. Mater.* **2011**, *23*, 791–795.
- (31) Zhang, Y.; Pan, A.; Wang, Y.; Wei, W.; Su, Y.; Hu, J.; Cao, G.; Liang, S. Dodecahedron-Shaped Porous Vanadium Oxide and Carbon Composite for High-Rate Lithium Ion Batteries. *ACS Appl. Mater. Interfaces* **2016**, *8*, 17303–17311.
- (32) Liu, H.; Yang, W. Ultralong Single Crystalline V_2O_5 Nanowire/Graphene Composite Fabricated by a Facile Green Approach and its Lithium Storage Behavior. *Energy Environ. Sci.* **2011**, *4*, 4000–4008.
- (33) Su, D.; Dou, S.; Wang, G. Hierarchical Orthorhombic V_2O_5 Hollow Nanospheres as High Performance Cathode Materials for Sodium-Ion Batteries. *J. Mater. Chem. A* **2014**, *2*, 11185–11194.
- (34) Tang, P. E.; Sakamoto, J. S.; Baudrin, E.; Dunn, B. V_2O_5 Aerogel as a Versatile Host for Metal Ions. *J. Non-Cryst. Solids* **2004**, *350*, 67–72.
- (35) Uchaker, E.; Zheng, Y.; Li, S.; Candelaria, S.; Hu, S.; Cao, G. Better Than Crystalline: Amorphous Vanadium Oxide for Sodium-Ion Batteries. *J. Mater. Chem. A* **2014**, *2*, 18208–18214.
- (36) Moretti, A.; Maroni, F.; Osada, I.; Nobili, F.; Passerini, S. V_2O_5 Aerogel as a Versatile Cathode Material for Lithium and Sodium Batteries. *ChemElectroChem* **2015**, *2*, 529–537.
- (37) Moretti, A.; Secchiarioli, M.; Buchholz, D.; Giuli, G.; Marassi, R.; Passerini, S. Exploring the Low Voltage Behavior of V_2O_5 Aerogel as Intercalation Host for Sodium Ion Battery. *J. Electrochem. Soc.* **2015**, *162*, A2723–A2728.
- (38) Zhao, Y.; Wang, L. P.; Sougrati, M. T.; Feng, Z.; Leconte, Y.; Fisher, A.; Srinivasan, M.; Xu, Z. A Review on Design Strategies for Carbon Based Metal Oxides and Sulfides Nanocomposites for High Performance Li and Na Ion Battery Anodes. *Adv. Energy Mater.* **2017**, *7*, 1601424.
- (39) Chen, Z.; Augustyn, V.; Jia, X.; Xiao, Q.; Dunn, B.; Lu, Y. High-Performance Sodium-Ion Pseudocapacitors Based on Hierarchically Porous Nanowire Composites. *ACS Nano* **2012**, *6*, 4319–4327.
- (40) Augustyn, V.; Simon, P.; Dunn, B. Pseudocapacitive Oxide Materials for High-Rate Electrochemical Energy Storage. *Energy Environ. Sci.* **2014**, *7*, 1597–1614.
- (41) Gu, W.; Yushin, G. Review of Nanostructured Carbon Materials for Electrochemical Capacitor Applications: Advantages and Limitations of Activated Carbon, Carbide-Derived Carbon, Zeolite-Templated Carbon, Carbon Aerogels, Carbon Nanotubes, Onion-Like Carbon, and Graphene. *Wiley Interdiscip. Rev.: Energy Environ.* **2014**, *3*, 424–473.
- (42) Wang, G.; Lu, C.; Zhang, X.; Wan, B.; Liu, H.; Xia, M.; Gou, H.; Xin, G.; Lian, J.; Zhang, Y. Toward Ultrafast Lithium Ion Capacitors: a Novel Atomic Layer Deposition Seeded Preparation of $Li_4Ti_5O_{12}$ /Graphene Anode. *Nano Energy* **2017**, *36*, 46–57.
- (43) Ahmed, B.; Anjum, D. H.; Gogotsi, Y.; Alshareef, H. N. Atomic Layer Deposition of SnO_2 on MXene for Li-Ion Battery Anodes. *Nano Energy* **2017**, *34*, 249–256.
- (44) Srimuk, P.; Ries, L.; Zeiger, M.; Fleischmann, S.; Jäckel, N.; Tolosa, A.; Krüner, B.; Aslan, M.; Presser, V. High Performance Stability of Titania Decorated Carbon for Desalination with Capacitive Deionization in Oxygenated Water. *RSC Adv.* **2016**, *6*, 106081–106089.

- (45) Srimuk, P.; Zeiger, M.; Jäckel, N.; Tolosa, A.; Krüner, B.; Fleischmann, S.; Grobelsek, I.; Aslan, M.; Shvartsev, B.; Suss, M. E.; Presser, V. Enhanced Performance Stability of Carbon/Titania Hybrid Electrodes During Capacitive Deionization of Oxygen Saturated Saline Water. *Electrochim. Acta* **2017**, *224*, 314–328.
- (46) Zhao, E.; Qin, C.; Jung, H.-R.; Berdichevsky, G.; Nese, A.; Marder, S.; Yushin, G. Lithium Titanate Confined in Carbon Nanopores for Asymmetric Supercapacitors. *ACS Nano* **2016**, *10*, 3977–3984.
- (47) George, S. M. Atomic Layer Deposition: An Overview. *Chem. Rev.* **2010**, *110*, 111–131.
- (48) Kim, H. G.; Lee, H.-B.-R. Atomic Layer Deposition on 2D Materials. *Chem. Mater.* **2017**, *29*, 3809–3826.
- (49) Boukhalifa, S.; Evanoff, K.; Yushin, G. Atomic Layer Deposition of Vanadium Oxide on Carbon Nanotubes for High-Power Supercapacitor Electrodes. *Energy Environ. Sci.* **2012**, *5*, 6872–6879.
- (50) Daubert, J. S.; Lewis, N. P.; Gotsch, H. N.; Mundy, J. Z.; Monroe, D. N.; Dickey, E. C.; Losego, M. D.; Parsons, G. N. Effect of Meso- and Micro-Porosity in Carbon Electrodes on Atomic Layer Deposition of Pseudocapacitive V_2O_5 for High Performance Supercapacitors. *Chem. Mater.* **2015**, *27*, 6524–6534.
- (51) Borchardt, L.; Oschatz, M.; Kaskel, S. Tailoring Porosity in Carbon Materials for Supercapacitor Applications. *Mater. Horiz.* **2014**, *1*, 157–168.
- (52) Watanabe, R.; Yokoi, T.; Kobayashi, E.; Otsuka, Y.; Shimojima, A.; Okubo, T.; Tatsumi, T. Extension of Size of Monodisperse Silica Nanospheres and their Well-Ordered Assembly. *J. Colloid Interface Sci.* **2011**, *360*, 1–7.
- (53) Jäckel, N.; Weingarh, D.; Schreiber, A.; Krüner, B.; Zeiger, M.; Tolosa, A.; Aslan, M.; Presser, V. Performance Evaluation of Conductive Additives for Activated Carbon Supercapacitors in Organic Electrolyte. *Electrochim. Acta* **2016**, *191*, 284–298.
- (54) Brunauer, S.; Emmett, P. H.; Teller, E. Adsorption of Gases in Multimolecular Layers. *J. Am. Chem. Soc.* **1938**, *60*, 309–319.
- (55) Gor, G. Y.; Thommes, M.; Cychosz, K. A.; Neimark, A. V. Quenched Solid Density Functional Theory Method for Characterization of Mesoporous Carbons by Nitrogen Adsorption. *Carbon* **2012**, *50*, 1583–1590.
- (56) Weingarh, D.; Zeiger, M.; Jäckel, N.; Aslan, M.; Feng, G.; Presser, V. Graphitization as a Universal Tool to Tailor the Potential-Dependent Capacitance of Carbon Supercapacitors. *Adv. Energy Mater.* **2014**, *4*, 1400316.
- (57) Lee, J.; Jäckel, N.; Kim, D.; Widmaier, M.; Sathyamoorthi, S.; Srimuk, P.; Kim, C.; Fleischmann, S.; Zeiger, M.; Presser, V. Porous Carbon as a Quasi-Reference Electrode in Aqueous Electrolytes. *Electrochim. Acta* **2016**, *222*, 1800–1805.
- (58) Widmaier, M.; Krüner, B.; Jäckel, N.; Aslan, M.; Fleischmann, S.; Engel, C.; Presser, V. Carbon as Quasi-Reference Electrode in Unconventional Lithium-Salt Containing Electrolytes for Hybrid Battery/Supercapacitor Devices. *J. Electrochem. Soc.* **2016**, *163*, A2956–A2964.
- (59) Athouël, L.; Moser, F.; Dugas, R.; Crosnier, O.; Bélanger, D.; Brousse, T. Variation of the MnO_2 Birnessite Structure upon Charge/Discharge in an Electrochemical Supercapacitor Electrode in Aqueous Na_2SO_4 Electrolyte. *J. Phys. Chem. C* **2008**, *112*, 7270–7277.
- (60) Huang, J.; Sumpter, B. G.; Meunier, V.; Yushin, G.; Portet, C.; Gogotsi, Y. Curvature Effects in Carbon Nanomaterials: Exohedral versus Endohedral Supercapacitors. *J. Mater. Res.* **2010**, *25*, 1525–1531.
- (61) Thommes, M.; Kaneko, K.; Neimark, A. V.; Olivier, J. P.; Rodriguez-Reinoso, F.; Rouquerol, J.; Sing, K. S. Physisorption of Gases, with Special Reference to the Evaluation of Surface Area and Pore Size Distribution (IUPAC Technical Report). *Pure Appl. Chem.* **2015**, *87*, 1051–1069.
- (62) Ferrari, A. C.; Robertson, J. Interpretation of Raman Spectra of Disordered and Amorphous Carbon. *Phys. Rev. B: Condens. Matter Mater. Phys.* **2000**, *61*, 14095.
- (63) Baddour-Hadjean, R.; Pereira-Ramos, J.; Navone, C.; Smirnov, M. Raman microspectrometry study of electrochemical lithium intercalation into sputtered crystalline V_2O_5 thin films. *Chem. Mater.* **2008**, *20*, 1916–1923.
- (64) Xu, C.; Zhang, P.; Yan, L. Blue Shift of Raman Peak from Coated TiO_2 Nanoparticles. *J. Raman Spectrosc.* **2001**, *32*, 862–865.
- (65) Bersani, D.; Lottici, P.; Ding, X.-Z. Phonon Confinement Effects in the Raman Scattering by TiO_2 Nanocrystals. *Appl. Phys. Lett.* **1998**, *72*, 73–75.
- (66) Simon, P.; Gogotsi, Y.; Dunn, B. Where Do Batteries End and Supercapacitors Begin? *Science* **2014**, *343*, 1210–1211.
- (67) Livage, J. Vanadium Pentoxide Gels. *Chem. Mater.* **1991**, *3*, 578–593.
- (68) Wang, J.; Polleux, J.; Lim, J.; Dunn, B. Pseudocapacitive Contributions to Electrochemical Energy Storage in TiO_2 (Anatase) Nanoparticles. *J. Phys. Chem. C* **2007**, *111*, 14925–14931.
- (69) Anjos, D. M.; McDonough, J. K.; Perre, E.; Brown, G. M.; Overbury, S. H.; Gogotsi, Y.; Presser, V. Pseudocapacitance and Performance Stability of Quinone-Coated Carbon Onions. *Nano Energy* **2013**, *2*, 702–712.
- (70) Fleischmann, S.; Zeiger, M.; Jäckel, N.; Krüner, B.; Lemkova, V.; Widmaier, M.; Presser, V. Tuning Pseudocapacitive and Battery-Like Lithium Intercalation in Vanadium Dioxide/Carbon Onion Hybrids for Asymmetric Supercapacitor Anodes. *J. Mater. Chem. A* **2017**, *5*, 13039.
- (71) Tepavcevic, S.; Xiong, H.; Stamenkovic, V. R.; Zuo, X.; Balasubramanian, M.; Prakapenka, V. B.; Johnson, C. S.; Rajh, T. Nanostructured Bilayered Vanadium Oxide Electrodes for Rechargeable Sodium-Ion Batteries. *ACS Nano* **2012**, *6*, 530–538.
- (72) Su, Y.; Pan, A.; Wang, Y.; Huang, J.; Nie, Z.; An, X.; Liang, S. Template-Assisted Formation of Porous Vanadium Oxide as High Performance Cathode Materials for Lithium Ion Batteries. *J. Power Sources* **2015**, *295*, 254–258.

Electronic Supplementary Information

**Tailored Mesoporous Carbon/Vanadium Pentoxide
Hybrid Electrodes for High Power Pseudocapacitive
Lithium and Sodium Intercalation**

**Simon Fleischmann,^{1,2} Desirée Leistenschneider,³ Valeria Lemkova,^{1,2}
Benjamin Krüner,^{1,2} Marco Zeiger,^{1,2} Lars Borchardt,^{3,*} and Volker Presser^{1,2,*}**

¹ INM - Leibniz Institute for New Materials, 66123 Saarbrücken, Germany

² Department of Materials Science and Engineering, Saarland University, 66123 Saarbrücken, Germany

³ Department of Inorganic Chemistry, Technische Universität Dresden, Bergstraße 66, 01062 Dresden, Germany

* Corresponding authors' eMails: LB: lars.borchardt@tu-dresden.de; VP: volker.presser@leibniz-inm.de

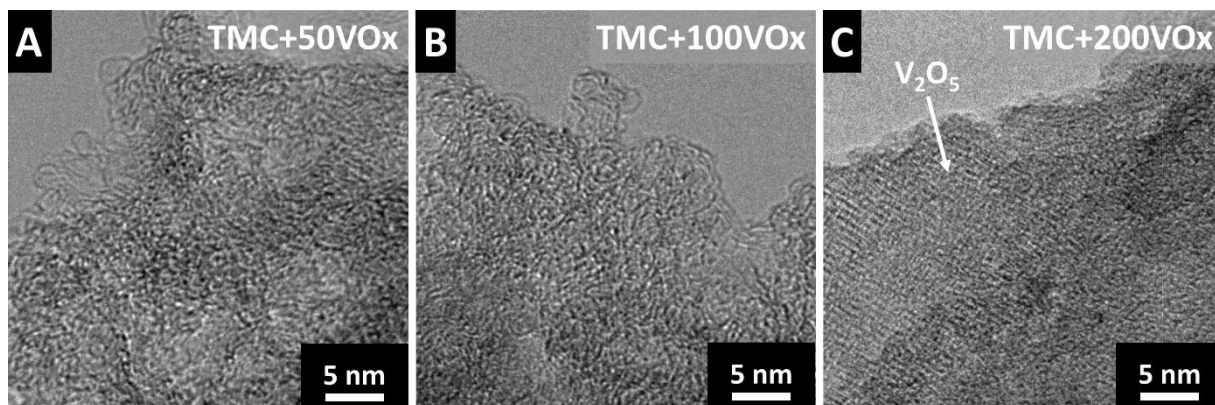


Figure S1: Transmission electron micrographs of samples TMC+50VOx (A), TMC+100VOx (B), and TMC+200VOx (C). Identification of vanadia in A and B is not easily possible because of the predominantly amorphous structure and/or small domain sizes. For sample TMC+200VOx, a larger vanadia domain size as compared to TMC+150VOx is clearly visible.

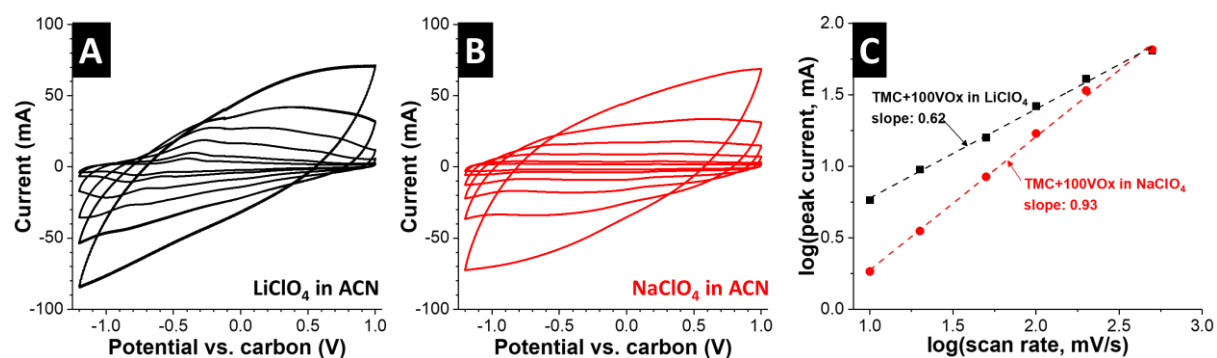


Figure S2: Cyclic voltammograms of TMC+100VOx in (A) LiClO₄ in ACN and (B) NaClO₄ in ACN at varying scan rates between 10-500 mV/s. (C) Logarithmic plots of cathodic current at -0.75 V vs. carbon against logarithmic scan rate, as well as a linear regression.

4.3 Tuning pseudocapacitive and battery-like lithium intercalation in vanadium dioxide/carbon onion hybrids for asymmetric supercapacitor anodes

Simon Fleischmann,^{1,2} Marco Zeiger,^{1,2} Nicolas Jäckel,^{1,2} Benjamin Krüner,^{1,2}
Valeria Lemkova,^{1,2} Mathias Widmaier,^{2,3} and Volker Presser^{1,2}

¹ INM – Leibniz Institute for New Materials, 66123 Saarbrücken, Germany

² Department of Materials Science and Engineering, Saarland University, 66123 Saarbrücken, Germany

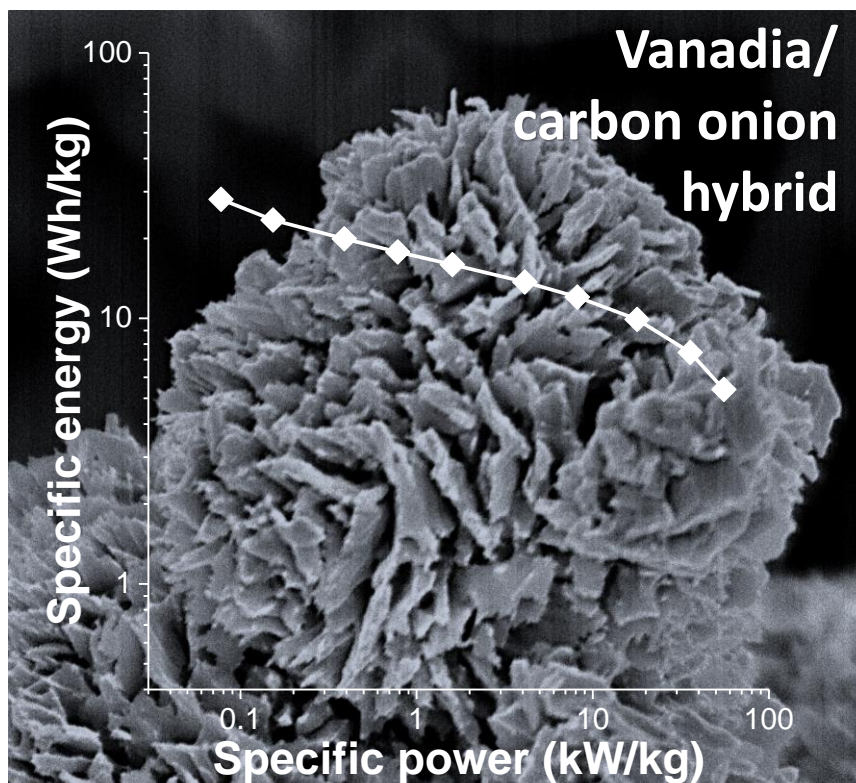
³ Robert Bosch GmbH, 70049 Stuttgart, Germany

Citation:

S. Fleischmann, M. Zeiger, N. Jäckel, B. Krüner, V. Lemkova, M. Widmaier and V. Presser, *Tuning pseudocapacitive and battery-like lithium intercalation in vanadium dioxide/carbon onion hybrids for asymmetric supercapacitor anodes*, *J. Mater. Chem. A*, **2017**, 5, 13039-13051. (DOI: 10.1039/c7ta02564e)

Own contribution:

Planning, hydrothermal synthesis, X-ray diffraction measurements, Raman measurements, thermogravimetric analysis, electrochemical measurements, writing.



Cite this: *J. Mater. Chem. A*, 2017, 5, 13039

Tuning pseudocapacitive and battery-like lithium intercalation in vanadium dioxide/carbon onion hybrids for asymmetric supercapacitor anodes†

Simon Fleischmann,^{ab} Marco Zeiger,^{ab} Nicolas Jäckel,^{ab} Benjamin Krüner,^{ab} Valeria Lemkova,^{ab} Mathias Widmaier^{bc} and Volker Presser^{ab}

The study presents the synthesis of vanadium oxide/carbon onion hybrid materials. Flower-like vanadium oxide nanostructures nucleate on carbon onion nanoparticles under hydrothermal conditions, forming a highly intertwined network. By varying the amount of added carbon onions during the synthesis, the number of possible nucleation sites can be adjusted, resulting in the preferential growth of vanadium dioxide in either $P2_1/c$ or $C2/m$ space group. When employed as a lithium intercalation electrode, $P2_1/c$ VO_2 exhibits capacitor-like (pseudocapacitive) lithium intercalation, whereas $C2/m$ VO_2 shows battery-like intercalation peaks with a maximum capacity of 127 mA h g^{-1} . By selecting an optimum ratio and thereby combining both intercalation mechanisms, enhanced kinetics with discharge capacities of 45 mA h g^{-1} and 29 mA h g^{-1} at high rates of 50 A g^{-1} and 100 A g^{-1} (equal to 394C and 788C) are obtained. This behavior can be translated to a device level by using the material as anodes in asymmetric supercapacitors with activated carbon cathodes, yielding a maximum specific energy of 45 W h kg^{-1} and a high power of 58 kW kg^{-1} , while longevity over 5000 charge/discharge cycles is demonstrated.

Received 23rd March 2017
Accepted 18th May 2017

DOI: 10.1039/c7ta02564e

rsc.li/materials-a

1. Introduction

Fast and reversible energy storage devices are in high demand, with applications ranging from electric vehicles to temporary storage of intermittent renewable energy sources, such as solar or wind power.¹ Electrical double-layer capacitors (EDLCs) have emerged as a promising technology for high power electrochemical energy storage.^{2,3} This kind of supercapacitor stores energy *via* the formation of an electrical double-layer at the fluid/solid interface, that is, electrosorption of electrolyte ions at the charged electrode of opposite polarity.⁴ Their purely physical charge storage mechanism enables high charge and discharge rates, yet the specific energy is much smaller compared to state-of-the-art lithium ion batteries.⁵ Typical EDLC electrodes consist of high specific surface area (SSA) carbons that can be distinguished into two groups:^{6,7} carbons with a high inner porosity, such as activated carbon⁸ or carbide-derived carbon (CDC),^{9,10} and carbons that exhibit exclusively external surfaces, such as carbon onions^{11,12} or carbon nanotubes (CNTs).¹³ The double-layer capacitance of EDLCs is

limited to about 0.1 F m^{-2} , related to a minimum in accessible pore size that is in the range of the ion size.^{14,15}

One promising strategy for increasing the energy storage capacity is the implementation of redox-active materials, such as metal oxides,^{16–18} surface functional groups,^{19,20} or redox-active electrolytes,^{21–23} to extend the purely capacitive carbon system by faradaic charge storage (redox reactions). Depending on the electrochemical response of the material, redox-active systems are either described as pseudocapacitive (linear charge–voltage profile, such as MnO_2 (ref. 24 and 25) or MXene ^{26,27}), or as battery-like (well-defined plateaus in the charge–voltage profile, such as VO_2 ,²⁸ V_2O_5 ,²⁹ or $\text{V}_x\text{Ti}_{1-x}\text{O}_2$,³⁰ among others).^{31,32} The synthesis of hybrid electrodes often employs wet-chemical approaches,^{33–35} atomic layer deposition,^{36,37} electrochemical deposition,³⁸ or drop-casting.^{39,40} Apart from tuning the intrinsic properties of the electrodes, optimization of the cell setup by using different electrodes as anodes and cathodes is fundamental for further improvements. For that purpose, hybrid or asymmetric supercapacitors typically employ a metal oxide anode that utilizes a battery-like energy storage mechanism, *versus* an EDLC cathode.^{41–43} In order to achieve an optimized potential profile at the anode and cathode, the different specific capacities of the two materials have to be taken into account and be charge balanced by adjusting the electrode masses, since they determine the distribution of the applied cell voltage.⁴⁴

The main obstacle of an asymmetric supercapacitor setup is to overcome the sluggish kinetics of the metal oxide anode,¹⁸

^a*INM – Leibniz Institute for New Materials, 66123 Saarbrücken, Germany. E-mail: volker.presser@leibniz-inm.de*

^b*Department of Materials Science and Engineering, Saarland University, 66123 Saarbrücken, Germany*

^c*Robert Bosch GmbH, 70049 Stuttgart, Germany*

† Electronic supplementary information (ESI) available. See DOI: 10.1039/c7ta02564e

creating a demand for novel hybrid materials that enable significantly faster rates.³¹ Therefore, recent studies have focused on (i) the use of tailored mesoporous carbons that allow for the efficient incorporation of $\text{Li}_4\text{Ti}_5\text{O}_{12}$ (e.g., ref. 45, up to 105 mA h g^{-1} at 350°C) or (ii) the synthesis of core-shell particles consisting of crystalline/amorphous LiFePO_4 mixtures encapsulated by carbon (e.g., ref. 46, up to 36 mA h g^{-1} at 300°C). The most commonly employed strategy is admixing conductive additives with the metal oxide, such as carbon black or carbon onions.^{47,48} Particularly, the latter exhibit superior properties when used as conductive additives in supercapacitor electrodes.⁴⁹ Carbon onions are spherical carbon nanoparticles consisting of several concentric sp^2 -hybridized carbon shells in the size range between 5 and 10 nm, depending on the synthesis method.¹¹ By annealing of detonation nanodiamonds in an inert gas atmosphere,⁵⁰ such as argon,⁵¹ a gradual transformation of diamond-like carbon to graphitic carbon is observed between 700 and 1700°C . Complete sp^3 -to- sp^2 conversion at around 1700°C yields a high electrical conductivity of ca. 4 S cm^{-1} .⁵² Besides the use as conductive additives, carbon onions have also served as substrates in hybrid electrodes.^{24,30,53} Particular attractions of carbon onions as substrates are the high interparticle pore volume and specific surface area of up to $1.2 \text{ cm}^3 \text{ g}^{-1}$ and $600 \text{ m}^2 \text{ g}^{-1}$, respectively, providing a large space for the deposition of redox-active materials within the conductive network.^{30,36}

Vanadium oxides have been widely researched as redox-active materials for lithium and sodium battery cathodes.^{54,55} They typically exhibit two-dimensional sheet structures formed by corner/edge/face-sharing octahedra⁵⁶ that accommodate ion intercalation reactions. Phases of V_2O_5 and VO_2 are typically studied as a negative electrode in a half-cell setup against lithium foil, exhibiting several steps of lithiation, depending on the applied potential vs. Li/Li^+ and on the crystal structure.^{28,56-58} Yet, only a few studies exist on vanadium oxide hybrid electrodes at a device level,^{33,59} that is, in a full-cell setup.

In a recent study, we investigated the properties of carbon onions coated with partially amorphous vanadium pentoxide *via* atomic layer deposition.³⁶ When measured in an asymmetric supercapacitor setup against an activated carbon cathode, we observed a maximum specific energy and power of 38 W h kg^{-1} and 2 kW kg^{-1} , respectively. Core-shell particles consisting of carbide-derived carbon shells and vanadium pentoxide cores showed even higher values of up to 84 W h kg^{-1} and 6 kW kg^{-1} with CDC as the cathode.⁶⁰ The high performance of the core-shell particles was a consequence of the continuous carbon network that successfully enhanced the sluggish kinetics of vanadium pentoxide, demonstrating the high impact of the carbon substrate on the electrochemical performance of anodes in a full-cell. Consequently, when designing advanced anodes for asymmetric supercapacitors, it is crucial to carefully tune their structural properties to achieve a synergistic interaction between the metal oxide (for lithium intercalation) and carbon (providing electrical conductivity).⁵

In this study, we investigate the unique ability to influence the crystal structure of vanadium dioxide by using carbon onions as the substrate or as the admixed conductive additive

for hydrothermally synthesized vanadia nanostructures, to obtain vanadia/carbon hybrids or composites. Carbon onions added directly to the solution during hydrothermal growth serve as nucleation sites for vanadium dioxide and are closely built into the nanohybrid, providing improved performance stability and rate behavior. Controlling the number of possible nucleation sites allowed us to adjust the crystal structure of vanadium dioxide. Our results reveal an optimum ratio of $C2/m$ and $P2_1/c$ for an enhanced capacity at ultrahigh discharge rates, owing to a combination of battery-like and capacitor-like (pseudocapacitive) Li^+ intercalation, both in half-cell experiments and as asymmetric supercapacitor anodes *versus* an activated carbon cathode.

2. Experimental section

2.1 Materials

Vanadia nanoflowers were obtained by a hydrothermal synthesis route, as established in ref. 61 and 62. First, 1 g of vanadium pentoxide powder (Sigma Aldrich) was dissolved in a mixture of 20 mL of deionized water (Milli-Q, Merck) and 10 mL of diethanolamine (Sigma Aldrich) on a magnetic stirrer for 4 h. The pH of the solution was determined to be 9.8, using a SevenGo pH meter (Mettler Toledo). The solution was then put into a polytetrafluoroethylene-lined (PTFE) steel autoclave and kept at 180°C for 48 h, before it was naturally cooled down. The product was then washed and centrifuged in a mixture of pure ethanol (Sigma Aldrich) and deionized water three times for three minutes at 1000 rpm. The resulting grey-black slurry was dried in an oven at 80°C overnight. To obtain a high degree of crystallinity, the vanadium oxide nanoflowers were thermally annealed in a quartz tube furnace in argon (flow rate 100 sccm) at 500°C for 60 min at a heating and cooling rate of $10^\circ\text{C min}^{-1}$ and $40^\circ\text{C min}^{-1}$, respectively.

Carbon onions (OLCs) were synthesized from detonation nanodiamond precursor (diameter 4–6 nm, NaBond Technologies) *via* thermal annealing in a water-cooled high temperature furnace (Thermal Technology Inc.) in argon atmosphere at 1700°C for 1 h, with a heating/cooling rate of $20^\circ\text{C min}^{-1}$.⁵¹ Different amounts of OLCs were employed as a conductive additive for vanadium oxide nanoflowers by simple mixing with a pestle and mortar (mass ratios of vanadium oxide to OLC were 7 : 2, 6 : 3, and 5 : 4) to obtain VO_2 -OLC-composite samples. For the hydrothermal synthesis of vanadia nanoflowers and OLCs (VO_2 -OLC-hybrid samples), different amounts of OLC powder were dispersed with vanadium oxide powder on a magnetic stirrer for 4 h (the same mass ratios as above; 7 : 2, 6 : 3, and 5 : 4), and the pH value was measured to be 9.8 (the same as without OLCs). The same hydrothermal synthesis process with subsequent thermal annealing as described above was carried out.

For electrode preparation, the powder materials were admixed with ethanol and PTFE (aqueous solution, 60%, Sigma Aldrich) in a mortar resulting in mass ratios of 7 : 2 : 1, 6 : 3 : 1, and 5 : 4 : 1 for vanadia nanoflowers to OLCs to PTFE. The obtained slurry was then rolled in a hot-rolling machine to about

100 μm thick electrodes and dried in a vacuum oven at 20 mbar and 120 $^{\circ}\text{C}$ overnight.

2.2 Materials characterization

Transmission electron microscopy (TEM) was performed with a JEOL 2100F system operating at 200 kV. Samples were prepared by dispersing and sonicating the powder samples in isopropanol and deposition on a copper grid with a lacey carbon film (Gatan Inc.). Elemental mappings were recorded using an energy dispersive X-ray spectrometer (EDX) with a Thermo Fisher Scientific EDX detector (UltraDry).

The electrode conductivity σ was analyzed by 4-point probe measurements (custom built, tip diameter: 1.5 mm, tip distance: 1.75 mm). Areal resistance measurements were conducted 6 times per electrode and the conductivity was normalized to the electrode thickness and calculated *via* eqn (1):

$$\sigma = \frac{\ln(2)}{\pi} \frac{I}{U \cdot d} \quad (1)$$

where I is the current, U the voltage, and d the electrode thickness (100 μm).

Thermogravimetric analysis (TGA) was performed on the electrode samples using a TG 209 F1 Libra system (Netzsch). The samples were heated in alumina crucibles from room temperature to 550 $^{\circ}\text{C}$ at a heating rate of 5 $^{\circ}\text{C min}^{-1}$ under a synthetic air atmosphere (80% N_2 and 20% O_2). Higher temperatures are to be avoided to stay below the melting point of vanadium pentoxide. The burn-off mass was used to calculate the metal oxide and carbon content of the sample.

Nitrogen gas sorption measurements were carried out with an Autosorb iQ system (Quantachrome) at the temperature of liquid nitrogen (-196°C) after degassing at 10^2 Pa and 150 $^{\circ}\text{C}$ for 10 h. For the measurements, the relative pressure (p/p_0) was varied from 5×10^{-7} to 1.0 in 58 steps. The specific surface area (SSA) was calculated with the ASiQwin-software using the Brunauer–Emmett–Teller (BET) equation in the linear relative pressure range of 0.1–0.25. Values for the total pore volume correspond to $p/p_0 = 0.95$.

Raman spectroscopy was carried out with a Renishaw inVia Raman Microscope that is equipped with an Nd:YAG laser with an excitation wavelength of 532 nm and a power of about 0.05 mW (measured on the sample). Using a low laser power prohibited an oxidation of VO_2 to V_2O_5 during measurements. A $50\times$ objective and a grating with 2400 lines per mm were used to reach a spectral resolution of about 1.2 cm^{-1} . Each spectrum was acquired with a measurement time of 30 s and 10 accumulations. Peak deconvolution of D- and G-bands was conducted using a baseline correction and assuming four Voigt profiles.

X-ray diffraction (XRD) experiments were conducted employing a D8 Advance diffractometer (Bruker AXS) with a copper X-ray source (CuK_{α} , 40 kV, 40 mA), a Göbel mirror, a 0.5 mm point focus, and a two-dimensional VANTEC500 detector that covers about $25^{\circ} 2\theta$. All samples were placed on a sapphire single crystal and measured in 3 steps at 20° , 40° , and $60^{\circ} 2\theta$

with a step duration of 33 min. Rietveld refinement was carried out using TOPAS Version 5 software (Bruker AXS).

2.3 Electrochemical characterization

The synthesized materials were characterized as working electrodes in a half-cell setup.⁶³ Typical working electrodes exhibited a thickness of about 100 μm and a mass of 1.5–2.0 mg. A five-times oversized, PTFE-bound activated carbon (type YP-80F, Kuraray) was used as counter electrode, and activated carbon (type YP-50F, Kuraray) served as quasi-reference electrode.⁶⁴ As current collectors, 12 mm diameter carbon-coated aluminum foils (Zflo 2653, Exopack Technologies) were employed and glass fiber mats (GF/A, Whatman) were used as separators. After assembly, the cells were first dried in a vacuum oven at 120 $^{\circ}\text{C}$ and 20 mbar overnight, before being transferred to an argon filled glovebox (MBraun Labmaster 130, O_2 and $\text{H}_2\text{O} < 1$ ppm), where they were vacuum-backfilled with 1 M LiClO_4 in acetonitrile (ACN) electrolyte (battery grade, BASF). Then, full-cells were assembled with the synthesized materials as anodes, and 5 mass% PTFE-bound activated carbon (type YP-80F, Kuraray, electrode thickness *ca.* 100 μm) served as cathodes. Charge-balancing was achieved by adjusting the anode–cathode mass ratio to 1 : 2.

Electrochemical characterization was carried out using a potentiostat/galvanostat (VSP300, Bio-Logic). In a half-cell setup, cyclic voltammetry (CV) was performed in a potential window from +1.0 V to -1.0 V *vs.* carbon at a scan rate of 1 mV s^{-1} . Galvanostatic charge/discharge with potential limitation (GCPL) was carried out by cycling between +1.0 V and -1.0 V *vs.* carbon with specific currents ranging from 0.05–100 A g^{-1} (equivalent to C-rates of 0.4–787C; $1\text{C} = 0.127 \text{ A g}^{-1}$), normalized to the total electrode mass, excluding the mass of the PTFE-binder. The specific capacity C_{sp} was calculated by integration of the reduction current I over the reduction time t accounting for the lithiation step from +1.0 V to -1.0 V *vs.* carbon, and normalizing to the total mass, m , of the working electrode, excluding the PTFE binder (eqn (2)):

$$C_{\text{sp}} = \frac{\int_{t_0}^t I \, dt}{m} \quad (2)$$

For investigation of full-cells, CVs were recorded up to a cell voltage of 2.3 V at a scan rate of 10 mV s^{-1} . GCPL measurements were carried out with specific currents ranging from 0.05 A g^{-1} to 50 A g^{-1} in a potential range between 0 V and 2.3 V cell voltage, with the specific currents being normalized to the mass of both electrodes, excluding the mass of the PTFE binder. The potential evolution at both the anode and cathode was measured by applying a spectator electrode, consisting of PTFE-bound activated carbon (type YP-50F, Kuraray). The specific energy E_{sp} was calculated by integration of the voltage profile (eqn (3)):

$$E_{\text{sp}} = \frac{I \int_{t_0}^t U(t) \, dt}{m} \quad (3)$$

where I is the applied current, $U(t)$ the time-dependent cell voltage and m the total mass of anode and cathode without binder. The specific power P_{sp} was calculated by dividing E_{sp} by the charge/discharge time. The energy efficiency was derived from the ratio of specific discharge and charge energy. The stability of full-cells was tested *via* GCPL between 0 V and 2.3 V cell voltage at a specific current of 1 A g⁻¹.

In situ dilatometry was carried out with an ECD-2-nano dilatometer (EL-CELL).⁶⁵ The measurements were performed in a climate chamber (25.0 ± 0.5 °C) in a two-electrode setup with the VO₂-OLC30-hybrid/VO₂-OLC30-composite as the working electrode and an oversized PTFE-bound activated carbon as the counter and quasi-reference electrode (type YP-80F, Kuraray); the separator and electrolyte were equivalent to the procedure in half- and full-cells. Prior to the experiments, the cell was dried for 24 h at 120 °C under vacuum (20 mbar). The working electrode was compressed between a movable titanium plunger with a constant load of 1 N. The strain was tracked with a DP1S displacement transducer (Solartron Metrology, accuracy ± 15 nm). Cyclic voltammograms were recorded at 1 mV s⁻¹ after a resting period of 48 h after electrolyte filling until equilibrium conditions were reached.

3. Results and discussion

3.1 Structural characterization

The structure and morphology of the synthesized electrode materials were characterized by electron microscopy. As seen from SEM images in Fig. 1, hydrothermally synthesized vanadium oxide forms in different structures depending on the synthesis route. When carbon onions (OLC = onion-like carbon) are present in the autoclave during synthesis, a hybrid material is formed consisting of vanadia and carbon,

with nanoscopic flower-like vanadia structures growing deeply interconnected within the OLC agglomerates that serve as nucleation sites (Fig. 1A–C). These samples are further labelled VO₂-OLC-hybrid. The term hybrid is chosen to emphasize the chemical connection of the two components, vanadia and carbon, on a nanoscopic scale. The vanadia-to-carbon ratio in the hybrid electrode is controlled by stoichiometric addition of carbon onions to the synthesis container; for example, the VO₂-OLC30-hybrid was produced by a precursor mass ratio of 6 : 3 vanadia to carbon onions. The remaining 10% of the final sample consists of PTFE-binder used during electrode production. In contrast, the hydrothermal process without OLCs yields arrays of nanoscopic, flower-like vanadia structures. They consist of several quasi-spherical nanoflowers that form connected structures of several micrometers in size (Fig. 1D). When admixing OLCs after the hydrothermal process to form a composite, vanadia and OLC agglomerates are spatially separated, with carbon being present around the vanadia structures, rather than interpenetrating them like seen for the hybrid material. These samples will further be described as VO₂-OLC-composites, emphasizing the post synthesis addition of OLCs, with the number indicating the stoichiometric amount of added OLCs to the composite material; for example, in the VO₂-OLC30-composite, vanadia nanoflowers were mixed with OLCs in a mass ratio of 6 : 3. In such composites, carbon onions are merely the mechanically admixed conductive additive, whereas the hybrid material shows highly intergrown carbon onion/vanadia domains with a nanotextured oxide/carbon interface formed by chemical bonds.⁶⁶

Both VO₂-OLC-hybrid and VO₂-OLC-composite samples were further analyzed by TEM (Fig. S1†) and chemically mapped *via* EDX (Fig. 2). A clear visualization with a smooth interface between OLCs and VO₂ is visible for the hybrid sample (Fig. S1A†), whereas

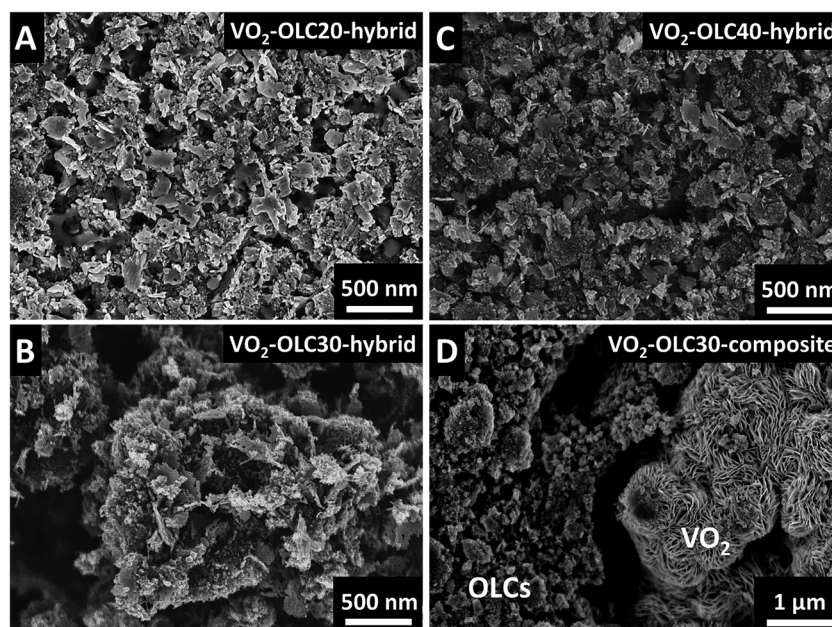


Fig. 1 Scanning electron micrographs of (A–C) VO₂-OLC-hybrid samples, and (D) the VO₂-OLC30-composite sample.

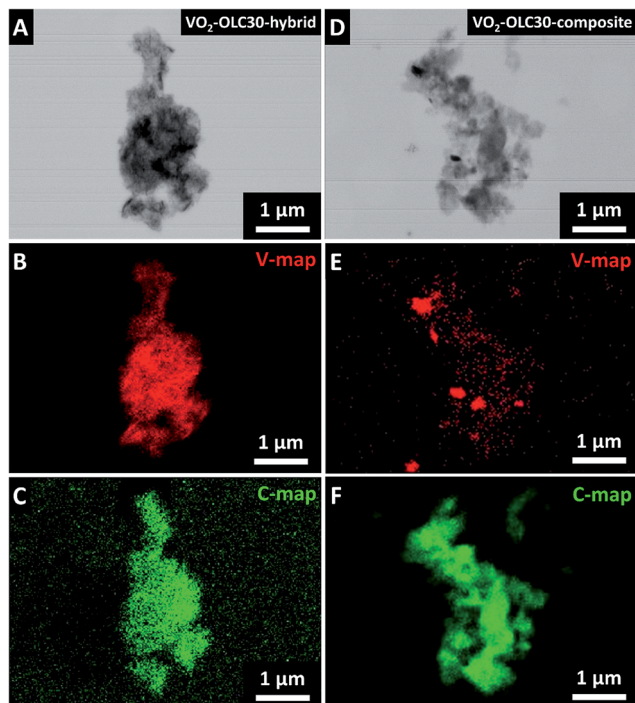


Fig. 2 Transmission electron micrographs of VO₂-OLC30-hybrid (A) and VO₂-OLC30-composite (D) samples, including EDX elemental mappings of vanadium (B and E) and carbon (C and F). The more homogenous distribution of vanadium resulting from the hydrothermal synthesis route is demonstrated.

VO₂ particles in the composite sample are separated from the OLCs, preventing a clear depiction of the interface of the two components. While the distribution of vanadium and carbon was found to be homogenous throughout the whole particle in the hybrid sample by EDX mapping (Fig. 2A), highly concentrated regions of vanadium were found in a rather homogenous matrix of carbon in the composite sample (Fig. 2B), being representative of the vanadia nanoflower clusters, separated by OLCs in the composite material. This further underlines the drastically changed morphological character of the samples resulting from the introduction of carbon at different stages of the synthesis. The influence of carbon-vanadia distribution on the macroscopic electrical conductivity of the electrodes was analyzed by 4-point probe measurements (Table S1†). By comparing VO₂-OLC30-hybrid and VO₂-OLC30-composite samples, it is obvious that the

homogenous distribution of elements from the hybridization leads to higher conductivity in the resulting electrode material because of more continuous electron pathways.

The elemental composition of the electrode materials was quantified by TGA and validated by semi-quantitative EDX (Table 1 and ESI, Fig. S2†). The sample inhomogeneity of the VO₂-OLC-composite yielded a high standard deviation of the EDX results. When deriving the vanadia content from TGA, it must be considered that during thermogravimetric measurements in synthetic air, VO₂ is oxidized to V₂O₅, causing an increase in mass per vanadium atom from 83 g mol⁻¹ to 91 g mol⁻¹. Moreover, the initial mass loss to 94% of the VO₂-OLC30-hybrid sample is caused by evaporation of adsorbed surface water.⁶⁷ While the general trend of an increasing carbon content for samples with larger amounts of added OLCs is confirmed, the vanadia/carbon ratio as chosen by precursor masses is not reached. Instead, the VO₂ contents of VO₂-OLC20-hybrid, VO₂-OLC30-hybrid, and VO₂-OLC40-hybrid samples were determined as 57 mass%, 47 mass%, and 32 mass%, respectively, while VO₂-OLC-composite samples contained 60 mass%, 48 mass%, and 45 mass% vanadia. The reasons for this behavior are (i) the partial dissolution of vanadia from the samples during wet electrode preparation in ethanol, as witnessed by yellow coloring of the solvent, and (ii) an incomplete reaction yield of vanadia during the synthesis of the hybrid materials. The TGA signal of pristine VO₂ nanoflowers shows a mass loss of about 3.5% which can be associated with adsorbed water on the surfaces.⁶⁷ The subsequent mass gain between 350 and 400 °C is a result of oxidation to V₂O₅ in the oxidizing air atmosphere.

The surface area and pore structure of the hybrid electrodes were assessed by nitrogen gas sorption analysis (GSA). The values of the specific surface area (BET-SSA) and pore volume are listed in ESI Table S2,† and nitrogen sorption isotherms are given in Fig. S3.† The type III isotherms describe the meso-/macro-porous interparticle/intercluster voids, whereas the H3 hysteresis describes the amount of incompletely filled macropores.⁶⁸ The SSA of the hybrid samples varies between about 80 m² g⁻¹ and 160 m² g⁻¹, which increases with increasing amount of added carbon onions, while the as-synthesized vanadium oxide nanoflower structures exhibit around 38 m² g⁻¹ in the absence of carbon onions. The increased SSA for higher amounts of OLC is related to the low density of carbon in comparison to vanadia and the mesoporous interparticle voids

Table 1 Chemical composition of the hybrid and composite electrodes by EDX, and vanadium oxide content based on EDX and TGA

Material	Elemental composition (EDX)				Vanadium oxide	
	C (mass%)	V (mass%)	O (mass%)	F (mass%)	EDX (mass%)	TGA (mass%)
VO ₂ -OLC20-hybrid	30 ± 5	46 ± 6	17 ± 1	7 ± 2	63 ± 7	57
VO ₂ -OLC30-hybrid	40 ± 3	36 ± 4	18 ± 1	6 ± 2	54 ± 5	47
VO ₂ -OLC40-hybrid	55 ± 4	27 ± 3	11 ± 1	7 ± 1	38 ± 4	32
VO ₂ -OLC20-composite	36 ± 29	42 ± 27	13 ± 9	9 ± 7	55 ± 36	60
VO ₂ -OLC30-composite	50 ± 26	30 ± 24	9 ± 8	11 ± 5	39 ± 32	48
VO ₂ -OLC40-composite	53 ± 17	26 ± 15	10 ± 5	11 ± 3	36 ± 20	45

between the spherical carbon onions ($352 \text{ m}^2 \text{ g}^{-1}$ for pristine OLCs).

Raman spectroscopy was carried out to characterize the crystalline structure of vanadia and carbon in the hybrid electrode materials (Fig. 3A and B). The signals below 1000 cm^{-1} are associated with vanadia, while the signals at 1345 cm^{-1} and 1595 cm^{-1} correspond to the D- and G-modes of carbon.^{69,70} The Raman peaks at 191, 221, 594, and 612 cm^{-1} seen for VO_2 -OLC-hybrid samples evidence the presence of the VO_2 phase.^{30,71} The intensity of these peaks decreases with an increased amount of OLCs in the hybrid materials relative to the carbon signal. The same behavior is observed for the VO_2 -OLC-composite (Fig. 3B); yet, the relative intensity of the VO_2 signals is much lower compared to the VO_2 -OLC-hybrid samples, and barely visible for the VO_2 -OLC40-composite. This can be explained by the randomly distributed vanadia clusters in these electrodes, which are surrounded by carbon onion agglomerates. Because of the relatively small probed volume and the surface sensitivity of the Raman measurements,⁷² the detected signals originate predominantly from the carbon species in the composite electrode materials. The Raman signal of pristine nanoflowers clearly aligns with VO_2 .³⁰

An analysis of the D- and G-peaks of VO_2 -OLC30-hybrid (Fig. 3C) and VO_2 -OLC30-composite samples (Fig. 3D) allows for a detailed examination of the carbon structure. Even though the same carbon onion materials were used for hybrid and composite electrodes, quantitative peak deconvolution reveals a difference in the carbon structure for the hydrothermally synthesized hybrid sample (ESI, Table S3†). While the areal intensity ratio of the D- and G-mode of carbon (I_D/I_G) is 2.3 for

the VO_2 -OLC30-composite, this value increases to 2.7 for the VO_2 -OLC30-hybrid sample. An increasing I_D/I_G ratio relates to increasing disorder of the graphitic structure, caused by the introduction of defects.^{70,73,74} This aligns with an increase of the FWHM of D- and G-peaks for the VO_2 -OLC30-hybrid (ESI, Table S3†).⁵¹ These observations can be explained by a change in the carbon structure during hydrothermal synthesis and confirm the strong interconnections of carbon and vanadia on the nanoscale. When vanadia flowers nucleate from the solution on the outer shells of the carbon onion nanoparticles, an ordering reduction of the graphitic sp^2 -hybridized rings is expected due to surface stresses induced by non-epitaxially bound vanadia. This observation is in line with findings for the growth of vanadia layers deposited by atomic layer deposition on carbon onions.³⁶

The crystalline structure of vanadia in the hybrid electrodes was further analyzed by XRD (Fig. 4). For VO_2 -OLC-hybrid samples, vanadia was found in the monoclinic VO_2 structure, with both $C2/m$ and $P2_1/c$ space groups verified per JCPDS 65-7960 and JCPDS 65-2358, respectively (Fig. 4A). In general, both structures are characterized by corner-sharing octahedra (ESI, Fig. S3†), with the distance between the shared oxygen atoms at the corners of the octahedra showing a fixed distance of 3.3 \AA in the $C2/m$ structure (ESI Fig. S4A†) and varying distances between 2.9 \AA and 6.4 \AA in the $P2_1/c$ structure (ESI, Fig. S4B†). The peak at *ca.* $18^\circ 2\theta$ is attributed to the polymer binder in the electrode (PTFE; JCPDS 54-1595). The diffractograms of VO_2 -OLC-composite samples, as well as of pristine VO_2 nanoflowers, exhibit the signals of the VO_2 $P2_1/c$ space group, PTFE at $18^\circ 2\theta$, and a broad shoulder around $26^\circ 2\theta$ that is indicative of

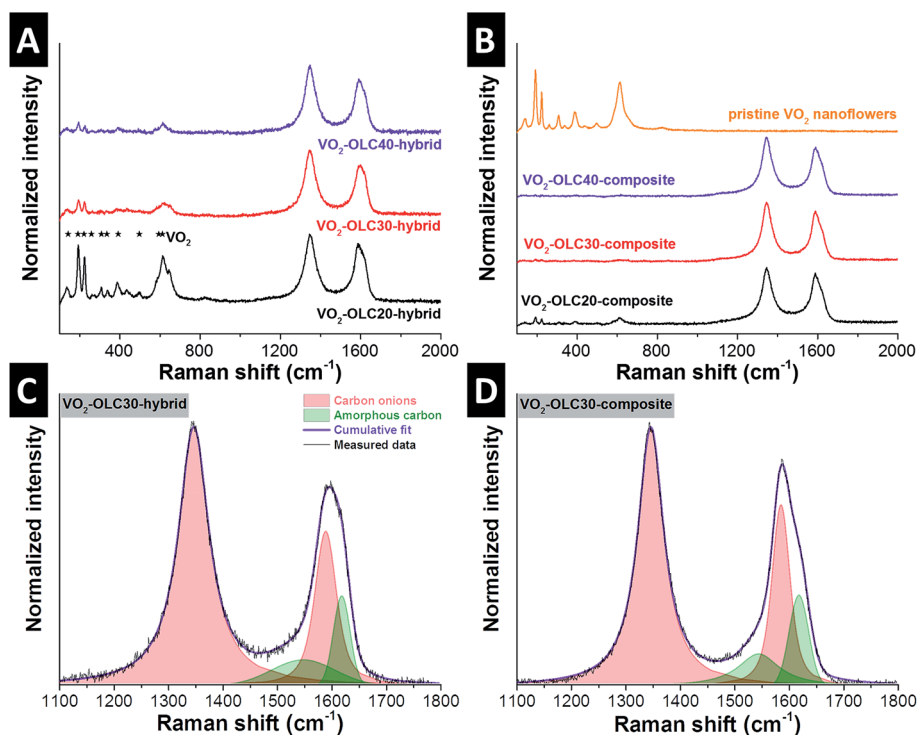


Fig. 3 Raman spectra of (A) VO_2 -OLC-hybrid and (B) VO_2 -OLC-composite and pristine VO_2 nanoflower samples, including markers for the ideal peak positions of VO_2 . Peak deconvolution of D- and G-peaks of VO_2 -OLC30-hybrid (C) and VO_2 -OLC30-composite (D) samples.

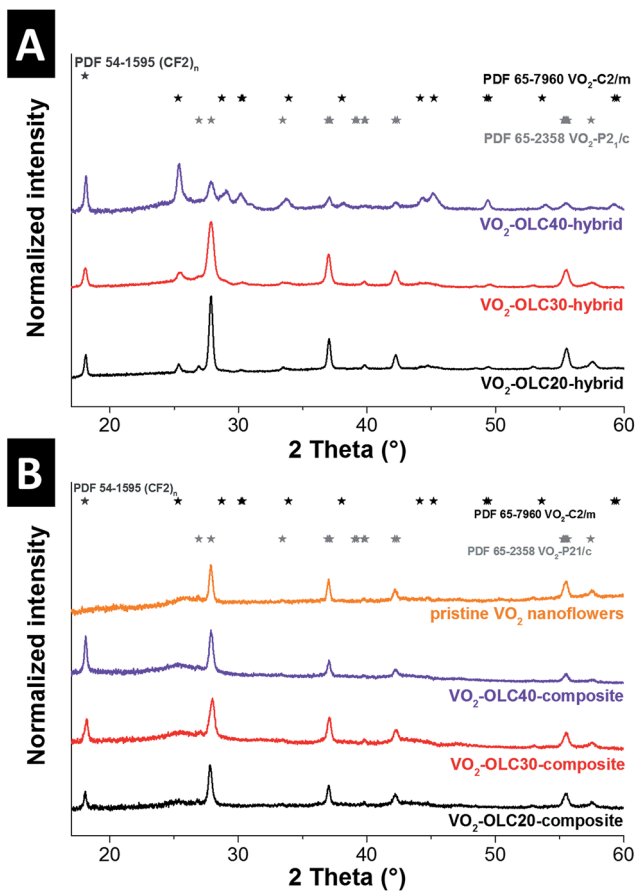
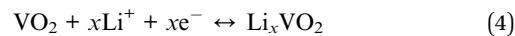


Fig. 4 X-ray diffractograms of (A) VO₂-OLC-hybrid and (B) VO₂-OLC-composite and pristine VO₂ nanoflower samples, including markers for the ideal peak positions of C2/m VO₂ (JCPDS 65-7960), P2₁/c VO₂ (JCPDS 65-2358), and polymer binder PTFE (JCPDS 54-1595).

nanocrystalline carbon. The absence of the C2/m space group signal for VO₂-OLC-composite samples indicates a preferential growth of P2₁/c vanadia during hydrothermal synthesis, when no OLCs are present in the solution. Since OLCs caused no change in the pH value of the solution, the change in crystallization behavior can be explained by an increasing amount of available nucleation sites with the addition of OLCs during the synthesis. By adding carbon particles to the solution, the rate of heterogeneous nucleation, that is, energetically favored nucleation on an existing surface, is increased. The significantly reduced nucleation energy of vanadia on OLC surfaces leads to a homogenous morphology of the VO₂-OLC-hybrid samples. The intensity of the C2/m space group in VO₂-OLC-hybrid samples grows relative to the P2₁/c intensity for an increasing amount of OLCs in the hybrid material, as further quantified by Rietveld refinement. The amount of C2/m VO₂ space group is calculated to be 3% (VO₂-OLC20-hybrid), 35% (VO₂-OLC30-hybrid), and 77% (VO₂-OLC40-hybrid; difference to 100% = P2₁/c VO₂). The larger number of nucleation sites provided by carbon onions seemingly leads to favored growth kinetics for C2/m VO₂ over P2₁/c VO₂.

3.2 Electrochemical characterization

The electrochemical performances of the hybrid and composite electrodes were characterized in half-cells using cyclic voltammetry (CV) at a scan rate of 1 mV s⁻¹ (Fig. 5A and B). The CVs of VO₂-OLC-hybrid samples (Fig. 5A) exhibited two features that can be attributed to (1) the double-layer capacitance originating from the carbon onions in the hybrid material^{52,75} and (2) the faradaic charge storage mechanism of vanadium dioxide. Electrical double-layer capacitance is characterized by a rectangular CV pattern, as observed between *ca.* 0 V and +1.0 V *vs.* carbon.¹⁹ However, considering the specific surface area of VO₂-OLC-hybrid samples between 81 m² g⁻¹ and 160 m² g⁻¹, the contribution of the double-layer capacitance of OLCs to the overall charge storage is very small, as compared to the faradaic charge storage contribution of VO₂. The prominent redox peak pair observed at *ca.* -0.55 V *vs.* carbon in the cathodic scan and at -0.4 V *vs.* carbon in the anodic scan is caused by battery-like lithiation and delithiation of the VO₂ structure, respectively.⁵⁸ Differences in the size of the redox peaks can be noticed, especially for the VO₂-OLC40-hybrid, and less pronounced for the VO₂-OLC30-hybrid, when compared to the VO₂-OLC20-hybrid sample that contains most vanadia and would be expected to exhibit the largest peak. The reason is that battery-like Li⁺ intercalation at this voltage is only expected for C2/m VO₂.^{30,58} The reaction mechanism of lithium intercalation in the VO₂ structure is described by:⁵⁶



where *x* describes the molar fraction of intercalated lithium ions.

In contrast, VO₂-OLC-hybrid samples containing more P2₁/c VO₂ exhibit a rather pseudocapacitive feature up to around -1.0 V *vs.* carbon. That is, an increased specific current without showing distinctive lithiation and delithiation peaks.³¹ This Li⁺ intercalation pseudocapacitance has been described in literature for nanostructured T-Nb₂O₅ and nanocrystalline V₂O₅ electrode materials,^{16,76,77} but presents, to the best of our knowledge, a new feature for P2₁/c VO₂. It is defined as lithium intercalation causing faradaic charge transfer without causing crystallographic phase changes to the host material.⁷⁸

The CVs of VO₂-OLC-composite samples most noticeably do not exhibit redox peaks (Fig. 5B). Instead, in the potential region, where lithiation peaks emerged for VO₂-OLC-hybrid samples, pseudocapacitive behavior is observed with a steadily rising specific current from around -0.15 V up to -1.0 V *vs.* carbon in the cathodic scan. Considering that VO₂-OLC-composite samples only contain P2₁/c VO₂, this behavior is in line with the observations made for VO₂-OLC-hybrid samples, where redox peaks were associated with C2/m VO₂.

We carried out a kinetic analysis to separate battery-like from pseudocapacitive (capacitor-like) contribution to the overall charge transfer.^{79,80} Cyclic voltammograms were recorded at varying scanning rates *ν* between 10 and 1000 mV s⁻¹ (ESI, Fig. S5A-C†) and the reduction peak current *i* at a potential of -0.7 V *vs.* carbon is tracked.¹⁹ Logarithmic plotting of *i* as a function of *ν* in accordance with eqn (5):⁸¹

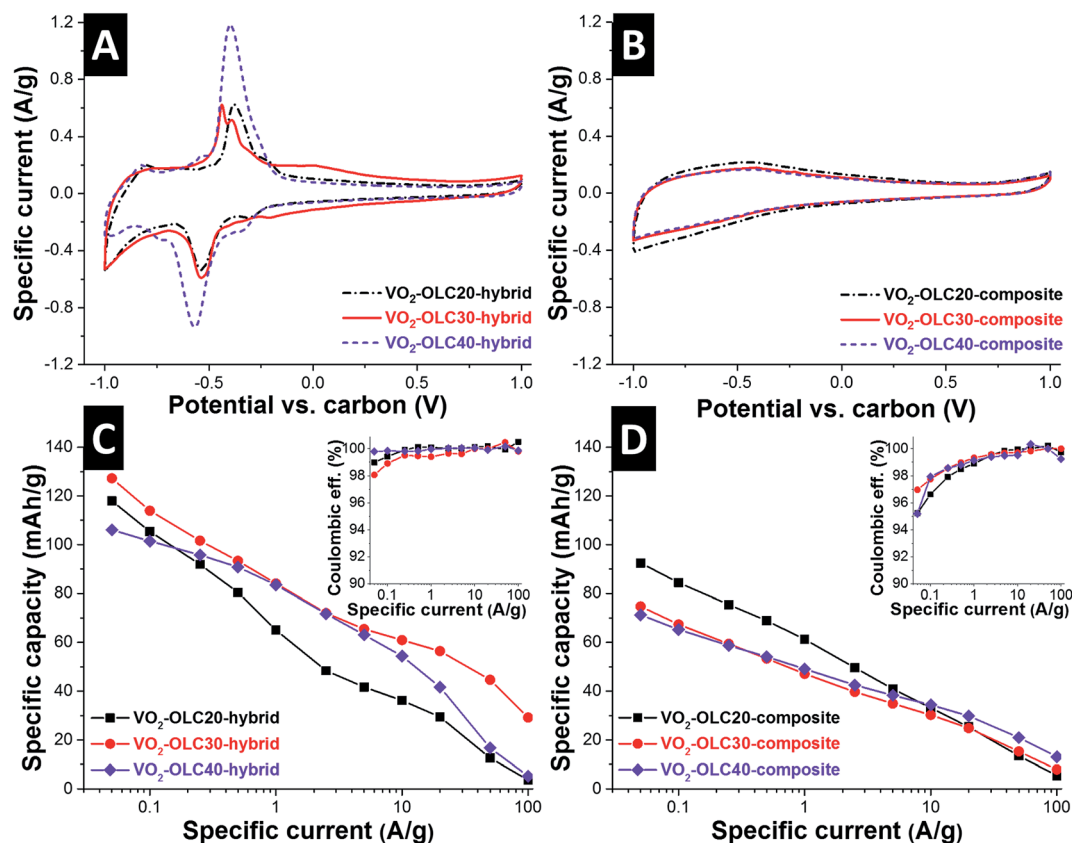


Fig. 5 Cyclic voltammograms of (A) VO₂-OLC-hybrid and (B) VO₂-OLC-composite samples recorded at 1 mV s⁻¹. Specific capacities of (C) VO₂-OLC-hybrid and (D) VO₂-OLC-composite samples derived from the galvanostatic reduction step at varying rates between 0.05 A g⁻¹ and 100 A g⁻¹ (corresponding to C-rates of 0.4–787C), normalized to the combined mass of carbon and vanadia. Insets in (C) and (D) show the coulombic efficiency (ratio reduction/oxidation capacity) at varying rates.

$$i = av^b \quad (5)$$

where a and b are variables, yields directly a slope of b (ESI, Fig. S5D[†]). Battery-like charge transfer, being diffusion limited, exhibits a current i proportional to \sqrt{v} (*i.e.*, $b = 0.5$), whereas ideal pseudocapacitive charge transfer is not limited by solid-state diffusion and behaves capacitor-like, that is, proportional to v (*i.e.*, $b = 1$).^{81,82} For VO₂-OLC40-hybrid and VO₂-OLC30-hybrid samples, b -values of 0.54 and 0.68 were calculated, confirming a mainly battery-like and a combined pseudocapacitive and battery-like charge transfer, respectively.¹⁹ The VO₂-OLC30-composite sample, for comparison, exhibits a b -value of 0.77, confirming a predominantly pseudocapacitive charge transfer behavior for P2₁/c VO₂.

A quantitative investigation of the performance metrics of the hybrid electrodes regarding specific capacity and rate handling was carried out by galvanostatic charge/discharge with potential limitation (GCPL) at different rates between 0.05 A g⁻¹ and 100 A g⁻¹ (Fig. 5C and D). All values were normalized to the mass of the electrode, including carbon and vanadia (but without the mass of the polymer binder). The specific capacity of VO₂-OLC-hybrid samples at low rates was above 105 mA h g⁻¹, with the highest capacity exhibited by the VO₂-OLC30-hybrid with 127 mA h g⁻¹ (270 mA h per g per mass of VO₂). This

sample also showed the highest capacity retention with 45 mA h g⁻¹ (96 mA h per g per VO₂) and 29 mA h g⁻¹ (62 mA h per g per VO₂) at ultrahigh rates of 50 A g⁻¹ and 100 A g⁻¹ (*i.e.*, C-rates of 394C and 788C), respectively. This behavior can be explained as follows: it is indicated that (1) the composition of the VO₂-OLC30-hybrid sample yields the most favorable balance between carbon and vanadia as the conductive matrix and high energy density material, respectively. Furthermore, (2) the amount of carbon onions in the VO₂-OLC30-hybrid sample gave rise to an optimum vanadia composition regarding the ratio of P2₁/c and C2/m configurations that is a result of the number of available nucleation sites. We propose that this combination of battery-like and pseudocapacitive Li⁺ intercalation synergistically benefits high capacity retention at ultrahigh rates.

The specific capacity of VO₂-OLC-composite samples varies between 71 mA h g⁻¹ and 92 mA h g⁻¹ at low rates and steadily decreases for increased cycling rates. The highest initial capacity is observed for VO₂-OLC20-composite, whereas VO₂-OLC40-composite exhibits the highest retention at an ultrahigh rate of 100 A g⁻¹, owing to the larger amount of carbon onions as the conductive additive.

The performance of the hybrid electrode was further investigated as a full-cell by employing this material as the anode in

an asymmetric supercapacitor setup against an activated carbon cathode. By selecting the mass ratio of anode to cathode as 1 : 2, charge balancing was achieved to ensure a symmetric potential development between the two electrodes. CVs were recorded at a scan rate of 10 mV s^{-1} up to a cell voltage of 2.3 V (Fig. 6A and B). For the cells containing $\text{VO}_2\text{-OLC-hybrid}$ anodes, a broad lithium intercalation peak is observed between about 0.7 V and 1.7 V cell voltage (Fig. 6A). As already seen for the half-cell measurements, this peak is larger for samples containing higher amounts of carbon onions, that is, a higher amount of $\text{C}_2/\text{m VO}_2$. The cell employing $\text{VO}_2\text{-OLC30-hybrid}$ as

the anode exhibits the highest capacity, showing a large intercalation peak in combination with a constant, high specific current above 1.5 V cell voltage, being characteristic of pseudocapacitive charge storage. On the other hand, the cells containing $\text{VO}_2\text{-OLC-composite}$ anodes only show pseudocapacitive charge storage, and no intercalation peaks emerge during cycling (Fig. 6B), in agreement with the half-cell data.

The specific energy and power of the cells were derived from GCPL at different rates, and plotted in a Ragone chart (Fig. 6C and D); a typical galvanostatic cycle of cells containing $\text{VO}_2\text{-}$

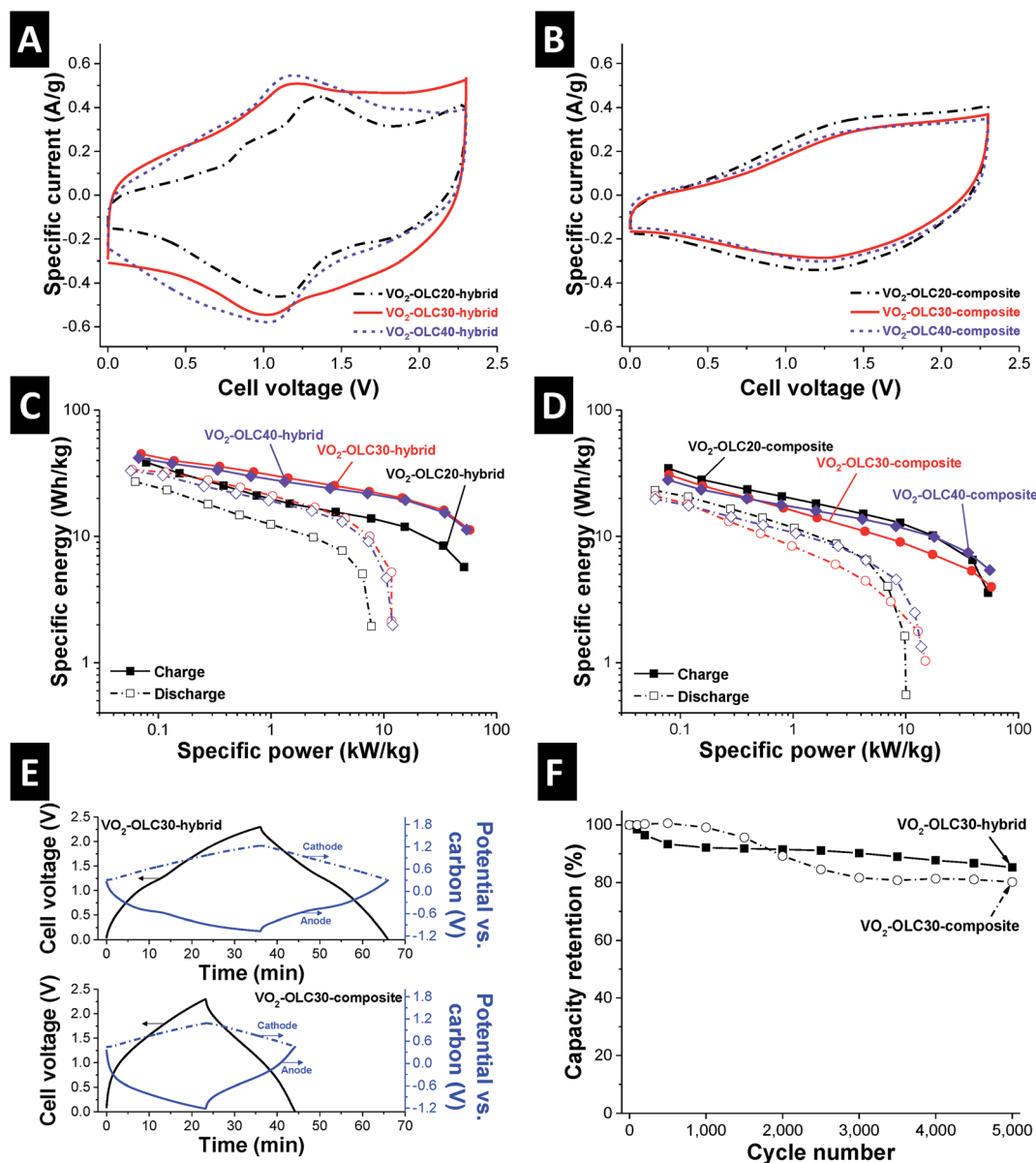


Fig. 6 Cyclic voltammograms of asymmetric supercapacitor full-cells at 10 mV s^{-1} , employing anodes of (A) $\text{VO}_2\text{-OLC-hybrid}$ and (B) $\text{VO}_2\text{-OLC-composite}$ samples and activated carbon cathodes. Ragone-plots of samples employing anodes of (C) $\text{VO}_2\text{-OLC-hybrid}$ and (D) $\text{VO}_2\text{-OLC-composite}$ samples, derived from galvanostatic cycling at different rates, with the straight lines corresponding to the charging cycle and the dashed lines to the discharging cycle. (E) Voltage-profile of a galvanostatic cycle of full-cells employing $\text{VO}_2\text{-OLC30-hybrid}$ (top) and $\text{VO}_2\text{-OLC30-composite}$ (bottom) anodes, including the potential development at the cathode and anode, monitored against a carbon reference electrode. (F) Electrochemical cycling stability over 5000 cycles, measured at a specific current of 1 A g^{-1} for full-cells employing $\text{VO}_2\text{-OLC30-hybrid}$ and $\text{VO}_2\text{-OLC30-composite}$ anodes.

Table 2 Literature comparison of asymmetric supercapacitor devices that employ the vanadia/carbon hybrid material as the anode and carbon as the cathode. Abbreviations: OLC: onion-like carbon, AC: activated carbon, ACN: acetonitrile, PVA: polyvinyl alcohol, EC/DMC: ethylene carbonate/dimethyl carbonate, Pln: polyindole, rGO: reduced graphene oxide, CDC: carbide-derived carbon, PC: propylene carbonate and ECF: electrospun carbon fiber

Anode	Cathode	Electrolyte	Specific energy (W h kg ⁻¹)	Specific power (kW kg ⁻¹)	Reference
VO ₂ /OLC	AC	1 M LiClO ₄ in ACN	45	58	This work
V ₂ O ₅ /Pln/AC	rGO/AC	LiNO ₃ /PVA gel	38.7	18	86
V _x Ti _{1-x} O ₂ /OLC	AC	1 M LiClO ₄ in EC/DMC	110	6	30
VO _x /OLC	AC	1 M LiClO ₄ in ACN	38	5.9	36
VO ₂ /AC	AC	1 M LiClO ₄ in ACN	29	4.3	36
V ₂ O ₅ /CDC	CDC	1 M LiClO ₄ in ACN	84	6.7	60
V ₂ O ₅ /CNT	AC	1 M LiClO ₄ in PC	40	6.3	33
V ₂ O ₅ /ECF	ECF	LiCl-PVA gel	22.3	1.5	87

OLC30-hybrid and VO₂-OLC30-composite anodes at a rate of 0.05 A g⁻¹ is given in Fig. 6E. At a low rate, VO₂-OLC-hybrid cells exhibit specific energies between 39 W h kg⁻¹ and 45 W h kg⁻¹ during charging, with the highest energy observed for the VO₂-OLC30-hybrid (Fig. 6C). When increasing the rate, the cell containing the VO₂-OLC20-hybrid anode quickly drops in energy, retaining 6 W h kg⁻¹ at a high power of 51 kW kg⁻¹. In contrast, asymmetric cells containing VO₂-OLC30-hybrid anodes are distinguished by an outstanding rate performance, with an increased energy retention of 11.3 W h kg⁻¹ at a high power of 58 kW kg⁻¹. This behavior demonstrates that the beneficial combination of battery-like and pseudocapacitive Li⁺ intercalation mechanisms observed in half-cells can be translated to a device level application, yielding asymmetric supercapacitor cells with enhanced specific energy and ultrafast cycling ability. A comparison of these values with the current literature on asymmetric supercapacitors employing vanadia/carbon hybrid anodes is given in Table 2. While the maximum specific energy of the VO₂-OLC30-hybrid cells is in alignment with most other reports, the maximum specific power of 58 kW kg⁻¹ is unprecedentedly high for hybrid supercapacitors.

Cells with VO₂-OLC-composite anodes exhibit specific energies between 28 W h kg⁻¹ and 35 W h kg⁻¹ in the charging step, with the VO₂-OLC20-composite showing the highest energy at low rates, while the VO₂-OLC40-composite showed the highest energy retention with 5.4 W h kg⁻¹ at a high rate, yielding a maximum specific power of 55.5 kW kg⁻¹ (Fig. 6D). The cell potential in the galvanostatic cycle, including the separate potential evolution at the anode and cathode, monitored against a carbon reference electrode, is illustrated in Fig. 6E. The formation of a plateau-like region during charging of the VO₂-OLC30-hybrid anode is observed at around -0.6 V vs. carbon, corresponding to the intercalation peak in the half-cell. At more negative potentials, an almost linear potential increase evidences pseudocapacitive Li⁺ intercalation. In contrast, the VO₂-OLC30-composite anode only exhibits a pseudocapacitive region with linearly increasing potential above -0.5 V vs. carbon, resulting in a decreased specific energy.

The electrochemical cycling stability of the hybrid electrode materials was assessed by galvanostatic cycling of asymmetric supercapacitor full-cells at a rate of 1 A g⁻¹. After 200 cycles, both VO₂-OLC30-hybrid and VO₂-OLC30-composite cells

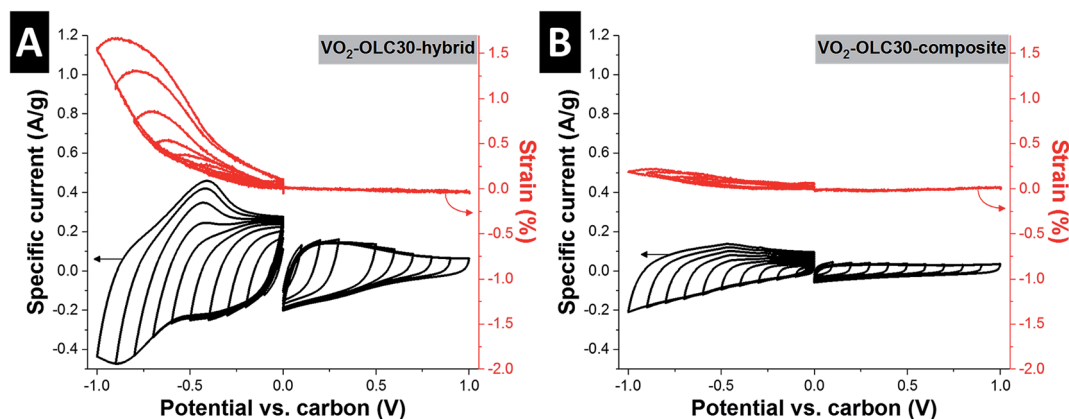


Fig. 7 Half-cell cyclic voltammograms recorded at 1 mV s⁻¹ with potential window opening (black curves) and combined *in situ* electrical dilatometry (red curves) to track the electrode strain during intercalation reactions in (A) VO₂-OLC30-hybrid and (B) VO₂-OLC30-composite electrodes.

faded in capacity to about 90%. Further cycling revealed a highly stable capacity development of both cells over more than 5000 charge/discharge cycles, with retentions of 85% and 80% compared to the starting value for VO₂-OLC30-hybrid and VO₂-OLC30-composite, respectively. Capacity fading is a result of vanadia degradation that is caused by repetitive volumetric changes during long-term electrochemical cycling.^{36,83}

The electrode strain of both hybrid and composite materials during cycling was further quantified by electrochemical *in situ* dilatometry (Fig. 7).⁸⁴ It is revealed that VO₂-OLC30-hybrid electrodes undergo a strain of about 1.5% when fully lithiated at -1.0 V vs. carbon (Fig. 7A), whereas VO₂-OLC30-composite electrodes exhibit no significant strain build-up during cycling (Fig. 7B). Consequently, the battery-like lithium intercalation evidenced by a pair of redox peaks in the CV of VO₂-OLC30-hybrid yields significant macroscopic volume changes of the electrode during negative polarization. However, the longevity of the electrode was not affected by strain formation, which can be explained by the nanoscopic size of vanadia particles in the hybrid material that significantly lowers intraparticle stresses, as compared to micrometer-sized particles. Additionally, in the highly intertwined network with carbon onions, the surrounding carbon particles prevent vanadia from disintegrating, as it was described in the literature, for example, in silicon/graphene anode materials.⁸⁵ In contrast, pseudocapacitive lithium intercalation in VO₂-OLC30-composite electrodes occurs almost without causing a strain to the electrode material, leading to highly stable cycling behavior.

4. Conclusions

Flower-like vanadium dioxide nanostructures were prepared by a facile and scalable hydrothermal synthesis. Employing a hydrothermal synthesis route and adding a defined amount of carbon onions during synthesis yield a highly interconnected hybrid material with a tunable ratio of the VO₂ crystal structure. A larger amount of added carbon onions provides a higher number of available nucleation sites for vanadium oxide, inducing a kinetically favored VO₂ growth as C2/m over P2₁/c. When employed as electrodes for lithium intercalation, the former configuration shows a battery-like mechanism with intercalation peaks, while the latter exhibits pseudocapacitive Li⁺ intercalation with a linear charge-voltage profile. By tuning the ratio of both crystal structures, an optimum composition is found, where a combination of both intercalation mechanisms synergistically benefits the performance, showing high capacity retentions of 45 mA h g⁻¹ (96 mA h per g per VO₂) and 29 mA h g⁻¹ (62 mA h per g per VO₂) at ultrahigh rates of 50 A g⁻¹ and 100 A g⁻¹ (*i.e.*, 394C and 788C), respectively. This behavior is transferred to a device level by using the hybrid material as the anode in an asymmetric supercapacitor setup. While exhibiting a maximum specific energy of 45 W h kg⁻¹, an outstanding energy retention of 11.3 W h kg⁻¹ at an ultrahigh power of 58 kW kg⁻¹ was achieved and longevity over 5000 charge/discharge cycles was demonstrated. This novel approach of combining intercalation mechanisms is easily scalable and might be transferred to other electrode materials or ion systems beyond

lithium, providing new opportunities in the design of asymmetric supercapacitor systems.

Acknowledgements

This work was part of the Carbon Metal Oxide Nanohybrid project (CarMON) supported by the Leibniz Association (SAW-2017). We acknowledge funding from the German Federal Ministry for Economic Affairs and Energy (BMWi) in support of the HyBaCap project (award number 03ET6113C). We thank Prof. Arzt for his continuing support, Dr Grobelsek for contributing to Rietveld refinement, and Juhan Lee for scientific discussions (all at INM).

References

- Z. Yang, J. Zhang, M. C. W. Kintner-Meyer, X. Lu, D. Choi, J. P. Lemmon and J. Liu, *Chem. Rev.*, 2011, **111**, 3577–3613.
- J. R. Miller and P. Simon, *Science*, 2008, **321**, 651–652.
- P. Simon and Y. Gogotsi, *Nat. Mater.*, 2008, **7**, 845–854.
- F. Beguin, V. Presser, A. Balducci and E. Frackowiak, *Adv. Mater.*, 2014, **26**, 2219–2251.
- M. Salanne, B. Rotenberg, K. Naoi, K. Kaneko, P. L. Taberna, C. P. Grey, B. Dunn and P. Simon, *Nat. Energy*, 2016, **1**, 16070.
- J. Huang, B. G. Sumpter, V. Meunier, G. Yushin, C. Portet and Y. Gogotsi, *J. Mater. Res.*, 2010, **25**, 1525–1531.
- W. Gu and G. Yushin, *Wiley Interdiscip. Rev.: Energy Environ.*, 2014, **3**, 424–473.
- D. Qu and H. Shi, *J. Power Sources*, 1998, **74**, 99–107.
- M. Oschatz, L. Borchardt, K. Pinkert, S. Thieme, M. R. Lohe, C. Hoffmann, M. Benusch, F. M. Wissler, C. Ziegler, L. Giebeler, M. H. Rummeli, J. Eckert, A. Eychmüller and S. Kaskel, *Adv. Energy Mater.*, 2014, **4**, 1300645.
- V. Presser, M. Heon and Y. Gogotsi, *Adv. Funct. Mater.*, 2011, **21**, 810–833.
- M. Zeiger, N. Jäckel, V. N. Mochalin and V. Presser, *J. Mater. Chem. A*, 2016, **4**, 3172–3196.
- J. K. McDonough and Y. Gogotsi, *Electrochem. Soc. Interface*, 2013, **22**, 61–66.
- E. Frackowiak, K. Metenier, V. Bertagna and F. Beguin, *Appl. Phys. Lett.*, 2000, **77**, 2421–2423.
- T. A. Centeno, O. Sereda and F. Stoeckli, *Phys. Chem. Chem. Phys.*, 2011, **13**, 12403–12406.
- N. Jäckel, P. Simon, Y. Gogotsi and V. Presser, *ACS Energy Lett.*, 2016, **1**, 1262–1265.
- V. Augustyn, J. Come, M. A. Lowe, J. W. Kim, P.-L. Taberna, S. H. Tolbert, H. D. Abruna, P. Simon and B. Dunn, *Nat. Mater.*, 2013, **12**, 518–522.
- A. Tolosa, B. Krüner, S. Fleischmann, N. Jäckel, M. Zeiger, M. Aslan, I. Grobelsek and V. Presser, *J. Mater. Chem. A*, 2016, **4**, 16003–16016.
- E. Lim, H. Kim, C. Jo, J. Chun, K. Ku, S. Kim, H. I. Lee, I.-S. Nam, S. Yoon, K. Kang and J. Lee, *ACS Nano*, 2014, **8**, 8968–8978.
- D. M. Anjos, J. K. McDonough, E. Perre, G. M. Brown, S. H. Overbury, Y. Gogotsi and V. Presser, *Nano Energy*, 2013, **2**, 702–712.

- 20 S. Roldán, C. Blanco, M. Granda, R. Menéndez and R. Santamaría, *Angew. Chem.*, 2011, **123**, 1737–1739.
- 21 J. Lee, B. Krüner, A. Tolosa, S. Sathyamoorthi, D. Kim, S. Choudhury, K.-H. Seo and V. Presser, *Energy Environ. Sci.*, 2016, **9**, 3392–3398.
- 22 J. Lee, A. Tolosa, B. Krüner, N. Jäckel, S. Fleischmann, M. Zeiger, D. Kim and V. Presser, *Sustainable Energy Fuels*, 2017, **1**, 299–307.
- 23 S. E. Chun, B. Evanko, X. Wang, D. Vonlanthen, X. Ji, G. D. Stucky and S. W. Boettcher, *Nat. Commun.*, 2015, **6**, 7818.
- 24 M. Zeiger, S. Fleischmann, B. Krüner, A. Tolosa, S. Bechtel, M. Baltés, A. Schreiber, R. Moroni, S. Vierrath, S. Thiele and V. Presser, *RSC Adv.*, 2016, **6**, 107163–107179.
- 25 J.-G. Wang, F. Kang and B. Wei, *Prog. Mater. Sci.*, 2015, **74**, 51–124.
- 26 M. D. Levi, M. R. Lukatskaya, S. Sigalov, M. Beidaghi, N. Shpigel, L. Daikhin, D. Aurbach, M. W. Barsoum and Y. Gogotsi, *Adv. Energy Mater.*, 2015, **5**, 1400815.
- 27 P. Srimuk, F. Kaasik, B. Krüner, A. Tolosa, S. Fleischmann, N. Jäckel, M. C. Tekeli, M. Aslan, M. E. Suss and V. Presser, *J. Mater. Chem. A*, 2016, **4**, 18265–18271.
- 28 L. Mai, Q. Wei, Q. An, X. Tian, Y. Zhao, X. Xu, L. Xu, L. Chang and Q. Zhang, *Adv. Mater.*, 2013, **25**, 2969–2973.
- 29 G. Yilmaz, C. X. Guo and X. Lu, *ChemElectroChem*, 2016, **3**, 158–164.
- 30 S. Fleischmann, A. Tolosa, M. Zeiger, B. Krüner, N. J. Peter, I. Grobelsek, A. Quade, A. Kruth and V. Presser, *J. Mater. Chem. A*, 2017, **5**, 2792–2801.
- 31 P. Simon, Y. Gogotsi and B. Dunn, *Science Magazine*, 2014, **343**, 1210–1211.
- 32 T. Brousse, D. Bélanger and J. W. Long, *J. Electrochem. Soc.*, 2015, **162**, A5185–A5189.
- 33 Z. Chen, V. Augustyn, J. Wen, Y. Zhang, M. Shen, B. Dunn and Y. Lu, *Adv. Mater.*, 2011, **23**, 791–795.
- 34 P. Srimuk, L. Ries, M. Zeiger, S. Fleischmann, N. Jäckel, A. Tolosa, B. Krüner, M. Aslan and V. Presser, *RSC Adv.*, 2016, **6**, 106081–106089.
- 35 P. Srimuk, M. Zeiger, N. Jäckel, A. Tolosa, B. Krüner, S. Fleischmann, I. Grobelsek, M. Aslan, B. Shvartsev, M. E. Suss and V. Presser, *Electrochim. Acta*, 2017, **224**, 314–328.
- 36 S. Fleischmann, N. Jäckel, M. Zeiger, B. Krüner, I. Grobelsek, P. Formanek, S. Choudhury, D. Weingarth and V. Presser, *Chem. Mater.*, 2016, **28**, 2802–2813.
- 37 S. Boukhalfa, K. Evanoff and G. Yushin, *Energy Environ. Sci.*, 2012, **5**, 6872–6879.
- 38 I.-H. Kim, J.-H. Kim, B.-W. Cho, Y.-H. Lee and K.-B. Kim, *J. Electrochem. Soc.*, 2006, **153**, A989–A996.
- 39 D. Vonlanthen, P. Lazarev, K. A. See, F. Wudl and A. J. Heeger, *Adv. Mater.*, 2014, **26**, 5095–5100.
- 40 M. Zeiger, D. Weingarth and V. Presser, *ChemElectroChem*, 2015, **2**, 1117–1127.
- 41 K. Naoi, S. Ishimoto, Y. Isobe and S. Aoyagi, *J. Power Sources*, 2010, **195**, 6250–6254.
- 42 K. Naoi, S. Ishimoto, J.-i. Miyamoto and W. Naoi, *Energy Environ. Sci.*, 2012, **5**, 9363–9373.
- 43 G. G. Amatucci, F. Badway, A. Du Pasquier and T. Zheng, *J. Electrochem. Soc.*, 2001, **148**, A930–A939.
- 44 V. Khomenko, E. Raymundo-Piñero and F. Béguin, *J. Power Sources*, 2006, **153**, 183–190.
- 45 E. Zhao, C. Qin, H.-R. Jung, G. Berdichevsky, A. Nese, S. Marder and G. Yushin, *ACS Nano*, 2016, **10**, 3977–3984.
- 46 K. Naoi, K. Kisu, E. Iwama, S. Nakashima, Y. Sakai, Y. Orikasa, P. Leone, N. Dupre, T. Brousse, P. Rozier, W. Naoi and P. Simon, *Energy Environ. Sci.*, 2016, **9**, 2143–2151.
- 47 A. S. Arico, P. Bruce, B. Scrosati, J.-M. Tarascon and W. van Schalkwijk, *Nat. Mater.*, 2005, **4**, 366–377.
- 48 N. Jäckel, D. Weingarth, A. Schreiber, B. Krüner, M. Zeiger, A. Tolosa, M. Aslan and V. Presser, *Electrochim. Acta*, 2016, **191**, 284–298.
- 49 N. Jäckel, D. Weingarth, M. Zeiger, M. Aslan, I. Grobelsek and V. Presser, *J. Power Sources*, 2014, **272**, 1122–1133.
- 50 V. L. Kuznetsov, A. L. Chuvilin, Y. V. Butenko, I. Y. Mal'kov and V. M. Titov, *Chem. Phys. Lett.*, 1994, **222**, 343–348.
- 51 M. Zeiger, N. Jäckel, D. Weingarth and V. Presser, *Carbon*, 2015, **94**, 507–517.
- 52 J. K. McDonough, A. I. Frolov, V. Presser, J. J. Niu, C. H. Miller, T. Ubieto, M. V. Fedorov and Y. Gogotsi, *Carbon*, 2012, **50**, 3298–3309.
- 53 K. Makgopa, P. M. Ejikeme, C. J. Jafta, K. Raju, M. Zeiger, V. Presser and K. I. Ozoemena, *J. Mater. Chem. A*, 2015, **3**, 3480–3490.
- 54 A. Moretti and S. Passerini, *Adv. Energy Mater.*, 2016, **6**, 1600868.
- 55 D. Chao, C. Zhu, X. Xia, J. Liu, X. Zhang, J. Wang, P. Liang, J. Lin, H. Zhang, Z. X. Shen and H. J. Fan, *Nano Lett.*, 2015, **15**, 565–573.
- 56 N. A. Chernova, M. Roppolo, A. C. Dillon and M. S. Whittingham, *J. Mater. Chem.*, 2009, **19**, 2526–2552.
- 57 C. Nethravathi, C. R. Rajamathi, M. Rajamathi, U. K. Gautam, X. Wang, D. Golberg and Y. Bando, *ACS Appl. Mater. Interfaces*, 2013, **5**, 2708–2714.
- 58 C. Niu, J. Meng, C. Han, K. Zhao, M. Yan and L. Mai, *Nano Lett.*, 2014, **14**, 2873–2878.
- 59 S. D. Perera, B. Patel, N. Nijem, K. Roodenko, O. Seitz, J. P. Ferraris, Y. J. Chabal and K. J. Balkus, *Adv. Energy Mater.*, 2011, **1**, 936–945.
- 60 M. Zeiger, T. Ariyanto, B. Krüner, N. J. Peter, S. Fleischmann, B. J. M. Etzold and V. Presser, *J. Mater. Chem. A*, 2016, **4**, 18899–18909.
- 61 V. Presser and C. Vakifahmetoglu, *CrystEngComm*, 2012, **14**, 4525–4526.
- 62 S.-f. Ma, J. Liang, J.-f. Zhao and B.-s. Xu, *CrystEngComm*, 2010, **12**, 750–754.
- 63 D. Weingarth, M. Zeiger, N. Jäckel, M. Aslan, G. Feng and V. Presser, *Adv. Energy Mater.*, 2014, **4**, 1400316.
- 64 M. Widmaier, B. Krüner, N. Jäckel, M. Aslan, S. Fleischmann, C. Engel and V. Presser, *J. Electrochem. Soc.*, 2016, **163**, A2956–A2964.
- 65 N. Jäckel, B. Krüner, K. L. van Aken, M. Alhabet, B. Anasori, F. Kaasik, Y. Gogotsi and V. Presser, *ACS Appl. Mater. Interfaces*, 2016, **8**, 32089–32093.
- 66 J. J. Vilatela and D. Eder, *ChemSusChem*, 2012, **5**, 456–478.

- 67 L. Athouël, F. Moser, R. Dugas, O. Crosnier, D. Bélanger and T. Brousse, *J. Phys. Chem. C*, 2008, **112**, 7270–7277.
- 68 M. Thommes, K. Kaneko, A. V. Neimark, J. P. Olivier, F. Rodriguez-Reinoso, J. Rouquerol and K. S. W. Sing, *Pure Appl. Chem.*, 2015, **87**, 1051–1069.
- 69 A. C. Ferrari and J. Robertson, *Phys. Rev. B: Condens. Matter Mater. Phys.*, 2000, **61**, 14095.
- 70 G. A. Zickler, B. Smarsly, N. Gierlinger, H. Peterlik and O. Paris, *Carbon*, 2006, **44**, 3239–3246.
- 71 G. I. Petrov, V. V. Yakovlev and J. Squier, *Appl. Phys. Lett.*, 2002, **81**, 1023–1025.
- 72 V. Presser, K. G. Nickel, A. Loges and C. Berthold, *Scr. Mater.*, 2010, **62**, 219–222.
- 73 J. Cebik, J. K. McDonough, F. Peerally, R. Medrano, I. Neitzel, Y. Gogotsi and S. Osswald, *Nanotechnology*, 2013, **24**, 205703.
- 74 M. Zeiger, N. Jäckel, M. Aslan, D. Weingarth and V. Presser, *Carbon*, 2015, **84**, 584–598.
- 75 K. L. van Aken, K. Maleski, T. S. Mathis, J. P. Breslin and Y. Gogotsi, *ECS J. Solid State Sci. Technol.*, 2017, **6**, M3103–M3108.
- 76 J. W. Kim, V. Augustyn and B. Dunn, *Adv. Energy Mater.*, 2012, **2**, 141–148.
- 77 M. Sathiya, A. S. Prakash, K. Ramesha, J. M. Tarascon and A. K. Shukla, *J. Am. Chem. Soc.*, 2011, **133**, 16291–16299.
- 78 V. Augustyn, P. Simon and B. Dunn, *Energy Environ. Sci.*, 2014, **7**, 1597–1614.
- 79 S. Ardizzone, G. Fregonara and S. Trasatti, *Electrochim. Acta*, 1990, **35**, 263–267.
- 80 J. Wang, J. Polleux, J. Lim and B. Dunn, *J. Phys. Chem. C*, 2007, **111**, 14925–14931.
- 81 H. Lindström, S. Södergren, A. Solbrand, H. Rensmo, J. Hjelm, A. Hagfeldt and S.-E. Lindquist, *J. Phys. Chem. B*, 1997, **101**, 7717–7722.
- 82 A. J. Bard and L. R. Faulkner, *Electrochemical Methods: Fundamentals and Applications*, John Wiley & Sons, 2001.
- 83 N. Shpigel, M. D. Levi, S. Sigalov, O. Girshevitz, D. Aurbach, L. Daikhin, P. Pikma, M. Marandi, A. Jänes, E. Lust, N. Jäckel and V. Presser, *Nat. Mater.*, 2016, **15**, 570–575.
- 84 F. Kaasik, T. Tamm, M. M. Hantel, E. Perre, A. Aabloo, E. Lust, M. Z. Bazant and V. Presser, *Electrochem. Commun.*, 2013, **34**, 196–199.
- 85 J. K. Lee, K. B. Smith, C. M. Hayner and H. H. Kung, *Chem. Commun.*, 2010, **46**, 2025–2027.
- 86 X. Zhou, Q. Chen, A. Wang, J. Xu, S. Wu and J. Shen, *ACS Appl. Mater. Interfaces*, 2016, **8**, 3776–3783.
- 87 L. Li, S. Peng, H. B. Wu, L. Yu, S. Madhavi and X. W. Lou, *Adv. Energy Mater.*, 2015, **5**, 1500753.

Electronic Supplementary Information

**Tuning pseudocapacitive and battery-like lithium
intercalation in vanadium dioxide/carbon onion
hybrids for asymmetric supercapacitor anodes**

Simon Fleischmann,^{1,2} Marco Zeiger,^{1,2} Nicolas Jäckel,^{1,2} Benjamin Krüner,^{1,2}

Valeria Lemkova,^{1,2} Mathias Widmaier,^{2,3} and Volker Presser^{1,2,*}

¹ INM – Leibniz Institute for New Materials, 66123 Saarbrücken, Germany

² Department of Materials Science and Engineering, Saarland University, 66123 Saarbrücken, Germany

³ Robert Bosch GmbH, 70049 Stuttgart, Germany

* Corresponding author's eMail: volker.presser@leibniz-inm.de

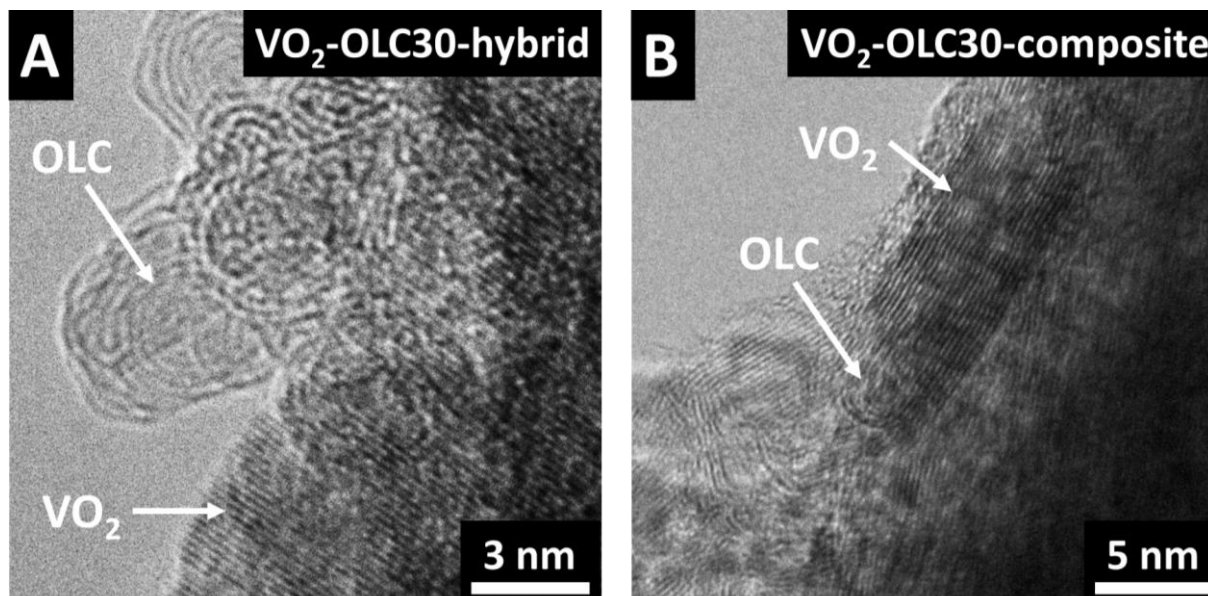


Figure S1: Transmission electron micrographs of (A) VO₂-OLC30-hybrid and (B) VO₂-OLC30-composite samples.

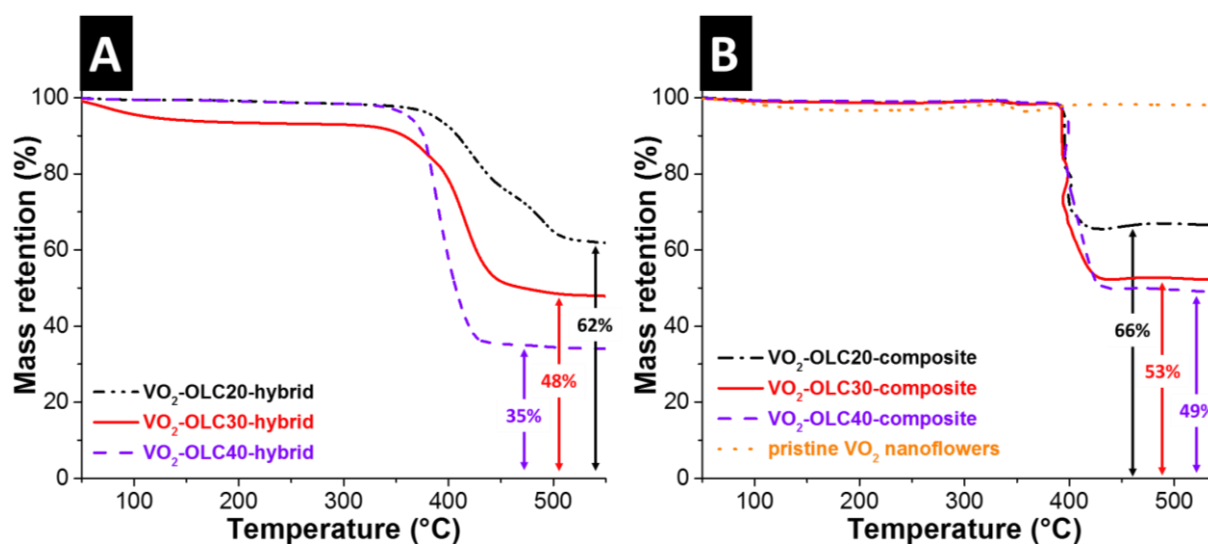


Figure S2: Thermogravimetric analysis of (A) VO₂-OLC-hybrid samples and (B) VO₂-OLC-composite samples and pristine VO₂ nanoflowers, carried out in synthetic air (flow rate of 20 mL·min⁻¹) up to a temperature of 550 °C at a heating rate of 5 °C·min⁻¹.

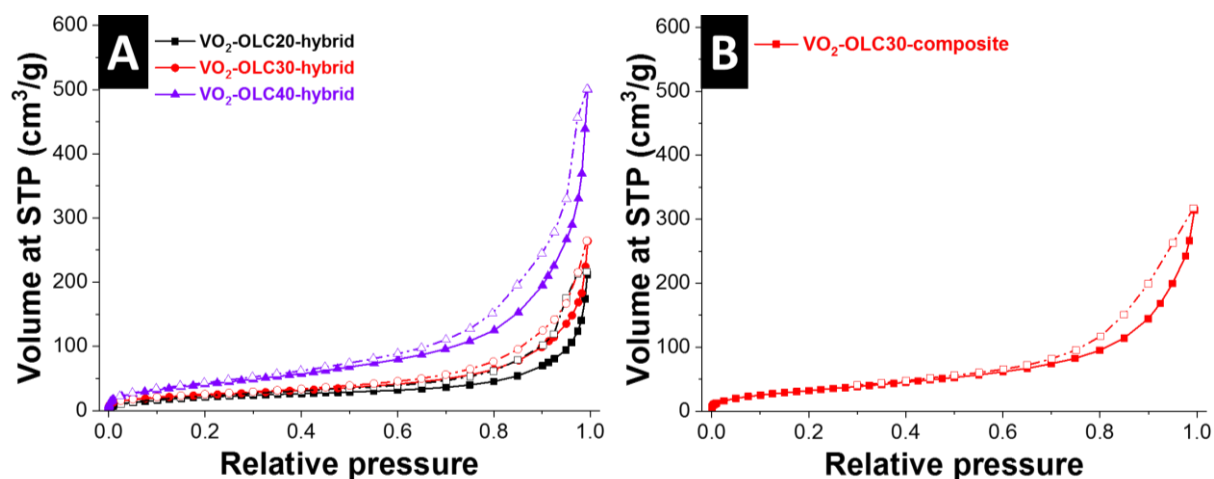


Figure S3: Nitrogen sorption isotherms at standard temperature and pressure of (A) VO₂-OLC-hybrid samples and (B) VO₂-OLC30-composite sample. The dashed lines correspond to the desorption branch.

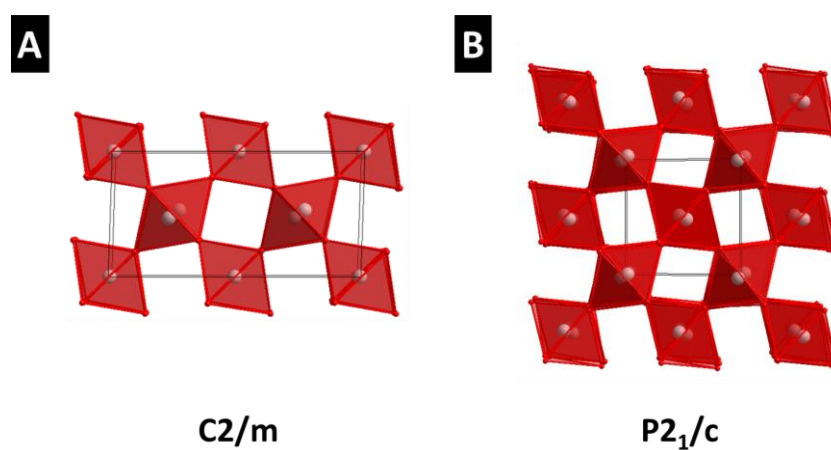


Figure S4: Crystal structures of the monoclinic VO₂ structure in (A) C2/m and (B) P2₁/c space group. The vanadium atoms are represented by white spheres, oxygen atoms by red spheres. The distances between the shared oxygen atoms at the corners of the octahedra show a fixed distance of 3.3 Å for C2/m and a varying distance between 2.9 Å and 6.4 Å for P2₁/c.

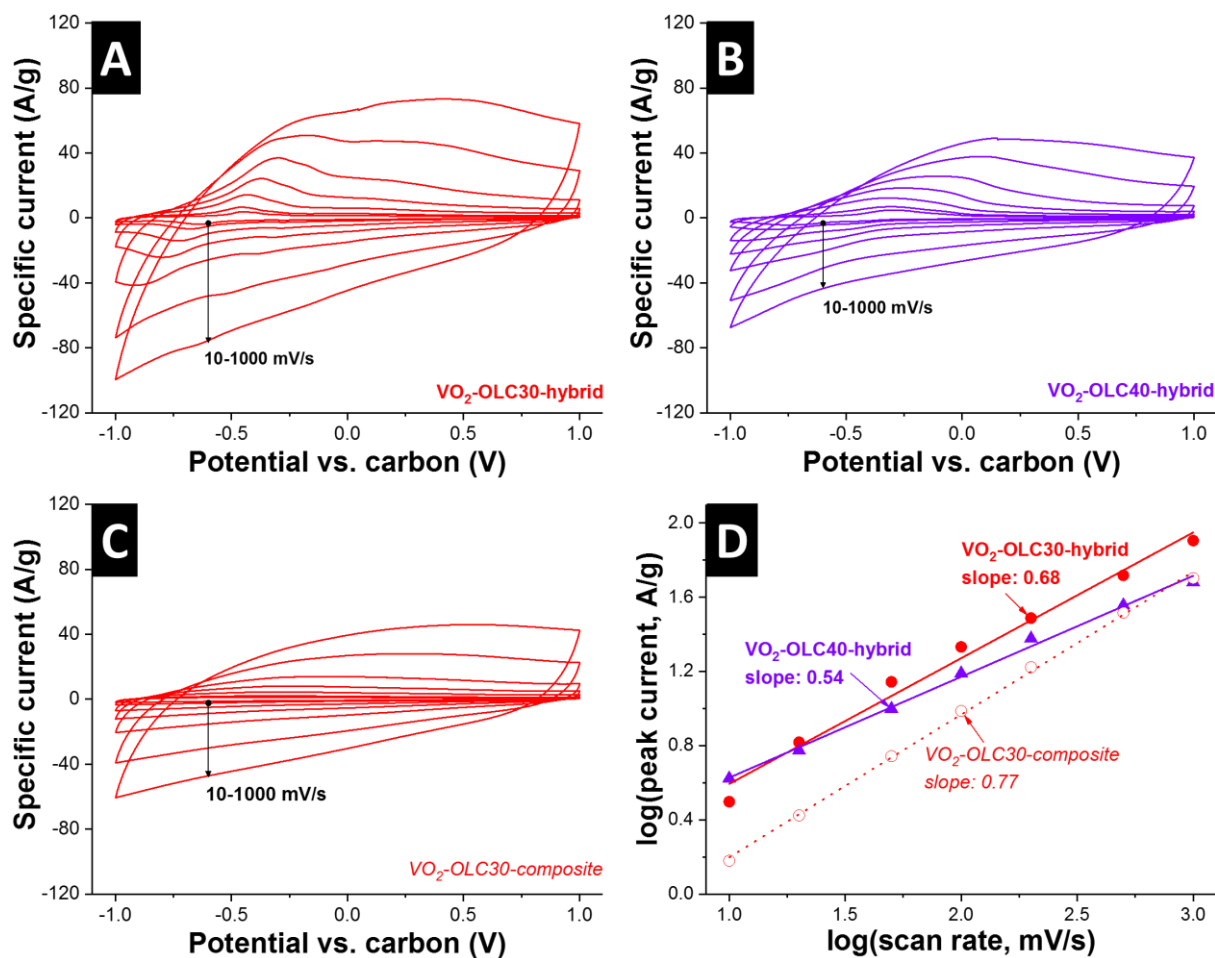


Figure S5: CVs of (A) VO₂-OLC30-hybrid, (B) VO₂-OLC40-hybrid, and (C) VO₂-OLC30-composite samples measured in half-cells and varying scanning speeds of 10-1000 mV·s⁻¹. (D) Kinetic analysis via logarithmic plotting of the peak current at -0.7 V vs. carbon against the scan rate and linear regression applied to the data points.

Table S1: Electrode conductivity of VO₂-OLC30-hybrid and VO₂-OLC30-composite electrodes by 4-point probe as an average of six measurements.

Material	Electrode conductivity (S·cm ⁻¹)
VO ₂ -OLC30-hybrid	0.30 ± 0.03
VO ₂ -OLC30-composite	0.16 ± 0.05

Table S2: Specific surface area (BET) and pore volume (at P/P₀=0.95) of VO₂-OLC samples and as synthesized vanadium oxide nanoflowers and carbon onions.

Material	SSA (BET) (m ² ·g ⁻¹)	Pore volume (cm ³ ·g ⁻¹)
VO ₂ -OLC20-hybrid	81	0.15
VO ₂ -OLC30-hybrid	89	0.21
VO ₂ -OLC40-hybrid	160	0.41
VO ₂ -OLC30-composite	118	0.31
VO ₂ as synthesized	38	0.04
OLCs as synthesized	352	0.93

Table S3: Analysis of D- and G-bands of the samples VO₂-OLC30-hybrid and VO₂-OLC30-composite, calculated by peak deconvolution.

Material	FWHM D (cm ⁻¹)	FWHM G (cm ⁻¹)	I _D /I _G	Pos. D-band (cm ⁻¹)	Pos. G-band (cm ⁻¹)
VO ₂ -OLC30-hybrid	69	48	2.7	1347	1590
VO ₂ -OLC30-composite	58	40	2.3	1347	1587

4.4 Design of carbon/metal oxide hybrids for electrochemical energy storage

Simon Fleischmann,^{1,2} Aura Tolosa,^{1,2} Volker Presser^{1,2}

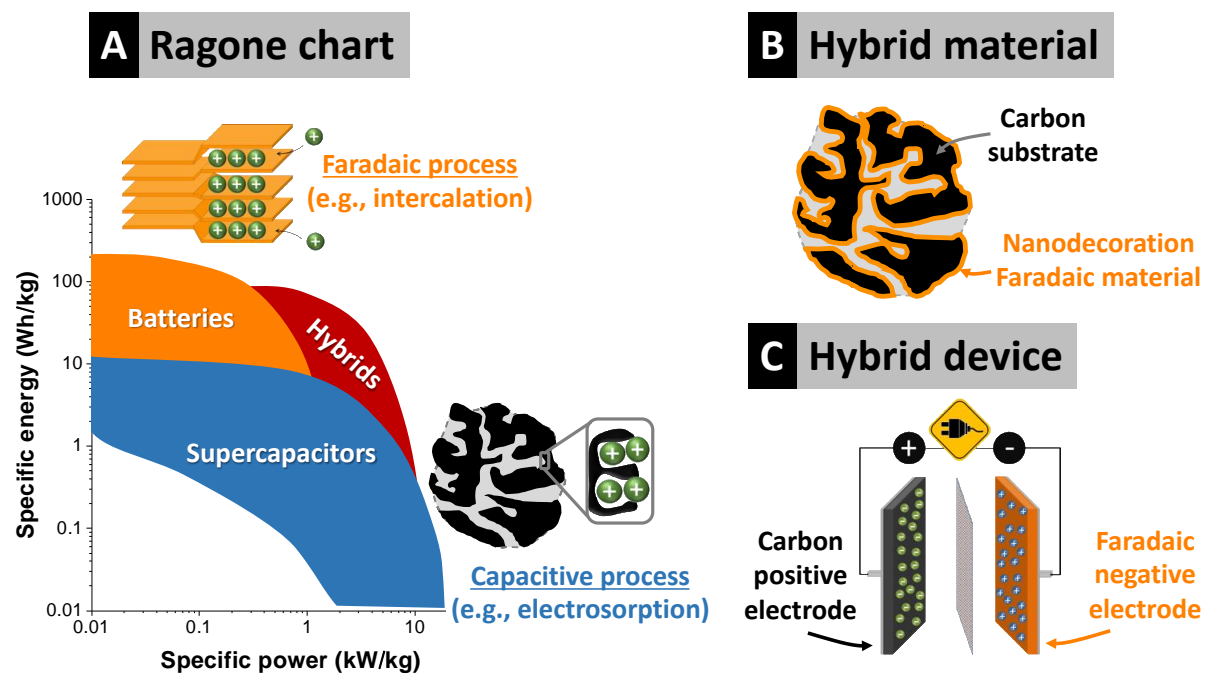
¹ INM - Leibniz Institute for New Materials, 66123 Saarbrücken, Germany

² Department of Materials Science and Engineering, Saarland University, 66123 Saarbrücken, Germany

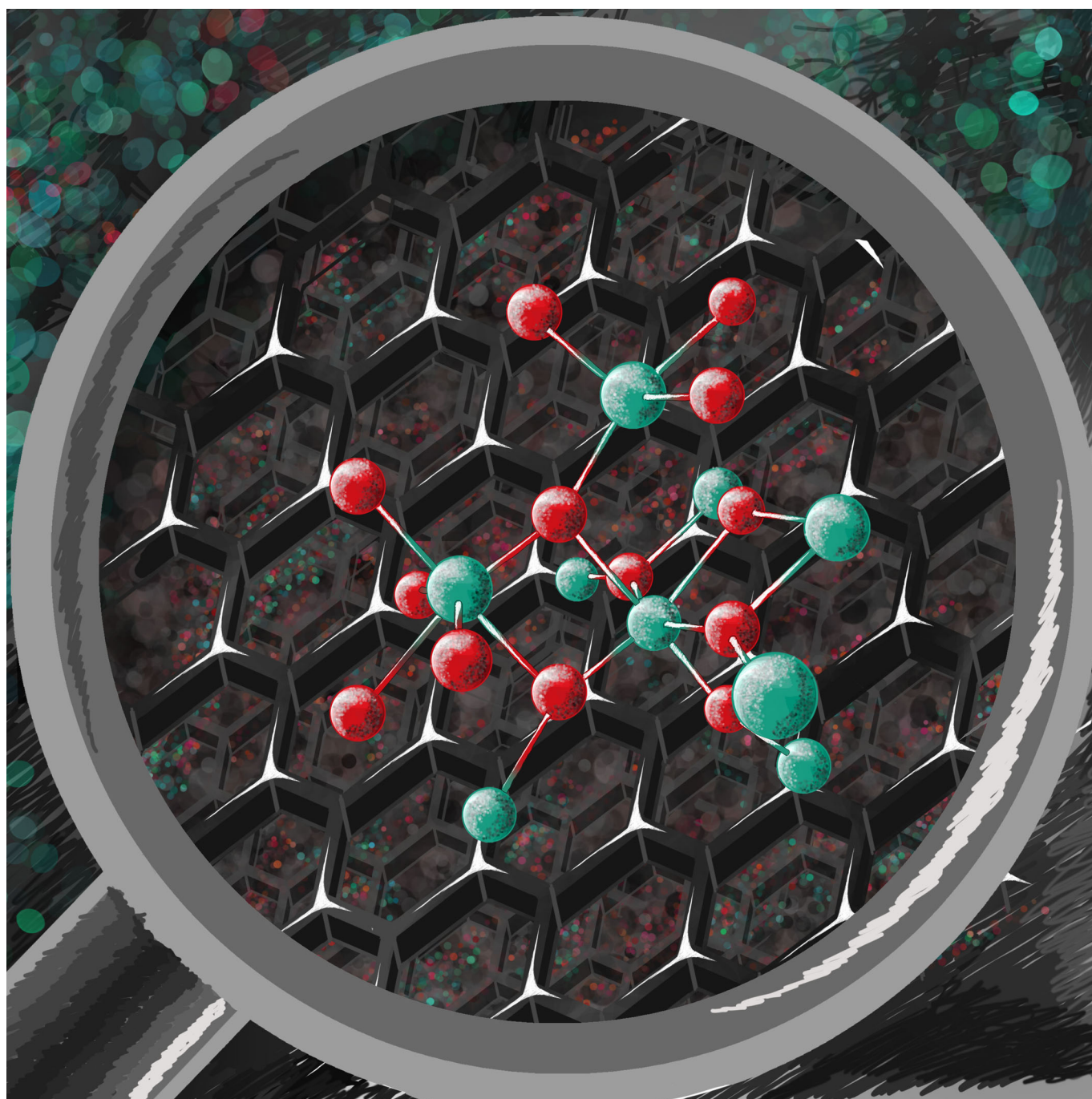
Citation:

S. Fleischmann, A. Tolosa and V. Presser, *Design of carbon/metal oxide hybrids for electrochemical energy storage*, Chem. - Eur. J., **2018**, DOI: 10.1002/chem.201800772.

Own contribution: Paper design, planning, writing.



■ Renewable Energy

Yc Design of Carbon/Metal Oxide Hybrids for Electrochemical Energy StorageSimon Fleischmann,^[a, b] Aura Tolosa,^[a, b] and Volker Presser^{*[a, b]}

Abstract: Next generation electrochemical energy storage materials that enable a combination of high specific energy, specific power, and cycling stability can be obtained by a hybridization approach. This involves electrode materials that contain carbon and metal oxide phases linked on a nanoscopic level and combine characteristics of supercapacitors and batteries. The combination of the components requires careful design to create synergistic effects for an increased electrochemical performance. Improved understanding of the role of carbon as a substrate has advanced the power handling and cycling stability of hybrid materials significantly in recent years. This Concept outlines different design strategies for the design of hybrid electrode materials: (1) the deposition of metal oxides on readily existing carbon substrates and (2) co-synthesizing both carbon and metal oxide phase during the synthesis procedure. The implications of carbon properties on the hybrid material's structure and performance will be assessed and the impact of the hybrid electrode architecture will be analyzed. The advantages and disadvantages of all approaches are highlighted and strategies to overcome the latter will be proposed.

Introduction

Electrochemical energy storage

In the face of global warming, scarcity of fossil fuels, and a steadily growing energy demand, the transition to renewable energy sources has been identified as one of the most urgent tasks to the scientific community during the next decades.^[1] The large-scale implementation of renewable energy, however, leads to a shifting paradigm for power generation, that is, from production on demand to production when available. The resulting fluctuations make the use of fast-responding electrochemical energy storage (EES) devices indispensable.^[2] Generally, EES devices can typically be divided into two groups, (1) supercapacitors, or electrical double-layer capacitors (EDLCs) that store energy by physical electrosorption of ions at the surface of their electrodes, and (2) batteries that employ Faradaic reactions in the bulk volume of their electrodes.

EDLCs are a prominent technology for rapid and highly reversible energy storage that utilize the separation of electrical

charges at the interface of electrodes and electrolyte.^[3] When an EDLC is charged, electrolyte ions diffuse to and electrosorb on the surface of the oppositely charged electrode, forming the electrical double-layer. Suitable electrode materials offer a high surface area for ion adsorption, as well as good electrical conductivity. These properties are well met by microporous carbons, such as activated carbons^[4] or carbide-derived carbons^[5] and nanocarbons like graphene,^[6] carbon onions,^[7] or carbon nanotubes.^[8] The electrosorption process is distinguished by very fast charge/discharge kinetics, leading to a quick energy uptake/release of supercapacitors (over 10 kW kg⁻¹). In contrast, the specific energy remains about an order of magnitude below that of batteries.^[3b] Despite efforts to further increase the specific energy of EDLCs by extending the surface area of microporous carbons or matching their pore sizes with the electrolyte ion sizes,^[9] the capacitance (and therefore the energy) of an EDLC is intrinsically limited to about 0.1 F m⁻² because even smaller pores can no longer accommodate ions and thinner pore walls can no longer screen electrical charges.^[10]


In contrast, a battery stores energy by Faradaic processes such as intercalation, conversion, or alloying reactions between its electrolyte ions and its electrodes. The most prominent system is the lithium-ion intercalation battery, but because of the high cost and geographically limited availability of lithium,^[11] alternative ionic systems like sodium^[12] or potassium^[13] are being explored. Unlike an EDLC, lithium-ion batteries employ two different materials as anode and cathode. When charged, lithium ions are extracted from the cathode and inserted into the anode material, resulting in Faradaic charge transfer. The different electrochemical potentials of the anode and the lithium and cathode determine the cell voltage of the battery.^[14] The electrode materials need to enable the insertion (intercalation) of lithium and should show a low (anode) or a high standard reduction potential (cathode). Typical candidates for intercalation-type electrodes are graphite^[15] or metal oxides^[16] that exhibit a layered structure, in between which the lithium ions can be stored or released. During intercalation, lithium ions must diffuse through the electrode material to reach the reaction sites, which is a kinetically limited process and leads to a relatively low power output of batteries (<1 kW kg⁻¹). Furthermore, intercalation and deintercalation processes are associated with expansion and shrinking of the electrodes, which exercises substantial mechanical stresses on the host material,^[17] limiting the cycling life of a battery to typically below 1000 cycles.


Hybrid electrochemical energy storage materials

It is obvious that EDLCs and batteries offer both certain distinct advantages. Therefore, hybridization of EDLC and batteries is highly attractive. Nowadays, hybridization is becoming increasingly popular in the field of electrochemical energy storage for the creation of novel electrode materials that offer both a high specific energy and power. Yet, improved performance can only be reached when following certain design

[a] S. Fleischmann, A. Tolosa, Prof. Dr. V. Presser
INM-Leibniz Institute for New Materials
66123 Saarbrücken (Germany)
E-mail: volker.presser@leibniz-inm.de

[b] S. Fleischmann, A. Tolosa, Prof. Dr. V. Presser
Department of Materials Science and Engineering
Saarland University, 66123 Saarbrücken (Germany)

 The ORCID numbers for the authors of this article can be found under:
<https://doi.org/10.1002/chem.201800772>

 Part of a Special Issue to commemorate young and emerging scientists. To view the complete issue, visit Issue 47.

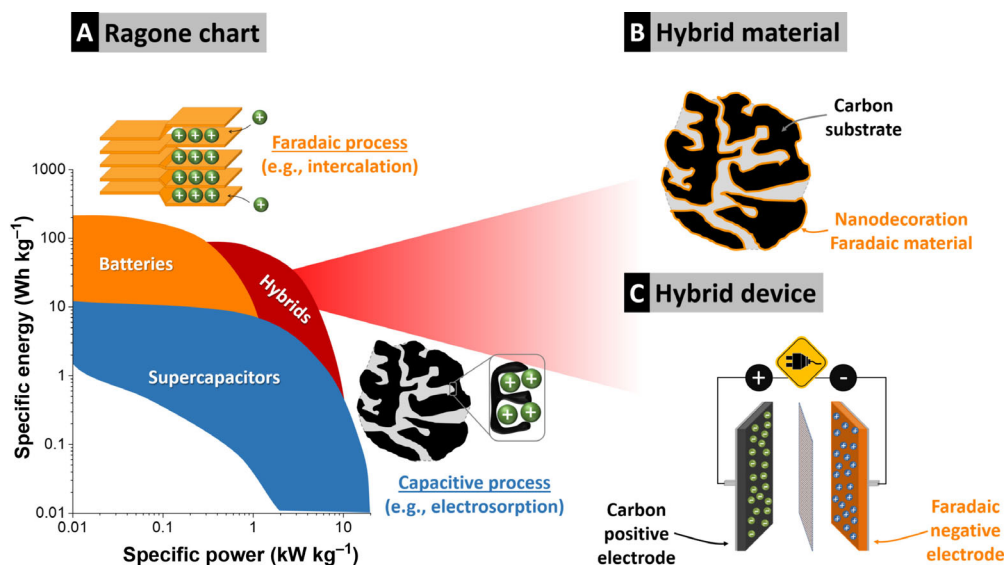


Figure 1. (A) Ragone chart displaying typical ranges of specific energy and specific power for supercapacitors, batteries, and hybrids. (B) Scheme of a hybrid material consisting of a porous carbon substrate coated with Faradaic material. (C) Scheme of a hybrid supercapacitor device using a capacitive positive electrode and a Faradaic negative electrode.

guidelines to avoid the detrimental effects intrinsic to both individual technologies.

Supercapacitors and batteries are often compared in a Ragone chart (Figure 1A), comparing energy and power performances. A synergistic combination of the two technologies can yield superior properties regarding specific energy and power handling of the resulting material or device.^[18] Yet, such hybridization can be realized in different ways. On an electrode material level, the introduction of thin layers or nanoparticles of Faradaic materials to a high surface area carbon yields a hybrid material (Figure 1B). By this way, high conductivity, high specific surface area, and redox-active surfaces are combined in one material. Common synthesis techniques to assure a homogenous mixing of both components include wet-chemical approaches^[16b, 19] and non-line-of-sight vapor deposition like atomic layer deposition^[20] or chemical vapor deposition.^[21] Yet, hybridization can also be realized from a device engineering point of view. Hybrid supercapacitors (also referred to as asymmetric supercapacitors or lithium-ion capacitors)^[22] combine two electrodes that each use a different charge storage mechanism; for example, a nanoporous carbon employing double-layer capacitance as the positive electrode and a material enabling intercalation reactions as the negative electrode (Figure 1C). The resulting devices may yield attractive performance metrics that constitute an intriguing alternative to pure supercapacitor or battery systems, if the used Faradaic electrode offers sufficient reaction kinetics.^[23] This makes hybrid materials excellent candidates for the use as the Faradaic electrode in hybrid supercapacitors. This Concept article will focus exclusively on hybridization of electrode materials. These materials will find use in advanced hybrid supercapacitor devices and enable batteries with improved power handling.

Although the surface of carbons used for EDLC electrodes is ideally chemically inert towards the ions of the electrolyte, Faradaic materials undergo redox reactions with the ions. Nano-

scale decoration of carbons with a battery material introduces Faradaic charge transfer to the system, thereby significantly enhancing the specific capacity. The nanoscopic size of the Faradaic materials incorporated in the carbon electrodes leads to a confinement of the redox reactions close to the electrode/electrolyte interface. Therefore, pathways for ions to the reaction sites are short and high rates, comparable to EDLCs, are enabled as the system is significantly less limited by solid-state diffusion in the electrode bulk.^[24] Further, maintaining a continuous carbon network throughout the hybrid electrode ensures electrical percolation and enables facile electron transport to the often electrically insulating domains of Faradaic material. This combination of Faradaic materials and carbon, which are chemically linked on a molecular scale, yields a hybrid electrode material (Figure 2). That way, synergistic effects between both phases can be created. An alternative to hybridization is the mechanical mixing of Faradaic materials with conductive additives to form composite electrodes (Figure 2). Here, usually no chemical bonding between the separate phases is created

Volker Presser obtained his Ph.D. in 2006 from the Eberhard Karls University in Tübingen, Germany. As a Humboldt Research Fellow and Research Assistant Professor, he worked between 2010 and 2012 at the A. J. Drexel Nanotechnology Institute in the team of Yury Gogotsi at Drexel University, Philadelphia, USA. Today, he is Full Professor at the Department of Materials Science and Engineering at Saarland University and Program Division Leader at the INM-Leibniz Institute for New Materials in Saarbrücken, Germany. His current work focusses on nanocarbon and hybrid nanomaterials for electrochemical applications, such as energy storage, harvesting, and water desalination.



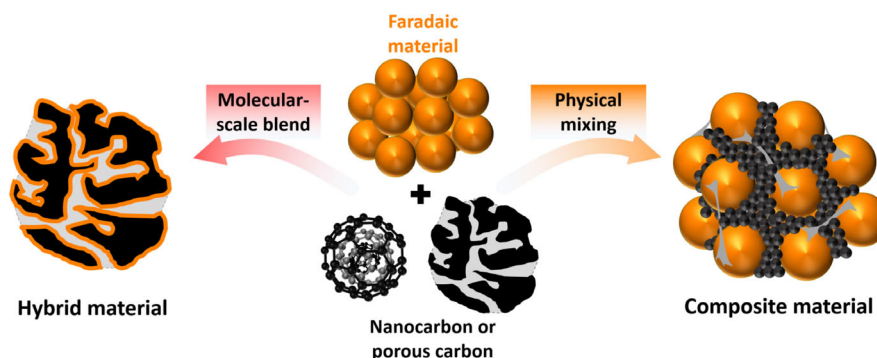


Figure 2. Schematic representation of different synthetic approaches for the combination of carbon with Faradaic material and proposed terminology. Hybridization yields a chemical connection of the two components on a nanoscale and creates synergistic interactions (left). Composite materials are obtained by a physical mixing of the two components, usually without chemical bonding between separate phases, using individual properties of both phases (right).

and the individual properties of the components (e.g., redox activity and electrical conductivity) are used.^[25] Hybridization enables a much more intimate interface between the two components, as clustering of two separate phases with often dissimilar surface chemistries is avoided, leading to enhanced charge transfer in hybrid materials.^[25,26] The proposed terminology in Figure 2 is inspired by Eder and co-workers^[25] and enables us to differentiate between these two types of electrode materials in a clear and consistent manner throughout the paper.

A variety of Faradaic materials has been employed in hybrid electrodes, most prominently metal oxides for intercalation-type hybrids (e.g., V_2O_5 ,^[16a] MnO_2 ,^[27] Nb_2O_5 ,^[28] TiO_2 ,^[29] MoO_2),^[30] but recently, also carbon/sulfur hybrids^[31] and carbon/transition-metal dichalcogenide hybrids^[32] have been introduced. The design of hybrid electrode materials requires a firm understanding for the role of both components (carbon and Faradaic material) and how a synergy between both can be created. Most studies solely focus on the optimization of the Faradaic component, for example, by modifying the crystal structure by doping with foreign atoms^[33] or the introduction of oxygen vacancies.^[34] It is often neglected that also the properties of the carbon substrate have a major impact on the electrochemical properties of the hybrid material. The choice of the type of carbon must be adjusted to the used Faradaic material, the synthesis technique, and the desired application. There is a plethora of carbon materials with vast differences in morphology, graphitization, surface area, and porosity, with the latter being considerably the most important property for many applications.

When comparing carbon materials, it is helpful to differentiate two types of pore architectures (according to ref. [35]):

- (1) Endohedral carbons exhibit a negative surface curvature and show intraparticle porosity, meaning pores are located inside the particles or fibers. Common carbons of this group are activated carbons, carbide-derived carbons, or templated carbons (Figure 3A). Typically, such carbons show high specific surface areas ($> 1500 \text{ m}^2 \text{ g}^{-1}$; inner surface) and are mainly microporous (pore sizes $< 2 \text{ nm}$). They are usually synthesized by physicochemical activation

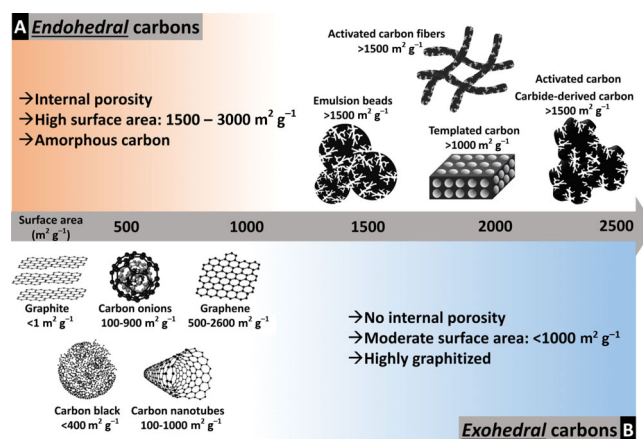


Figure 3. Classification of carbon materials according to their porosity and specific surface area. (A) Endohedral carbons that show internal porosity and typically high specific surface area. (B) Exohedral carbons without internal porosity, often nanocarbons with moderate specific surface area.

or etching processes. Such internal pores create structural disruptions, yielding a reduced graphitic order with incompletely crystalline/amorphous carbon.

- (2) Exohedral carbons with positive surface curvatures show mostly external surface area outside the bulk particle (outer surface; Figure 3B). These materials include nanocarbons such as carbon nanotubes or carbon onions with specific surface areas below $1000 \text{ m}^2 \text{ g}^{-1}$. They form predominantly meso- and macropores in between the particles or aggregates, in the interparticle volume. Exohedral carbons exhibit far less defective graphitic structures, yielding electrical conductivity that is superior to that of endohedral carbons.

In a hybrid electrode, requirements of the carbon component include a high specific surface area to maximize the electrode/electrolyte interface, a pore structure that provides easy access for electrolyte ions and allows for the incorporation of large amounts of Faradaic material, and a graphitic structure that maximizes electrical conductivity. Conventional carbons do not meet all of these properties; for example, increasing the specific surface area often comes at the cost of narrower,

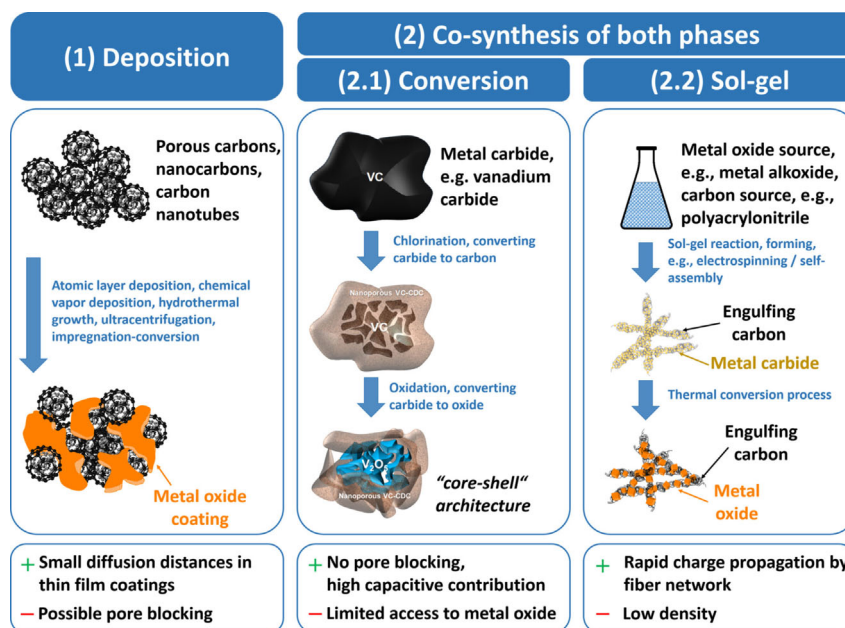


Figure 4. Illustration of discussed synthesis strategies for hybrid materials. (1) Deposition of metal oxide onto an existing carbon substrate. (2) Co-synthesizing metal oxide engulfed by a carbon phase by either (2.1) conversion of a single precursor or (2.2) controlled sol-gel synthesis.

less accessible pores. Strategies to address these issues for carbon/metal oxide hybrid materials will be discussed in the following sections. Figure 4 provides an outline of the discussed synthesis routes with distinction between two general concepts: (1) the deposition of a metal oxide onto an already existing carbon substrate, and (2) co-synthesizing both carbon and metal oxide components during the synthesis procedure.

Strategy 1: Thin Metal Oxide Coating on a Carbon Substrate

A common route to obtain hybrid electrode materials is the deposition of metal oxide on a carbon substrate. In that case, a metal oxide will be incorporated into the interparticle and/or intraparticle volume of the carbon. Consequently, the porosity of the substrate strongly influences the structure of the final hybrid material. For example, atomic layer deposition (ALD) can be employed to deposit metal oxide directly on free-standing or casted thin-film carbon electrodes. ALD allows non-line-of-sight decoration of a substrate by use of self-limiting vapor deposition through binary cycles.^[20] During each reaction cycle, ideally one atomic layer of the desired material is deposited (Figure 5A), giving precise control over the coating thickness by adjusting the number of deposition cycles.

In a recent study by our group, representatives of endohedral carbon (activated carbon) and exohedral carbon (carbon onions) were employed as substrates for atomic layer deposited vanadium oxide (Figure 5B) to give insights into the influence of porosity on the resulting hybrid electrode structure and electrochemical performance.^[36] First indications for the structural changes are given by the mass change of the electrodes during the ALD process. The mass of carbon onion-based electrodes increases linearly with the number of deposi-

tion cycles (Figure 5C), which indicates highly conformal ALD in which a constant number of adsorption sites for the precursor molecules is maintained throughout the process. Contrarily, the mass gain of activated carbon-based electrodes reaches a saturation after 100 ALD cycles (Figure 5C). This reveals that internal surface area of activated carbon becomes blocked by growing vanadium oxide layers, drastically reducing the number of available growth sites for further vanadium oxide deposition. Pore blocking, which was further verified in the study by gas sorption analysis, is unwanted for hybrid electrodes because it seals the activated carbon particles and prevents access to the inner surface area for electrolyte ions. Therefore, the high surface area advantage of activated carbon over carbon onions is negated.

Other studies came to similar conclusions. Daubert et al. described difficulties in the coating process when carbon substrate pore sizes were in the range of the ALD precursor molecule size, effectively inhibiting precursor diffusion.^[37] The latter work also determined a critical pore diameter for successful vanadium oxide deposition by modeling carbon pores as a series of connected, narrowing tubes. It was shown that pores below a diameter of 1.3 nm become completely sealed during the ALD process because of size limitations posed by the precursor dimensions.^[38] Thereby, we can formulate the following guideline for coating porous materials by ALD: Pores smaller than 2 nm are inaccessible to the precursors and become blocked by growing layers at higher mass loadings; mesopores larger than 2–3 nm, however, are well-suited for metal oxide deposition by ALD.^[36]

In a further study by our group, the benefits of mesopores were exemplified for a carbon substrate with a well-tailored pore size distribution. Hard-templating using silica nanoparticles yielded an well-defined mesoporous carbon with a con-

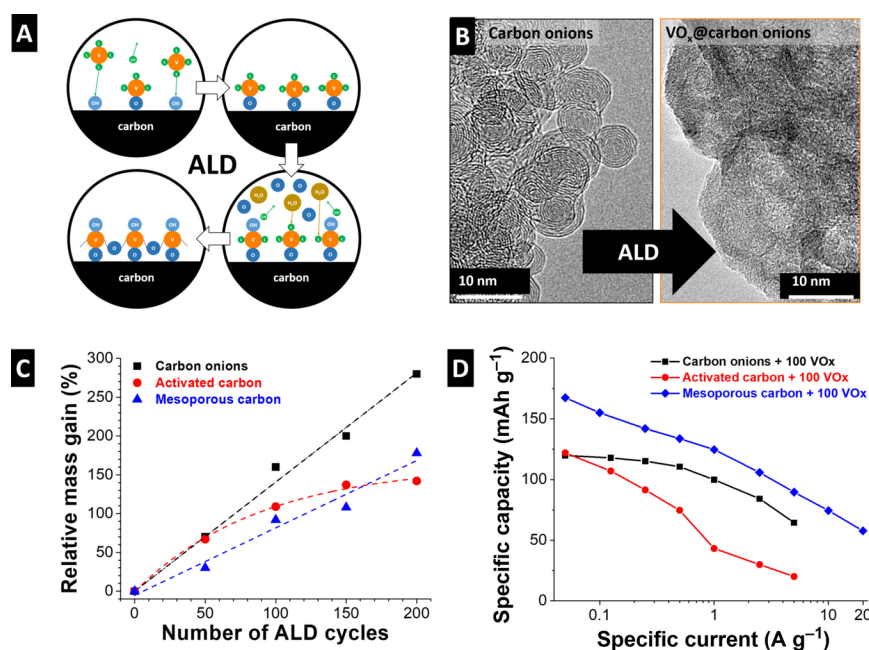


Figure 5. (A) Representation of a single atomic layer deposition (ALD) reaction cycle depositing vanadium oxide. (B) Transmission electron micrographs of carbon onions before and after deposition of 200 ALD cycles of vanadium oxide. (C) Measured mass gain of carbon onion, activated carbon, and tailored mesoporous carbon electrodes when coating with 50, 100, 150, and 200 ALD cycles of vanadium oxide. (D) Rate handling behavior of the respective hybrid materials coated with 100 ALD cycles in 1 M LiClO₄ in acetonitrile as electrolyte. Data replotted from ref. [36,39].

trollable pore structure in the size range of the used silica particles.^[39] This endohedral carbon consisted of micrometer-sized particles with internal porosity and a specific surface area of 1000 m²g⁻¹ which was mostly created by mesopores in range the of 5–20 nm. During the vanadium oxide growth by ALD, a linear mass gain relation similar to carbon onions was observed for mesoporous carbon (Figure 5C), indicating the absence of pore blocking. Hence, mesoporous carbons combine a large specific surface area, leading to a large electrode/electrolyte interface, with a pore structure that is suitable for metal oxide deposition.

The electrochemical performance of carbon onions, activated carbon, and mesoporous carbon coated with 100 ALD cycles of vanadium oxide was compared in 1 M LiClO₄ in acetonitrile organic electrolyte (Figure 5D). When cycling the electrodes at a very low current, carbon onion- and activated carbon-based hybrids show similar specific capacity of about 120 mAh g⁻¹ because the system is given enough time for solid-state diffusion. Therefore, Li ions can reach the intercalation sites in both the open, exohedral carbon onion-hybrid structure, as well as in the partially blocked, endohedral activated carbon particles. Higher charging currents, however, reveal the advantage of carbon onions as a substrate that offers better access for Li ions and a superior electrical conductivity. Mesoporous carbon as a substrate exhibited a higher initial capacity of around 170 mAh g⁻¹ and the best rate handling. The reason for the higher specific capacity is that more of the vanadium oxide coating is connected to the conductive network and able to partake in Faradaic reactions with Li ions. This is related to the well-defined, spherical mesopore structure that leads to more homogeneously distributed vanadium

oxide domains. The high specific surface area of the endohedral structure further leads to thinner coatings that are responsible for the improved rate handling, with mesoporous carbon hybrids showing the same capacity of around 65 mAh g⁻¹ at a 4-fold higher discharging current (20 A g⁻¹) when compared to the carbon onion hybrid (5 A g⁻¹).

Volumetric expansion of Faradaic material during intercalation may lead to disintegration and loss of contact from the conducting network of the electrode.^[17] Here lies a distinct advantage of substrates with endohedral porosity: The internal porosity can effectively prevent this disintegration by confining the metal oxide coating inside the limited pore space. Cycling stability measurements of mesoporous carbon-based hybrid electrodes showed a slightly increasing specific capacity after more than 2000 charge/discharge cycles in 1 M LiClO₄ in acetonitrile electrolyte, and only small capacity decay using 1 M NaClO₄ electrolyte, which represented the most stable performance of vanadium oxide-based materials for sodium intercalation.^[39]

The findings gained from hybrid materials obtained by ALD can also be transferred to other synthesis techniques. A cheap and large-scale production of hybrid material can be achieved through wet-chemical methods. Comparing the suitability of activated carbon and carbon onions as substrates for hydrothermally grown manganese oxide showed similar findings like the studies using ALD. Carbon onions provided good conditions for homogenous deposition of birnessite-type manganese oxide,^[40] whereas blocking of internal surface area was observed for activated carbon. However, considering that the hydrothermal approach is less precise compared to ALD, the minimum accessible pore size was bigger, and a sealing of the

activated carbon particles was already observed at lower mass loadings.^[16b] The study further concluded that the degree of carbon onion graphitization had a substantial impact on the electrochemical properties of the hybrid materials. Carbon onions synthesized at 1700 °C yielded higher electrical conductivity than at 1300 °C, resulting in an improved rate handling of the carbon onion/manganese oxide hybrid electrodes in 1 M Na₂SO₄ aqueous electrolyte.^[16b]

A study by Zhang et al. investigated the suitability of layered carbide-derived carbon (CDC) as a substrate for hydrothermally deposited niobia.^[41] It was found that even by the use of a guiding agent during deposition, about 80% of the surface area became blocked by introducing niobia, resulting in a limited maximum capacity of about 44 mAh g⁻¹ at 20 C. The follow-up study of Lai et al. found an intriguing concept to avoid blocking of internal surface area.^[42] By first depositing niobia on a reduced graphene oxide substrate before introducing to the CDC scaffold, niobia/graphene oxide material preferentially anchored at the edges of CDC layers due to controlled surface charges, thus avoiding blocking of internal CDC surface area. The resulting niobia/reduced graphene oxide/CDC hybrid material showed improved capacity and rate handling with about 100 mAh g⁻¹ at 1 C and 60 mAh g⁻¹ at 40 C, owing to an additional double-layer component to the overall charge storage and better accessibility for the electrolyte.^[42]

Achieving high loadings of Faradaic materials in hybrid electrodes is of particular interest for the transfer to industrial applications, because the mass proportion of electrode to other inactive device components is increased.^[43] High areal mass loadings can be reached by increasing the thickness of the hybrid electrode, which often significantly decreases the gravimetric performance compared to thin electrodes.^[43] Addressing this issue, Sun et al. used holey graphene as a substrate for niobium oxide with varying areal loadings of 1–11 mg cm⁻².^[44] The influence of graphene porosity was investigated by introducing in-plane pores by H₂O₂ activation, in which an increasing activation time led to larger average pore sizes (up to 2.7 nm) and higher specific surface area. Electrochemical impedance spectroscopy indicated a decreased ionic resistance for larger graphene pores, which led to a more than 2-fold increase in rate handling for lithiation reactions compared to non-activated graphene/niobia hybrids. When increasing the areal mass loading from 1 mg cm⁻² to 11 mg cm⁻², holey graphene/niobia hybrids with high mass loading demonstrated a capacity retention of about 110 mAh g⁻¹ at 20 C, whereas non-activated graphene/niobia exhibited a significant capacity drop at higher rates, with a retention of only about 20 mAh g⁻¹ at 20 C (Figure 6A). The porosity of the holey graphene substrates provided ion transport shortcuts, reducing diffusion limitations even in thick electrodes (Figure 6B,C).^[44] Thus, the study underlines a feasible method to exploit carbon porosity to enable the use of high areal mass loadings that are attractive for practical application.

As a further approach to grow of Faradaic material on carbon substrates, Naoi et al. introduced ultracentrifugation to create hybrid materials. By inducing high mechanical force of 65 000 N through centrifugation at 75 000 G, various metal

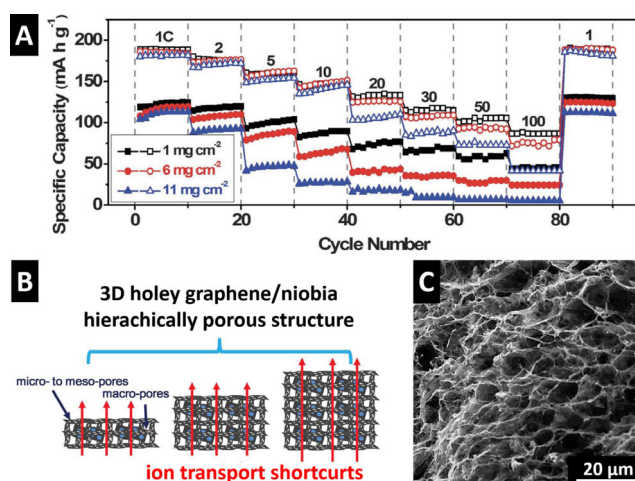


Figure 6. (A) Rate handling of holey graphene/niobia hybrids (open symbols) and graphene/niobia hybrid materials (closed symbols) at different areal loadings. (B) Schematic illustration and (C) scanning electron micrograph of holey graphene/niobia hybrid material offering ion transport shortcuts even at high thicknesses. Adapted from ref. [44]. Reprinted with permission from AAAS.

oxides are grown from in situ sol-gel reactions directly on different carbon substrates.^[45] In a study on carbon fiber/lithium titanate hybrid materials, the carbon fibers became well-distributed in the lithium titanate precursor solution by mechanical agitation, before nucleation occurred by sol-gel reaction on the carbon surface. That way, homogeneously distributed lithium titanate nanoparticles were obtained within the carbon fiber network, leading to high surface area and conductivity of the hybrid material.^[45a,d] This synthesis approach is particularly effective because carbon synergistically interacts during reaction towards an optimized hybrid material. By acting as an anchor for lithium titanate precursors, metal oxide coarsening was prevented during the crystallization reaction because lithium titanate grew following the carbon fiber shape. The influence of the carbon substrate was further underlined by replacing the carbon fibers with especially designed single-walled carbon nanotubes. Thus, the number of anchoring sites is increased, leading to even better dispersion of the lithium titanate. The resulting hybrid electrodes showed remarkable rate handling performance, with a retention of up to 60% of the maximum capacity (130 mAh g⁻¹) at an ultrahigh C-rate of 1200.^[45d]

Carbon/lithium titanate hybrid material was synthesized by a vacuum-impregnation method by Zhao et al.^[46] Using three different kinds of porous carbons with different mesopore volumes, they impregnated the particles dropwise with a liquid precursor solution and applied vacuum in several intervals for homogenous distribution. After calcination at 800 °C, nano-sized lithium titanate particles (< 4 nm) formed inside the pore volume and made up about 52 mass% of the hybrid material. It was found that the carbon particles that offered the largest mesopore volume showed the best electrochemical performance in 1 M LiPF₆ in acetonitrile electrolyte, exhibiting a high capacity retention of 105 mAh g⁻¹ at a rate of 350 C (in addition to the hybrid material, the electrode contained 15

mass 6% conductive additive for comparability with previous studies). The carbon mesopores were necessary to synthesize this sample because they trapped the titanate particles to avoid coarsening during calcination at a high temperature.

In summary, we conclude that the choice of an optimized carbon substrate and a suitable synthesis protocol can significantly enhance all performance metrics of hybrid electrode materials, including specific capacity, rate behavior, and longevity. When designing an idealized carbon substrate, properties should be prioritized in this order:

- (1) Pores must be in an accessible size range for the used synthesis method to avoid pore blocking effects and diffusion limitations at high mass loadings.
- (2) The specific surface area must be maximized to obtain thinner coatings at constant mass loading.
- (3) Internal porosity offers confinement of Faradaic material to enhance the longevity by preventing disintegration and to avoid particle coarsening during heat treatment.
- (4) A higher degree of carbon ordering of the substrate leads to enhanced electrical conductivity of the hybrid electrode.

Strategy 2: Co-Synthesizing Faradaic Materials Engulfed by Carbon

Conversion of one precursor material to carbon/metal oxide hybrid

Creating hybrid electrode materials by deposition of Faradaic material onto a carbon substrate is a highly attractive approach to maximize the specific surface area of the hybrid and obtain nanoscale mixing of the two components. However,

issues may arise from possible pore blocking and several synthesis steps are necessary to obtain the final product. An alternative path towards hybrid electrode fabrication is to inverse the electrode architecture and tailor the carbon phase around the Faradaic component. Recently, we presented a promising concept of a vanadium pentoxide/carbide-derived carbon (V_2O_5/CDC) hybrid material with core-shell architecture.^[47] The goal was to employ an endohedral carbon with a large specific surface area to maximize the capacitive charge storage component of the hybrid electrode. The intriguing aspect of arranging the carbon phase around the Faradaic core is that difficulties arising from pore blocking can be completely avoided. The hybrid material is synthesized using only one precursor (e.g., vanadium carbide) that serves as carbon and vanadium source (Figure 7A). In a first step, vanadium was etched from the outside towards the inside of the vanadium carbide particles by chlorine gas treatment, until only a small vanadium carbide (VC) core remained. By selectively etching vanadium from the lattice, a high surface area ($1500 \text{ m}^2 \text{ g}^{-1}$) microporous carbide-derived carbon shell is obtained (Figure 7B). In a second step, the remaining VC is calcinated under oxidizing atmosphere to form a V_2O_5 core (Figure 7C). The hybrid electrode composition (i.e., the V_2O_5/CDC ratio) can be precisely tuned by adjusting the degree of chlorination. The necessary high control over the chlorination step was achieved by using in situ formation of chlorine gas in which nickel chloride was homogeneously mixed with VC and served as chlorine source. Upon heating, Cl_2 was locally released from decomposing $NiCl_2$, ensuring a homogeneous chlorination of the entire synthesized batch. By variation of the $NiCl_2$ amount, the degree of chlorination and the amount of CDC is determined. This allows to finely tune the capacitive and Faradaic contributions to the overall charge storage of the hybrid electrode. However, the oxidation step

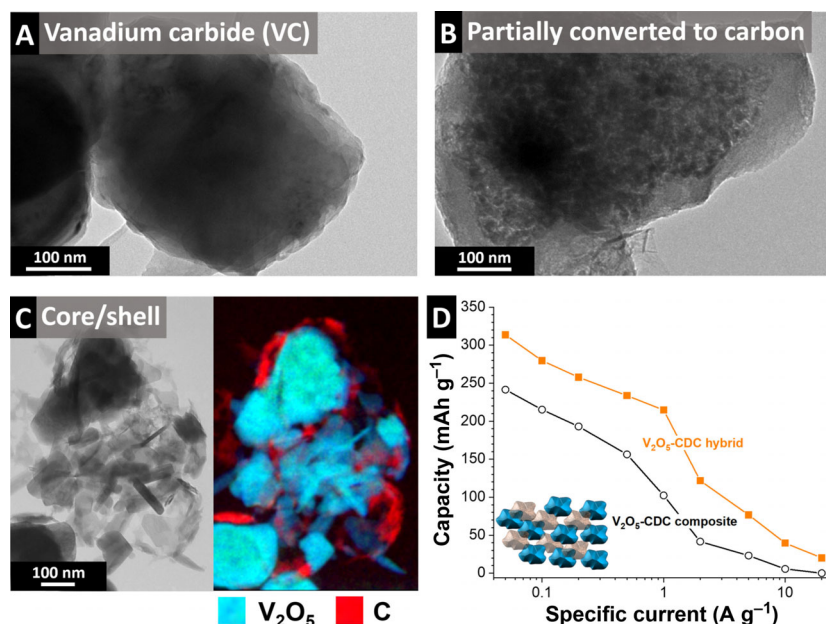


Figure 7. Transmission electron micrographs of (A) precursor vanadium carbide particles, (B) after partial chlorination to form the CDC shell, and (C) final hybrid material after oxidation to form the V_2O_5 core, including chemical mapping from electron energy loss spectroscopy. (D) Electrochemical characterization of V_2O_5 -CDC core-shell hybrid material (orange) and V_2O_5 -CDC composite by galvanostatic cycling in 1 M $LiClO_4$ in ACN electrolyte. Adapted from ref. [47] and reproduced with permission of the Royal Society of Chemistry.

must be precisely adjusted to avoid burning of the carbon phase. The method is therefore limited to Faradaic materials that crystallize at lower temperature and pressure than carbon oxidation.

To analyze the impact of the core-shell architecture on the electrochemical performance of the hybrid material, a composite material was synthesized from mechanically mixing fully chlorinated CDC particles with fully oxidized V_2O_5 particles, both derived from VC, for comparison. Electrochemical characterization in 1 M $LiClO_4$ in acetonitrile electrolyte revealed a higher maximum specific capacity of 310 mAh g^{-1} for the hybrid material, compared to the composite electrode with 240 mAh g^{-1} (Figure 7D). Also, the rate handling of the hybrid was improved, with a retention of 70% of the maximum capacity at 1 Ag^{-1} , compared to a retention of 42% for the composite material at the same rate.

We believe this core-shell architecture provides several key advantages. (1) The surrounding carbon shell can be highly porous because no pore blocking is expected, yielding a high surface area and a large capacitive contribution to the overall charge storage. (2) By encapsulating V_2O_5 with a carbon shell, large contact resistances between the insulating particles are avoided and a highly conductive electrode is obtained. (3) The domain sizes of V_2O_5 are kept very small, reducing the limitations posed by solid-state diffusion. (4) Disintegration of V_2O_5 particles is reduced by the surrounding carbon phase improving longevity of the hybrid material. Yet, the disadvantage compared to carbon substrates coated with Faradaic material lies in the accessibility for ions to the reaction sites. In core-shell materials, the carbon shell enclosing the metal oxide needs to be highly penetrable for the intercalating ions. Though sealing of internal carbon surface area is avoided by the core-shell architecture, sealing effects of metal oxide particles by dense carbon layers must be considered.

Controlled sol-gel approaches

Carbon-coated, porous metal oxide particles have also been synthesized by other approaches. For example, Lim et al. investigated a block-copolymer assisted self-assembly synthesis for mesoporous Nb_2O_5 -C hybrid material.^[48] The carbon phase was obtained by the thermal decomposition of the hydrophobic part in the block-copolymer phase during calcination and it surrounded the Nb_2O_5 phase. In a different approach, the group synthesized Li_3VO_4 -C hybrids by water-in-oil microemulsion, in which the carbon was obtained by carbonization of the emulsifier.^[49] In both studies, the advantage of the hybridization approach over pristine metal oxide particles was clearly demonstrated by comparison of their electrochemical properties. The Nb_2O_5 -C hybrid and the corresponding composite showed a similar maximum capacity of around 180 mAh g^{-1} at a rate of 0.01 Ag^{-1} , however, the hybrid retained about 60% of the maximum capacity at 5 Ag^{-1} , whereas the capacity of the composite faded almost completely.^[48] The presence of the carbonized phase drastically improved the conductivity of the electrode materials and improved the rate handling. The good rate handling enabled a successful use of both hybrid materials

when employed as anodes in lithium-ion capacitor cells, with maximum specific energies of 74 Wh kg^{-1} for the Nb_2O_5 -C hybrid device^[48] and up to 190 Wh kg^{-1} for the Li_3VO_4 -C hybrid device.^[49] However, the as-formed carbon did not exhibit notable porosity and, therefore, may be less penetrable for the electrolyte ions and it does not contribute a capacitive charge storage component to the hybrid electrode. Possibly, a subsequent activation step inducing microporosity to the carbon phase could further elevate the electrochemical performance of these intriguing systems by allowing easier ion access and adding double-layer capacitance.

Compared to these particle-based hybrid materials, fiber-shaped materials offer several advantages. Fibers can form free-standing electrodes without the need for additional binder material. They present continuous conductive networks with improved electrical conductivity without conductive additives, and nanofibers offer short diffusion distances for intercalating ions (Figure 8A). In particle-based systems with conductive additives, the surface chemistry of the metal oxide particles (hydrophilic) and the carbon particles (often hydrophobic)

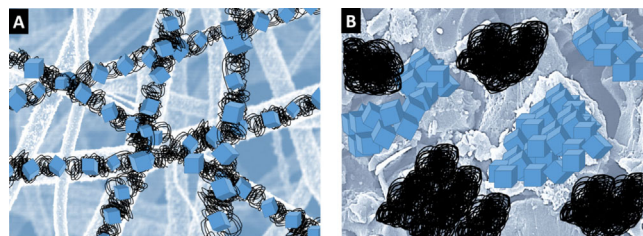


Figure 8. Comparison of fiber-based hybrid electrode material (A) and particle-based composite electrode material (B). Although in the electrospun fibers, metal oxide domains (blue) are engulfed by a continuous conductive carbon network (black), particles can experience disruptions in the conductive network due to agglomerations of metal oxide and carbon domains.

may lead to agglomeration and inhomogeneous material distribution (Figure 8B). Electrospinning has been demonstrated as a suitable synthesis method to obtain free-standing microporous carbon electrodes for supercapacitor applications.^[50] By adjusting the synthesis protocol, our group demonstrated that it is possible to obtain niobium oxide or mixed niobium-titanium oxide/carbon hybrid fiber materials in a one-pot synthesis.^[28,51] During electrospinning, metal alkoxide fibers with thicknesses below 100 nm can be obtained, which are transformed to metal carbide/carbon fibers by annealing in argon atmosphere. By subsequently introducing an oxidizing atmosphere, a transformation to metal oxide/carbon fibers can be achieved. The oxidation process must be precisely controlled to achieve full metal carbide to metal oxide transformation, while preventing burn-off of the carbon phase and maintaining of the fiber-shape. It was demonstrated that the use of CO_2 as oxidizing atmosphere at elevated temperatures above 850°C with reduced partial pressures is a suitable method.^[28,51] In the hybrid material, nanoscopic metal oxide domains are engulfed by a highly porous, conducting carbon network. Niobium pentoxide/carbon hybrid fiber materials showed excellent electrochemical properties, with a maximum capacity of

160 mAhg⁻¹ and a retention of 70% at high rate of 5 Ag⁻¹, allowing for a successful transfer as anodes in lithium-ion capacitor cells with a maximum specific energy of up to 86 Wh kg⁻¹.^[28] Advantages of the electrospinning approach include the few synthesis steps necessary to obtain the final hybrid material that works free of conductive additives and polymer binders. The microporous carbon encapsulating metal oxide domains brings additional double-layer capacitance, electrical conductivity and structural integrity to the continuous fiber network. However, the main disadvantage of fiber systems is the relatively low packing density, which significantly decreases the volumetric capacity of such materials. However, we believe that adjustments to the electrospinning protocol can in part resolve this issue. By use of a rotating disc current collector, alignment of the electrospun fibers can be achieved that exhibits much higher packing densities compared to randomly oriented fibers obtained on a static collector.^[52]

Summary and Outlook

This article introduces hybrid materials consisting of carbon and metal oxides for electrochemical energy storage, with an emphasis on the role of the carbon component towards the structure and performance of the hybrid electrode. Two general types of electrode architectures are discussed: (1) the use of an existing carbon as a substrate for the nanoscopic decoration with redox active metal oxides and (2) co-synthesis of metal oxide and an engulfing carbon component in a simultaneous manner.

When using carbon as a substrate, the porosity plays a critical role as metal oxide is mainly deposited in the carbon interparticle or intraparticle pore volume. Carbons with internal porosity yield higher specific surface area and can prevent disintegration of the metal oxide phase upon volumetric expansions during operation. Microporous carbons can only accommodate small metal oxide loadings because micropores may become sealed by metal oxide coatings, drastically reducing the hybrid electrode performance. By determining the minimum accessible pore size for the chosen coating method, ideal carbon substrates can be tailored that exhibit high internal surface area without pore blocking issues. Further research on tailored mesoporous carbon substrates towards the utilization with sodium or potassium that cause larger volumetric changes during intercalation could address issues with the longevity of these systems. Considering the recent emergence of studies on transition metal dichalcogenide electrodes storing charge by conversion reactions, the use of appropriate mesoporous carbon substrates can greatly benefit their often poor kinetical and stability properties.

Alternative architectures of using metal oxides surrounded by the carbon phase can prevent the issues arising from unwanted pore blocking effects. The striking advantage of this approach is that even microporous carbons with very high specific surface areas can be used in hybrid electrodes, increasing the capacitive component of the electrodes' charge storage behavior and minimizing contact resistances in the hybrid electrodes. Achieving this architecture requires advanced syn-

thesis protocols because the activation of the carbon phase must be carried out with the metal oxide phase present, which can lead to a change in crystal structure. Also, effective access of the electrolyte to the Faradaic metal oxide core must be ensured. With further research addressing these obstacles, this intriguing hybrid electrode architecture holds the potential to further elevate the power handling of electrochemical energy storage devices.

Acknowledgements

The work at INM was part of the Carbon Metal Oxide Nanohybrid project (CarMON) supported by the Leibniz Association (SAW-2017). We thank Eduard Arzt (INM) for his continuing support. The authors also thank Valeria Lemkova, Eunho Lim, and Marco Zeiger (all at INM) for discussions and creative graphical support.

Conflict of interest

The authors declare no conflict of interest.

Keywords: core-shell material · hybrid material · lithium-ion battery · sol-gel synthesis · supercapacitor

- [1] V. S. Arunachalam, E. L. Fleischer, *MRS Bull.* **2008**, *33*, 264–288.
- [2] a) Z. Yang, J. Zhang, M. C. Kintner-Meyer, X. Lu, D. Choi, J. P. Lemmon, J. Liu, *Chem. Rev.* **2011**, *111*, 3577–3613; b) B. Dunn, H. Kamath, J.-M. Tarascon, *Science* **2011**, *334*, 928–935.
- [3] a) P. Simon, Y. Gogotsi, *Nat. Mater.* **2008**, *7*, 845–854; b) F. Béguin, V. Presser, A. Balducci, E. Frackowiak, *Adv. Mater.* **2014**, *26*, 2219–2251.
- [4] D. Qu, H. Shi, *J. Power Sources* **1998**, *74*, 99–107.
- [5] V. Presser, M. Heon, Y. Gogotsi, *Adv. Funct. Mater.* **2011**, *21*, 810–833.
- [6] M. D. Stoller, C. W. Magnuson, Y. Zhu, S. Murali, J. W. Suk, R. Piner, R. S. Ruoff, *Energy Environ. Sci.* **2011**, *4*, 4685–4689.
- [7] a) D. Pech, M. Brunet, H. Durou, P. Huang, V. Mochalin, Y. Gogotsi, P.-L. Taberna, P. Simon, *Nat. Nanotechnol.* **2010**, *5*, 651–654; b) M. Zeiger, N. Jäckel, V. N. Mochalin, V. Presser, *J. Mater. Chem. A* **2016**, *4*, 3172–3196.
- [8] E. Frackowiak, K. Metenier, V. Bertagna, F. Béguin, *Appl. Phys. Lett.* **2000**, *77*, 2421–2423.
- [9] C. Largeot, C. Portet, J. Chmiola, P.-L. Taberna, Y. Gogotsi, P. Simon, *J. Am. Chem. Soc.* **2008**, *130*, 2730–2731.
- [10] N. Jäckel, M. Rodner, A. Schreiber, J. Jeongwook, M. Zeiger, M. Aslan, D. Weingarh, V. Presser, *J. Power Sources* **2016**, *326*, 660–671.
- [11] N. Ortiz-Vitoriano, N. E. Drewett, E. Gonzalo, T. Rojo, *Energy Environ. Sci.* **2017**, *10*, 1051–1074.
- [12] M. D. Slater, D. Kim, E. Lee, C. S. Johnson, *Adv. Funct. Mater.* **2013**, *23*, 947–958.
- [13] S. Komaba, T. Hasegawa, M. Dahbi, K. Kubota, *Electrochem. Commun.* **2015**, *60*, 172–175.
- [14] M. S. Whittingham, *Chem. Rev.* **2004**, *104*, 4271–4302.
- [15] E. Peled, C. Menachem, D. Bar-Tow, A. Melman, *J. Electrochem. Soc.* **1996**, *143*, L4–L7.
- [16] a) S. Boukhalfa, K. Evanoff, G. Yushin, *Energy Environ. Sci.* **2012**, *5*, 6872–6879; b) M. Zeiger, S. Fleischmann, B. Krüner, A. Tolosa, S. Bechtel, M. Baltes, A. Schreiber, R. Moroni, S. Vierrath, S. Thiele, V. Presser, *RSC Adv.* **2016**, *6*, 107163–107179.
- [17] N. Shpigel, M. D. Levi, S. Sigalov, O. Girshevitz, D. Aurbach, L. Daikhin, P. Pikma, M. Marandi, A. Jänes, E. Lust, N. Jäckel, V. Presser, *Nat. Mater.* **2016**, *15*, 570–575.
- [18] D. Dubal, O. Ayyad, V. Ruiz, P. Gómez-Romero, *Chem. Soc. Rev.* **2015**, *44*, 1777–1790.
- [19] E. Lim, C. Jo, J. Lee, *Nanoscale* **2016**, *8*, 7827–7833.

- [20] S. M. George, *Chem. Rev.* **2010**, *110*, 111–131.
- [21] X. Wang, G. Yushin, *Energy Environ. Sci.* **2015**, *8*, 1889–1904.
- [22] G. G. Amatucci, F. Badway, A. Du Pasquier, T. Zheng, *J. Electrochem. Soc.* **2001**, *148*, A930–A939.
- [23] M. R. Lukatskaya, B. Dunn, Y. Gogotsi, *Nat. Commun.* **2016**, *7*, 12647.
- [24] a) V. Augustyn, J. Come, M. A. Lowe, J. W. Kim, P.-L. Taberna, S. H. Tolbert, H. D. Abruña, P. Simon, B. Dunn, *Nat. Mater.* **2013**, *12*, 518–522; b) V. Augustyn, P. Simon, B. Dunn, *Energy Environ. Sci.* **2014**, *7*, 1597–1614.
- [25] J. J. Vilatela, D. Eder, *ChemSusChem* **2012**, *5*, 456–478.
- [26] a) G. Kickelbick, *Hybrid materials: synthesis, characterization, and applications*, Wiley, Hoboken, **2007**; b) S. Fleischmann, M. Zeiger, N. Jäckel, B. Krüner, V. Lemkova, M. Widmaier, V. Presser, *J. Mater. Chem. A* **2017**, *5*, 13039–13051.
- [27] Y. He, W. Chen, X. Li, Z. Zhang, J. Fu, C. Zhao, E. Xie, *ACS Nano* **2013**, *7*, 174–182.
- [28] A. Tolosa, B. Krüner, S. Fleischmann, N. Jäckel, M. Zeiger, M. Aslan, I. Grobelsek, V. Presser, *J. Mater. Chem. A* **2016**, *4*, 16003–16016.
- [29] Z. Le, F. Liu, P. Nie, X. Li, X. Liu, Z. Bian, G. Chen, H. B. Wu, Y. Lu, *ACS Nano* **2017**, *11*, 2952–2960.
- [30] H.-S. Kim, J. B. Cook, S. H. Tolbert, B. Dunn, *J. Electrochem. Soc.* **2015**, *162*, A5083–A5090.
- [31] a) S. Choudhury, P. Srimuk, K. Raju, A. Tolosa, S. Fleischmann, M. Zeiger, K. I. Ozoemena, L. Borchardt, V. Presser, *Sustainable Energy Fuels* **2018**, *2*, 133–146; b) S. Choudhury, M. Zeiger, P. Massuti-Ballester, S. Fleischmann, P. Formanek, L. Borchardt, V. Presser, *Sustainable Energy Fuels* **2017**, *1*, 84–94.
- [32] a) J. B. Cook, H. S. Kim, T. C. Lin, C. H. Lai, B. Dunn, S. H. Tolbert, *Adv. Energy Mater.* **2017**, *7*, 1601283; b) Z. Zhang, H. Zhao, Y. Teng, X. Chang, Q. Xia, Z. Li, J. Fang, Z. Du, K. Świerczek, *Adv. Energy Mater.* **2018**, *8*, 1700174.
- [33] S. Fleischmann, A. Tolosa, M. Zeiger, B. Krüner, N. J. Peter, I. Grobelsek, A. Quade, A. Kruth, V. Presser, *J. Mater. Chem. A* **2017**, *5*, 2792–2801.
- [34] H.-S. Kim, J. B. Cook, H. Lin, J. S. Ko, S. H. Tolbert, V. Ozolins, B. Dunn, *Nat. Mater.* **2017**, *16*, 454–460.
- [35] J. Huang, B. G. Sumpter, V. Meunier, *Chem. Eur. J.* **2008**, *14*, 6614–6626.
- [36] S. Fleischmann, N. Jäckel, M. Zeiger, B. Krüner, I. Grobelsek, P. Formanek, S. Choudhury, D. Weingarh, V. Presser, *Chem. Mater.* **2016**, *28*, 2802–2813.
- [37] J. S. Daubert, N. P. Lewis, H. N. Gotsch, J. Z. Mundy, D. N. Monroe, E. C. Dickey, M. D. Losego, G. N. Parsons, *Chem. Mater.* **2015**, *27*, 6524–6534.
- [38] J. S. Daubert, R. Wang, J. S. Ovental, H. F. Barton, R. Rajagopalan, V. Augustyn, G. N. Parsons, *J. Mater. Chem. A* **2017**, *5*, 13086–13097.
- [39] S. Fleischmann, D. Leistenschneider, V. Lemkova, B. Krüner, M. Zeiger, L. Borchardt, V. Presser, *Chem. Mater.* **2017**, *29*, 8653–8662.
- [40] K. Makgopa, P. M. Ejikeme, C. J. Jafta, K. Raju, M. Zeiger, V. Presser, K. I. Ozoemena, *J. Mater. Chem. A* **2015**, *3*, 3480–3490.
- [41] C. J. Zhang, R. Maloney, M. R. Lukatskaya, M. Beidaghi, B. Dyatkin, E. Perre, D. Long, W. Qiao, B. Dunn, Y. Gogotsi, *J. Power Sources* **2015**, *274*, 121–129.
- [42] C.-H. Lai, D. Ashby, M. K. Moz, Y. Gogotsi, L. Pilon, B. S. Dunn, *Langmuir* **2017**, *33*, 9407–9415.
- [43] Y. Gogotsi, P. Simon, *Science* **2011**, *334*, 917–918.
- [44] H. Sun, L. Mei, J. Liang, Z. Zhao, C. Lee, H. Fei, M. Ding, J. Lau, M. Li, C. Wang, X. Xu, G. Hao, B. Papandrea, I. Shakir, B. Dunn, Y. Huang, X. Duan, *Science* **2017**, *356*, 599–604.
- [45] a) K. Naoi, S. Ishimoto, Y. Isobe, S. Aoyagi, *J. Power Sources* **2010**, *195*, 6250–6254; b) K. Naoi, K. Kisu, E. Iwama, S. Nakashima, Y. Sakai, Y. Oriksa, P. Leone, N. Dupré, T. Brousse, P. Rozier, W. Naoi, P. Simon, *Energy Environ. Sci.* **2016**, *9*, 2143–2151; c) K. Naoi, T. Kurita, M. Abe, T. Furuhashi, Y. Abe, K. Okazaki, J. Miyamoto, E. Iwama, S. Aoyagi, W. Naoi, P. Simon, *Adv. Mater.* **2016**, *28*, 6751–6757; d) K. Naoi, W. Naoi, S. Aoyagi, J.-i. Miyamoto, T. Kamino, *Acc. Chem. Res.* **2013**, *46*, 1075–1083.
- [46] E. Zhao, C. Qin, H.-R. Jung, G. Berdichevsky, A. Nese, S. Marder, G. Yushin, *ACS Nano* **2016**, *10*, 3977–3984.
- [47] M. Zeiger, T. Ariyanto, B. Krüner, N. J. Peter, S. Fleischmann, B. J. M. Etzold, V. Presser, *J. Mater. Chem. A* **2016**, *4*, 18899–18909.
- [48] E. Lim, H. Kim, C. Jo, J. Chun, K. Ku, S. Kim, H. I. Lee, I.-S. Nam, S. Yoon, K. Kang, *ACS Nano* **2014**, *8*, 8968–8978.
- [49] E. Lim, W.-g. Lim, C. Jo, J. Chun, M.-H. Kim, K. C. Roh, J. Lee, *J. Mater. Chem. A* **2017**, *5*, 20969–20977.
- [50] a) V. Presser, L. Zhang, J. J. Niu, J. McDonough, C. Perez, H. Fong, Y. Gogotsi, *Adv. Energy Mater.* **2011**, *1*, 423–430; b) A. Tolosa, B. Krüner, N. Jäckel, M. Aslan, C. Vakifahmetoglu, V. Presser, *J. Power Sources* **2016**, *313*, 178–188.
- [51] A. Tolosa, S. Fleischmann, I. Grobelsek, A. Quade, E. Lim, V. Presser, *ChemSusChem* **2018**, *11*, 159–170.
- [52] L. E. Sperling, K. P. Reis, L. G. Pozzobon, C. S. Girardi, P. Pranke, *J. Biomed. Mater. Res. Part A* **2017**, *105*, 1333–1345.

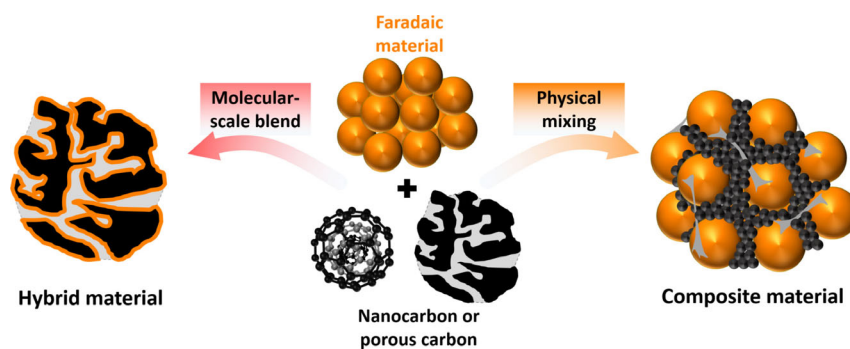
Manuscript received: February 14, 2018

Accepted manuscript online: April 19, 2018

Version of record online: ■ ■ ■ 0000

CONCEPT

Renewable Energy

*S. Fleischmann, A. Tolosa, V. Presser**Yc Design of Carbon/Metal Oxide Hybrids
for Electrochemical Energy Storage

Carbon for storing energy: Electrochemical energy storage materials that combine a high specific energy, power, and cycling stability can be obtained by hybridizing carbon with metal oxides. The combination of the components on a nanoscopic scale requires careful

design. Here, we discuss different synthesis strategies to achieve synergistic effects for an increased electrochemical performance. The focus of this Concept article is on the role of the carbon component of the hybrid material.

Hybridization of carbon with metal oxides is an intriguing approach in the field of electrochemical energy storage to create electrode materials that provide a high specific energy and power. The carbon phase offers a high specific surface area and electrical conductivity, whereas the metal oxide introduces Faradaic charge transfer to the system. To achieve synergistic effects between the components that are chemically linked on a molecular scale, their interface must be carefully designed. In this Concept, several hybridization strategies are discussed as well as the impact of the carbon phase on the resulting hybrid material properties.

4.5 Vanadia–titania multilayer nanodecoration of carbon onions via atomic layer deposition for high performance electrochemical energy storage

Simon Fleischmann,¹ Aura Tolosa,^{1,2} Marco Zeiger,^{1,2} Benjamin Krüner,^{1,2}
Nicolas J. Peter,³ Ingrid Grobelsek,² Antje Quade,⁴ Angela Kruth,⁴ and Volker Presser^{1,2}

¹ Department of Materials Science and Engineering, Saarland University, 66123 Saarbrücken, Germany

² INM – Leibniz Institute for New Materials, 66123 Saarbrücken, Germany

³ Max-Planck-Institut für Eisenforschung GmbH, 40237 Düsseldorf, Germany

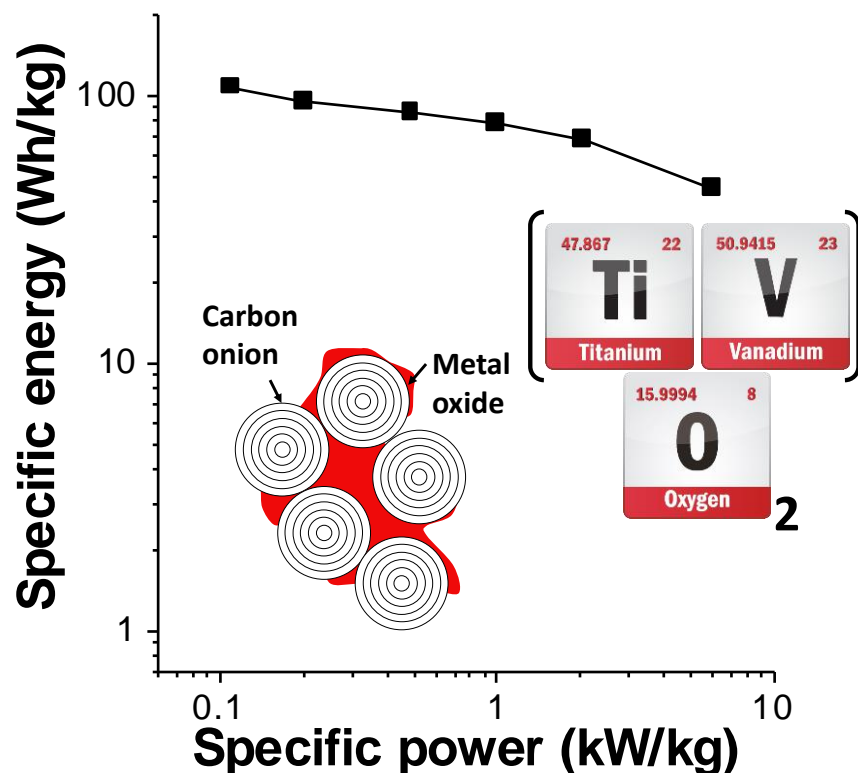
⁴ Leibniz Institute for Plasma Science and Technology, 17489 Greifswald, Germany

Citation:

S. Fleischmann, A. Tolosa, M. Zeiger, B. Krüner, N. J. Peter, I. Grobelsek, A. Quade, A. Kruth and V. Presser, *Vanadia–titania multilayer nanodecoration of carbon onions via atomic layer deposition for high performance electrochemical energy storage*, *J. Mater. Chem. A*, **2017**, *5*, 2792-2801. (DOI: 10.1039/c6ta09890h)

Own contribution:

Planning, ALD synthesis, X-ray diffraction measurements, calculation of lattice parameters, Raman measurements, thermogravimetric analysis, electrochemical measurements, writing.



CrossMark
click for updatesCite this: *J. Mater. Chem. A*, 2017, 5, 2792

Vanadia–titania multilayer nanodecoration of carbon onions *via* atomic layer deposition for high performance electrochemical energy storage†

Simon Fleischmann,^a Aura Tolosa,^{ab} Marco Zeiger,^{ab} Benjamin Krüner,^{ab} Nicolas J. Peter,^c Ingrid Grobelsek,^b Antje Quade,^d Angela Kruth^d and Volker Presser^{*ab}

Atomic layer deposition has proven to be a particularly attractive approach for decorating mesoporous carbon substrates with redox active metal oxides for electrochemical energy storage. This study, for the first time, capitalizes on the cyclic character of atomic layer deposition to obtain highly conformal and atomically controlled decoration of carbon onions with alternating stacks of vanadia and titania. The addition of 25 mass% TiO₂ leads to expansion of the VO₂ unit cell, thus greatly enhancing lithium intercalation capacity and kinetics. Electrochemical characterization revealed an ultrahigh discharge capacity of up to 382 mA h g⁻¹ of the composite electrode (554 mA h g⁻¹ per metal oxide) with an impressive capacity retention of 82 mA h g⁻¹ (120 mA h g⁻¹ per metal oxide) at a high discharge rate of 20 A g⁻¹ or 52C. Stability benchmarking showed stability over 3000 cycles when discharging to a reduced potential of -1.8 V vs. carbon. These capacity values are among the highest reported for any metal oxide system, while in addition, supercapacitor-like power performance and longevity are achieved. At a device level, high specific energy and power of up to 110 W h kg⁻¹ and 6 kW kg⁻¹, respectively, were achieved when employing the hybrid material as anode *versus* activated carbon cathode.

Received 15th November 2016
Accepted 21st December 2016

DOI: 10.1039/c6ta09890h

www.rsc.org/MaterialsA

1. Introduction

Electrochemical energy storage devices are typically divided into two categories: (1) supercapacitors, including electrical double-layer capacitors (EDLCs), which store energy by fast and reversible electrosorption of ions at the charged interface of high surface area electrodes and the electrolyte^{1,2} and (2) batteries that utilize redox reactions in the bulk of the electrodes for energy storage. The non-faradaic charge storage mechanism of EDLCs is characterized by a rapid response and high achievable power ratings, yet they suffer from a relatively low energy density, compared to state-of-the-art lithium ion batteries.³ Typical electrode materials for EDLCs are carbons with a high specific surface area (SSA), such as activated carbon,^{4,5} carbide-derived carbon,^{6,7} carbon onions (onion-like carbon, OLC),^{8,9} carbon nanotubes (CNTs),^{10,11} or carbon nanofibers.^{12,13} The double-layer capacitance of these materials is limited to about 0.1 F m⁻²,^{14,15} which is why the implementation

of faradaic charge transfer into the supercapacitor system is explored as a way to further increase their energy capacity.¹⁶ For the latter, a common strategy is the creation of hybrid electrodes by nanoscopically decorating carbon with redox-active materials, such as metal oxides,¹⁷ or surface functional groups.^{18,19} Various processing methods have been employed to coat carbon surfaces with metal oxides, such as chemical vapor deposition,²⁰ atomic layer deposition (ALD),^{21,22} or wet-chemical approaches.²³ Especially ALD has been found to be a very promising technique to fabricate nanoscopic films on various carbon surfaces because of the highly controllable film thickness at a sub-nanometer level, the conformity of the layers, and the possibility of coating small nanopores that exhibit sizes above 1–2 nm.^{22,24} By utilizing nanoscopic layers of redox-active materials, faradaic reactions are localized near the electrode surface, avoiding long diffusion paths of ions to reach reactive sites, which results in a high power handling.^{25,26}

In a hybrid electrode, the carbon substrate is required to provide a sufficiently high SSA, good electrical conductivity, and accessible pore volume.²² In a previous study, we have investigated the influence of the carbon porosity on the resulting electrochemical performance of carbon/vanadia hybrid electrodes, concluding that carbon materials which exhibit exclusively external surface area, such as OLCs, yield beneficial properties compared to nanoporous carbons.²² OLCs are spherical carbon nanoparticles that consist of several concentric shells of sp²

^aDepartment of Materials Science and Engineering, Saarland University, 66123 Saarbrücken, Germany. E-mail: volker.presser@leibniz-inm.de

^bINM – Leibniz Institute for New Materials, 66123 Saarbrücken, Germany

^cMax-Planck-Institut für Eisenforschung GmbH, 40237 Düsseldorf, Germany

^dLeibniz Institute for Plasma Science and Technology, 17489 Greifswald, Germany

† Electronic supplementary information (ESI) available. See DOI: 10.1039/c6ta09890h



carbon and that are typically smaller than 10 nm, depending on the synthesis method and precursor. They possess a SSA of up to $600 \text{ m}^2 \text{ g}^{-1}$,⁸ a high electrical conductivity of up to 4 S cm^{-1} ,²⁷ and form mainly interparticle and intercluster pores.²⁸ Our study clearly demonstrated that the interparticle pore space of OLCs provides favorable conditions for a conformal and nanocrystalline vanadia film growth *via* ALD.²²

Depending on the observed charge–voltage-profile, redox systems are categorized either as pseudocapacitors (“capacitor-like”, exhibition of constant charge-*vs.*-voltage profiles, *e.g.*, MnO_2 ,^{29–31} RuO_2 ,³² MXene³³), or as battery-like devices (showing well-defined redox peaks; *e.g.*, V_2O_5 ,^{34,35} polyaniline³⁶).³⁷ In particular, vanadia has gained considerable attention as both a cathode material in lithium batteries³⁸ and a redox-active component in hybrid electrodes.²¹ It features the ability to intercalate Li^+ ions, which manifests in a battery-like response for crystalline V_2O_5 and VO_2 ,³⁹ and exhibits pseudocapacitive behavior in amorphous and nanocrystalline states.²⁵ When discharging to 3.2 V *vs.* Li, crystalline V_2O_5 can reversibly facilitate 0.5 Li for each V by forming $\delta\text{-LiV}_2\text{O}_5$, which yields a theoretical capacity of 147 mA h g^{-1} .³⁹ Higher degrees of lithiation are achieved by discharging up to 2.3 V *vs.* Li, yielding an irreversible phase transformation to $\gamma\text{-Li}_x\text{V}_2\text{O}_5$ with theoretical capacities as high as 300 mA h g^{-1} .³⁹ Monoclinic $\text{VO}_2(\text{M})$ (rutile type) exhibits a performance of around 120 mA h g^{-1} ,⁴⁰ while higher capacities have been reported for metastable $\text{VO}_2(\text{B})$ phases due to the presence of V_4O_{10} -type double layers, which share corners to form tunnel-like structures, enabling rapid Li transport.^{39,41} Cycling of $\text{VO}_2(\text{B})$ between 4 V and 1 V *vs.* Li leads to the formation of LiVO_2 , corresponding to a theoretical capacity of 320 mA h g^{-1} .⁴² For nanostructured $\text{VO}_2(\text{B})$ aerogels, initial discharge capacities as high as 500 mA h g^{-1} have been reported, yet a stable performance of 175 mA h g^{-1} over 20 cycles was only achieved when operating within a smaller voltage window between 4 V and 2.4 V *vs.* Li.⁴³

Instead of using a single metal oxide, the addition of a second phase may further enhance the electrochemical properties of redox systems. In a study by Takahashi *et al.*, the addition of anatase TiO_2 to the V_2O_5 structure led to a significant rise in capacity from 120 mA h g^{-1} to 180 mA h g^{-1} , compared to pure V_2O_5 nanorods.⁴⁴ The authors ascribed the effect to possible modifications in the V_2O_5 lattice structure, yielding a more open space for Li intercalation, yet analytical evidence was not provided by the authors.⁴⁴ Jampani *et al.* reported a similar capacity increase resulting from Ti-doping of the vanadia structure, which was correlated with an increase in electrical conductivity, caused by incorporation of titanium at vanadium lattice sites.²⁰ Park *et al.* investigated the effect of lattice strain on the electrochemical performance of rutile-type $\text{VO}_2\text{:Sb:SnO}_2$ which was chosen as a substrate for VO_2 deposition because of its appropriate lattice mismatch towards rutile VO_2 . As a result, an in-plane expansion of the rutile type structure was achieved at the interface of the two materials, yielding an enhanced capacity of 350 mA h g^{-1} per mass of VO_2 .⁴⁵

In this study, we introduce a novel approach for creating hybrid electrodes combining both high specific energy and high power. Owing to the cyclic process characteristics of ALD that allow for ultra-precise deposition of sub-nanometer layers,

highly conformal and atomically controlled decoration of carbon onions with alternating stacks of vanadia and titania was obtained. Due to excellent control over multilayer growth and composition, first conclusive analytical evidence of the origin of improved energy storage performance for the mixed vanadia/titania system was obtained. The addition of about 25 mass% TiO_2 leads to an expansion of the VO_2 unit cell, greatly enhancing lithium intercalation capacity and kinetics, as we demonstrate in both half-cell and asymmetrical full-cell setups.

2. Materials and methods

2.1 Materials

To obtain OLCs, a detonation nanodiamond precursor (diameter 4–6 nm, NaBond Technologies) was thermally annealed in a water-cooled high temperature furnace (Thermal Technology Inc.). The synthesis was carried out in an argon atmosphere at $1700 \text{ }^\circ\text{C}$ for 1 h, with a heating/cooling rate of 20 K min^{-1} . From the resulting OLC powder, $50 \text{ }\mu\text{m}$ thick electrodes were prepared by admixing 10 mass% of polytetrafluoroethylene (aqueous solution of 60 mass% of PTFE, Sigma Aldrich), a detailed description is given elsewhere.⁴⁶

Carbon onion electrodes were coated with an open-load atomic layer deposition system (Oxford Instruments) that was placed inside an argon filled glovebox (M. Braun Intertgas-Systeme) in order to ensure dry loading of the samples. Vanadium(v)-oxytriisopropoxide (VOTIP, SAFC Hitech) and tetrakis(dimethylamido)titanium(IV) (TDMAT, SAFC Hitech) were employed as metalorganic precursors for the deposition of vanadium oxide and titanium oxide, respectively, and deionized water vapor (Milli-Q, Merck) was chosen as reactant gas. The precursors were delivered by an argon carrier gas, with dosage over a period of 20 s during each reaction cycle, followed by purging of the reactor with pure argon over a period of 10 s after each precursor dosage step. After each ALD cycle, the reactor was evacuated for 8 s. During the ALD process, the reactor temperature was kept at $180 \text{ }^\circ\text{C}$. In general, for each coating, 100 ALD cycles were applied. For synthesis of multilayer coatings, alternating sequences of vanadia and titania were deposited as indicated by the sample nomenclature; for example, OLC/ VTiO ^{6:2} was fabricated by repetitively alternating sequences of 6 and 2 ALD cycles of vanadia and titania, respectively, until 100 cycles were reached.

Thermal annealing of the coated samples was carried out in a quartz tube furnace under an argon atmosphere at a flow rate of 100 sccm. During the annealing procedure, all samples were heated at $5 \text{ }^\circ\text{C min}^{-1}$ to $500 \text{ }^\circ\text{C}$, held for 0.5 h at that temperature, and cooled down to room temperature at $40 \text{ }^\circ\text{C min}^{-1}$. Thereby, the PTFE fully decomposes to volatile species, leaving a connected, binder-free network of OLC/metal oxide hybrid electrodes.

2.2 Materials characterization

Transmission electron microscopy (TEM) was carried out using a JEOL 2100F system operating at 200 kV. Sample preparation was performed by dispersion and sonication of the powder samples in isopropanol and deposition on a copper grid with a lacey carbon film (Gatan Inc.).



X-ray diffraction (XRD) experiments were conducted employing a D8 Advance diffractometer (Bruker AXS) with a copper X-ray source ($\text{Cu}_{K\alpha}$, 40 kV, 40 mA), a nickel filter and a LYNXEYE detector. All samples were placed on a sapphire single crystal and measured in a range from 10 to 80° 2θ with a step width of 0.01° 2θ and a step duration of 10 s. Calculation of the lattice parameters was carried out using the EVA Diffrac Suite software.

Raman spectroscopy was performed with a Renishaw inVia Raman Microscope using an Nd:YAG laser with an excitation wavelength of 532 nm and a power of about 0.25 mW. A 50× objective and a grating with 2400 lines per mm were used to reach a spectral resolution of about 1.2 cm^{-1} . The acquisition time for each spectrum was 30 s with 10 accumulations.

The vanadium and titanium binding energies in different coating compositions were determined by X-ray photo-electron spectroscopy (XPS). The measurements were carried out on an AXIS Ultra DLD electron spectrometer (Kratos Analytical). For the excitation of the photoelectron spectra, monochromatic Al $K\alpha$ was used. The spectra were acquired by setting the instrument to medium magnification (field of view 2) lens mode and by selecting the slot mode. Charge neutralization was implemented by low energy electrons injected into the magnetic field of the lens from a filament located directly above the sample. Three sets of measurements were performed. Survey scans and individual photo-electron lines were acquired using the X-ray source operating at 150 W power and 80 eV analyzer pass energy. Additionally, high resolution measurements of the C 1s, Ti 2p, and V 2p lines with the pass energy of 10 eV at the power of 225 W were performed. Three spots at different positions on each sample were analyzed and averaged. Data acquisition and processing were carried out using CasaXPS (Casa Software Ltd.). After subtraction of Shirley background, the peaks were fitted using the Gaussian Lorentzian GL(30) peak shape. The binding energy (BE) scale was corrected for charging using an electron BE of 285.0 eV for the C- C_{aliph} component in the C 1s spectra.

Thermogravimetric analysis (TGA) was carried out using a TG 209 F1 Libra system (Netzsch). The samples were heated from room temperature to 650 °C (TiO_2 to 750 °C) at a heating rate of 5 °C min^{-1} under a synthetic air atmosphere (80% N_2 , 20% O_2). The change in mass during heating was used to determine the metal oxide content of the sample. For samples containing vanadia, the $\text{V}^{4+}/\text{V}^{5+}$ oxidation process and the associated increase in mass occurring during the transition from VO_2 to V_2O_5 were considered.

2.3 Electrochemical benchmarking

The electrochemical performance was evaluated in a three-electrode setup (half-cell), which has been described in detail elsewhere,⁴⁷ and in a two-electrode setup (full-cell). In half-cells, ALD-coated carbon onion electrodes with masses varying between 1.0 and 1.5 mg were employed as a working electrode, whereas an about five times oversized PTFE-bound activated carbon (type YP80-F, Kuraray) was used as a counter electrode. The potential was measured against an activated carbon reference electrode (type YP50-F, Kuraray). In full-cell

measurements, OLC/ $\text{VTiO}^{6:2}$ electrodes with masses between 1.0 and 1.5 mg were used as the anode and PTFE-bound activated carbon (type YP80-F, 5 mass% PTFE) as the cathode with a mass ratio of 1 : 3.5 to achieve charge-balance. In addition, the potential evolution at the cathode and anode was monitored with a separate, PTFE-bound activated carbon reference electrode (type YP50-F). Carbon-coated, 12 mm diameter aluminum foils (Zflo 2653, Exopack Technologies) and glass fiber mats (GF/D, Whatman) were employed as current collectors and separators, respectively. Prior to electrolyte filling in an argon filled glovebox (MBraun Labmaster 130, O_2 and H_2O < 1 ppm), the cells were dried in a vacuum oven at 120 °C overnight. 1 M LiClO_4 (battery grade, Sigma Aldrich) in a 50 : 50 mixture of ethylene carbonate and dimethyl carbonate (EC/DMC; battery grade, BASF) was used as the electrolyte.

Electrochemical testing procedures were carried out using a potentiostat/galvanostat (VSP300, Bio-Logic). For half-cells, cyclic voltammetry (CV) was performed in a potential window from +1.0 V to -2.0 V vs. carbon, at a scanning rate of 1 mV s^{-1} . Galvanostatic charge/discharge with potential limitation (GCPL) was carried out by cycling between +1.0 V and -2.0 V vs. carbon with specific currents ranging from 0.05 to 20 A g^{-1} , normalized to the total composite electrode mass. The specific capacity C_{sp} was calculated by integration of the discharge current I over the discharge time t accounting for the lithiation step from +1.0 V to -2.0 V vs. carbon, normalized to the full composite electrode mass, m :

$$C_{\text{sp}} = \frac{\int_{t_0}^t I dt}{m} \quad (1)$$

For investigation of the cycling stability, galvanostatic discharge was carried out at 1 A g^{-1} in the potential window from +1.0 V to -2.0 V and -1.8 V vs. carbon. In full-cells, CV experiments ranged from 0 V up to 3.5 V cell voltage at a scanning rate of 1 mV s^{-1} . GCPL procedures were performed by cycling to 3.2 V cell voltage at different rates between 0.05 A g^{-1} and 2.5 A g^{-1} , normalized to the total mass of both electrodes. The specific energy E_{sp} was calculated by integration of the voltage profile:

$$E_{\text{sp}} = \frac{I \int_{t_0}^t U(t) dt}{m} \quad (2)$$

where I is the applied current, $U(t)$ is the time-dependent cell voltage and m is the total mass of the anode and cathode. The specific power P_{sp} was calculated by dividing E_{sp} by the charge/discharge time. The energy efficiency was derived from the ratio of specific discharge and charge energy.

3. Results and discussion

3.1 Structure and composition

The morphology of the annealed hybrid materials was studied by TEM. The synthesized OLCs are spherical, non-porous nanoparticles with diameters of 5–7 nm, present as



agglomerates in the size-range of several 100 nm. Their pore volume consists of interparticle voids in the agglomerate network,²⁸ which is where the metal oxide coating is mostly located, as shown in Fig. 1A–E, and schematically illustrated in Fig. 1F. After deposition of 100 ALD cycles onto the OLCs, most of the pore volume throughout the agglomerates is homogeneously occupied by the metal oxide, with little remaining pore space still visible in TEM images. These observations are confirmed by gas sorption analysis, showing a decline in the specific surface area from $352 \text{ m}^2 \text{ g}^{-1}$ to $50 \text{ m}^2 \text{ g}^{-1}$ (SSA_{BET}) and in the total pore volume from $0.93 \text{ cm}^3 \text{ g}^{-1}$ to $0.12 \text{ cm}^3 \text{ g}^{-1}$ for the OLC/ VO_2 hybrids (ESI, Fig. S1†). The deposited single and bimetal oxides are mostly present in nanocrystalline form, with visible crystal sizes ranging between 5 and 20 nm.

The chemical composition of the hybrid material, especially regarding the metal oxide content, was analyzed by means of thermogravimetric analysis (TGA) and energy dispersive X-ray spectroscopy (EDX); the quantitative results are given in Table 1 and Fig. 2. Application of 100 ALD cycles resulted in a metal oxide content between 66 and 72 mass%, as measured by TGA, being in line with semi-quantitative EDX analysis, where 61–66% were observed.

To characterize the crystalline structure of the deposited metal oxides in the hybrid materials, X-ray diffraction (XRD) was carried out (Fig. 3A). In the sample OLC/ VO_2 , vanadia is present in the monoclinic $\text{VO}_2(\text{M})$ structure in space group $C2/m$ (JCPDS 65-7960), most concisely represented by the (001) and (200) reflections occurring at $14.4^\circ 2\theta$ and $15.3^\circ 2\theta$, respectively. In OLC/ TiO_2 , tetragonal anatase TiO_2 (JCPDS 78-2486) is formed, as clearly indicated by the presence of the (101) reflection

at $25.2^\circ 2\theta$. The three multilayer systems, OLC/ $\text{VTiO}^{6:2}$, OLC/ $\text{VTiO}^{4:2}$, and OLC/ $\text{VTiO}^{2:2}$, all exhibit diffraction patterns that strongly resemble the monoclinic $C2/m$ crystal lattice, similar to that of $\text{VO}_2(\text{M})$ vanadia, while no additional peaks are found that might indicate the presence of an anatase-type crystalline phase, as observed for OLC/ TiO_2 . This leads to the conclusion that in multilayer samples, the titania species is present in another configuration. The diffraction peaks detected for multilayer samples are found to be shifted towards lower diffraction angles, 2θ , with respect to peaks arising from the pure $\text{VO}_2(\text{M})$ phase, as exemplified for the (110) reflection in Fig. 3B. Hence, the crystal structures of the newly formed multilayer phases are isomorphs of the monoclinic vanadia system. This could be explained by (1) the formation of a solid solution of vanadia and titania, $\text{V}_{1-x}\text{Ti}_x\text{O}_2$, or (2) by the occurrence of crystal lattice strain in $\text{VO}_2(\text{M})$, induced by epitaxially grown $\text{TiO}_2(\text{B})$ -interlayers that also are isomorph to $\text{VO}_2(\text{M})$ (JCPDS 74-1940, orange line in Fig. 3B).⁴⁸ The observation of one sharp peak suggests the formation of a homogenous solid solution, since for two separate, epitaxially grown phases, two peaks in close proximity or a broad diffraction signal would be expected. The calculated lattice parameters of the multilayer phases are shown in Table 2. The atomically controlled insertion of two titania layers between arrays of six, four, or two vanadia layers *via* ALD led to an enlargement of the $\text{VO}_2(\text{M})$ unit cell in all three crystallographic directions, leading to an expansion of the cell volume from 273 \AA^3 to 279 \AA^3 , 280 \AA^3 , and 281 \AA^3 for the samples OLC/ $\text{VTiO}^{6:2}$, OLC/ $\text{VTiO}^{4:2}$, and OLC/ $\text{VTiO}^{2:2}$, respectively. The expansion can be explained by the larger ionic radius of

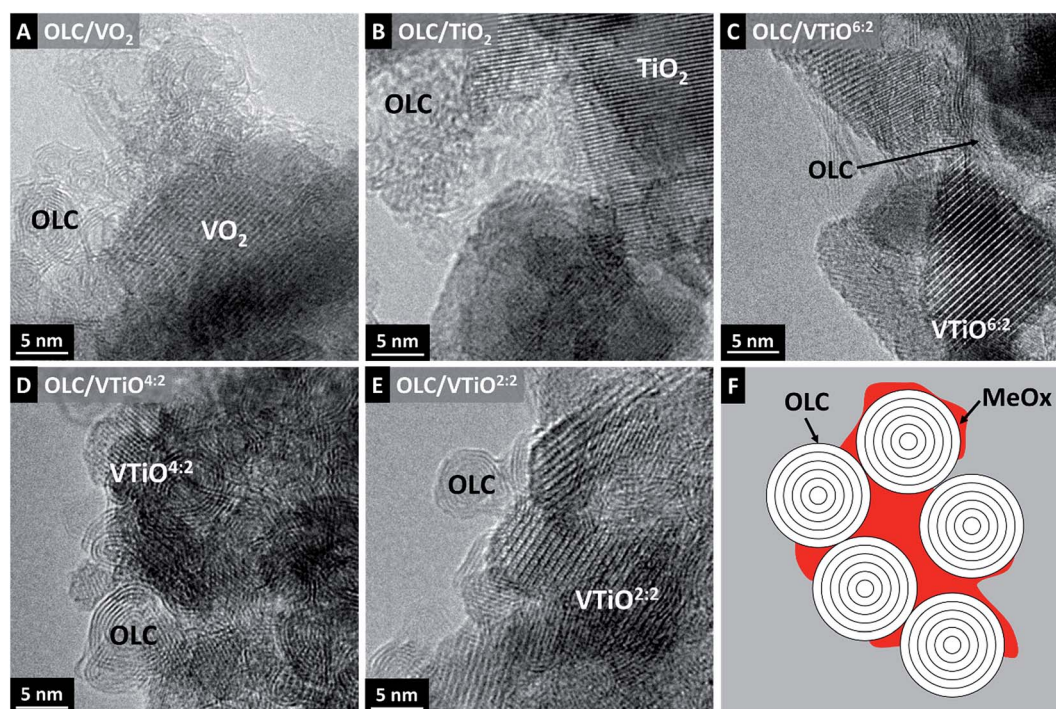


Fig. 1 (A–E) Transmission electron micrographs of all fabricated hybrid electrodes; (F) schematic illustration of the homogenous metal oxide distribution in the mesopore volume of OLC agglomerates.



Table 1 Chemical composition of the samples by EDX and metal oxide content based on EDX and TGA

	Elemental composition (EDX)				Metal oxide content	
	C, mass%	V, mass%	Ti, mass%	O, mass%	EDX (mass%)	TGA (mass%)
OLC/VTiO _{6:2}	35 ± 4	25 ± 3	18 ± 3	22 ± 5	65 ± 11	69
OLC/VTiO _{4:2}	34 ± 5	23 ± 2	19 ± 2	24 ± 3	66 ± 7	67
OLC/VTiO _{2:2}	38 ± 5	17 ± 2	20 ± 2	25 ± 4	62 ± 8	72
OLC/VO ₂	39 ± 3	43 ± 7	—	18 ± 5	61 ± 12	67
OLC/TiO ₂	34 ± 4	—	37 ± 4	29 ± 2	66 ± 6	66

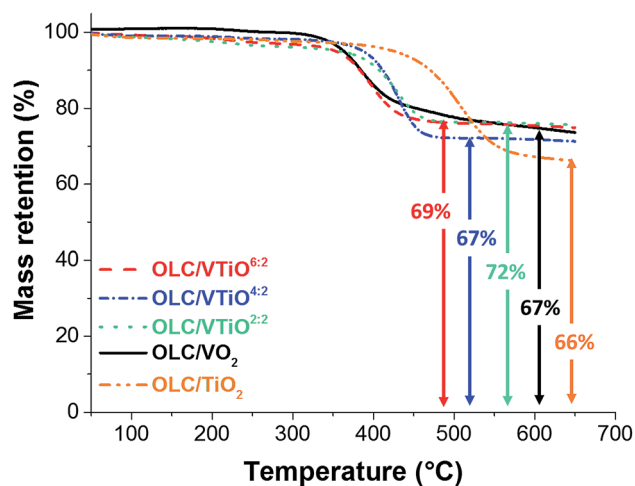


Fig. 2 Thermogravimetric analysis of all hybrid electrode samples. The measurements were carried out in synthetic air with a flow rate of 20 ml min⁻¹ up to a temperature of 650 °C at a heating rate of 5 °C min⁻¹.

titanium ($r = 0.60 \text{ \AA}$) for Ti⁴⁺ in 6-fold coordination as opposed to $r = 0.58 \text{ \AA}$ for V⁴⁺.⁴⁹

Raman spectroscopy was performed to further analyze the metal oxide structure (Fig. 3C). The findings of the XRD experiments for OLC/VO₂ and OLC/TiO₂ were confirmed: the observed Raman signals are characteristic of monoclinic vanadia and tetragonal titania.^{50,51} The Raman spectra of the multilayer samples are in stark contrast to the respective pure phases. A distinct peak at 195 cm⁻¹, which decreases in intensity for increasing Ti-content, can be related to VO₂(M). Furthermore, the broad shoulder centered at 910 cm⁻¹ that also decreases with increasing Ti-content has been described for mixtures of vanadia with both alumina and titania.^{52,53} The signal is a result of polyvanadate chains bonded to the foreign metal.⁵³ The broad feature around 250 cm⁻¹ that becomes sharper for increasing Ti-content has also been described in the literature. It was attributed to a disordered rutile structure⁵⁴ and second-order signals of octahedrally coordinated Ti in SrTiO₃ compounds.⁵¹ Thus, the emergence of the fundamentally changed Raman spectra for the multilayer systems is a further strong indicator of the formation of a solid solution with modified bond structures.

X-ray photoelectron spectroscopy (XPS) was performed on OLC/VO₂, OLC/TiO₂, and OLC/VTiO_{6:2} samples to evaluate the change in vanadium and titanium binding energy when

forming in a multilayer system. Survey spectra are given in Fig. S2A;† high resolution measurements of V 2p and Ti 2p are given in Fig. S2B† and 3D, respectively. The high resolution spectra of V 2p and Ti 2p in the multilayer sample show a reduced intensity, which is explained by the reduced content of the respective materials. While the signals of V 2p are located around roughly the same binding energy ($517.7 \pm 0.2 \text{ eV}$) for OLC/VO₂ and OLC/VTiO_{6:2}, a significant shift of the Ti 2p peaks is observed when being present in the multilayer system. The binding energy of titanium is reduced by a magnitude of 1.2 eV (Ti 2p_{3/2} shifts from 459.6 eV in anatase OLC/TiO₂ (ref. 55) to 458.4 eV in OLC/VTiO_{6:2}), which matches the value of previously reported titania doped vanadia phases.²⁰ This is in agreement with the XRD and Raman results, suggesting the formation of a solid solution of vanadia and titania, with a change in the binding structure of titanium in the hybrid samples.

3.2 Electrochemical performance

The electrochemical properties of the hybrid electrodes were evaluated using cyclic voltammetry (CV) at a scanning rate of 1 mV s⁻¹ (Fig. 4A and B). The OLCs used as substrates typically exhibit capacitive charge storage *via* double-layer formation, as has been well established in the literature.^{56–58} This behavior is reflected by a very small, rectangular shaped background in the CVs, best visible for sample OLC/TiO₂ in the range between 0 V and +1.0 V *vs.* carbon. The main charge storage mechanism of the hybrid electrodes, however, is lithium intercalation into the redox-active metal oxide layers, which is synergistically promoted by the conducting network provided by OLCs. In the cathodic scan of sample OLC/VO₂, a first lithiation peak occurs at -0.3 V *vs.* carbon, followed by a second, more pronounced peak at -0.5 V *vs.* carbon (corresponding to 2.9 V and 2.7 V *vs.* Li/Li⁺, respectively), indicating a two-step lithiation of the material, in accordance with the literature,⁵⁹ with a total intercalation of about 0.8–1.1 Li per VO₂.⁴⁰ The anodic scan also exhibits two peaks, completing the delithiation around -0.1 V *vs.* carbon. In contrast, OLC/TiO₂ exhibits only one pair of redox-peaks, with the lithiation process starting at -1.2 V *vs.* carbon and ending at -1.6 V *vs.* carbon (*i.e.*, +2.0 V to +1.6 V *vs.* Li/Li⁺), which corresponds to the insertion of 0.4–0.5 Li per TiO₂, as reported in the literature.^{60,61} The delithiation during the anodic scan is completed at -0.6 V *vs.* carbon. The larger voltage gap between the reactions, compared to OLC/VO₂, indicates slower lithium intercalation kinetics in the OLC/TiO₂ system.



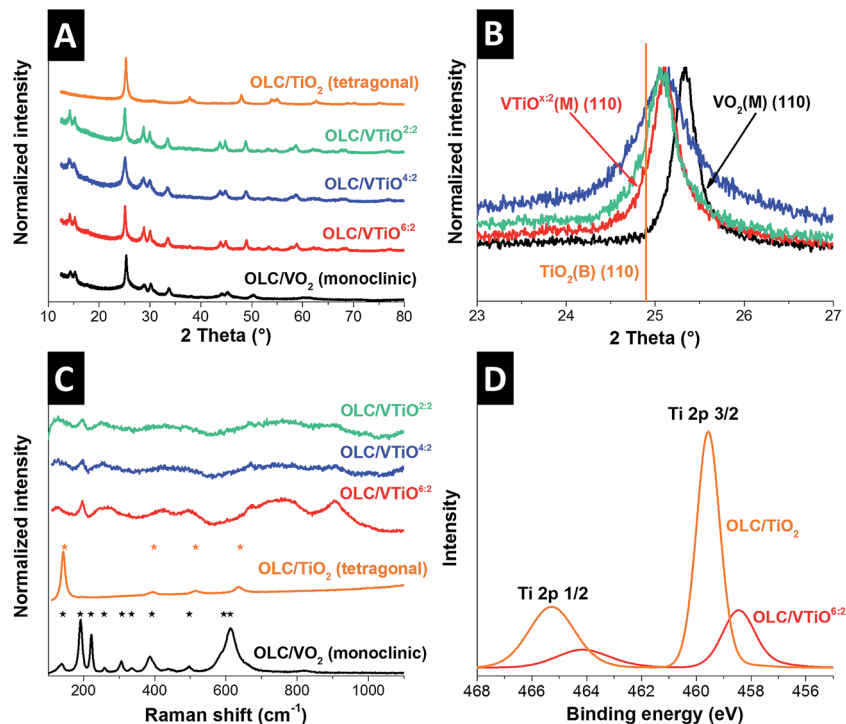


Fig. 3 (A) Survey of X-ray diffractograms of all fabricated hybrid electrodes, (B) detailed view of the (110) signal of OLC/VO₂ and all multilayer hybrid samples, including the (110) reflection position of TiO₂(B), (C) Raman spectra of all hybrid samples, including ideal peak positions of VO₂(M) and anatase, and (D) high resolution X-ray photoelectron spectra of the Ti 2p signal for hybrid samples OLC/TiO₂ and OLC/VTiO₂^{6:2}.

Table 2 Structural parameters of metal oxide crystalline phases calculated from XRD data, using EVA Diffrac Suite software

	<i>a</i> (Å)	<i>b</i> (Å)	<i>c</i> (Å)	β (°)	Volume (Å ³)	Type
VTiO ₂ ^{6:2}	12.12	3.72	6.45	106.6	279.2	Monoclinic
VTiO ₂ ^{4:2}	12.13	3.72	6.46	105.9	280.8	Monoclinic
VTiO ₂ ^{2:2}	12.14	3.73	6.48	106.6	281.1	Monoclinic
VO ₂	12.06	3.69	6.42	107.0	273.0	Monoclinic
TiO ₂	3.79	3.79	9.51	90.0	136.7	Tetragonal

The CV curves of the multilayer hybrid electrodes (Fig. 4B) exhibit a greater number of redox peaks, as compared to the single phase systems. In the cathodic scan of sample OLC/VTiO₂^{6:2}, lithiation can already be detected starting at -0.2 V vs. carbon, going through at least three steps up to -1.2 V vs. carbon. At -1.3 V vs. carbon, a further, separated peak emerges, indicating a fourth step of lithium intercalation. The anodic scan shows little shift for all corresponding peaks, indicating fast lithium diffusion kinetics in OLC/VTiO₂^{6:2}. With an increased titania content in the samples OLC/VTiO₂^{4:2} and OLC/VTiO₂^{2:2}, two significant observations are made in comparison to OLC/VTiO₂^{6:2}: (1) the area of the first set of peaks decreases, while the single, separated peak at a more negative potential increases in size and (2) the voltage shift between related cathodic and anodic peaks increases. This leads to the conclusions that (1) the cathodic peaks between -0.2 V and -1.2 V vs. carbon can be associated with a multistep reaction of Li with the vanadia species in the solid solution, while the peak

at the more negative potential originates from the reaction between Li and the titania species. Also, (2) the intercalation kinetics drop with increasing titania content in the solid solution, in accordance with the observations made in pristine OLC/TiO₂.

The capacity and power handling of the hybrid electrodes were evaluated using galvanostatic cycling with potential limitation (GCPL), shown in Fig. 4C. In the battery community, it is customary to normalize performance metrics to the mass of the redox-active material in the electrode. However, since both metal oxide and OLCs contribute to the electrochemical performance of the presented hybrid electrodes, it is appropriate to normalize to the entire electrode mass.⁶² For better comparability with literature values, the data for the best performing sample (OLC/VTiO₂^{6:2}) will also be reported with respect to the metal oxide content.

The OLC/VO₂ electrode exhibited a maximum specific discharge capacity of 198 mA h g⁻¹, with a high capacity retention of 51 mA h g⁻¹ at an ultrahigh discharge rate of 20 A g⁻¹ or 101C, while the OLC/TiO₂ electrode performed considerably worse with a maximum of 166 mA h g⁻¹ and a retention of 20 mA h g⁻¹ at 20 A g⁻¹ or 120C. The multilayer hybrid electrodes exhibited a strongly improved maximum specific capacity of above 330 mA h g⁻¹, with OLC/VTiO₂^{6:2} reaching the highest value of 382 mA h g⁻¹ (554 mA h g⁻¹ per metal oxide), thereby outperforming state-of-the-art metal oxide hybrid systems (ESI, Table S1†). This is a consequence of enhanced lithium intercalation capacity that can be related to the larger unit cell volume of VTiO, compared to VO₂(M) and



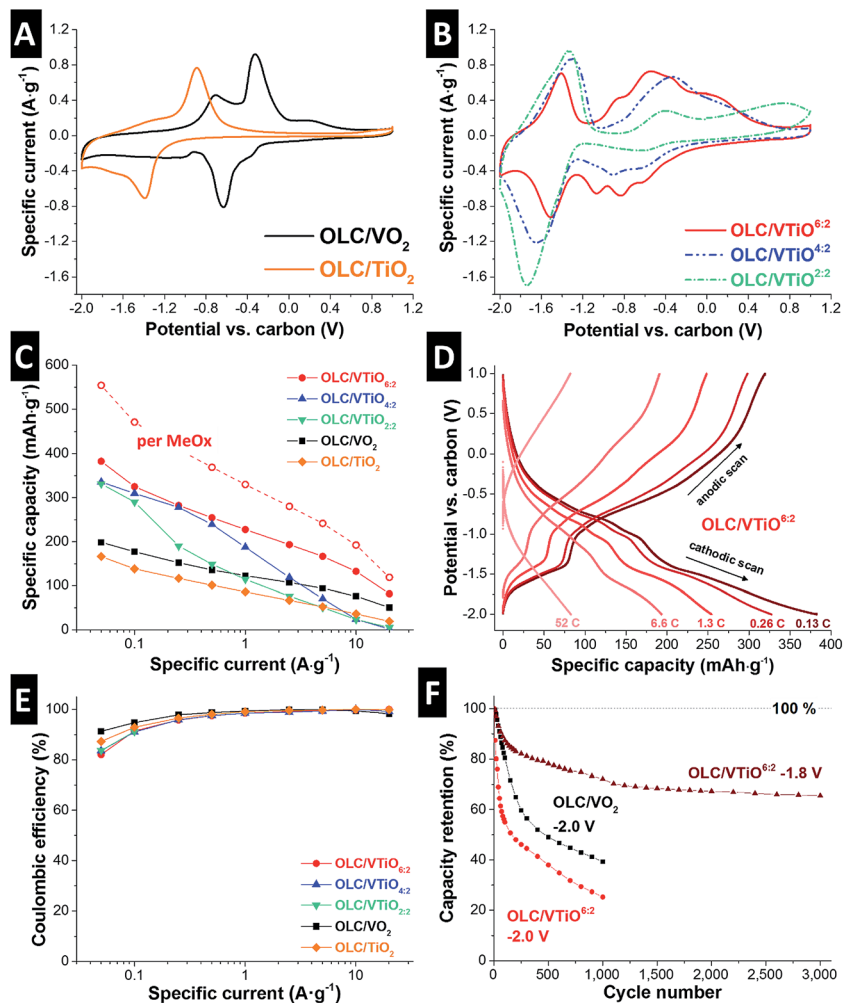
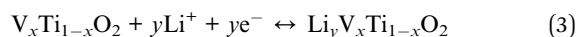


Fig. 4 (A) Cyclic voltammograms of single phase and (B) multilayer hybrid electrodes recorded at a scan rate of 1 mV s^{-1} . (C) Discharge capacity of all hybrid electrodes, derived from galvanostatic discharge from $+1.0 \text{ V}$ to -2.0 V vs. carbon at rates between 0.05 A g^{-1} and 20 A g^{-1} . (D) Voltage–capacity profiles for sample $\text{OLC/VTiO}^{6:2}$ at rates between 0.05 A g^{-1} and 20 A g^{-1} (corresponding to 0.13C to 52C) and (E) coulombic efficiency of all multilayer hybrid samples, derived from galvanostatic cycling at different rates. (F) Cycling stability test from galvanostatic cycling between $+1.0 \text{ V}$ and -2.0 V (-1.8 V) vs. carbon at 1 A g^{-1} .

tetragonal TiO_2 . In addition, the number of possible lithiation reactions is increased due to the presence of both vanadia and titania species. The lithiation follows this reaction path, with x defining the composition of the multilayer system and y the number of lithium ions intercalated:



When evaluating the power handling ability of the multilayer hybrid electrodes, the trend of decreased kinetic properties with higher titania contents seen in the CVs is confirmed. The samples $\text{OLC/VTiO}^{4:2}$ and $\text{OLC/VTiO}^{2:2}$ dramatically decline in performance at high rates above 2.5 A g^{-1} (about 10C), while $\text{OLC/VTiO}^{6:2}$ exhibits an extraordinary power handling, with a capacity retention of 82 mA h g^{-1} at 20 A g^{-1} or 52C (equivalent to 120 mA h g^{-1} normalized to the metal oxide mass), even reaching power values of novel hybrid supercapacitor materials (60 mA h g^{-1} at 17 A g^{-1} or 100C).⁶³

The electrochemical performance of $\text{OLC/VTiO}^{6:2}$ is further outlined by voltage–capacity profiles at various cycling rates (Fig. 4D). Two plateaus can be observed in the cathodic scan, corresponding to lithiation reactions with the vanadia and titania species of the material. When increasing the rate, the second plateau associated with lithiation of titania becomes smaller, thereby confirming that titania is the kinetically limiting part. The charge efficiency of all samples is determined to be well above 80% at very low rates of 0.05 A g^{-1} , and reaches 100% at medium–high rates above 0.25 A g^{-1} (Fig. 4E). The charge efficiency below 100% at low rates is explained by the charge contribution of irreversible side reactions, which commonly occur with high surface area materials offering a high reaction interface between the electrode and electrolyte. The high degrees of lithiation reached at low specific currents are also in part not fully reversible at the same discharging rate, leading to irreversibly intercalated Li, further contributing to a charge efficiency below 100% .



The longevity of the hybrid electrodes was evaluated using GCPL at a rate of 1 A g^{-1} (Fig. 4F). For discharging to $-2.0 \text{ V vs. carbon}$, after 200 cycles, a decline in discharge capacity was detected to 65% and 50% of the initial value for OLC/ VO_2 and OLC/ $\text{VTiO}^{6:2}$, respectively. This is characteristic of vanadia-containing electrodes that struggle with vanadium dissolution at low voltages.^{39,43} Decreasing the voltage window was found as a facile way to resolve this critical issue: by only discharging to a voltage of $-1.8 \text{ V vs. carbon}$ (*i.e.*, $1.4 \text{ V vs. Li/Li}^+$), the OLC/ $\text{VTiO}^{6:2}$ hybrid system showed a remarkably stable performance over 3000 cycles. After an initial drop to 83% after 200 cycles, stable cycling with minor capacity fading was observed. Although the maximum specific capacity was slightly

reduced to 315 mA h g^{-1} (457 mA h g^{-1} per metal oxide), reducing the maximum voltage it is proposed as an effective strategy to significantly enhance the longevity of VO_2 -containing electrodes.

In order to demonstrate a device level application of the hybrid electrodes, charge-balanced full-cells composed of OLC/ $\text{VTiO}^{6:2}$ (anode) and activated carbon (cathode) were investigated. The CVs of the full-cells show electrolyte stability up to at least $3.2 \text{ V cell voltage}$ (Fig. 5A). The CV shape clearly demonstrates two smeared out peaks between about 0 V and 1.8 V , and 2.3 V to 3.2 V , respectively, which correspond to the two regimes of lithium intercalation observed in the half-cell setup. This is confirmed by the two plateau-like regions in the voltage-profile (Fig. 5B). During galvanostatic cycling, the anode potential was monitored by a carbon reference and kept well above $-1.8 \text{ V vs. carbon}$ to stay within the stable potential range determined in half-cell experiments (blue line, Fig. 5B). The specific energy and power of full-cells are commonly displayed in a Ragone plot (Fig. 5C). The specific energy reaches a maximum value of 110 W h kg^{-1} for charging (76 W h kg^{-1} for discharging) with a maximum specific power of 6 kW kg^{-1} for charging (2.2 kW kg^{-1} for discharging). This outstanding device level performance is among the highest reported in the literature for hybrid supercapacitor full-cells and underlines the potential of the herein presented vanadia/titania multilayer system.

4. Conclusions

Vanadia-titania/carbon onion hybrid electrodes were synthesized by atomic layer deposition with different stacking orders of the respective metal oxides. By employing this novel approach and repetitively stacking atomically controlled vanadia and titania layers with high conformity, a solid solution with an expanded vanadia unit cell was fabricated, leading to a highly improved specific capacity of 382 mA h g^{-1} (554 mA h g^{-1} normalized to metal oxide mass) in comparison to 198 mA h g^{-1} for pristine VO_2 . In synergy with the highly conductive network of carbon onions, an impressive capacity retention of 82 mA h g^{-1} (120 mA h g^{-1} per metal oxide) when discharging at a rate of 20 A g^{-1} or 52C was attained. By benchmarking for cycling stability, discharging to a reduced potential of $-1.8 \text{ V vs. carbon}$ was found as a solution to obtain longevity over 3000 cycles. Device level performance of up to 110 W h kg^{-1} in asymmetrical full-cells underlines the future potential of the presented vanadia/titania multilayer system.

Acknowledgements

We acknowledge funding from the German Federal Ministry for research and Education (BMBF) in support of the nanoEES^{3D} project (award number 03EK3013) as part of the strategic funding initiative energy storage framework. This work is part of the CREATE-Network Project, Horizon 2020 of the European Commission (RISE Project No. 644013). We thank Prof. Artzt (INM) for his continuing support and Juhan Lee (INM) for discussions.

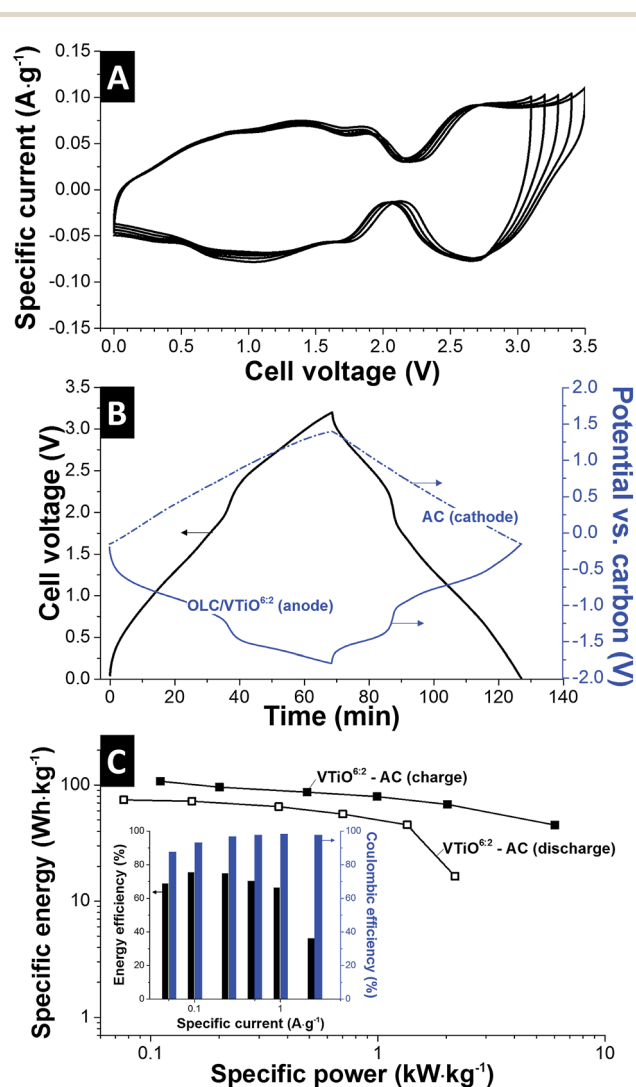


Fig. 5 Electrochemical benchmarking of hybrid supercapacitor full cells composed of OLC/ $\text{VTiO}^{6:2}$ (anode) and activated carbon (cathode). (A) Cyclic voltammograms to different maximum cell voltages between 3.0 V and 3.5 V . (B) Voltage profile of a galvanostatic cycle to 3.2 V at a rate of 0.05 A g^{-1} . The blue curves show the potential evolution at the cathode and anode, monitored against a carbon reference. (C) Ragone-plot displaying specific energy and power, derived from galvanostatic cycling to 3.2 V at different rates. Inset: energy efficiency and coulombic efficiency at different cycling rates.



References

- 1 F. Béguin, V. Presser, A. Balducci and E. Frackowiak, *Adv. Mater.*, 2014, **26**, 2219–2251.
- 2 B. E. Conway, *Electrochemical supercapacitors: scientific fundamentals and technological applications*, Springer Science & Business Media, 2013.
- 3 P. Simon and Y. Gogotsi, *Nat. Mater.*, 2008, **7**, 845–854.
- 4 D. Qu and H. Shi, *J. Power Sources*, 1998, **74**, 99–107.
- 5 H. Shi, *Electrochim. Acta*, 1996, **41**, 1633–1639.
- 6 V. Presser, M. Heon and Y. Gogotsi, *Adv. Funct. Mater.*, 2011, **21**, 810–833.
- 7 Y. Korenblit, M. Rose, E. Kockrick, L. Borchardt, A. Kvit, S. Kaskel and G. Yushin, *ACS Nano*, 2010, **4**, 1337–1344.
- 8 M. Zeiger, N. Jäckel, V. N. Mochalin and V. Presser, *J. Mater. Chem. A*, 2016, **4**, 3172–3196.
- 9 E. Bushueva, P. Galkin, A. Okotrub, L. Bulusheva, N. Gavrilov, V. Kuznetsov and S. Moiseev, *Phys. Status Solidi B*, 2008, **245**, 2296–2299.
- 10 E. Frackowiak, K. Metenier, V. Bertagna and F. Beguin, *Appl. Phys. Lett.*, 2000, **77**, 2421–2423.
- 11 T. M. Higgins, D. McAteer, J. C. M. Coelho, B. M. Sanchez, Z. Gholamvand, G. Moriarty, N. McEvoy, N. C. Berner, G. S. Duesberg and V. Nicolosi, *ACS Nano*, 2014, **8**, 9567–9579.
- 12 J. S. Atchison, M. Zeiger, A. Tolosa, L. M. Funke, N. Jäckel and V. Presser, *RSC Adv.*, 2015, **5**, 35683–35692.
- 13 A. Tolosa, B. Krüner, N. Jäckel, M. Aslan, C. Vakifahmetoglu and V. Presser, *J. Power Sources*, 2016, **313**, 178–188.
- 14 T. A. Centeno, O. Sereda and F. Stoeckli, *Phys. Chem. Chem. Phys.*, 2011, **13**, 12403–12406.
- 15 N. Jäckel, M. Rodner, A. Schreiber, J. Jeongwook, M. Zeiger, M. Aslan, D. Weingarth and V. Presser, *J. Power Sources*, 2016, **326**, 660–671.
- 16 Y. Zhang, H. Feng, X. Wu, L. Wang, A. Zhang, T. Xia, H. Dong, X. Li and L. Zhang, *Int. J. Hydrogen Energy*, 2009, **34**, 4889–4899.
- 17 K. Makgopa, P. M. Ejikeme, C. J. Jafta, K. Raju, M. Zeiger, V. Presser and K. I. Ozoemena, *J. Mater. Chem. A*, 2015, **3**, 3480–3490.
- 18 D. M. Anjos, J. K. McDonough, E. Perre, G. M. Brown, S. H. Overbury, Y. Gogotsi and V. Presser, *Nano Energy*, 2013, **2**, 702–712.
- 19 M. Zeiger, D. Weingarth and V. Presser, *ChemElectroChem*, 2015, **2**, 1117–1127.
- 20 P. H. Jampani, O. Velikokhatnyi, K. Kadakia, D. H. Hong, S. S. Damle, J. A. Poston, A. Manivannan and P. N. Kumta, *J. Mater. Chem. A*, 2015, **3**, 8413–8432.
- 21 S. Boukhalifa, K. Evanoff and G. Yushin, *Energy Environ. Sci.*, 2012, **5**, 6872–6879.
- 22 S. Fleischmann, N. Jäckel, M. Zeiger, B. Krüner, I. Grobelsek, P. Formanek, S. Choudhury, D. Weingarth and V. Presser, *Chem. Mater.*, 2016, **28**, 2802–2813.
- 23 M. V. K. Azhagan, M. V. Vaishampayan and M. V. Shelke, *J. Mater. Chem. A*, 2014, **2**, 2152–2159.
- 24 X. Wang and G. Yushin, *Energy Environ. Sci.*, 2015, **8**, 1889–1904.
- 25 V. Augustyn, P. Simon and B. Dunn, *Energy Environ. Sci.*, 2014, **7**, 1597–1614.
- 26 M. Salanne, B. Rotenberg, K. Naoi, K. Kaneko, P.-L. Taberna, C. Grey, B. Dunn and P. Simon, *Nature Energy*, 2016, **1**, 16070.
- 27 C. Portet, G. Yushin and Y. Gogotsi, *Carbon*, 2007, **45**, 2511–2518.
- 28 M. Zeiger, N. Jäckel, M. Aslan, D. Weingarth and V. Presser, *Carbon*, 2015, **84**, 584–598.
- 29 J. Liu, J. Essner and J. Li, *Chem. Mater.*, 2010, **22**, 5022–5030.
- 30 Y. He, W. Chen, X. Li, Z. Zhang, J. Fu, C. Zhao and E. Xie, *ACS Nano*, 2012, **7**, 174–182.
- 31 M. Zeiger, S. Fleischmann, B. Krüner, A. Tolosa, S. Bechtel, M. Baltes, A. Schreiber, R. Moroni, S. Vierrath, S. Thiele and V. Presser, *RSC Adv.*, 2016, **6**, 107163–107179.
- 32 K. E. Gregorczyk, A. C. Kozen, X. Chen, M. A. Schroeder, M. Noked, A. Cao, L. Hu and G. W. Rubloff, *ACS Nano*, 2014, **9**, 464–473.
- 33 M. D. Levi, M. R. Lukatskaya, S. Sigalov, M. Beidaghi, N. Shpigel, L. Daikhin, D. Aurbach, M. W. Barsoum and Y. Gogotsi, *Adv. Energy Mater.*, 2015, **5**, 1400815.
- 34 X. Chen, H. Zhu, Y.-C. Chen, Y. Shang, A. Cao, L. Hu and G. W. Rubloff, *ACS Nano*, 2012, **6**, 7948–7955.
- 35 M. Zeiger, T. Ariyanto, B. Krüner, N. J. Peter, S. Fleischmann, B. J. M. Etzold and V. Presser, *J. Mater. Chem. A*, 2016, **4**, 18899–18909.
- 36 I. Kovalenko, D. G. Bucknall and G. Yushin, *Adv. Funct. Mater.*, 2010, **20**, 3979–3986.
- 37 P. Simon, Y. Gogotsi and B. Dunn, *Science Magazine*, 2014, **343**, 1210–1211.
- 38 K. West, B. Zachau-Christiansen, T. Jacobsen and S. Skaarup, *Electrochim. Acta*, 1993, **38**, 1215–1220.
- 39 N. A. Chernova, M. Roppolo, A. C. Dillon and M. S. Whittingham, *J. Mater. Chem.*, 2009, **19**, 2526–2552.
- 40 D. Munoz-Rojas and E. Baudrin, *Solid State Ionics*, 2007, **178**, 1268–1273.
- 41 L. Mai, Q. Wei, Q. An, X. Tian, Y. Zhao, X. Xu, L. Xu, L. Chang and Q. Zhang, *Adv. Mater.*, 2013, **25**, 2969–2973.
- 42 C. Tsang and A. Manthiram, *J. Electrochem. Soc.*, 1997, **144**, 520–524.
- 43 E. Baudrin, G. Sudant, D. Larcher, B. Dunn and J.-M. Tarascon, *Chem. Mater.*, 2006, **18**, 4369–4374.
- 44 K. Takahashi, Y. Wang, K. Lee and G. Cao, *Appl. Phys. A*, 2006, **82**, 27–31.
- 45 S. Park, C. W. Lee, J.-C. Kim, H. J. Song, H.-W. Shim, S. Lee and D.-W. Kim, *ACS Energy Lett.*, 2016, **1**, 216–224.
- 46 D. Weingarth, H. Noh, A. Foelske-Schmitz, A. Wokaun and R. Kötz, *Electrochim. Acta*, 2013, **103**, 119–124.
- 47 D. Weingarth, M. Zeiger, N. Jäckel, M. Aslan, G. Feng and V. Presser, *Adv. Energy Mater.*, 2014, **4**, 1400316.
- 48 R. Yoshida, Y. Suzuki and S. Yoshikawa, *J. Solid State Chem.*, 2005, **178**, 2179–2185.
- 49 R. Shannon, *Acta Crystallogr., Sect. A: Cryst. Phys., Diffraction, Theor. Gen. Crystallogr.*, 1976, **32**, 751–767.



- 50 G. Petrov, V. Yakovlev and J. Squier, *Appl. Phys. Lett.*, 2002, **81**, 1023–1025.
- 51 U. Balachandran and N. Eror, *J. Solid State Chem.*, 1982, **42**, 276–282.
- 52 N.-Y. Topsøe, M. Anstrom and J. Dumesic, *Catal. Lett.*, 2001, **76**, 11–20.
- 53 G. T. Went, S. T. Oyama and A. T. Bell, *J. Phys. Chem.*, 1990, **94**, 4240–4246.
- 54 Y. Hara and M. Nicol, *Phys. Status Solidi B*, 1979, **94**, 317–322.
- 55 I. Chashechnikova, V. Vorotyntsev, V. Borovik, G. Golodets, I. Plyuto and A. Shpak, *Theor. Exp. Chem.*, 1993, **28**, 176–178.
- 56 W. Gu, N. Peters and G. Yushin, *Carbon*, 2013, **53**, 292–301.
- 57 M. Zeiger, N. Jäckel, D. Weingarh and V. Presser, *Carbon*, 2015, **94**, 507–517.
- 58 J. K. McDonough, A. I. Frolov, V. Presser, J. Niu, C. H. Miller, T. Ubieta, M. V. Fedorov and Y. Gogotsi, *Carbon*, 2012, **50**, 3298–3309.
- 59 D. Chao, C. Zhu, X. Xia, J. Liu, X. Zhang, J. Wang, P. Liang, J. Lin, H. Zhang and Z. X. Shen, *Nano Lett.*, 2014, **15**, 565–573.
- 60 S. Huang, L. Kavan, I. Exnar and M. Grätzel, *J. Electrochem. Soc.*, 1995, **142**, L142–L144.
- 61 N. Li, G. Liu, C. Zhen, F. Li, L. Zhang and H. M. Cheng, *Adv. Funct. Mater.*, 2011, **21**, 1717–1722.
- 62 F. Gschwind, G. Rodriguez-Garcia, D. Sandbeck, A. Gross, M. Weil, M. Fichtner and N. Hörmann, *J. Fluorine Chem.*, 2016, **182**, 76–90.
- 63 K. Naoi, K. Kisu, E. Iwama, S. Nakashima, Y. Sakai, Y. Orikasa, P. Leone, N. Dupré, T. Brousse, P. Rozier, W. Naoi and P. Simon, *Energy Environ. Sci.*, 2016, **9**, 2143–2151.



Electronic Supplementary Information

**VANADIA-TITANIA MULTILAYER NANODECORATION OF
CARBON ONIONS VIA ATOMIC LAYER DEPOSITION FOR
HIGH PERFORMANCE ELECTROCHEMICAL ENERGY STORAGE**

**Simon Fleischmann,¹ Aura Tolosa,^{1,2} Marco Zeiger,^{1,2} Benjamin Krüner,^{1,2}
Nicolas J. Peter,³ Ingrid Grobelsek,² Antje Quade,⁴ Angela Kruth,⁴ and Volker Presser^{1,2,*}**

¹ Department of Materials Science and Engineering, Saarland University, 66123 Saarbrücken, Germany

² INM – Leibniz Institute for New Materials, 66123 Saarbrücken, Germany

³ Max-Planck-Institut für Eisenforschung GmbH, 40237 Düsseldorf, Germany

⁴ Leibniz Institute for Plasma Science and Technology, 17489 Greifswald, Germany

* Corresponding author's eMail: volker.presser@leibniz-inm.de

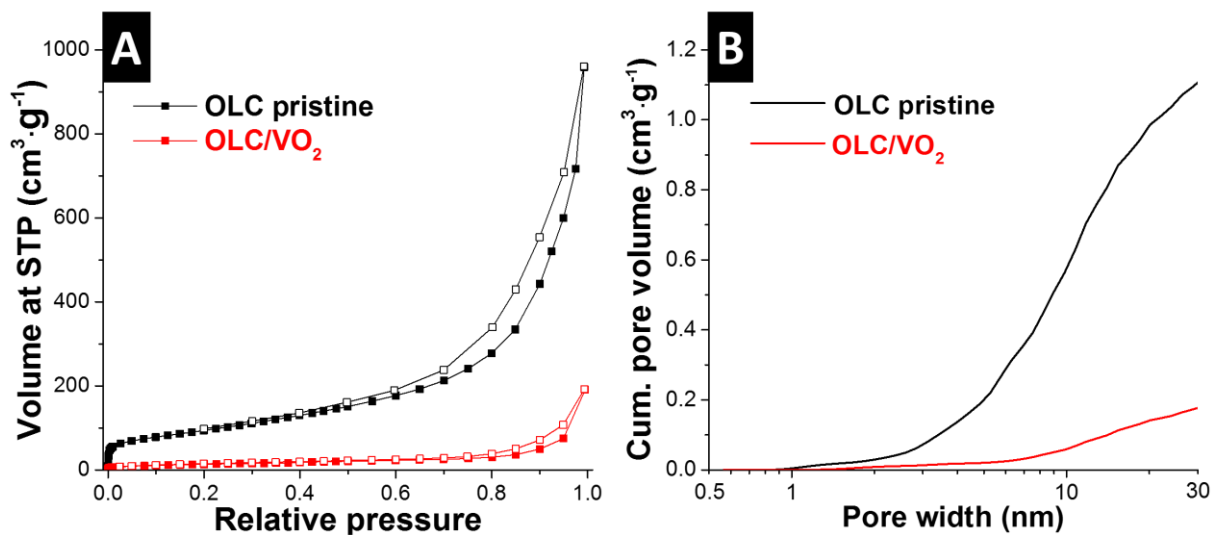


Figure S1: Nitrogen sorption isotherms at standard temperature and pressure (A) and specific cumulative pore volume of uncoated carbon onions and OLC/VO₂ (B). Data modified from Ref. ¹.

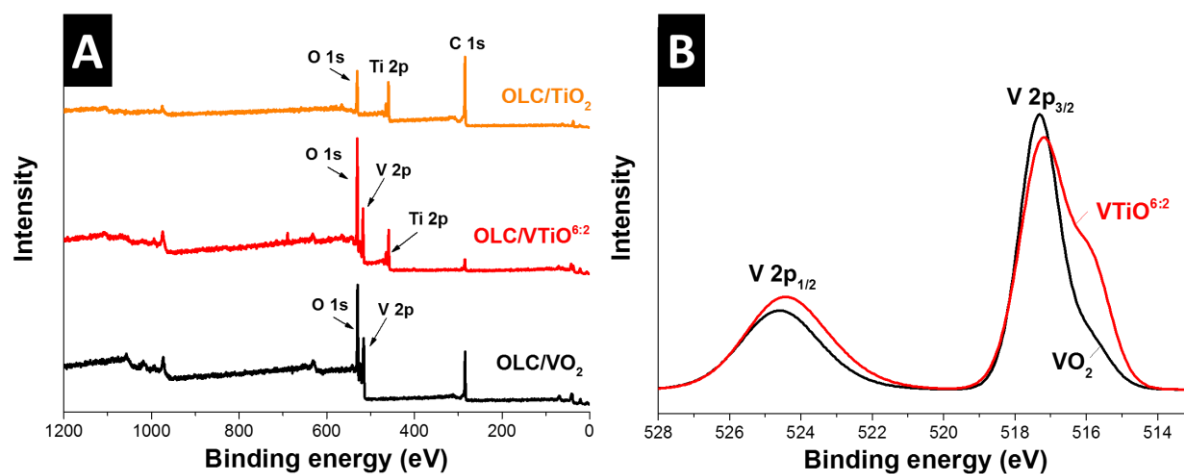


Figure S2: XPS survey spectra of OLC/VO₂, OLC/VTiO_{6:2}, OLC/TiO₂ (A), high resolution V 2p signals of OLC/VO₂ and OLC/VTiO_{6:2} (B).

Table S1: Comparison of specific capacities for recently reported vanadium oxide hybrid systems.

Electrode material	Specific capacity per electrode (mAh·g ⁻¹)	Specific capacity per metal oxide (mAh·g ⁻¹)	Discharge rate	Reference
OLC/VTiO ^{6:2}	382	554	0.05 A·g ⁻¹	This work
V ₂ O ₅ /CDC (core-shell)	310	420	0.05 A·g ⁻¹	2
CNT/V ₂ O ₅ (+TiO ₂ protective layer)	256	400	0.1 A·g ⁻¹	3
Graphene/VO ₂	206	421	0.14 A·g ⁻¹	4
VO ₂ /Sb:SnO ₂	154	350	0.1 A·g ⁻¹	5
CNT/VO _x :Ti (Ti-doped)	-	157	2 mV·s ⁻¹	6
OLC/VO _x	120	200	0.05 A·g ⁻¹	1
AC/VO _x	122	240	0.05 A·g ⁻¹	1

References:

1. S. Fleischmann, N. Jäckel, M. Zeiger, B. Krüner, I. Grobelsek, P. Formanek, S. Choudhury, D. Weingarth and V. Presser, *Chem. Mater.*, 2016, **28**, 2802-2813.
2. M. Zeiger, T. Ariyanto, B. Krüner, N. J. Peter, S. Fleischmann, B. J. M. Etzold and V. Presser, *J. Mater. Chem. A*, 2016, **4**, 18899-18909.
3. M. Xie, X. Sun, H. Sun, T. Porcelli, S. M. George, Y. Zhou and J. Lian, *J. Mater. Chem. A*, 2016, **4**, 537-544.
4. D. Chao, C. Zhu, X. Xia, J. Liu, X. Zhang, J. Wang, P. Liang, J. Lin, H. Zhang and Z. X. Shen, *Nano Lett.*, 2014, **15**, 565-573.
5. S. Park, C. W. Lee, J.-C. Kim, H. J. Song, H.-W. Shim, S. Lee and D.-W. Kim, *ACS Energy Lett.*, 2016, **1**, 216-224.
6. P. H. Jampani, O. Velikokhatnyi, K. Kadakia, D. H. Hong, S. S. Damle, J. A. Poston, A. Manivannan and P. N. Kumta, *J. Mater. Chem. A*, 2015, **3**, 8413-8432.

4.6 Atomic layer deposited molybdenum oxide / carbon nanotube hybrid electrodes: Influence of crystal structure on lithium-ion capacitor performance

Simon Fleischmann,^{1,2} Marco Zeiger,^{1,2}
Antje Quade,³ Angela Kruth,³ and Volker Presser^{1,2}

¹ INM - Leibniz Institute for New Materials, 66123 Saarbrücken, Germany

² Department of Materials Science and Engineering, Saarland University, 66123 Saarbrücken, Germany

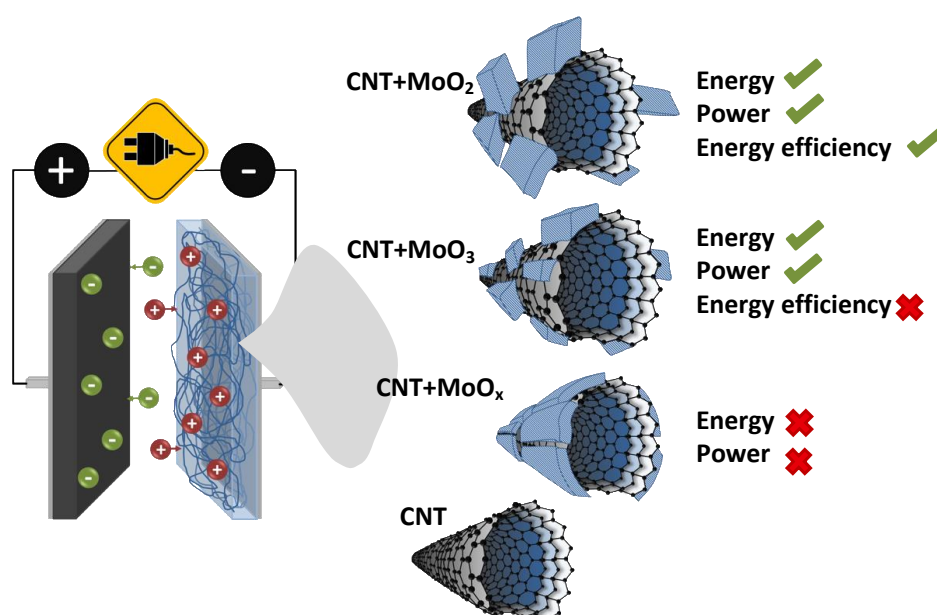
³ Leibniz Institute for Plasma Science and Technology, 17489 Greifswald, Germany

Citation:

S. Fleischmann, M. Zeiger, A. Quade, A. Kruth and V. Presser, *Atomic layer deposited molybdenum oxide/carbon nanotube hybrid electrodes: Influence of crystal structure on lithium-ion capacitor performance*, *ACS Appl. Mater. Interfaces*, **2018**, 10, 18675-18684. (DOI: 10.1021/acsami.8b03233)

Own contribution:

Planning, ALD synthesis, thermal annealing, X-ray diffraction measurements, Raman measurements, Raman peak deconvolution, thermogravimetric analysis, scanning electron microscopy, electrochemical measurements, writing.



Atomic Layer-Deposited Molybdenum Oxide/Carbon Nanotube Hybrid Electrodes: The Influence of Crystal Structure on Lithium-Ion Capacitor Performance

Simon Fleischmann,^{†,‡} Marco Zeiger,^{†,‡} Antje Quade,[§] Angela Kruth,[§] and Volker Presser^{*,†,‡,§}

[†]INM—Leibniz Institute for New Materials, 66123 Saarbrücken, Germany

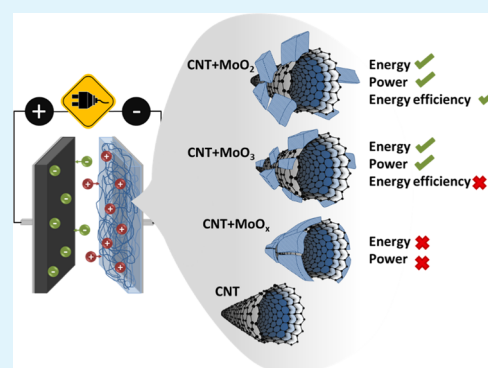
[‡]Department of Materials Science and Engineering, Saarland University, 66123 Saarbrücken, Germany

[§]Leibniz Institute for Plasma Science and Technology, 17489 Greifswald, Germany

Supporting Information

ABSTRACT: Merging of supercapacitors and batteries promises the creation of electrochemical energy storage devices that combine high specific energy, power, and cycling stability. For that purpose, lithium-ion capacitors (LICs) that store energy by lithiation reactions at the negative electrode and double-layer formation at the positive electrode are currently investigated. In this study, we explore the suitability of molybdenum oxide as a negative electrode material in LICs for the first time. Molybdenum oxide–carbon nanotube hybrid materials were synthesized via atomic layer deposition, and different crystal structures and morphologies were obtained by post-deposition annealing. These model materials are first structurally characterized and electrochemically evaluated in half-cells. Benchmarking in LIC full-cells revealed the influences of crystal structure, half-cell capacity, and rate handling on the actual device level performance metrics. The energy efficiency, specific energy, and power are mainly influenced by the overpotential and kinetics of the lithiation reaction during charging. Optimized LIC cells show a maximum specific energy of about 70 W·h·kg⁻¹ and a high specific power of 4 kW·kg⁻¹ at 34 W·h·kg⁻¹. The longevity of the LIC cells is drastically increased without significantly reducing the energy by preventing a deep cell discharge, hindering the negative electrode from crossing its anodic potential limit.

KEYWORDS: lithium-ion capacitor, hybrid materials, electrochemical energy storage, asymmetric supercapacitor, molybdenum oxide



1. INTRODUCTION

In the face of global warming and climate change, the mitigation of CO₂ emissions is considered to be a key challenge for the next decades.¹ Therefore, a transition from fossil to renewable energy sources in the electricity and mobility sectors has to be realized, requiring the availability of efficient fast-responding electrochemical energy storage devices.^{2,3} Electrical double-layer capacitors (EDLCs) employ high-surface area electrodes that store energy by formation of the electrical double-layer via adsorption of ions at the charged interface to the electrolyte.⁴ Most commonly, carbons with high internal porosity are used as electrodes, such as activated carbons (ACs)^{5,6} or carbide-derived carbons,^{7,8} offering a high surface area (2000–3000 m²·g⁻¹) for ion electroadsorption. Carbon nanomaterials such as carbon nanotubes (CNTs)⁹ and carbon onions^{10,11} with a large outer surface area find use in high-power applications, as they enable even faster double-layer formation by offering shorter diffusion paths to the electrolyte ions.¹² Though they provide a high specific power (>10 kW·kg⁻¹) and long lifetimes (>100 000 cycles), the main drawback of EDLCs is their low specific energy (<20 W·h·kg⁻¹).^{4,12} Consequently, most commercial mobile applications rely on lithium-ion batteries (LIBs) instead of EDLCs, as they employ

faradaic electrode materials that enable lithium intercalation reactions, exhibiting a higher energy storage capacity (>100 W·h·kg⁻¹).¹³ Commonly found faradaic materials are metal oxides such as MoO₃,¹⁴ V₂O₅,¹⁵ MnO₂,¹⁶ Nb₂O₅,¹⁷ or LTO,¹⁸ which are combined with conductive carbons to form a composite electrode because of their oftentimes poor electrical conductivity. Yet, intercalation reactions are kinetically limited by solid-state diffusion and may cause significant volumetric changes to the electrode materials during operation,¹⁹ thereby limiting the specific power (<1 kW·kg⁻¹) and cyclability (<1000 cycles).²⁰

A synergistic combination of both technologies, EDLC and battery, shows promise to improve the performance metrics of the resulting materials.²¹ High-surface area carbons that have been nanoscopically decorated with faradaic materials form hybrid materials with a large electrode/electrolyte interface and good electrical conductivity.²² Such hybrid materials that are closely linked on a nanoscopic level show superior electrochemical properties compared to composite materials that are

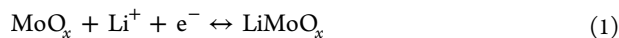
Received: February 26, 2018

Accepted: May 11, 2018

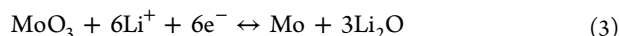
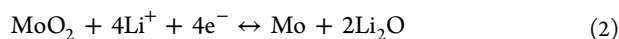
Published: May 11, 2018

created by mere mechanical mixing of the two components.^{23,24} Possible synthesis routes for the decoration of carbon substrates with faradaic materials include atomic layer deposition (ALD),²⁵ hydrothermal synthesis,²⁶ wet-chemical synthesis,²⁷ melt infiltration,²⁸ or self-assembly reactions.²⁹ A requirement for the carbon substrate material is (ideally full) surface accessibility for noncarbon species, generally favoring nanocarbons with external surface area over porous ACs, where pore blocking can occur;³⁰ however, especially, tailored mesoporous carbons with high internal surface areas also showed a high suitability as substrates.^{31,32} ALD is a vapor deposition technique that occurs in binary, self-limited reaction cycles. During each reaction cycle, one atomic layer of the desired material is deposited.³³ This allows for designing highly conformal coatings with enhanced control over the mass loading on the carbon electrodes and enables the layer-by-layer deposition of different components.³⁴ Consequently, ALD is a powerful tool for the synthesis of model hybrid materials with well-defined properties.

Merging of supercapacitors and batteries is also an intriguing concept on a cell design level: by the use of an anode material that enables lithium intercalation (metal oxide) and an EDLC cathode material (nanoporous carbon), a lithium-ion capacitor (LIC) is obtained that exhibits higher energies than conventional EDLCs while still showing attractive power handling and longevity.^{35,36} This cell setup was first introduced in 2001 by Amatucci et al. and has also been called a hybrid or asymmetric supercapacitor.³⁷ To compensate for the higher specific capacity of the anode, a cathode with oversized mass can be chosen.³⁸ The slow kinetics of ion intercalation in the metal oxide anode as compared to electrosorption at the carbon cathode is a key issue of this cell concept, creating a need for metal oxide/carbon hybrid materials that present good electron and ion mobility.³⁹ A possible candidate is molybdenum oxide, a layered transition-metal oxide that has been widely studied as an anode material for LIBs, as it exhibits a high theoretical specific capacity, depending on the crystal structure and cutoff voltage.^{40–42} Charge storage is accomplished by two different types of faradaic reactions: (1) lithium intercalation in a potential range between 3 and 1 V versus Li/Li⁺ and (2) a conversion reaction below 1 V versus Li/Li⁺.⁴³ The intercalation reaction involves up to one electron transfer according to



The conversion reaction below 1 V yields a transfer of up to six electrons depending on the oxidation state of molybdenum oxide⁴⁴



Conversion-type reactions typically exhibit poor kinetics and reversibility, making them unfavorable for high-power applications.⁴³ Recently, the pseudocapacitive charge storage properties of molybdenum oxides have been investigated by Dunn and co-workers: they concluded that (1) nanosizing MoO₂ and hybridizing with reduced graphene oxide⁴³ and (2) the introduction of oxygen vacancies into the orthorhombic structure of MoO₃⁴⁵ greatly enhance the kinetics of the lithium intercalation reactions. On the basis of those first findings, molybdenum oxide-based hybrid materials appear attractive for the use as anodes in LICs. Though MoO₃/carbon fiber hybrid

materials were used in an asymmetric supercapacitor setup, these devices employed aqueous or gel electrolytes in a small potential window, therefore capitalizing on surface redox reactions rather than lithium intercalation reactions.^{46,47} However, there is an apparent lack of studies on the suitability of kinetically attractive molybdenum oxide/carbon hybrid materials as LIC anode materials. Further, a comparison of intercalation kinetics of different molybdenum oxidation states and their impact on the performance in LICs need to be explored.

Herein, we investigate molybdenum oxide–CNT hybrid electrodes synthesized by ALD and heat-treated in different atmospheres to obtain various crystal structures. These model materials are electrochemically benchmarked both in half-cells and as anodes in a LIC full-cell. Our study provides valuable insights into the relations between crystallographic structure of molybdenum oxide, its morphology, and the resulting LIC performances.

2. EXPERIMENTAL SECTION

2.1. Preparation of CNT/Molybdenum Oxide Hybrid Electrodes. CNT paper electrodes (i.e., binder-free) were prepared by dispersion of multiwalled CNT powder (Nanocyl NC7000) by sonication in ethanol on a magnetic stirrer for 30 min. Then, the obtained solution was vacuum-filtered through a Durapore membrane filter (Merck Millipore). Finally, the obtained CNT paper electrode was dried for 3 h at 120 °C to remove any residual solvents, yielding freestanding, binder-free electrodes (diameter: 50 mm and thickness: 50 ± 10 μm).

The obtained CNT paper was transferred to an OpAL (open-load ALD, Oxford Instruments) system. The molybdenum oxide coating was synthesized by subsequent cycles of molybdenum hexacarbonyl (Mo(CO)₆, Pegasus Chemicals) as metal precursor and ozone as reactant gas. Mo(CO)₆ was preheated to 60 °C in a bubbler and delivered to the reaction chamber by argon carrier gas. One ALD cycle consisted of a dosing period of Mo(CO)₆ for 15 s, 10 s of purging with argon gas, 45 s of ozone dosage, and a final 15 s pumping step. The temperature of the reactor during deposition was maintained at 165 °C. The CNT paper electrodes were placed in the reactor in a vertical alignment, so as to allow effective precursor penetration from both sides, enabling coating over the entire thickness of the CNT electrode.

To achieve the desired crystalline structure after ALD, the MoO_x–CNT samples were further thermally annealed. MoO₃–CNT was obtained by annealing in a synthetic air atmosphere at 360 °C for 1 h, whereas MoO₂–CNT was produced by annealing in an argon atmosphere at 500 °C for 1 h. All annealing steps were carried out with heating and cooling rates of 10 °C·min⁻¹.

2.2. Structural Characterization. Scanning electron microscopy (SEM) was carried out using a JEOL JSM-7500F system with an acceleration voltage of 3 kV. Energy-dispersive X-ray spectroscopy was carried out with an X-Max-150 detector from Oxford Instruments using a voltage of 10 kV.

Raman spectroscopy was performed with a Renishaw inVia Raman Microscope with a Nd/YAG laser (532 nm wavelength), a 2400 lines·mm⁻¹ grating, and a 50× objective (numeric aperture: 0.9). The resulting laser spot covered about 1 μm in diameter and exhibited a power of 0.05 mW. All spectra were recorded for 30 s with 10 accumulations. Peak deconvolution was carried out using two Gaussian and three Lorentzian peaks to fit the amorphous and ordered carbon structures.

The elemental surface chemical composition and chemical binding properties of the samples were determined by X-ray photoelectron spectroscopy (XPS), using an AXIS Ultra spectrometer from Kratos. Monochromatic Al Kα (150 W), implementation of charge neutralization, and a pass energy of the analyzer of 80 eV were used for determining the elemental composition. A highly resolved Mo 3d peak was measured with a pass energy of 10 eV (225 W).

X-ray diffraction experiments were carried out with a D8 Discover XRD from Bruker AXS (corundum standard calibrated). A copper X-ray source was employed (Cu $K\alpha$, 40 kV, 40 mA), with a Göbel mirror, a 0.5 mm point focus, and a VANTEC-500 detector. The detector simultaneously covered a range of about $20^\circ 2\theta$ per measurement step, and the samples were measured in three steps with the detector positioned at 20, 40, and $60^\circ 2\theta$ for 17 min each.

Thermogravimetric analysis was performed with a TG 209 F1 Libra system from Netzsch. The samples were measured in alumina crucibles at a heating rate of $5 \text{ K}\cdot\text{min}^{-1}$ to a temperature of 650°C in a synthetic air atmosphere (flow rate: 20 sccm).

2.3. Electrochemical Characterization. Electrochemical measurements were performed in a custom-built cell with a polyether ether ketone body and spring-loaded titanium pistons, as further described in ref 48. For half-cell characterization, 10 mm discs of $\text{MoO}_x\text{-CNT}$ electrodes with a mass loading of $1.3 \pm 0.3 \text{ mg}/\text{cm}^2$ were used as working electrodes and a metallic lithium chip served as the reference and counter electrodes. The electrodes were separated by a glass fiber separator (GF/D, Whatman), and 12 mm copper foil and aluminum foil served as current collectors on the negative and positive sides, respectively. In the LIC setup, $\text{MoO}_x\text{-CNT}$ served as a negative electrode, AC (type YP-80F, Kuraray, 5 mass % polytetrafluoroethylene (PTFE) bound, $100 \mu\text{m}$ thickness) was the positive electrode, and a piece of lithium metal was used as a spectator reference electrode. Charge balance was achieved by oversizing the AC electrode, using electrode mass ratios of 1:2.5. All electrodes were dried in a vacuum oven at 120°C and 20 mbar prior to use. Cell assembly was carried out in an argon-filled glovebox (MBraun Labmaster 130, O_2 and $\text{H}_2\text{O} < 1 \text{ ppm}$), and the cells were vacuum-backfilled with 1 M LiClO_4 in a mixture of ethylene carbonate and dimethyl carbonate electrolyte (EC/DMC, vol 1:1) from BASF (battery grade).

Electrochemical testing was performed with a VSP300 potentiostat/galvanostat from Bio-Logic. In half-cells, cyclic voltammograms were recorded at a scanning rate of $1 \text{ mV}\cdot\text{s}^{-1}$ and galvanostatic cycling was conducted with specific currents between 0.05 and $20 \text{ A}\cdot\text{g}^{-1}$ in a potential range between 1 and 3 V versus Li/Li^+ . All performance metrics were normalized to the full hybrid electrode mass m (i.e., metal oxide and CNT mass) unless declared otherwise. The specific capacity C_{sp} is calculated by integration of the current I over time $t - t_0$ during the delithiation step according to

$$C_{\text{sp}} = \frac{\int_{t_0}^t I dt}{m} \quad (4)$$

The Coulombic efficiency is derived by dividing C_{sp} by the specific capacity of the lithiation step. In the LIC setup, cyclic voltammograms are recorded with $1 \text{ mV}\cdot\text{s}^{-1}$ and galvanostatic cycling with specific currents between 0.1 and $10 \text{ A}\cdot\text{g}^{-1}$ in a cell voltage range from 0 to 3.2 V while simultaneously monitoring the potential development with a lithium spectator reference electrode. The specific discharge energy E_{sp} is calculated by numeric integration of the voltage $U(t)$ over discharge time $t - t_0$ according to

$$E_{\text{sp}} = \frac{I \int_{t_0}^t U(t) dt}{M} \quad (5)$$

The specific discharge power was calculated by dividing E_{sp} by the discharge time $t - t_0$, and the energy efficiency is calculated by dividing by the specific energy during the charge step. LIC metrics are reported with respect to the combined mass M of both electrodes, excluding the PTFE-binder mass of the AC electrode.

3. RESULTS AND DISCUSSION

3.1. Structural Characterization. Molybdenum oxide decoration of CNTs was obtained by ALD directly on freestanding, binder-free CNT paper. After the deposition process, two different annealing procedures are carried out to obtain different crystal structures of molybdenum oxide (Figure

1A). After the ALD process, molybdenum oxide is homogeneously deposited on the entangled CNT substrate network,

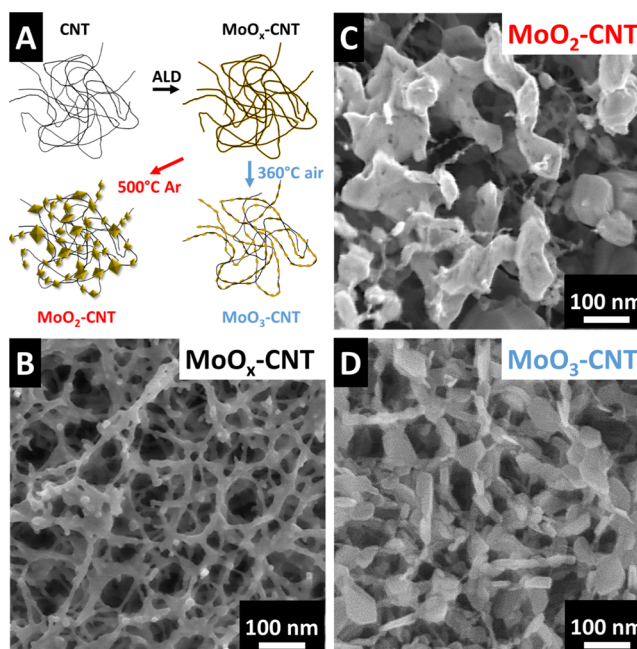


Figure 1. Schematic illustration of the synthesis process (A) and SEM images of the as-deposited $\text{MoO}_x\text{-CNT}$ (B), $\text{MoO}_2\text{-CNT}$ after annealing at 500°C in an argon atmosphere (C), and $\text{MoO}_3\text{-CNT}$ after annealing at 360°C in a synthetic air atmosphere (D).

showing average tube diameters of 15–30 nm according to the scanning electron micrograph of the as-deposited $\text{MoO}_x\text{-CNT}$ in Figure 1B, with the CNTs being completely covered. After annealing of the hybrid electrodes in argon at 500°C for 1 h, flake-like crystallites are observed within the CNT network that are up to 150 nm in lateral size and up to about 50 nm in thickness (Figure 1C). These crystallites appear to be formed during annealing by coarsening of molybdenum oxide that covered the CNTs after ALD, as evident by the reduction of tube radius before and after annealing. Coarsening is also observed when annealing the hybrid electrodes in air at 360°C for 1 h, where flakes smaller than 50 nm in diameter and below 20 nm in thickness are formed (Figure 1D). This coarsening results from thermodynamically driven crystallization enabled by elevated temperatures, which explains the formation of larger crystallites at higher temperatures.⁴⁹

A more thorough investigation of the coating morphology was carried out by transmission electron microscopy (TEM). The as-deposited $\text{MoO}_x\text{-CNT}$ hybrid electrodes show a very uniform coating of molybdenum oxide on the CNTs with a thickness of around 1.5–2 nm (Figure 2A,B), confirming an ALD process with homogenous layer growth. Diffusion of the as-deposited molybdenum oxide, as it was already observed in SEM, can also be confirmed by TEM measurements. Crystallites are formed by the material that homogeneously covered the CNTs before, which fully consumes the thin films, as diffusion is enabled by annealing in argon (Figure 2C,D) and air atmospheres (Figure 2E,F). These particles remain intimately entangled within the CNT substrates (Figure 2D,F).

Raman spectra of all hybrid samples are shown in Figure 3A, with all data being normalized to the carbon D-peak. The spectra can be divided into two regions: At low Raman

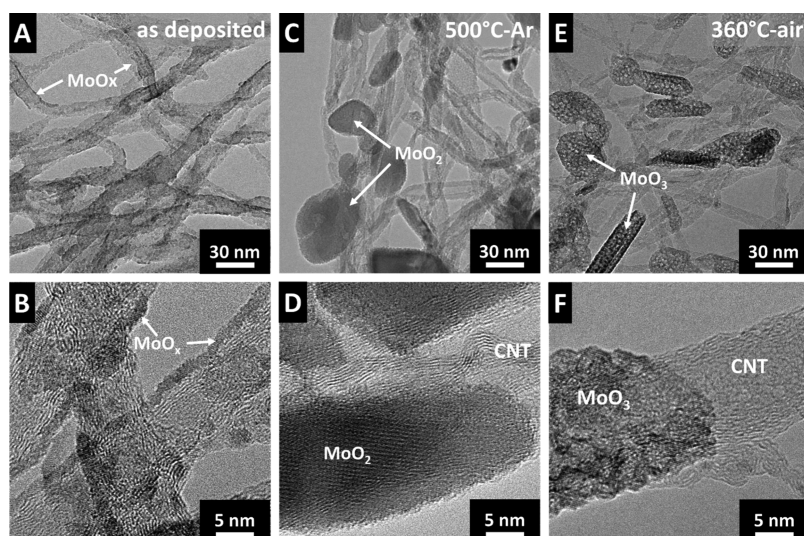


Figure 2. Transmission electron micrographs of the as-deposited MoO_x -CNT (A,B), MoO_2 -CNT after annealing at 500 °C in an argon atmosphere (C,D), and MoO_3 -CNT after annealing at 360 °C in a synthetic air atmosphere (E,F).

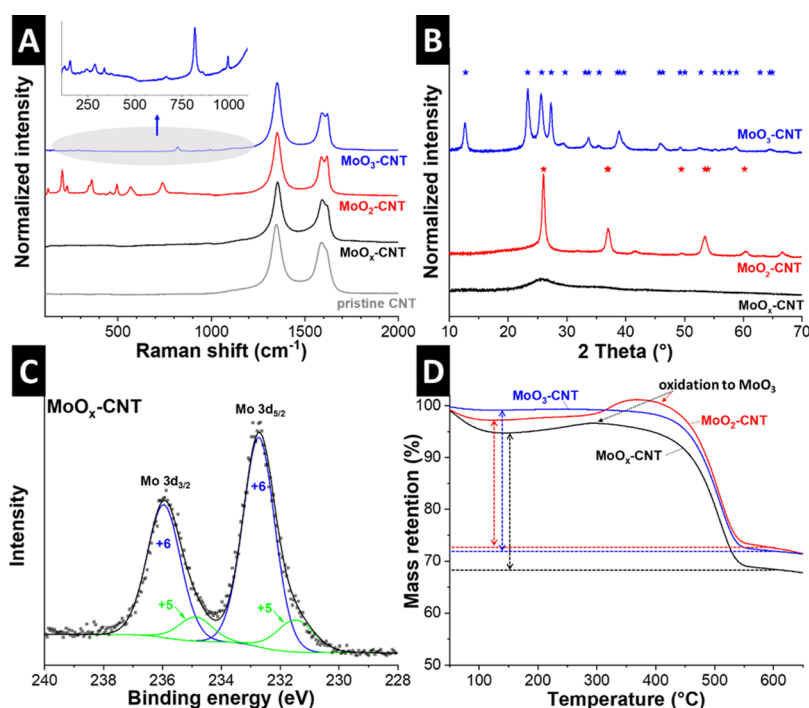


Figure 3. Raman spectra of all hybrid samples, with the inset magnifying 100–1000 cm^{-1} section of MoO_3 -CNT (A). X-ray diffractograms of all samples including ideal markers for ideal peak positions of MoO_2 and MoO_3 according to PDF 32-0671 and PDF 05-0508, respectively (B). High-resolution XPS measurement of the Mo 3d peak of the as-deposited MoO_x -CNT sample with Gaussian–Lorentzian fits (C) and thermogravimetric measurements of all hybrid samples (D).

frequencies at 100–1000 cm^{-1} , characteristic signals of molybdenum oxide are found, whereas the D- and G-modes of carbon are located at higher frequencies of 1350 and 1605 cm^{-1} , respectively. Sample MoO_x -CNT does not exhibit characteristic molybdenum oxide signals in the region below 1000 cm^{-1} , which can be explained by the extremely small domain sizes⁵⁰ below 2 nm, as seen in Figure 2B. Therefore, a determination of the oxidation state of the as-deposited molybdenum oxide is not possible via Raman spectroscopy. After thermal annealing, several distinct signals are detected in the range below 1000 cm^{-1} . For the sample annealed in argon, typical signals of MoO_2 are detected, with the largest peaks at

202 and 740 cm^{-1} .⁵¹ When analyzing the structure of incompletely oxidized samples, low laser powers are to be used to avoid oxidation of MoO_2 to MoO_3 during Raman measurement, which may lead to incorrect assignment of peak positions of the MoO_2 phase.⁵² The sample annealed in synthetic air shows the main characteristic MoO_3 signal at 820 cm^{-1} (Figure 3A),⁵³ confirming a successful transformation of the samples MoO_2 -CNT and MoO_3 -CNT into the desired phases. An analysis of the D- and G-modes yields information about the multiwalled CNT structure in the hybrid samples. The shape and position of the D-mode at around 1352 cm^{-1} is the same for pristine multiwalled CNT and all three hybrid

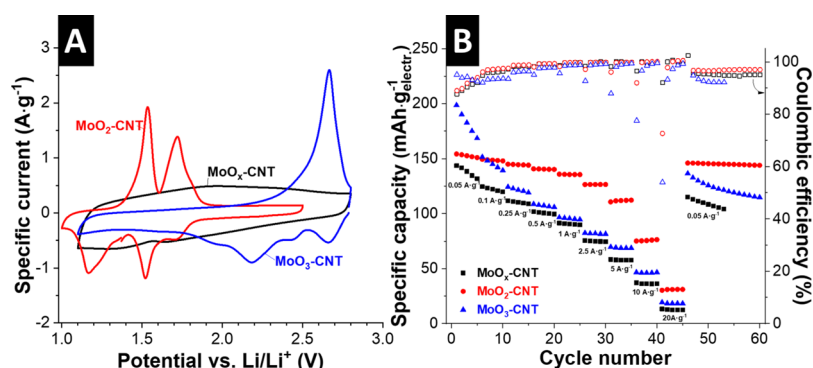


Figure 4. Cyclic voltammograms of all hybrid samples measured at $1 \text{ mV}\cdot\text{s}^{-1}$ (A) and specific delithiation capacity and Coulombic efficiency derived from galvanostatic cycling at specific currents between 0.05 and $20 \text{ A}\cdot\text{g}^{-1}$ (B).

samples, whereas the G-mode shows distinct differences. The D-mode originates from double-resonant Raman scattering, which is influenced by structural disorder, such as defects or heteroatoms in the graphitic structure.⁵⁴ Because all samples show similar D-modes, there are no differences expected concerning defect density. The G-mode is a first-order Raman signal and corresponds to in-plane stretching of the C–C bonds. In contrast to pure graphite, the G-band of single-walled CNTs is typically split into several features.⁵⁵ This peak splitting is observed to a small extent for the annealed hybrid samples because of the reduction of the amorphous carbon phase during annealing, reducing the background signal (A-mode) and sharpening the distinct G-bands. Deconvolution of the carbon signals is exemplified for $\text{MoO}_3\text{-CNT}$ in Supporting Information Figure S1A, and the decreasing amount of the amorphous carbon content after annealing is laid out in Figure S1B.

X-ray diffraction was carried out to identify the molybdenum oxide crystal structure (Figure 3B). The as-deposited $\text{MoO}_x\text{-CNT}$ hybrid samples showed only a broad signal at around $26^\circ 2\theta$, which is caused by amorphous carbon of the CNT substrate. No crystalline peaks indicative of molybdenum oxides are detected in this sample, confirming the findings from Raman spectroscopy of very small domain sizes. For the annealed samples, the expected molybdenum oxide phases are confirmed, according to Powder Diffraction File (PDF) #32–0671 and #05–0508 for MoO_2 and MoO_3 , respectively. The crystal structure of MoO_2 corresponds to the monoclinic $P2_1/n$ space group, whereas MoO_3 crystallizes as $\alpha\text{-MoO}_3$ in the orthorhombic $Pbnm$ symmetry. All peaks present in the diffractograms can be assigned to a single crystal phase, suggesting the absence of intermediate phases or multiphase fields after the transformation process during annealing.

The oxidation state of molybdenum after the ALD process can be assessed by XPS to determine the binding energy of molybdenum in the $\text{MoO}_x\text{-CNT}$ hybrid sample. The highly resolved measured spectrum of the Mo 3d doublet is given in Figure 3C. Peak fitting with a Gaussian–Lorentzian model revealed a predominant valence state of Mo^{6+} , with small fractions of Mo^{5+} ,⁵¹ indicating the presence of an amorphous molybdenum trioxide structure directly after ALD. The formation of predominantly hexavalent Mo is in line with other reports of atomic layer-deposited molybdenum oxide from the same precursors.⁵⁶

Thermogravimetric analysis was used to quantify the ratio of molybdenum oxide to carbon in the hybrid electrodes. The samples were heated to 650°C in synthetic air, leading to a

complete burn-off of the carbon (Figure 3D). To determine the mass of burnt carbon, all processes leading to a mass change during the experiment have to be considered: (1) Up to a temperature of 120°C , water adsorbed on the sample and crucible surface evaporates,⁵⁷ leading to a mass loss of up to 5%. (2) A mass gain starting around 300°C is correlated with the oxidation of all non-hexavalent Mo species to Mo^{6+} . This mass gain is small for $\text{MoO}_x\text{-CNT}$, more pronounced for $\text{MoO}_2\text{-CNT}$, and nonexistent for $\text{MoO}_3\text{-CNT}$ as it only contains Mo^{6+} . (3) Finally, carbon burn-off is causing a mass loss between temperatures of around $420\text{--}550^\circ\text{C}$. To back-calculate to the initial carbon content of the dry hybrid samples, the mass gained by oxidation must be subtracted from the final mass in the crucible, leading to carbon contents of 31, 30, and 27 mass % for samples $\text{MoO}_x\text{-CNT}$, $\text{MoO}_2\text{-CNT}$, and $\text{MoO}_3\text{-CNT}$, respectively. The slightly lower carbon content of $\text{MoO}_3\text{-CNT}$ samples can be explained by a partial carbon burn-off during the annealing procedure in a synthetic air atmosphere at 360°C .

3.2. Electrochemical Characterization. 3.2.1. Half-Cell Performance. Molybdenum oxide–CNT hybrid electrodes are electrochemically characterized in a half-cell setup against a lithium metal counter/reference electrode. Cyclic voltammograms recorded at a scan rate of $1 \text{ mV}\cdot\text{s}^{-1}$ are shown in Figure 4A to provide a qualitative overview of their lithium intercalation behavior. The as-deposited $\text{MoO}_x\text{-CNT}$ hybrid electrodes show no redox peaks in the potential range between 2.8 and 1.1 V versus Li/Li^+ but a rectangular current signal corresponding to a pseudocapacitive lithium intercalation mechanism, that is, an intercalation reaction that exhibits a capacitor-like voltage profile. This effect is often observed in nanoscopic layers or particles of faradaic material, where intercalation is effectively no longer limited by solid-state diffusion since all reactions take place at the surface or near-surface region.^{32,58} $\text{MoO}_2\text{-CNT}$ shows two strong lithiation peaks at around 1.5 and 1.2 V versus Li/Li^+ , corresponding to a two-step lithiation process, in accordance with literature.⁴³ The potential shifts between oxidation and reduction peaks indicate a diffusion-limited intercalation process, which can be correlated with increased diffusion paths due to coarsening of MoO_2 particles during annealing. $\text{MoO}_3\text{-CNT}$ exhibits a two-step lithiation process with peaks at 2.65 and 2.2 V versus Li/Li^+ , which aligns with previous reports in the literature.^{45,59} The delithiation process occurs in one step with a large peak located at 2.65 V versus Li/Li^+ .

Galvanostatic cycling was carried out to obtain quantitative information on the capacity and rate behavior of the hybrid

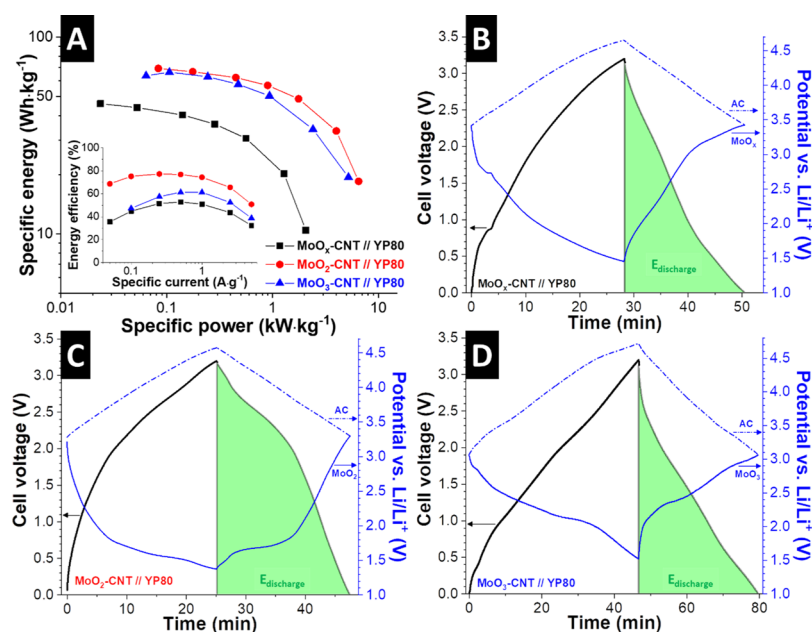


Figure 5. Ragone chart with specific energies and powers of LICs with hybrid material as the negative electrode and AC as the positive electrode (A) and voltage profile of LIC cells containing MoO_x -CNT (B), MoO_2 -CNT (C), and MoO_3 -CNT (D) as negative electrodes at a cycle rate of $0.1 \text{ A}\cdot\text{g}^{-1}$, including the potential development of the positive and negative electrodes measured against a lithium spectator electrode (blue lines).

electrodes (Figure 4B). It is noted that all values discussed are normalized to the full mass of the hybrid electrodes. The maximum specific capacity of MoO_x -CNT is around $145 \text{ mA}\cdot\text{h}\cdot\text{g}^{-1}$ at a rate of $0.05 \text{ A}\cdot\text{g}^{-1}$; however, a capacity decay to around $130 \text{ mA}\cdot\text{h}\cdot\text{g}^{-1}$ is observed during the first operation cycles, which further decreased to around $110 \text{ mA}\cdot\text{h}\cdot\text{g}^{-1}$ after 50 cycles. The MoO_2 -CNT electrodes exhibit a slightly higher maximum capacity of around $150 \text{ mA}\cdot\text{h}\cdot\text{g}^{-1}$; however, a far superior stability is observed with the capacity remaining at a constant value after over 60 cycles. This maximum specific capacity matches the maximum theoretic capacity of $210 \text{ mA}\cdot\text{h}\cdot\text{g}^{-1}$ of MoO_2 for one intercalated Li^+ per monoclinic MoO_2 ,⁴³ considering a CNT content of 30 mass % in the hybrid sample. MoO_3 -CNT electrodes exhibited the highest initial delithiation capacity of $200 \text{ mA}\cdot\text{h}\cdot\text{g}^{-1}$, but a strong decay over the first five cycles to $170 \text{ mA}\cdot\text{h}\cdot\text{g}^{-1}$ is observed and the performance stabilizes around $115 \text{ mA}\cdot\text{h}\cdot\text{g}^{-1}$ after 60 cycles. Capacity fading of hybrid electrodes containing large fractions of hexavalent Mo species has been described in previous publications and is caused by irreversible phase transitions during the first lithiation cycles.^{45,60} This behavior was less severe for amorphous MoO_x -CNT compared to MoO_3 -CNT, possibly because of the small domain sizes below 2 nm, but came at the cost of a reduced initial specific capacity. This reduced specific capacity of MoO_x -CNT is caused by the disordered molybdenum oxide phase, where a lower number of lithium ions can be reversibly stored. The rate handling behaviors of MoO_x -CNT and MoO_3 -CNT electrodes are comparable, with a retention of about $40 \text{ mA}\cdot\text{h}\cdot\text{g}^{-1}$ at a high rate of $10 \text{ A}\cdot\text{g}^{-1}$. In contrast, the MoO_2 -CNT hybrid samples show a superior rate handling, with almost a constant capacity up to a rate of $2.5 \text{ A}\cdot\text{g}^{-1}$. Only at ultrahigh rates of 10 and $20 \text{ A}\cdot\text{g}^{-1}$, the capacity drops rather significantly to around 75 and $30 \text{ mA}\cdot\text{h}\cdot\text{g}^{-1}$, respectively.

Rate handling is typically determined by two factors: (1) the electrical conductivity of the hybrid electrode and (2) the diffusion path length for lithium ions to their intercalation sites. In the presented case, it is obvious that diffusion had negligible

influence on the rate performance because the largest particles (MoO_2) showed the best rate handling, whereas nanoscopic MoO_x layers exhibited the poorest rate behavior. The reason for the improved rate handling is the metallic conductivity of MoO_2 , which is superior to insulating MoO_3 .^{61,62} In the case of atomic layer-deposited molybdenum oxide on CNTs, a post-deposition annealing process is favorable for the performance metrics for lithium intercalation in half-cells concerning longevity and rate behavior. Few-nanometer-thick coatings of amorphous MoO_x do not provide favorable kinetics compared to larger crystalline particles obtained by annealing.

3.2.2. LIC Full-Cell Performance. Full LIC cells were assembled by employing molybdenum oxide-CNT hybrid electrodes as a negative electrode and AC as a positive electrode. This concept employs two different charge storage mechanisms: lithium-ion intercalation at the negative electrode and physical ion electrosorption at the positive electrode. Because of the lower specific capacity of the positive electrode ($60 \text{ mA}\cdot\text{h}\cdot\text{g}^{-1}$ between 3 and 4.5 V versus Li/Li^+),⁶³ the mass of the positive electrode is increased by a factor of 2.5. In our LIC cells, a lithium spectator electrode monitors the potential development at both electrodes during operation. The specific energy and power of the LIC cells are shown in a Ragone chart (Figure 5A) and were determined by galvanostatic cycling at different rates and integrating the voltage profiles over discharge time. The highest specific energy is exhibited by the MoO_2 -CNT-containing LIC cell with about $70 \text{ W}\cdot\text{h}\cdot\text{kg}^{-1}$ at $83 \text{ W}\cdot\text{kg}^{-1}$, whereas the MoO_3 -CNT-containing cell showed $64 \text{ W}\cdot\text{h}\cdot\text{kg}^{-1}$ at $64 \text{ W}\cdot\text{kg}^{-1}$. The maximum energy of the MoO_x -CNT cell is $46 \text{ W}\cdot\text{h}\cdot\text{kg}^{-1}$ at $24 \text{ W}\cdot\text{kg}^{-1}$, being far below the performance of both other cells. Higher cycling rates show similar energy values for both MoO_2 -CNT and MoO_3 -CNT cells; however, MoO_2 -CNT cells exhibit a higher power at high rates. A specific energy of $34 \text{ W}\cdot\text{h}\cdot\text{kg}^{-1}$ is measured at a power of $2.4 \text{ kW}\cdot\text{kg}^{-1}$ for MoO_3 -CNT and at $4 \text{ kW}\cdot\text{kg}^{-1}$ for MoO_2 -CNT. For comparison, the MoO_x -CNT cell is far below these metrics with $20 \text{ W}\cdot\text{h}\cdot\text{kg}^{-1}$ at $1.3 \text{ kW}\cdot\text{kg}^{-1}$. The

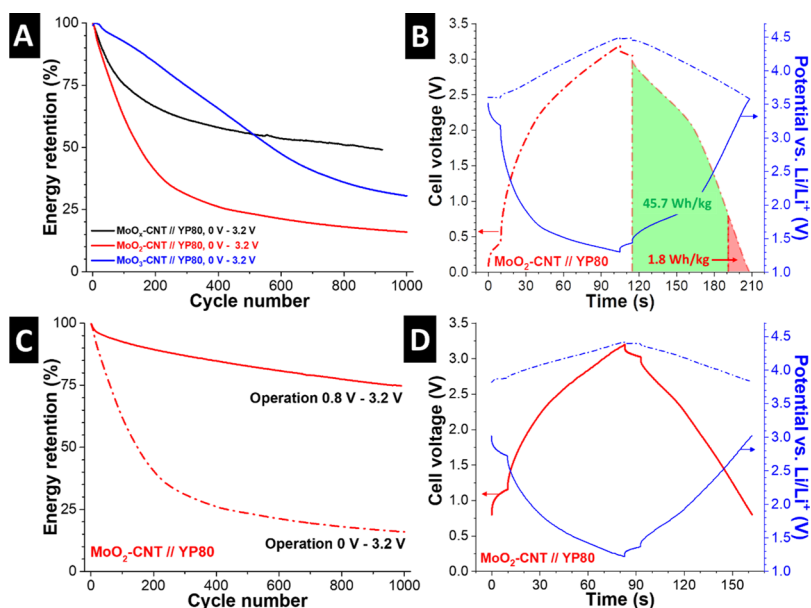


Figure 6. Cycling stability test of all LIC cells in an operation voltage between 0 and 3.2 V cell voltage at a rate of $1 \text{ A}\cdot\text{g}^{-1}$ (A). Corresponding voltage profile of the MoO_2 -CNT-containing cell, with marked areas comparing the discharge energy between 3.2 and 0.8 V cell voltage (green: $45.7 \text{ W}\cdot\text{h}\cdot\text{kg}^{-1}$) and the discharge energy between 0.8 and 0 V cell voltage (red: $1.8 \text{ W}\cdot\text{h}\cdot\text{kg}^{-1}$) (B). Cycling stability of MoO_2 -CNT-containing LIC in different operation voltages (C) and corresponding voltage profile operating between 3.2 and 0.8 V cell voltage (D).

energy efficiencies during cycling at various rates are shown in the inset of Figure 5A. MoO_x -CNT cells show the lowest energy efficiencies with 36% at the lowest rate and values around 50% for higher cycling rates. The MoO_3 -CNT cells exhibit energy efficiencies between 45 and 60%, and the MoO_2 -CNT cells show the highest values between roughly 70% at the lowest rate and 77% at elevated rates.

To analyze the differing performance metrics of the LIC cells, the potential development at both electrodes is separately monitored by a lithium spectator electrode during cycling. One typical cycle of LIC cells containing MoO_x -CNT, MoO_2 -CNT, and MoO_3 -CNT negative electrodes, respectively, is shown in Figure 5B–D. The energy consumed during charging and released during discharging is represented by the area under the cell voltage curve during the respective half-cycle. The cell voltage is equal to the potential difference between both electrodes, represented by the area between the blue curves. The potential development of the AC positive electrode is linear in all cases, as expected for the capacitive charge storage mechanism. However, the potential of the molybdenum oxide-CNT hybrid electrodes evolves differently with plateaus representing lithiation/delithiation reactions occurring at different potentials. MoO_x -CNT shows a discharge plateau region above 3 V versus Li/Li^+ , MoO_2 -CNT around 1.7 V versus Li/Li^+ , and MoO_3 -CNT around 2.3 V versus Li/Li^+ .

The lower the plateau potentials versus Li/Li^+ , the higher the cell voltage during the delithiation reaction, what leads to a larger area below the voltage curve (the green area in Figure 5B–D), explaining the different maximum specific energies of the LIC cells. Even though the maximum specific capacity of MoO_3 -CNT was superior to that of MoO_2 -CNT in the half-cell configuration, the specific energy of the MoO_2 -CNT LIC cell is higher because of the lower delithiation potential versus Li/Li^+ .

The energy efficiency of LICs is an important factor in cases where the cost of charging is a major point of concern, such as in electric vehicles. An energy efficiency far below 100% is not

uncommon, and it is caused by overpotentials during charging, based on lithiation reactions typically occurring at a higher cell voltage as the corresponding delithiation reactions.⁶⁴ This explains the differing efficiencies of the examined LIC cells. MoO_2 -CNT hybrid electrodes exhibiting a small overpotential of around 0.1 V during lithiation (Figure 5C) showed attractive energy efficiencies, whereas the slow kinetics of MoO_x -CNT make this material unsuitable for practical application.

Finally, the longevity of the LIC cells is tested by operation over 1000 charge/discharge cycles at a specific current of $1 \text{ A}\cdot\text{g}^{-1}$ (Figure 6A). A rapid decay of specific energy is observed for all LICs, especially for the MoO_2 -CNT cell, which deems them not practical for application under these operational settings. There are two reasons for the instable behavior, depending on the negative electrode materials. (1) MoO_x -CNT and MoO_3 -CNT show vastly different specific capacities depending on the cycling rate (i.e., they exhibit limited rate handling). When the cell is charge-balanced for low cycling currents, operation at high currents shifts the potentials of both electrodes and the negative electrode (that has a much lower specific capacity at high currents) operates in a largely increased potential window. Consequently, these cells need to be charge-balanced for only one distinct cycling current, leading to a decreased positive electrode mass for higher cycling currents. (2) MoO_2 -CNT, which shows an almost constant specific capacity over a wide current range, degrades most rapidly because of the instability of the material above a potential of 3 V versus Li/Li^+ . As can be seen from the voltage profile during operation at $1 \text{ A}/\text{g}$ in Figure 6B, the MoO_2 -CNT electrode reaches a potential of about 3.6 V versus Li/Li^+ when the LIC is fully discharged to a cell voltage of 0 V. This issue can be resolved by preventing a deep discharge of the LIC and adjusting the operation voltage to 0.8–3.2 V cell voltage. The specific energy of the cell remains almost unchanged, as geometrically emphasized in Figure 6B, where the specific energy is only reduced by $1.8 \text{ W}\cdot\text{h}\cdot\text{kg}^{-1}$ when integrating the discharge curve to 0.8 V instead of 0 V. Testing a LIC cell with

Table 1. Literature Overview of LICs or Asymmetric Supercapacitor Performance Metrics Using Metal Oxide–Carbon Hybrid Materials as Electrodes^a

negative electrode	positive electrode	electrolyte	specific energy (W·h·kg ⁻¹)	specific power (kW·kg ⁻¹)	energy efficiency (%)	refs
graphene/MoO ₃	graphene/MnO ₂	1 M Na ₂ SO ₄ aqueous	43(34.4)	0.28(0.224)	not reported	65
Nb ₂ O ₅ /C fiber	AC	1 M LiClO ₄ in EC/DMC	86	0.02	not reported	67
V ₂ O ₅ /CDC	CDC	1 M LiClO ₄ in ACN	51(45.9)	0.17(0.153)	60	66
AC	MnO ₂	1 M Na ₂ SO ₄ aqueous	51	0.10	not reported	68
MoO ₃ –CNT	AC	1 M LiClO ₄ in EC/DMC	66	0.10	47	this work
MoO ₂ –CNT	AC	1 M LiClO ₄ in EC/DMC	67	0.18	75	this work
MoO _x –CNT	AC	1 M LiClO ₄ in EC/DMC	44	0.05	45	this work

^aAbbreviations: activated carbon (AC), carbide-derived carbon (CDC), acetonitrile (ACN), ethylene carbonate (EC), dimethyl carbonate (DMC). The values in brackets are normalized to full electrode mass.

a MoO₂–CNT electrode for longevity in the adjusted voltage range, stable cycling behavior can be observed with an energy retention of about 75% after 1000 cycles (Figure 6C). The corresponding voltage profile reveals a potential limitation to about 3 V versus Li/Li⁺ for the negative electrode under these cycling conditions (Figure 6D), making them stable for long-term operation.

Our report is the first study on molybdenum oxide-based materials as negative electrodes in the LIC setup. Therefore, a comparison of performance metrics with literature values is limited to other metal oxide–carbon hybrid materials used as negative electrodes in LICs (Table 1). However, a comparison with MoO₃/graphene in an asymmetric aqueous supercapacitor⁶⁵ shows that the specific energy of LICs capitalizing on intercalation reactions is superior. With respect to LICs using optimized hybrid electrode architectures of carbon with V₂O₅⁶⁶ and Nb₂O₅,⁶⁷ our MoO₂–CNT model material already shows either a higher specific energy and power or a much higher specific power at a slightly reduced energy, respectively. On a broader note, literature comparison reveals that the energy efficiency of other LICs or asymmetric systems is rarely reported. However, when estimating the energy efficiency from the voltage profiles provided in the literature, values far below 50% can often be found, deeming the systems as impractical.⁶⁴ In this context, it is worth noting that the energy efficiency of our MoO₂–CNT LIC cell of 70–77% for a wide current range is standing out from most works on LICs. This is traced back to the small overpotential of the lithiation reaction in the MoO₂–CNT negative electrode material, which we identify as a crucial factor for the transfer of LIC systems to application.

On the basis of this first study using model materials, we believe that further tuning of the electrode architecture could elevate the performance of MoO₂-based hybrid materials as negative electrodes in LICs. For example, reducing MoO₂ particle coarsening during the annealing procedure could provide even shorter diffusion paths for lithium ions and further improve power and energy efficiency of the LIC device. This could be achieved by trapping MoO₂ domains in carbon mesopores, as we recently demonstrated for vanadium pentoxide hybrid materials.³² Increasing or decreasing the molybdenum oxide content in the hybrid materials can also elevate the maximum energy or improve the rate handling of the resulting LIC devices, respectively.

4. CONCLUSIONS

Molybdenum oxide–CNT hybrid materials were synthesized by ALD, and different crystal structures were obtained by post-deposition annealing. The crystal phases were identified by material characterization as amorphous, mostly hexavalent

molybdenum oxide, monoclinic MoO₂, and orthorhombic α -MoO₃ for samples MoO_x–CNT, MoO₂–CNT, and MoO₃–CNT, respectively. Electrochemical characterization in half-cells showed the highest initial capacity for MoO₃–CNT, yet rate handling and cycling stability of MoO₂–CNT were superior to those of the other hybrid samples. LICs were assembled by using the hybrid electrodes as negative electrodes and AC as positive electrodes. LICs containing MoO₂–CNT negative electrodes exhibited the highest specific energy and power with 70 W·h·kg⁻¹ at 83 W·kg⁻¹ and 34 W·h·kg⁻¹ at 4 kW·kg⁻¹. A spectator electrode was employed to monitor the potential development of each electrode during operation. It was concluded that the overpotential and kinetics of the lithiation reaction were the most important factors influencing the device level performance. Preventing deep discharge of the LIC cell was revealed as a strategy to ensure stable cyclability. The study provides, for the first time, a guideline for the use of molybdenum oxide as a negative LIC electrode. The importance of finely adjusting the electrode structure and operation settings to obtain attractive performance metrics is underlined.

■ ASSOCIATED CONTENT

Supporting Information

The Supporting Information is available free of charge on the ACS Publications website at DOI: 10.1021/acsami.8b03233.

Peak deconvolution of D-, G-, and A-modes from Raman measurements and comparison of amorphous carbon in each sample (PDF)

■ AUTHOR INFORMATION

Corresponding Author

*E-mail: volker.presser@leibniz-inm.de.

ORCID

Volker Presser: 0000-0003-2181-0590

Notes

The authors declare no competing financial interest.

■ ACKNOWLEDGMENTS

The work at INM was part of the Carbon Metal Oxide Nanohybrid project (CarMON) supported by the Leibniz Association (SAW-2017). V.P. acknowledges funding from the German Federal Ministry for Economic Affairs and Energy (BMWi) in support of the HyBaCap project (award number 03ET6113C). The authors thank Eduard Arzt for his continuing support and Ingrid Grobelsek and Valeria Lemkova (all INM) for technical support.

REFERENCES

- (1) Cox, P. M.; Betts, R. A.; Jones, C. D.; Spall, S. A.; Totterdell, I. J. *Nature* **2000**, *408*, 184.
- (2) Yang, Z.; Zhang, J.; Kintner-Meyer, M. C. W.; Lu, X.; Choi, D.; Lemmon, J. P.; Liu, J. *Chem. Rev.* **2011**, *111*, 3577–3613.
- (3) Dunn, B.; Kamath, H.; Tarascon, J.-M. *Science* **2011**, *334*, 928–935.
- (4) Simon, P.; Gogotsi, Y. *Nat. Mater.* **2008**, *7*, 845–854.
- (5) Shi, H. *Electrochim. Acta* **1996**, *41*, 1633–1639.
- (6) Qu, D.; Shi, H. *J. Power Sources* **1998**, *74*, 99–107.
- (7) Dash, R.; Chmiola, J.; Yushin, G.; Gogotsi, Y.; Laudisio, G.; Singer, J.; Fischer, J.; Kucheyev, S. *Carbon* **2006**, *44*, 2489–2497.
- (8) Presser, V.; Heon, M.; Gogotsi, Y. *Adv. Funct. Mater.* **2011**, *21*, 810–833.
- (9) Frackowiak, E.; Metenier, K.; Bertagna, V.; Beguin, F. *Appl. Phys. Lett.* **2000**, *77*, 2421–2423.
- (10) Pech, D.; Brunet, M.; Durou, H.; Huang, P.; Mochalin, V.; Gogotsi, Y.; Taberna, P.-L.; Simon, P. *Nat. Nanotechnol.* **2010**, *5*, 651–654.
- (11) Zeiger, M.; Jäckel, N.; Mochalin, V. N.; Presser, V. *J. Mater. Chem. A* **2016**, *4*, 3172–3196.
- (12) Béguin, F.; Presser, V.; Balducci, A.; Frackowiak, E. *Adv. Mater.* **2014**, *26*, 2219–2251.
- (13) Scrosati, B.; Garche, J. *J. Power Sources* **2010**, *195*, 2419–2430.
- (14) Sun, Y.; Hu, X.; Luo, W.; Huang, Y. *ACS Nano* **2011**, *5*, 7100–7107.
- (15) Yue, Y.; Liang, H. *Adv. Energy Mater.* **2017**, *7*, 1602545.
- (16) Zeiger, M.; Fleischmann, S.; Krüner, B.; Tolosa, A.; Bechtel, S.; Baltés, M.; Schreiber, A.; Moroni, R.; Vierrath, S.; Thiele, S.; Presser, V. *RSC Adv.* **2016**, *6*, 107163–107179.
- (17) Tolosa, A.; Fleischmann, S.; Grobelsek, I.; Quade, A.; Lim, E.; Presser, V. *ChemSusChem* **2018**, *11*, 159–170.
- (18) Wang, G.; Lu, C.; Zhang, X.; Wan, B.; Liu, H.; Xia, M.; Gou, H.; Xin, G.; Lian, J.; Zhang, Y. *Nano Energy* **2017**, *36*, 46–57.
- (19) Shpigel, N.; Levi, M. D.; Sigalov, S.; Girshevitz, O.; Aurbach, D.; Daikhin, L.; Pikma, P.; Marandi, M.; Jänes, A.; Lust, E.; Jäckel, N.; Presser, V. *Nat. Mater.* **2016**, *15*, 570–575.
- (20) Wu, Z.-S.; Zhou, G.; Yin, L.-C.; Ren, W.; Li, F.; Cheng, H.-M. *Nano Energy* **2012**, *1*, 107–131.
- (21) Dubal, D.P.; Ayyad, O.; Ruiz, V.; Gómez -Romero, P. *Chem. Soc. Rev.* **2015**, *44*, 1777–1790.
- (22) Zhi, M.; Xiang, C.; Li, J.; Li, M.; Wu, N. *Nanoscale* **2013**, *5*, 72–88.
- (23) Fleischmann, S.; Zeiger, M.; Jäckel, N.; Krüner, B.; Lemkova, V.; Widmaier, M.; Presser, V. *J. Mater. Chem. A* **2017**, *5*, 13039–13051.
- (24) Vilatela, J. J.; Eder, D. *ChemSusChem* **2012**, *5*, 456–478.
- (25) Boukhalifa, S.; Evanoff, K.; Yushin, G. *Energy Environ. Sci.* **2012**, *5*, 6872–6879.
- (26) Nethravathi, C.; Rajamathi, C. R.; Rajamathi, M.; Gautam, U. K.; Wang, X.; Golberg, D.; Bando, Y. *ACS Appl. Mater. Interfaces* **2013**, *5*, 2708–2714.
- (27) Srimuk, P.; Zeiger, M.; Jäckel, N.; Tolosa, A.; Krüner, B.; Fleischmann, S.; Grobelsek, I.; Aslan, M.; Shvartsev, B.; Suss, M. E.; Presser, V. *Electrochim. Acta* **2017**, *224*, 314–328.
- (28) Choudhury, S.; Zeiger, M.; Massuti-Ballester, P.; Fleischmann, S.; Formanek, P.; Borchardt, L.; Presser, V. *Sustainable Energy Fuels* **2017**, *1*, 84–94.
- (29) Lim, E.; Jo, C.; Kim, M. S.; Kim, M.-H.; Chun, J.; Kim, H.; Park, J.; Roh, K. C.; Kang, K.; Yoon, S. *Adv. Funct. Mater.* **2016**, *26*, 3711–3719.
- (30) Fleischmann, S.; Jäckel, N.; Zeiger, M.; Krüner, B.; Grobelsek, I.; Formanek, P.; Choudhury, S.; Weingarth, D.; Presser, V. *Chem. Mater.* **2016**, *28*, 2802–2813.
- (31) Daubert, J. S.; Wang, R.; Ovental, J. S.; Barton, H. F.; Rajagopalan, R.; Augustyn, V.; Parsons, G. N. *J. Mater. Chem. A* **2017**, *5*, 13086–13097.
- (32) Fleischmann, S.; Leistenschneider, D.; Lemkova, V.; Krüner, B.; Zeiger, M.; Borchardt, L.; Presser, V. *Chem. Mater.* **2017**, *29*, 8653–8662.
- (33) George, S. M. *Chem. Rev.* **2010**, *110*, 111–131.
- (34) Fleischmann, S.; Tolosa, A.; Zeiger, M.; Krüner, B.; Peter, N. J.; Grobelsek, I.; Quade, A.; Kruth, A.; Presser, V. *J. Mater. Chem. A* **2017**, *5*, 2792–2801.
- (35) Naoi, K.; Ishimoto, S.; Isobe, Y.; Aoyagi, S. *J. Power Sources* **2010**, *195*, 6250–6254.
- (36) Aricò, A. S.; Bruce, P.; Scrosati, B.; Tarascon, J.-M.; Van Schalkwijk, W. *Nat. Mater.* **2005**, *4*, 366–377.
- (37) Amatucci, G. G.; Badway, F.; Du Pasquier, A.; Zheng, T. *J. Electrochem. Soc.* **2001**, *148*, A930–A939.
- (38) Khomeiko, V.; Raymundo-Piñero, E.; Béguin, F. *J. Power Sources* **2006**, *153*, 183–190.
- (39) Lim, E.; Jo, C.; Lee, J. *Nanoscale* **2016**, *8*, 7827–7833.
- (40) Dahn, J.; McKinnon, W. *Solid State Ionics* **1987**, *23*, 1–7.
- (41) Chernova, N. A.; Roppolo, M.; Dillon, A. C.; Whittingham, M. S. *J. Mater. Chem.* **2009**, *19*, 2526–2552.
- (42) Bhaskar, A.; Deepa, M.; Narasinga Rao, T. *ACS Appl. Mater. Interfaces* **2013**, *5*, 2555–2566.
- (43) Kim, H.-S.; Cook, J. B.; Tolbert, S. H.; Dunn, B. *J. Electrochem. Soc.* **2015**, *162*, A5083–A5090.
- (44) Yu, S.-H.; Lee, S. H.; Lee, D. J.; Sung, Y.-E.; Hyeon, T. *Small* **2016**, *12*, 2146–2172.
- (45) Kim, H.-S.; Cook, J. B.; Lin, H.; Ko, J. S.; Tolbert, S. H.; Ozolins, V.; Dunn, B. *Nat. Mater.* **2016**, *16*, 454–460.
- (46) Yu, M.; Cheng, X.; Zeng, Y.; Wang, Z.; Tong, Y.; Lu, X.; Yang, S. *Angew. Chem., Int. Ed.* **2016**, *55*, 6762–6766.
- (47) Noh, J.; Chang-Min, Y.; Yun Ki, K.; Jyongsik, J. *Carbon* **2017**, *116*, 470–478.
- (48) Weingarth, D.; Zeiger, M.; Jäckel, N.; Aslan, M.; Feng, G.; Presser, V. *Adv. Energy Mater.* **2014**, *4*, 1400316.
- (49) Tan, S. T.; Sun, X. W.; Zhang, X. H.; Chua, S. J.; Chen, B.J.; Teo, C. C. *J. Appl. Phys.* **2006**, *100*, 033502.
- (50) Srimuk, P.; Ries, L.; Zeiger, M.; Fleischmann, S.; Jäckel, N.; Tolosa, A.; Krüner, B.; Aslan, M.; Presser, V. *RSC Adv.* **2016**, *6*, 106081–106089.
- (51) Spevack, P. A.; McIntyre, N. S. *J. Phys. Chem.* **1992**, *96*, 9029–9035.
- (52) Camacho-López, M.; Escobar-Alarcón, L.; Picquart, M.; Arroyo, R.; Córdoba, G.; Haro-Poniatowski, E. *Opt. Mater.* **2011**, *33*, 480–484.
- (53) Ou, J. Z.; Campbell, J. L.; Yao, D.; Wlodarski, W.; Kalantar-zadeh, K. *J. Phys. Chem. C* **2011**, *115*, 10757–10763.
- (54) Ferrari, A. C.; Robertson, J. *Phys. Rev. B: Condens. Matter Mater. Phys.* **2000**, *61*, 14095.
- (55) Dresselhaus, M. S.; Dresselhaus, G.; Saito, R.; Jorio, A. *Phys. Rep.* **2005**, *409*, 47–99.
- (56) Diskus, M.; Nilsen, O.; Fjellvåg, H. *J. Mater. Chem.* **2011**, *21*, 705–710.
- (57) Athouël, L.; Moser, F.; Dugas, R.; Crosnier, O.; Bélanger, D.; Brousse, T. *J. Phys. Chem. C* **2008**, *112*, 7270–7277.
- (58) Augustyn, V.; Simon, P.; Dunn, B. *Energy Environ. Sci.* **2014**, *7*, 1597–1614.
- (59) Li, W.; Cheng, F.; Tao, Z.; Chen, J. *J. Phys. Chem. B* **2006**, *110*, 119–124.
- (60) Tsumura, T.; Inagaki, M. *Solid State Ionics* **1997**, *104*, 183–189.
- (61) Rogers, D. B.; Shannon, R. D.; Sleight, A. W.; Gillson, J. L. *Inorg. Chem.* **1969**, *8*, 841–849.
- (62) Shi, Y.; Guo, B.; Corr, S. A.; Shi, Q.; Hu, Y.-S.; Heier, K. R.; Chen, L.; Seshadri, R.; Stucky, G. D. *Nano Lett.* **2009**, *9*, 4215–4220.
- (63) Lim, E.; Lim, W.-G.; Jo, C.; Chun, J.; Kim, M.-H.; Roh, K. C.; Lee, J. *J. Mater. Chem. A* **2017**, *5*, 20969–20977.
- (64) Eftekhari, A. *Sustainable Energy Fuels* **2017**, *1*, 2053–2060.
- (65) Chang, J.; Jin, M.; Yao, F.; Kim, T. H.; Le, V. T.; Yue, H.; Gunes, F.; Li, B.; Ghosh, A.; Xie, S. *Adv. Funct. Mater.* **2013**, *23*, 5074–5083.
- (66) Zeiger, M.; Ariyanto, T.; Krüner, B.; Peter, N. J.; Fleischmann, S.; Etzold, B. J. M.; Presser, V. *J. Mater. Chem. A* **2016**, *4*, 18899–18909.

(67) Tolosa, A.; Krüner, B.; Fleischmann, S.; Jäckel, N.; Zeiger, M.; Aslan, M.; Grobelsek, I.; Presser, V. *J. Mater. Chem. A* **2016**, *4*, 16003–16016.

(68) Fan, Z.; Yan, J.; Wei, T.; Zhi, L.; Ning, G.; Li, T.; Wei, F. *Adv. Funct. Mater.* **2011**, *21*, 2366–2375.

Supporting Information

Atomic layer deposited molybdenum oxide / carbon nanotube hybrid electrodes: Influence of crystal structure on lithium-ion capacitor performance

Simon Fleischmann,^{1,2} Marco Zeiger,^{1,2}

Antje Quade,³ Angela Kruth,³ and Volker Presser^{1,2,*}

¹ INM - Leibniz Institute for New Materials, 66123 Saarbrücken, Germany

² Department of Materials Science and Engineering, Saarland University, 66123 Saarbrücken, Germany

³ Leibniz Institute for Plasma Science and Technology, 17489 Greifswald, Germany

* Corresponding author's eMail: volker.presser@leibniz-inm.de

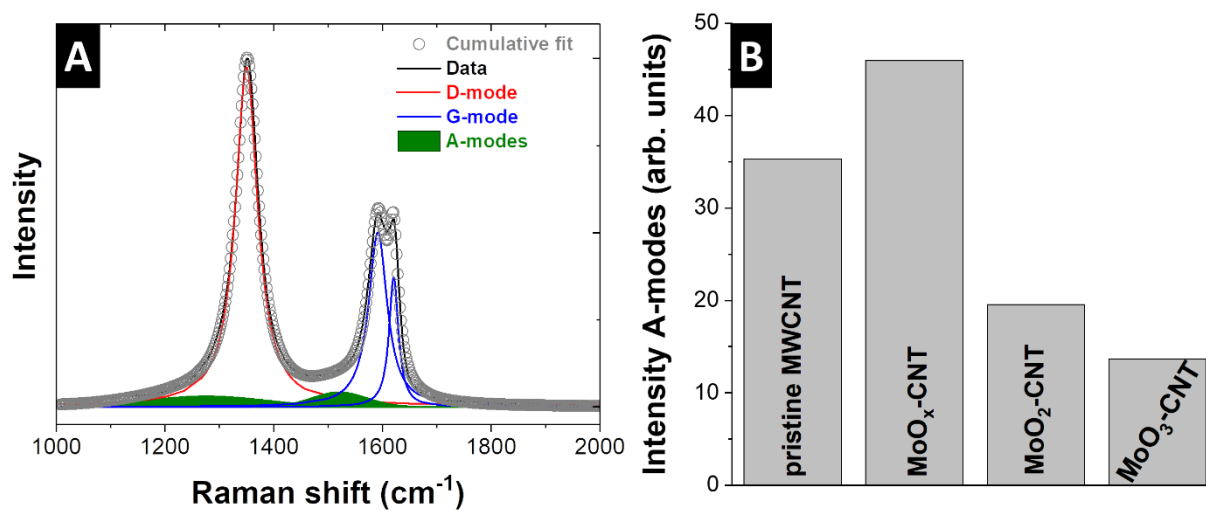


Figure S1: Peak deconvolution of hybrid electrode MoO₃-CNT into D-mode, G-mode, and A-modes representing amorphous carbon (A). Comparison of areal intensities of the amorphous carbon phases of all samples (B).

4.7 High voltage asymmetric hybrid supercapacitors using lithium- and sodium-containing ionic liquids

Simon Fleischmann,^{1,2} Mathias Widmaier,^{2,3} Anna Schreiber,¹ Hwirim Shim,^{1,2}
Frank M. Stiemke,⁴ Thomas J. S. Schubert,⁴ Volker Presser^{1,2}

¹ INM - Leibniz Institute for New Materials, 66123 Saarbrücken, Germany

² Department of Materials Science and Engineering, Saarland University, 66123 Saarbrücken, Germany

³ Robert Bosch GmbH, Robert-Bosch-Campus 1, 71272 Renningen, Germany

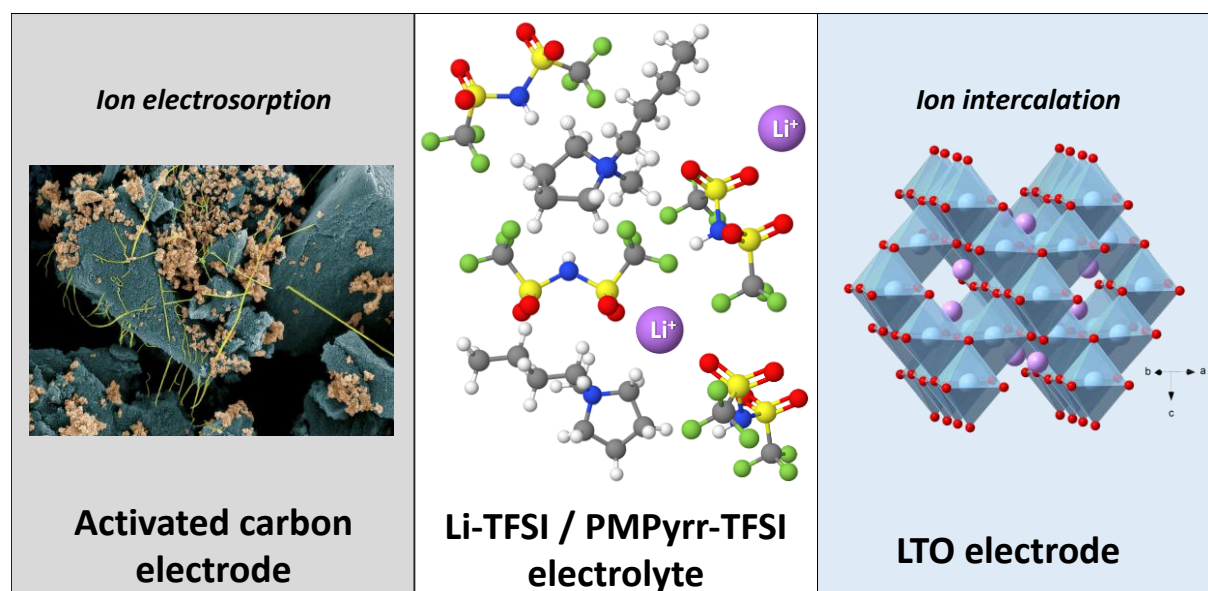
⁴ IOLITEC Ionic Liquids Technologies GmbH, 74076 Heilbronn, Germany

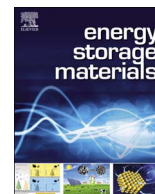
Citation:

S. Fleischmann, M. Widmaier, A. Schreiber, H. Shim, F. M. Stiemke, T. J. S. Schubert and V. Presser, *High voltage asymmetric hybrid supercapacitors using lithium- and sodium-containing ionic liquids*, *Energy Storage Mater.*, **2019**, 16, 391-399. (DOI: 10.1016/j.ensm.2018.06.011)

Own contribution:

Planning, formulation of ionic liquid electrolyte mixtures, X-ray diffraction measurements, electrochemical measurements, writing.





High voltage asymmetric hybrid supercapacitors using lithium- and sodium-containing ionic liquids



Simon Fleischmann^{a,b}, Mathias Widmaier^{b,c}, Anna Schreiber^a, Hwirim Shim^{a,b},
Frank M. Stiemke^d, Thomas J.S. Schubert^d, Volker Presser^{a,b,*}

^a INM - Leibniz Institute for New Materials, 66123 Saarbrücken, Germany

^b Department of Materials Science and Engineering, Saarland University, 66123 Saarbrücken, Germany

^c Robert Bosch GmbH, Robert-Bosch-Campus 1, 71272 Renningen, Germany

^d IOLITEC Ionic Liquids Technologies GmbH, 74076 Heilbronn, Germany

ARTICLE INFO

Keywords:

Asymmetric hybrid supercapacitor
lithium-ion capacitor
sodium-ion capacitor
lithium titanate
ionic liquid
battery-supercapacitor hybrid

ABSTRACT

Asymmetric hybrid supercapacitors (AHSCs) combine high specific energy and power by merging two electrodes with capacitive and Faradaic charge storage mechanisms. In this study, we introduce AHSC cells that use lithium titanate and activated carbon electrodes in an alkali-ion containing ionic liquid electrolyte. With this cell concept, it is possible to operate the activated carbon electrode in a higher potential window. Consequently, higher cell voltages and a reduced carbon electrode mass can be used, resulting in significantly increased energy compared to aqueous or organic electrolytes. We demonstrate the feasibility of this cell concept for both lithium- and sodium-ion intercalation, underlining the general validity of our approach. Our prototype cells already reach high specific energies of 100 Wh/kg, while maintaining a specific power of up to 2 kW/kg and cycling stability of over 1500 cycles. Owing to the IL electrolyte, stable cycling of an AHSC at 80 °C is demonstrated for the first time.

1. Introduction

Electrical double-layer capacitors (EDLCs) are electrochemical energy storage devices that store charge by electrosorption of ions at high surface area carbon electrodes [1]. Despite their high specific power and longevity, the widespread use of EDLCs is limited by the low specific energy, owing to the purely physical charge storage mechanism. Many efforts to increase the specific energy of supercapacitors have focused on novel materials and innovative cell design by introducing Faradaic charge transfer to the capacitive system [2]. These approaches include the decoration of high surface area carbons with thin layers of Faradaic material [3–5], the use of redox-active electrolytes [6–8], composite electrodes combining these two charge storage mechanisms [9–11], or the utilization of an asymmetric hybrid supercapacitor cell design [12,13].

Asymmetric hybrid supercapacitors (AHSCs) employ one electrode storing charge by Faradaic reactions and another by capacitive double-layer formation. The aim is to synergistically combine the merits of battery and supercapacitor technologies, to produce cells that show higher specific energy than supercapacitors and higher specific power and longevity than batteries [14]. The most common types use a Li-ion

intercalating negative electrode material and an activated carbon positive electrode [14]. More recent studies also investigated sodium intercalating negative electrode materials, creating so-called sodium-ion capacitors [15–17]. Most commonly, the negative electrode of AHSCs shows a relatively constant operation potential at which intercalation occurs, whereas the positive electrode shows a linear, capacitor-like potential development. Consequently, the maximum cell voltage is determined by the difference between the intercalation potential of the negative electrode and the anodic stability limit of the electrolyte at the positive electrode.

Using organic electrolytes like Li-ion containing acetonitrile or carbonate mixtures, the anodic limit at the positive electrode is mostly found at around 4 V vs. Li⁺/Li [18–20]. The most frequently chosen negative electrode material for AHSCs is graphite due to its low Li-ion intercalation potential of around 0.2 V vs. Li⁺/Li [18]. This low intercalation potential is beyond the stability boundary of most electrolytes and requires the formation of the so-called solid electrolyte interphase (SEI) for stable cell operation [21]. Since SEI formation consumes Li-ions from the electrolyte, a prelithiation of the graphite electrode is required in a conventional AHSC cell due to the absence of a Li-containing positive electrode [18,22]. Further, the SEI layer limits

* Corresponding author at: INM - Leibniz Institute for New Materials, 66123 Saarbrücken, Germany.
E-mail address: volker.presser@leibniz-inm.de (V. Presser).

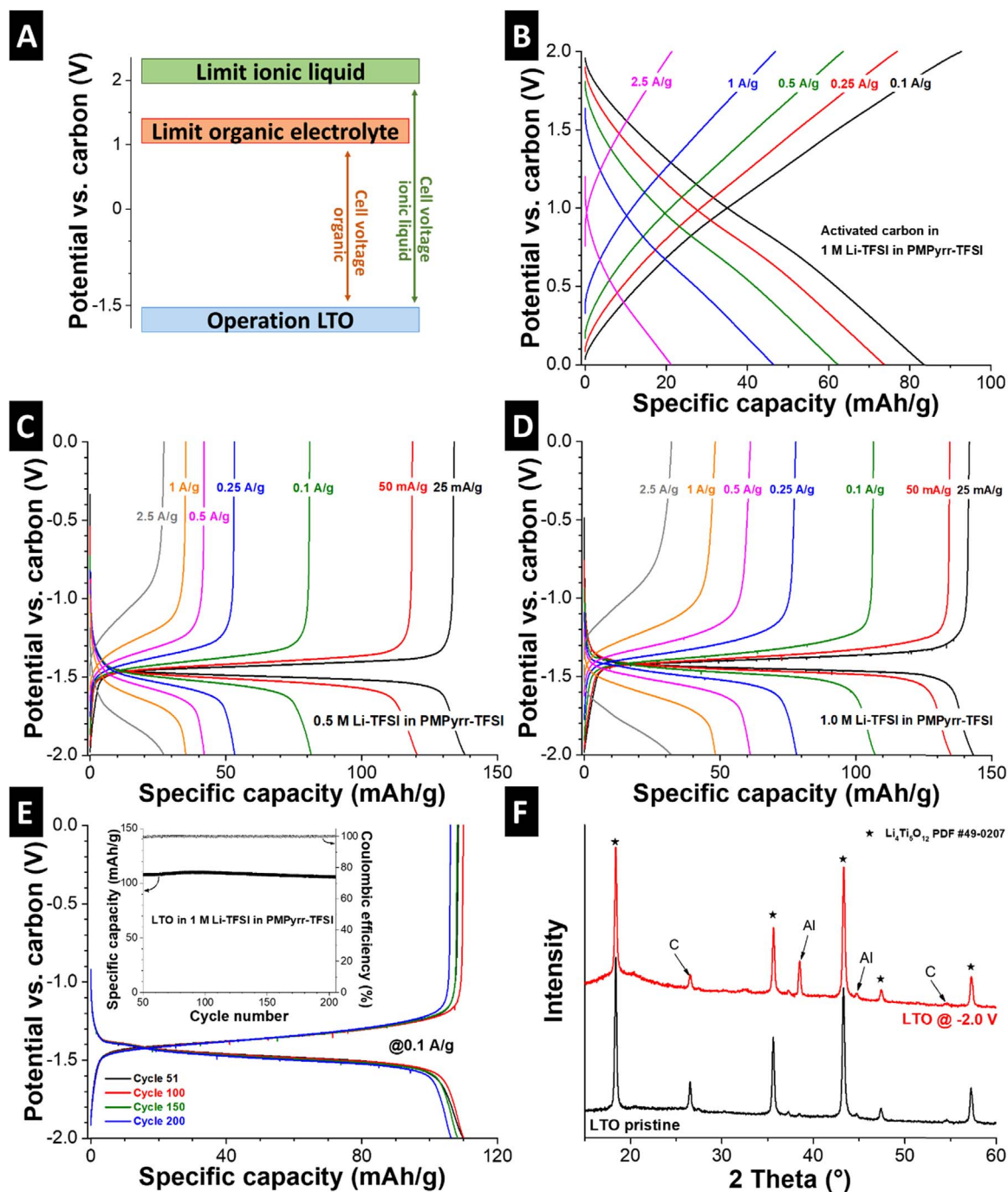


Fig. 1. Electrochemical and structural characterization of lithium half-cells. (A) Schematic representation of electrode potentials in an AHSC cell setup and the resulting maximum cell voltages depending on the electrolyte. Charge/discharge profiles of (B) activated carbon in 1 M Li-TFSI, (C) LTO in 0.5 M Li-TFSI, and (D) LTO in 1 M Li-TFSI electrolyte at different rates. (E) Charge/discharge profiles from the 51st to the 200th cycle of LTO in 1 M Li-TFSI at 0.1 A/g including specific capacity and Coulombic efficiency of every cycle in the inset. (F) X-ray diffractograms of pristine LTO electrode and ex situ measurement of fully lithiated LTO electrode in 1 M Li-TFSI electrolyte at -2.0 V vs. carbon. $\text{Li}_4\text{Ti}_5\text{O}_{12}/\text{Li}_7\text{Ti}_5\text{O}_{12}$ signals are indicated by a star (PDF 49–0207), graphite- and Al-peaks originate from the current collector.

the power performance of the cell and can lead to dendrite formation at low operating temperatures or high charging rates [23]. The use of a negative electrode with a higher intercalation potential, like spinel lithium titanate (LTO, $\text{Li}_4\text{Ti}_5\text{O}_{12}$), can effectively circumvent the necessity of SEI formation. Also, LTO is an attractive anode material for AHSCs because of its high rate capability, negligible volume change during intercalation and an intercalation potential of 1.55 V vs. Li/Li^+ [24–26]. However, these advantages come at the cost of a drastic reduction of AHSC cell voltage to about 2.5 V in organic electrolytes (Fig. 1A), thereby exhibiting much smaller specific energies as comparable AHSCs using graphite as negative electrodes [18,27].

A well-known strategy to increase the specific energy of EDLCs is the use of ionic liquids (IL) as an electrolyte, as they offer larger stable potential windows compared to organic electrolytes [1,14]. Furthermore, their non-flammability, low volatility, and broad liquid temperature range greatly enhance the safety of the respective devices [28,29], and allow for stable cycling at elevated temperatures up to 100 °C [28,30]. ILs have also been employed as battery electrolytes to capitalize on their distinct temperature and safety features. Therefore, they employ either an alkali metal electrode as ion-source [31] or a dissolved alkali salt [32–34].

In this study, we employ such an IL electrolyte with dissolved

alkali-ions for an AHSC with a negative intercalation electrode for the first time. By synergistically combining the distinct virtues of ILs, a significant advance to state-of-the-art AHSC technology is achieved: (1) The anodic stability at the positive electrode is expanded, thereby increasing the maximum accessible cell voltage and, in turn, the specific energy of the AHSC (Fig. 1A). (2) Higher operation temperatures are enabled, which is important to applications in the mobility sector where elevated temperatures are encountered. (3) The cell safety is improved because of the non-flammability and low vapor pressure of the ionic liquid. We explore this strategy for AHSCs, using a positive activated carbon electrode and a negative lithium titanate electrode. We demonstrate 4 V AHSC devices with high electrochemical cycling stability using both lithium- or sodium-containing ILs. These cells also function at an elevated temperature of 80 °C, which is the first report of the stable high-temperature operation of any AHSC device employing intercalation reactions. Our proof-of-concept study employs solely commercially available materials, underlining the possibility of straightforward application and large innovation potential of this cell concept by use of improved electrode materials or electrolyte mixtures.

2. Materials and methods

2.1. Electrode and electrolyte preparation

Activated carbon (type YP-80F, Kuraray) was admixed with 5 mass % polytetrafluoroethylene (60 mass% aqueous solution, Sigma Aldrich) and ethanol in a pestle and mortar until a dough-like paste is obtained. The mass was formed in a hot-rolling machine to $70 \pm 10 \mu\text{m}$ thick electrodes and dried in a vacuum oven overnight at 120 °C and 20 mbar. The material loading was $2.5 \pm 0.5 \text{ mg/cm}^2$. Additional information on the properties of the AC electrodes of type YP-80F is provided in Fig. S1.

For the preparation of LTO electrodes, lithium titanate (spinel $\text{Li}_4\text{Ti}_5\text{O}_{12}$, < 200 nm, Sigma Aldrich), carbon black (C-NERGY C65, Imerys Graphite & Carbon), and polyvinylidene fluoride (Solvay) were dissolved in dimethyl sulfoxide (Merck) with a mass ratio of 8:1:1 (dry mass) in a DAC400 FVZ speedmixer. Subsequently, the electrode slurry was doctor-bladed on a carbon-coated aluminum foil current collector (Ranafoil, Toyo Aluminium). The electrode sheets were dried for two days at ambient conditions in a fume hood, followed by drying in a vacuum oven at 120 °C and 20 mbar for 12 h. Dried electrodes typically possessed a thickness of $25 \pm 5 \mu\text{m}$ with a material loading of $3 \pm 1 \text{ mg/cm}^2$.

All electrolytes used are based on the ionic liquid 1-methyl-1-propylpyrrolidinium bis(trifluoromethylsulfonyl)imide (PMPyrr-TFSA, Iolitec, $\text{H}_2\text{O} < 10 \text{ ppm}$) which was dried with molecular sieves. For lithium-containing IL mixtures, lithium bis(trifluoromethylsulfonyl)imide (Li-TFSA, 99.9% purity, Iolitec) was used and for sodium-containing ILs, sodium bis(trifluoromethylsulfonyl)imide (Na-TFSA, 99.9% purity, Iolitec) was used. All reagents were transferred into an argon-filled glovebox (MBraun, $\text{O}_2/\text{H}_2\text{O} < 1 \text{ ppm}$) through a connected vacuum furnace, where they were dried at 120 °C and 20 mbar for 24 h. Properties of the electrolyte as given by the supplier are listed in Table S1.

2.2. Materials characterization

X-ray diffraction was carried out with a D8 Discover (Bruker AXS) with a copper X-ray source, a Göbel mirror, a 0.5 mm point focus, and a 2-dimensional VANTEC500 detector that was placed at 20°, 40°, and 60° 2θ for 17 min at each measurement step.

2.3. Electrochemical characterization

All electrochemical measurements were conducted in custom-build three-electrode cells with a polyether ether ketone body and titanium

pistons, more information on these cells is given in Ref. [35]. In half-cell measurements, 12 mm discs of AC or LTO were used as working electrodes and an at least 15-times mass-oversized activated carbon (type YP-80F, Kuraray, 5 mass% PTFE-bound) was used as a counter electrode. In full-cells, we used 12 mm discs of activated carbon and 10 mm discs of LTO. To achieve the exact mass ratio needed, small pieces of the 12 mm activated carbon electrodes were removed. As a quasi-reference electrode, activated carbon (type YP-50F, Kuraray, 5 mass% PTFE-bound) was used, which is highly reliable in ionic liquid electrolytes [36]. It was beneficial to use the same quasi-reference for all cells to provide easier comparability between lithium- and sodium-containing cells. The potential difference between the used YP-50F quasi-reference and metallic lithium is determined to 3.09 V. As current collector, we used 12 mm discs of carbon-coated aluminum foil (type EQ-CC-Al-18u-260, MTI Corporation) for all activated carbon electrodes and the separator was a 13 mm glass-fiber mat (GF/D, Whatman). After cell assembly, they were dried in a vacuum oven at 120 °C overnight and transferred to an argon filled glovebox (MBraun, $\text{O}_2/\text{H}_2\text{O} < 1 \text{ ppm}$), where they were filled with electrolyte.

Electrochemical measurements were carried out with a potentiostat/galvanostat (VMP-300, Bio-Logic) in a climate chamber at 25 °C or at 80 °C. Galvanostatic charge/discharge experiments were carried out at varying specific currents between 10 mA/g and 2.5 A/g, with 10 s resting after each half-cycle. The values are normalized to the active electrode mass, i.e., neglecting the PTFE binder in AC electrodes and neglecting carbon black and PVDF binder in LTO electrodes. AC half-cells with Li-TFSA electrolyte were first cycled at 0.1 A/g from 0 V to 1.2 V, 1.4 V, 1.6 V, 1.8 V, and 2.0 V vs. carbon, each step for 5 times, before being cycled between 0 V and 2.0 V vs. carbon at varying rates between 0.1 A/g and 2.5 A/g, 5 times for each rate. LTO half-cells with Li-TFSA electrolyte were cycled from 0 V to -2.0 V vs. carbon at rates of 25 mA/g to 2.5 A/g, each step for 5 times, before being cycled for 200 times in the same range at 0.1 A/g. LTO half-cells with Na-TFSA electrolyte were cycled from 0 V to -2.4 V vs. carbon at rates of 10 mA/g to 1 A/g, each step for 5 times, before being cycled for 200 times in the same range at 0.1 A/g.

The specific capacity C_{sp} in all half-cells was calculated according to Eq. (1):

$$C_{sp} = \frac{\int_{t_0}^t I dt}{m} \quad (1)$$

with current I , duration of the delithiation/desodiation/desorption step $t-t_0$, and m the active electrode mass as defined above.

Li-AHSC cells were assembled with an AC: $\text{Li}_4\text{Ti}_5\text{O}_{12}$ active mass ratio of 1.5:1. Galvanostatic cycling was carried out by charge/discharge at different rates between 10 mA/g to 1 A/g between 1 V and 4 V. Each charging/discharging step was repeated 5 times, with 10 s resting after each half-cycle. Na-AHSC cells employed an active mass ratio AC: $\text{Li}_4\text{Ti}_5\text{O}_{12}$ of 1.2:1 and were cycled at the same rates as Li-AHSCs. Cycling stability was tested by galvanostatic cycling at 0.1 A/g for Na-AHSC cells and at 0.2 A/g for Li-AHSC cells, since they initially exhibited about the same specific energy at these rates. All normalizations are calculated with respect to the sum of active masses of both electrodes, i.e., of activated carbon and $\text{Li}_4\text{Ti}_5\text{O}_{12}$ masses, excluding PTFE, PVDF and carbon black in the LTO electrode. The specific energy E_{sp} of the cells was calculated by numeric integration according to Eq. (2):

$$E_{sp} = \frac{I \int_{t_0}^t U(t) dt}{M} \quad (2)$$

where I is the current, $U(t)$ the voltage profile during the discharge step, $t-t_0$ the discharge time and M the sum of active masses of both electrodes. The specific power was calculated by dividing E_{sp} by the discharge time, the energy efficiency by dividing E_{sp} by the energy spent in the charging step, and the Coulombic efficiency by dividing the charge delivered in the discharge step by the charge spent in the charging step.

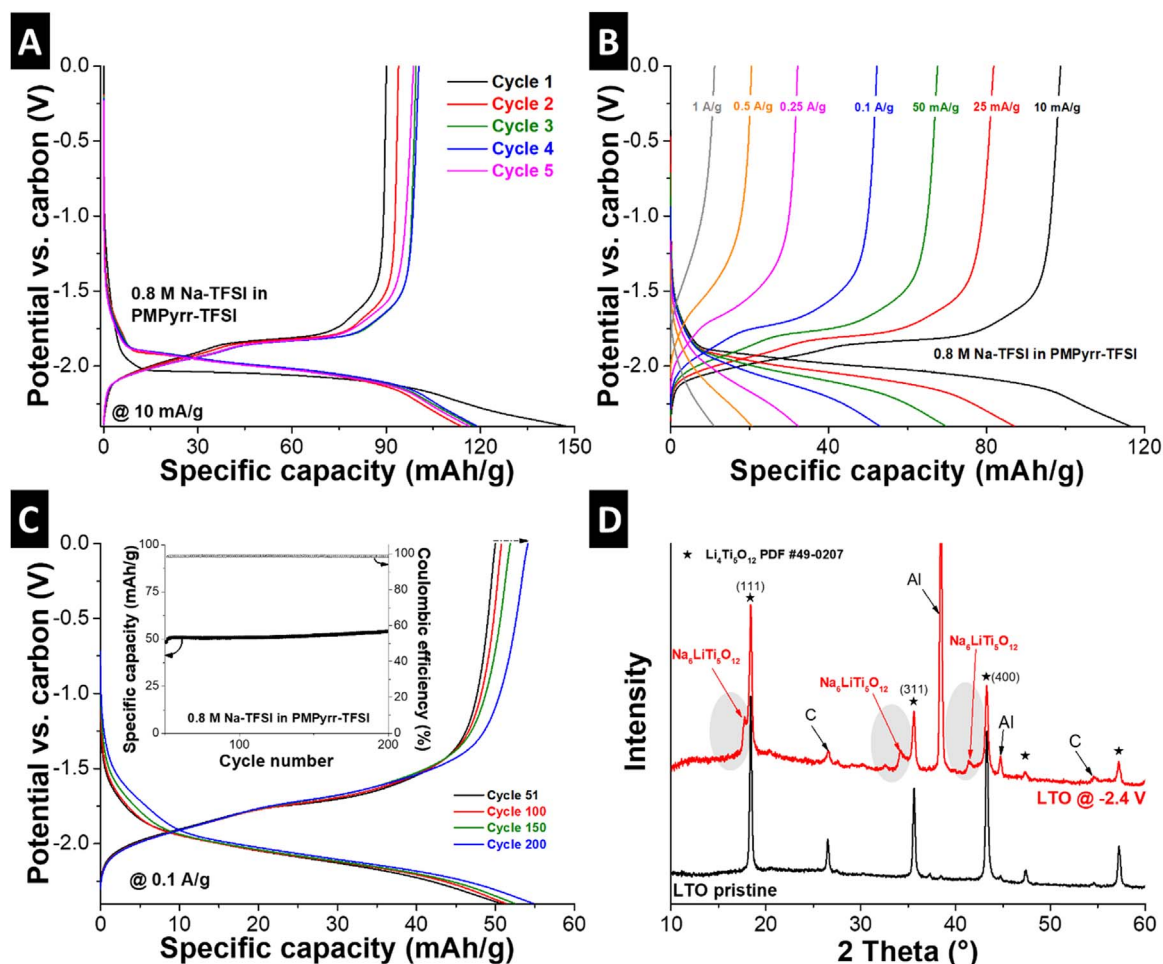


Fig. 2. Electrochemical and structural characterization of sodium half-cells. Charge/discharge profiles of LTO in 0.8 M Na-TFSI in PMPyrr-TFSI electrolyte (A) for the first five cycles at 10 mA/g, (B) at different rates and (C) from the 51th to 200th cycle at 0.1 A/g, including specific capacity and Coulombic efficiency of every cycle in the inset. (D) X-ray diffractograms of pristine LTO electrode and ex situ measurement of the fully sodiated LTO electrode in 0.8 M Na-TFSI electrolyte at -2.4 V vs. carbon. $\text{Li}_4\text{Ti}_5\text{O}_{12}$ / $\text{Li}_7\text{Ti}_5\text{O}_{12}$ signals are indicated by a star (PDF 49–0207), the $\text{Na}_6\text{LiTi}_5\text{O}_{12}$ phase developed as a shoulder towards lower 2θ is highlighted; graphite- and Al-signals labeled accordingly originate from the current collector.

3. Results and discussion

3.1. Lithium half-cells

Lithium-containing electrolytes were prepared by dissolving lithium bis(trifluoromethylsulfonyl)imide (Li-TFSI) in 1-methyl-1-propylpyrrolidinium bis(trifluoromethylsulfonyl)imide (PMPyrr-TFSI) to obtain 0.5 M and 1 M solutions. The anodic stability limits of the lithium-containing electrolytes with activated carbon electrodes (AC) were evaluated in a half-cell setup. The 1 M IL mixture still showed 90% Coulombic efficiency at 2.0 V vs. carbon (equal to 5.09 V vs. Li^+/Li), which enables stable cycling for EDLCs [37,38]. The potential profiles of AC in 1 M Li-TFSI electrolyte show a linear, capacitor-like behavior between 0 V and 2.0 V vs. carbon, with a capacity of around 80 mAh/g at 0.1 A/g (Fig. 1B). Further details of AC performance can be found in Supplemental Information (Fig. S2 and Fig. S3).

LTO electrodes were employed and the lithium intercalation behavior was evaluated as a function of the Li-TFSI concentration. In 0.5 M Li-TFSI electrolyte, a maximum specific capacity of 138 mAh/g is measured at a rate of 25 mA/g and 81 mAh/g at 0.1 A/g (Fig. 1C). In 1 M Li-TFSI electrolyte, a similar maximum capacity of 143 mAh/g is exhibited, while the rate handling with 108 mAh/g at 0.1 A/g is far superior compared to 0.5 M Li-TFSI electrolyte (Fig. 1D, Fig. S4A). The hysteresis between lithiation and delithiation reactions is extremely narrow and remains below 100 mV at a rate of 25 mA/g. A narrow hysteresis is important to achieve high energy efficiency on an AHSC

device level [39,40]. Both electrolyte mixtures show a maximum capacity that is similar to comparable literature [41] and close to the theoretical capacity of LTO (175 mAh/g for fully lithiated $\text{Li}_7\text{Ti}_5\text{O}_{12}$) [42] with a high Coulombic efficiency of 99.0% at 25 mA/g, suggesting high compatibility of the IL electrolytes with LTO. The superior rate handling of 1 M Li-TFSI electrolyte implies that the Li-ion conductivity in the 1 M mixture is higher compared to 0.5 M. Higher Li-TFSI concentration increases the viscosity of the electrolyte mixture, leading to lower overall ion mobility. However, Li-ion mobility has a much greater impact on the rate performance of the LTO electrode. Further optimization work for the electrolyte formulation to achieve a perfect balance between general conductivity and Li-ion mobility, possibly with other ILs or mixtures thereof, should be conducted in the future. The cycling stability of LTO electrodes in 1 M Li-TFSI electrolyte was tested by galvanostatic cycling at 0.1 A/g (Fig. 1E). The shape of the voltage profiles remains unchanged, and the specific capacity only shows a minor fading from initially 108 mAh/g to 106 mAh/g after 200 cycles. The Coulombic efficiency remains at 99.8%, underlining high stability of the system in 1 M Li-TFSI electrolyte.

To study the intercalation mechanism of lithium ions from the IL electrolyte, XRD measurements were conducted to compare a fully charged with a pristine LTO electrode (Fig. 1F). A comparison of both diffractograms reveals signals at identical positions, where spinel $\text{Li}_4\text{Ti}_5\text{O}_{12}$ can be identified according to PDF 49–0207. LTO is known as a so-called zero-strain material, and the transformation from $\text{Li}_4\text{Ti}_5\text{O}_{12}$ to $\text{Li}_7\text{Ti}_5\text{O}_{12}$ during lithiation occurs with only 0.2% volume

change [42]. Our XRD data with unchanged LTO peak positions and the straight voltage profile suggest that the lithiation mechanism does not change in Li-ion containing IL as compared to the conventional organic electrolytes. Undesired co-intercalation of IL cations into the LTO crystal structure is therefore unlikely.

3.2. Sodium half-cells

An emerging alternative to lithium-ion technology is the use of sodium-ion intercalating materials [43]. This motivated us to expand our AHSC cell concept to sodium-containing IL by replacing Li-TFSI with sodium bis(trifluoromethylsulfonyl)imide (Na-TFSI). We use a 0.8 M solution of Na-TFSI in PMPyrr-TFSI, which we determined to be the maximum soluble Na-TFSI concentration in the IL at ambient conditions. LTO has been employed as anode material in sodium-ion batteries with organic carbonate electrolytes and showed a sodiation potential of around 0.9 V vs. Na⁺/Na [44–46]. This relatively high sodiation potential might circumvent SEI formation compared to other typical sodium-ion anode materials like hard carbon [47]. So far, sodium-ion intercalation in LTO from an IL electrolyte has not been reported. Using a 0.8 M Na-TFSI electrolyte, we observed an initial intercalation potential of around –2.0 V vs. carbon at a rate of 10 mA/g with a maximum specific capacity of 100 mAh/g, showing a relatively flat plateau and a first cycle Coulombic efficiency of 61.2% (Fig. 2A, Fig. S4B).

Sodium-ion intercalation in Li₄Ti₅O₁₂ from organic electrolytes is expected to follow a three-phase mechanism with the formation of a lithium-rich phase Li₇Ti₅O₁₂ and a sodium-rich phase Na₆LiTi₅O₁₂ during sodiation [44]. Low efficiency in the first cycle is known from organic electrolytes and was linked to structural rearrangements of the LTO crystal structure [46,48]. Over the next cycles, the onset of sodiation slightly shifts to a more positive potential of –1.85 V vs. carbon and the specific capacity increases, indicating that initial conditioning facilitates further sodiation reactions (Fig. 2A) [46]. The increased sodiation potential of the second cycle and subsequent cycles indicates the absence of SEI formation since the charge transfer resistance of the SEI would have shifted the sodiation towards more negative potentials. Rate handling tests at increased currents showed a capacity of 53 mA h/g at 0.1 A/g with a Coulombic efficiency of 98.5% (Fig. 2B). LTO showed stable cycling performance in the sodium-containing IL, exhibiting a slightly increased capacity of 54 mA h/g after 200 cycles at 0.1 A/g with a Coulombic efficiency over 98% (Fig. 2C).

We used XRD to examine the intercalation mechanism of sodium from IL electrolyte into LTO (Fig. 2D). The diffractogram of sodiated LTO confirms the formation of the sodium-rich Na₆LiTi₅O₁₂ phase by broad reflections located at slightly lower 2θ than the Li₄Ti₅O₁₂/Li₇Ti₅O₁₂ signals. These shoulders are visible below the (111), (311), and (400) reflections at around 18.4°, 35.6°, and 43.2° 2θ, respectively. At the same time, the main reflections of the Li₄Ti₅O₁₂/Li₇Ti₅O₁₂ phase are observed, confirming the presence of at least two separate phases in the sodiated state. This behavior aligns with sodium-ion intercalation in LTO in organic electrolytes [44,45] and shows that sodiation occurs according to the same mechanism for IL electrolyte.

3.3. AHSC full-cells

AHSC full-cells were assembled with LTO as a negative electrode and activated carbon as a positive electrode. For AHSCs employing lithium intercalation (Li-AHSC), we chose 1 M Li-TFSI in PMPyrr-TFSI electrolyte, sodium-AHSCs (Na-AHSC) used 0.8 M Na-TFSI in PMPyrr-TFSI electrolyte. The voltage profile of a Li-AHSC cell cycled between 1.0 V and 4.0 V at 50 mA/g is shown in Fig. 3A. The cell exhibits very small overpotential of the lithiation reaction and efficient utilization of the charge distributed to the two electrodes, resulting in the high energy efficiency of 74%. This performance demonstrates that the

promising electrochemical properties measured in half-cells can successfully be transferred to a Li-AHSC full cell employing IL electrolyte (further characterization in Supplemental Information, Fig. S6).

In Fig. 3B, the voltage profile of a Na-AHSC cell cycled between 1.0 V and 4.0 V cell voltage range at 25 mA/g is provided, also showing a symmetric profile with high energy efficiency of 75%. In case of the Na-AHSC cell, special consideration has to be paid to the structural rearrangements in LTO during the first cycles (Fig. S6B). The irreversible charge consumed during this process at the negative electrode must be balanced at the positive activated carbon electrode. Therefore, in the following cycles, the maximum accessible potential window of 2 V vs. carbon is not fully used.

We tested the galvanostatic cycling stability of Li-AHSCs between 1.0 V and 4.0 V cell voltage at a rate of 0.2 A/g (Fig. 3C). During the first cycles, a slight drop from about 36 Wh/kg to 32.5 Wh/kg is observed, before a continuing recovery over the next about 800 cycles back to 36 Wh/kg is exhibited. The fluctuations during the first cycles are associated with common side-reactions, which originate from impurities of electrode materials or IL electrolyte, leading to shifting operation potentials of the electrodes relative to each other. The Li-AHSC cell provides performance stability over 1,500 cycles, with only minor fading to 32.9 Wh/kg (91% retention). Cycling stability of the Na-AHSC cell (Fig. 3C) showed a significant increase in specific energy from about 35 Wh/kg to 44 Wh/kg during the first 50 cycles. Similar to half-cells, we expect the initial rearrangements inside the LTO particles during the three-phase intercalation reaction being the main cause for the increased capacity [46]. During subsequent cycles, the specific energy of Na-AHSC cells slowly decreases to about 24 Wh/kg after 1,500 cycles, corresponding to a retention of 69% of the initial energy. The lower stability compared to Li-AHSCs can be related to the increased mechanical stresses during sodiation and desodiation, owing to the high ionic radius of sodium ions (1.06 Å) [49]. Considering the use of commercially available LTO particles as an electrode material, the observed stability of our novel cell concept is very promising. By use of further optimized electrode materials, for example, by use of nanohybrid electrode materials [4,50], we expect a further improved stability.

The performance metrics of the AHSC cells are shown in a Ragone plot comparing specific energy and specific power (Fig. 3D), with the corresponding energy efficiency and Coulombic efficiency given in Fig. 3E. The specific energy of the Li-AHSC cell ranges from 98 Wh/kg to 10 Wh/kg at specific powers between 23 W/kg and 1.93 kW/kg. The Na-AHSC cell shows comparable results with a specific energy between 90 Wh/kg and 5.4 Wh/kg at a specific power of 26 W/kg and 1.78 kW/kg. The corresponding energy efficiencies reach 78% with the most efficient operation of both devices at a current between 50 mA/g and 0.25 A/g, where Coulombic efficiencies are nearly 100%, demonstrating high reversibility. Comparison with the state-of-the-art literature on AHSCs using AC as a positive electrode and a titanate-based negative electrode with organic electrolytes, it is confirmed that our cell concept significantly increases the energy of devices using both lithium- or sodium-intercalation (Fig. 3D, Table 1) [17,19,51,52]. We also provide a comparison using our Li-AHSC cell with 1 M LiClO₄ in acetonitrile electrolyte (Fig. 3D, Fig. S7, Table 1). The specific energy can be increased by more than a factor of three by use of IL electrolytes compared to the same electrodes in an organic electrolyte. However, the rather large viscosity of IL electrolytes at room temperature limits the resulting power performance. A cell employing acetonitrile at room temperature can deliver higher power.

3.4. High-temperature operation

IL electrolytes offer high safety because of their non-flammability and enable operation at elevated temperatures [53]. We demonstrate that these features can be transferred to our IL AHSC cell concept. Therefore, Li-AHSC cells are evaluated at a temperature of 80 °C. The

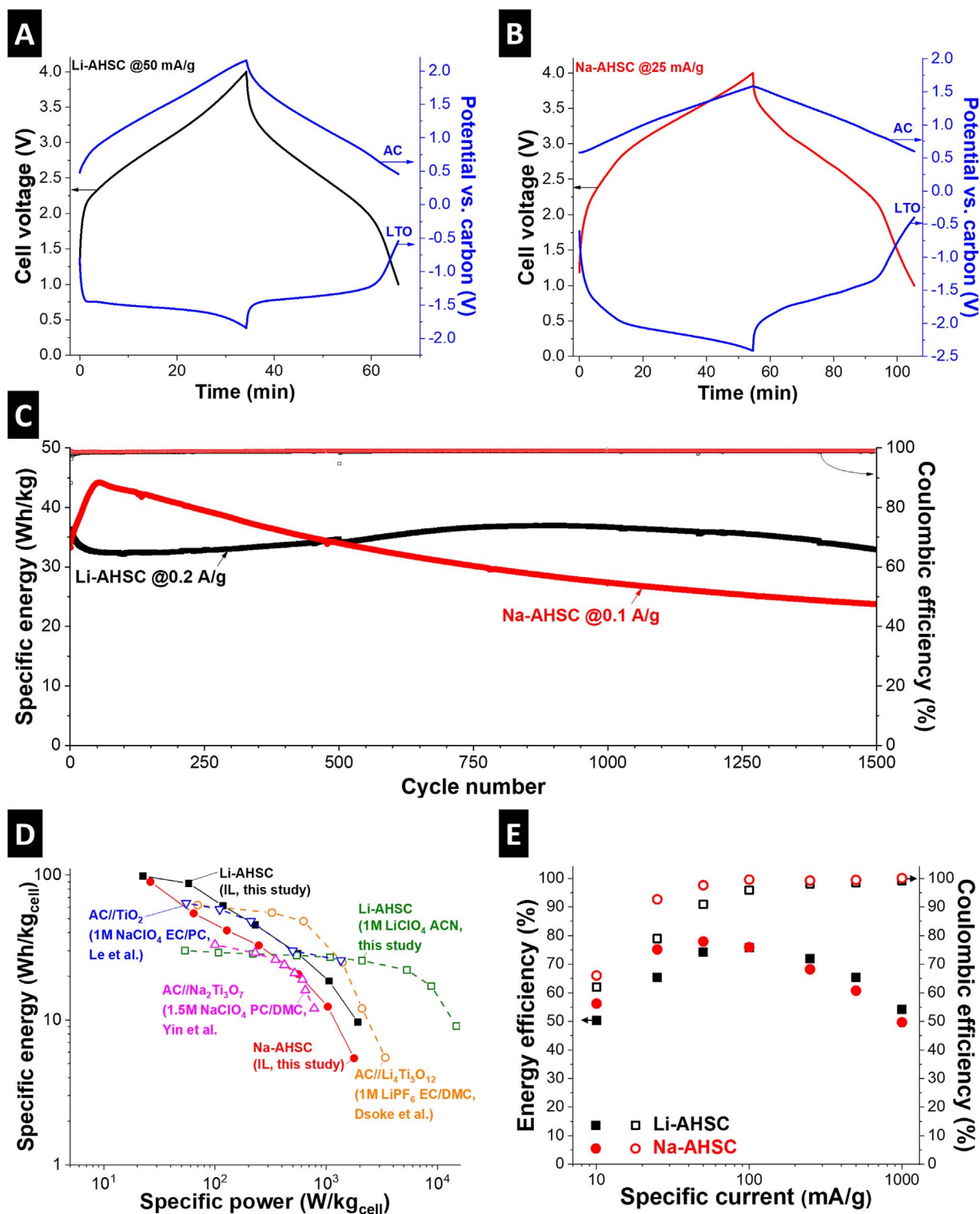


Fig. 3. Electrochemical characterization of AHSC full-cells. Voltage profiles of (A) Li-AHSC cell cycled at 50 mA/g and (B) Na-AHSC cell cycled at 25 mA/g, including potential development at negative LTO electrode and positive AC electrode monitored via quasi-reference spectator electrode. (C) Cycling stability of Li-AHSC cell cycled at 0.2 A/g, and Na-AHSC cell cycled at 0.1 A/g over 1500 cycles between 1 V and 4 V cell voltage. (D) Ragone chart of Li-AHSC and Na-AHSC cells cycled at rates between 10 mA/g and 1 A/g between 1 V and 4 V cell voltage with a comparison to literature (Refs [17,19,51].) and Li-AHSC cell with the same electrode materials filled with 1 M LiClO₄ in acetonitrile (ACN) electrolyte. (E) Energy efficiency and Coulombic efficiency of Li-AHSC and Na-AHSC cells.

power of the cells is highly increased because of the enhanced mobility of ions in the electrolyte. The voltage profile of a Li-AHSC cell cycled at 2.5 A/g is shown in Fig. 4A. With a limitation of the maximum cell voltage to 3.2 V, the positive electrode showed stable, linear potential development between 0 V and 1.2 V vs. carbon. At the same time, the

negative LTO electrode showed relatively constant lithiation plateaus around -1.4 V vs. carbon. The latter value is 50 mV above the onset of lithiation at 25 °C, indicating a reduced barrier for intercalation at 80 °C (in agreement with Nernst equation). At this rate and temperature, the specific energy reached 37.5 Wh/kg at a high specific power of

Table 1

Comparison of AHSC cell performance with IL electrolytes and organic electrolytes, including comparable literature employing titanate-based anodes for lithium- or sodium-intercalation.

Negative electrode	Positive electrode	Electrolyte	Specific energy (Wh kg ⁻¹)	Specific power (kW kg ⁻¹)	Maximum cell voltage (V)	References
Li ₄ Ti ₅ O ₁₂	AC	1 M Li-TFSI in PMPyrr-TFSI	98	1.9	4.0	This work
Li ₄ Ti ₅ O ₁₂	AC	0.8 M Na-TFSI in PMPyrr-TFSI	90	1.8	4.0	This work
Li ₄ Ti ₅ O ₁₂	AC	1 M LiClO ₄ in ACN	30	14.8	2.5	This work
Li ₄ Ti ₅ O ₁₂	AC	1 M LiPF ₆ in EC/DMC	62	3.4	2.8	[19]
Li ₄ Ti ₅ O ₁₂	AC	1.5 M NaClO ₄ in PC/DMC	33	0.78	3.0	[17]
Li ₄ Ti ₅ O ₁₂	AC	1 M NaClO ₄ in EC/PC	64	1.36	3.8	[51]

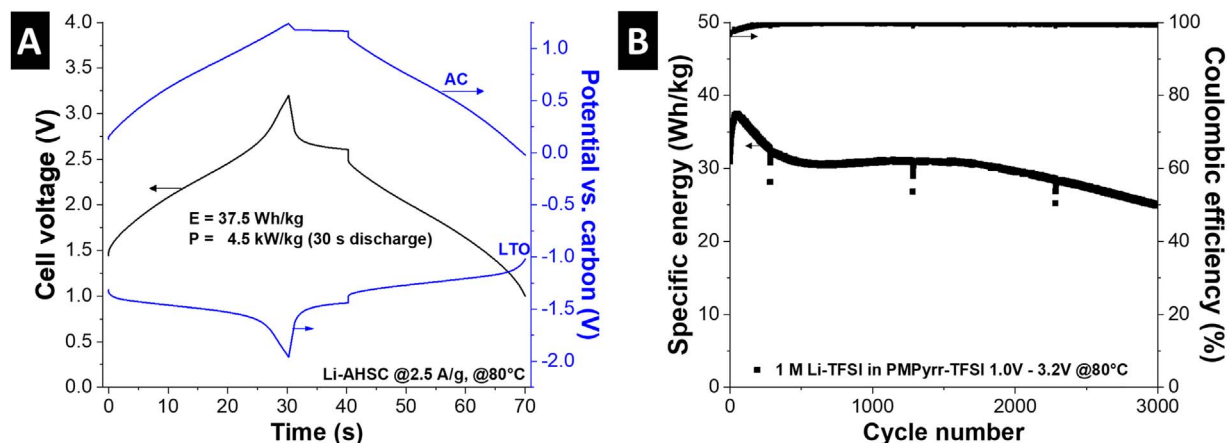


Fig. 4. High temperature operation. (A) Voltage profile of 50th cycle of a Li-AHSC cell cycled between 3.2 V and 1 V cell voltage at 2.5 A/g at a temperature of 80 °C. (B) Corresponding specific energy and Coulombic efficiency over 3000 cycles under these conditions.

4.5 kW/kg, corresponding to a discharge time of 30 s, with an energy efficiency of 77.4% and Coulombic efficiency of 98.2% (Fig. 4A). Stability testing was carried out at the same rate and in the same voltage window for over 3000 cycles, with a retention of 80% of the initial value (Fig. 4B, Fig. S8A). When cycling at a lower rate of 0.1 A/g, the cell voltage is reduced to 2.8 V, resulting in a specific energy of 71 Wh/kg at a power of 190 W/kg (Fig. S8B-C). To the best of our knowledge, no comparable hybrid supercapacitor cell that combines a Faradaic intercalation electrode with a capacitive electrode was shown to exhibit stable behavior at such a high temperature. The performance stability further underlines the promising performance of the Li-AHSC cell at elevated temperatures. By further improvement of the electrolyte formulation, for example, by creation of eutectic mixtures of ionic liquids [54,55] or mixing with organic solvent [56], even low temperature operation could be enabled for this AHSC cell concept in the future.

4. Conclusions

In conclusion, we prepared ionic liquid electrolytes with dissolved lithium- and sodium-salt, respectively, and applied them for the first time in an asymmetric hybrid supercapacitor cell employing ion intercalation at the negative electrode (LTO) and double-layer formation at the positive electrode (AC). After evaluation of half-cell performance, a successful transfer to full-cells was achieved and both the lithium- and the sodium-ion AHSC cells were operated at 4 V up to 1500 cycles with only minor capacity fading. The maximum specific energy of Li-AHSC cells was about 100 Wh/kg, while the maximum specific power was about 2 kW/kg. Na-AHSC cells showed similar values with slightly reduced specific energy. Finally, Li-AHSC cells were shown for the first time to exhibit stable behavior at a high temperature of 80 °C for more than 3000 cycles at a high rate, exhibiting up to 38 Wh/kg at high power of 4.5 kW/kg.

We believe that the presented approach is particularly promising as it combines all virtues of ILs synergistically in one cell concept. ILs expand the stability window for the positive electrode, giving access to larger cell voltages, as we showed by enabling 4 V for LTO-based AHSC devices. The demonstrated possibility of high-temperature operation in combination with the non-flammability of the device is important for many applications including the mobility sector, where mass, volume, and cost of cooling systems and impact-safe housing could be reduced. The viability of this novel cell concept was demonstrated for different alkali ion systems by using only commercially available materials. Thus, there is great potential for further improvement, for example, by use of more advanced electrode materials that can increase energy, power, and longevity, or the exploration of further ILs or their mixtures with organic solvents or further additives.

Acknowledgments

We acknowledge funding from the German Federal Ministry for Economic Affairs and Energy (BMWi) in support of the HyBaCap project (award number 03ET6113C). We thank Eduard Arzt for his continuing support, and Mesut Aslan and Pattarachai Srimuk (all INM) for discussions and technical support.

Declaration of interests

The authors declare no competing interests.

Supplemental information

The supplemental information includes supplemental materials characterization, Supplemental electrochemical characterization and supplemental experimental procedures.

Appendix A. Supporting information

Supplementary data associated with this article can be found in the online version at doi:10.1016/j.ensm.2018.06.011.

References

- [1] P. Simon, Y. Gogotsi, Materials for electrochemical capacitors, *Nat. Mater.* 7 (2008) 845–854.
- [2] S. Fleischmann, A. Tolosa, V. Presser, Design of carbon/metal oxide hybrids for electrochemical energy storage, *Chem. - Eur. J.* (2018). <http://dx.doi.org/10.1002/chem.201800772>.
- [3] S. Fleischmann, N. Jäckel, M. Zeiger, B. Krüner, I. Grobelsek, P. Formanek, S. Choudhury, D. Weingarth, V. Presser, Enhanced electrochemical energy storage by nanoscopic decoration of endohedral and exohedral carbon with vanadium oxide via atomic layer deposition, *Chem. Mater.* 28 (2016) 2802–2813.
- [4] S. Fleischmann, D. Leistenschneider, V. Lemkova, B. Krüner, M. Zeiger, L. Borchardt, V. Presser, Tailored mesoporous carbon/vanadium pentoxide hybrid electrodes for high power pseudocapacitive lithium and sodium intercalation, *Chem. Mater.* 29 (2017) 8653–8662.
- [5] S. Boukhalfa, K. Evanoff, G. Yushin, Atomic layer deposition of vanadium oxide on carbon nanotubes for high-power supercapacitor electrodes, *Energy Environ. Sci.* 5 (2012) 6872–6879.
- [6] J. Lee, B. Krüner, A. Tolosa, S. Sathyamoorthi, D. Kim, S. Choudhury, K.H. Seo, V. Presser, Tin/vanadium redox electrolyte for battery-like energy storage capacity combined with supercapacitor-like power handling, *Energy Environ. Sci.* 9 (2016) 3392–3398.
- [7] J. Lee, A. Tolosa, B. Krüner, N. Jäckel, S. Fleischmann, M. Zeiger, D. Kim, V. Presser, Asymmetric tin-vanadium redox electrolyte for hybrid energy storage with nanoporous carbon electrodes, *Sustain. Energy Fuels* 1 (2017) 299–307.
- [8] E. Mourad, L. Coustan, P. Lannelongue, D. Zigah, A. Mehdi, A. Vioux, S.A. Freunberger, F. Favier, O. Fontaine, Biredox ionic liquids with solid-like redox density in the liquid state for high-energy supercapacitors, *Nat. Mater.* 16 (2017) 446.
- [9] N. Böckenfeld, R.-S. Kühnel, S. Passerini, M. Winter, A. Balducci, Composite LiFePO₄/AC high rate performance electrodes for Li-ion capacitors, *J. Power Sources* 196 (2011) 4136–4142.
- [10] D. Cericola, P. Novák, A. Wokaun, R. Kötz, Hybridization of electrochemical capacitors and rechargeable batteries: an experimental analysis of the different possible approaches utilizing activated carbon, Li₄Ti₅O₁₂ and LiMn₂O₄, *J. Power Sources* 196 (2011) 10305–10313.
- [11] M. Widmaier, N. Jäckel, M. Zeiger, M. Abuzarli, C. Engel, L. Bommer, V. Presser, Influence of carbon distribution on the electrochemical performance and stability of lithium titanate based energy storage devices, *Electrochim. Acta* 247 (2017) 1006–1018.
- [12] G.G. Amatucci, F. Badway, A. Du Pasquier, T. Zheng, An asymmetric hybrid nonaqueous energy storage cell, *J. Electrochem. Soc.* 148 (2001) A930–A939.
- [13] W. Zuo, R. Li, C. Zhou, Y. Li, J. Xia, J. Liu, Battery-supercapacitor hybrid devices: recent progress and future prospects, *Adv. Sci.* 4 (2017) 1600539.
- [14] F. Béguin, V. Presser, A. Balducci, E. Frackowiak, Carbons and electrolytes for advanced supercapacitors, *Adv. Mater.* 26 (2014) 2219–2251.
- [15] J. Ding, H. Wang, Z. Li, K. Cui, D. Karpuzov, X. Tan, A. Kohandehghan, D. Mitlin, Peanut shell hybrid sodium ion capacitor with extreme energy–power rivals lithium ion capacitors, *Energy Environ. Sci.* 8 (2015) 941–955.
- [16] X. Wang, S. Kajiyama, H. Iinuma, E. Hosono, S. Oro, I. Moriguchi, M. Okubo, A. Yamada, Pseudocapacitance of MXene nanosheets for high-power sodium-ion hybrid capacitors, *Nat. Commun.* 6 (2015) 6544.
- [17] J. Yin, L. Qi, H. Wang, Sodium titanate nanotubes as negative electrode materials for sodium-ion capacitors, *ACS Appl. Mater. Interfaces* 4 (2012) 2762–2768.
- [18] P. Jeżowski, O. Crosnier, E. Deunf, P. Poizot, F. Béguin, T. Brousse, Safe and recyclable lithium-ion capacitors using sacrificial organic lithium salt, *Nat. Mater.* 17 (2017) 167.
- [19] S. Dsoke, B. Fuchs, E. Gucciardi, M. Wohlfahrt-Mehrens, The importance of the electrode mass ratio in a Li-ion capacitor based on activated carbon and Li₄Ti₅O₁₂, *J. Power Sources* 282 (2015) 385–393.
- [20] T. Zhang, B. Fuchs, M. Secchiarioli, M. Wohlfahrt-Mehrens, S. Dsoke, Electrochemical behavior and stability of a commercial activated carbon in various organic electrolyte combinations containing Li-salts, *Electrochim. Acta* 218 (2016) 163–173.
- [21] P. Verma, P. Maire, P. Novák, A review of the features and analyses of the solid electrolyte interphase in Li-ion batteries, *Electrochim. Acta* 55 (2010) 6332–6341.
- [22] S. Sivakumar, A. Pandolfo, Evaluation of lithium-ion capacitors assembled with pre-lithiated graphite anode and activated carbon cathode, *Electrochim. Acta* 65 (2012) 280–287.
- [23] K. Xu, Nonaqueous liquid electrolytes for lithium-based rechargeable batteries, *Chem. Rev.* 104 (2004) 4303–4418.
- [24] K. Naoi, S. Ishimoto, Y. Isobe, S. Aoyagi, High-rate nano-crystalline Li₄Ti₅O₁₂ attached on carbon nano-fibers for hybrid supercapacitors, *J. Power Sources* 195 (2010) 6250–6254.
- [25] K. Naoi, S. Ishimoto, J.-i Miyamoto, W. Naoi, Second generation 'nanohybrid supercapacitor': evolution of capacitive energy storage devices, *Energy Environ. Sci.* 5 (2012) 9363–9373.
- [26] M. Salanne, B. Rotenberg, K. Naoi, K. Kaneko, P.-L. Taberna, C. Grey, B. Dunn, P. Simon, Efficient storage mechanisms for building better supercapacitors, *Nat. Energy* 1 (2016) 16070.
- [27] V. Khomenko, E. Raymundo-Piñero, F. Béguin, High-energy density graphite/AC capacitor in organic electrolyte, *J. Power Sources* 177 (2008) 643–651.
- [28] M. Armand, F. Endres, D.R. MacFarlane, H. Ohno, B. Scrosati, Ionic-liquid materials for the electrochemical challenges of the future, *Nat. Mater.* 8 (2009) 621–629.
- [29] D.R. MacFarlane, N. Tachikawa, M. Forsyth, J.M. Pringle, P.C. Howlett, G.D. Elliott, J.H. Davis, M. Watanabe, P. Simon, C.A. Angell, Energy applications of ionic liquids, *Energy Environ. Sci.* 7 (2014) 232–250.
- [30] C. Largeot, P. Taberna, Y. Gogotsi, P. Simon, Microporous carbon-based electrical double layer capacitor operating at high temperature in ionic liquid electrolyte, *Electrochem. Solid-State Lett.* 14 (2011) A174–A176.
- [31] T. Mendes, F. Zhou, A.J. Barlow, M. Forsyth, P.C. Howlett, D. MacFarlane, An ionic liquid based sodium metal-hybrid supercapacitor-battery, *Sustain. Energy Fuels* 2 (2018) 763–771.
- [32] S. Rothermel, P. Meister, G. Schmuelling, O. Fromm, H.-W. Meyer, S. Nowak, M. Winter, T. Placke, Dual-graphite cells based on the reversible intercalation of bis (trifluoromethanesulfonyl) imide anions from an ionic liquid electrolyte, *Energy Environ. Sci.* 7 (2014) 3412–3423.
- [33] T. Yamamoto, T. Nohira, R. Hagiwara, A. Fukunaga, S. Sakai, K. Nitta, S. Inazawa, Charge–discharge behavior of tin negative electrode for a sodium secondary battery using intermediate temperature ionic liquid sodium bis (fluorosulfonyl) amide–potassium bis (fluorosulfonyl) amide, *J. Power Sources* 217 (2012) 479–484.
- [34] K. Beltrop, S. Beuker, A. Heckmann, M. Winter, T. Placke, Alternative electrochemical energy storage: potassium-based dual-graphite batteries, *Energy Environ. Sci.* 10 (2017) 2090–2094.
- [35] D. Weingarth, M. Zeiger, N. Jäckel, M. Aslan, G. Feng, V. Presser, Graphitization as a universal tool to tailor the potential-dependent capacitance of carbon supercapacitors, *Adv. Energy Mater.* 4 (2014) 1400316.
- [36] D. Weingarth, A. Foelske-Schmitz, A. Wokaun, R. Kötz, PTFE bound activated carbon—A quasi-reference electrode for ionic liquids, *Electrochem. Commun.* 18 (2012) 116–118.
- [37] K. Xu, S.P. Ding, T.R. Jow, Toward reliable values of electrochemical stability limits for electrolytes, *J. Electrochem. Soc.* 146 (1999) 4172–4178.
- [38] D. Weingarth, H. Noh, A. Foelske-Schmitz, A. Wokaun, R. Kötz, A reliable determination method of stability limits for electrochemical double layer capacitors, *Electrochim. Acta* 103 (2013) 119–124.
- [39] A. Eftekhari, Energy efficiency: a critically important but neglected factor in battery research, *Sustain. Energy Fuels* 1 (2017) 2053–2060.
- [40] S. Fleischmann, M. Zeiger, A. Quade, A. Kruth, V. Presser, Atomic layer deposited molybdenum oxide/carbon nanotube hybrid electrodes: influence of crystal structure on lithium-ion capacitor performance, *ACS Appl. Mater. Interfaces* 10 (2018) 18675–18684.
- [41] P. Reale, A. Ferriccola, B. Scrosati, Compatibility of the Py₂₄TFSI–LiTFSI ionic liquid solution with Li₄Ti₅O₁₂ and LiFePO₄ lithium ion battery electrodes, *J. Power Sources* 194 (2009) 182–189.
- [42] T. Ohzuku, A. Ueda, N. Yamamoto, Zero-strain insertion material of Li[Li_{1/3}Ti_{5/3}]O₄ for rechargeable lithium cells, *J. Electrochem. Soc.* 142 (1995) 1431–1435.
- [43] N. Yabuuchi, K. Kubota, M. Dahbi, S. Komaba, Research development on sodium-ion batteries, *Chem. Rev.* 114 (2014) 11636–11682.
- [44] Y. Sun, L. Zhao, H. Pan, X. Lu, L. Gu, Y.-S. Hu, H. Li, M. Armand, Y. Ikuhara, L. Chen, Direct atomic-scale confirmation of three-phase storage mechanism in Li₄Ti₅O₁₂ anodes for room-temperature sodium-ion batteries, *Nat. Commun.* 4 (2013) 1870.
- [45] M. Kitta, K. Kuratani, M. Tabuchi, N. Takeichi, T. Akita, T. Kiyobayashi, M. Kohyama, Irreversible structural change of a spinel Li₄Ti₅O₁₂ particle via Na insertion-extraction cycles of a sodium-ion battery, *Electrochim. Acta* 148 (2014) 175–179.
- [46] G. Hasegawa, K. Kanamori, T. Kiyomura, H. Kurata, K. Nakanishi, T. Abe, Hierarchically porous Li₄Ti₅O₁₂ anode materials for Li- and Na-ion batteries: effects of nanoarchitectural design and temperature dependence of the rate capability, *Adv. Energy Mater.* 5 (2015).
- [47] S. Komaba, W. Murata, T. Ishikawa, N. Yabuuchi, T. Ozeki, T. Nakayama, A. Ogata, K. Gotoh, K. Fujiwara, Electrochemical Na insertion and solid electrolyte interphase for hard-carbon electrodes and application to Na-ion batteries, *Adv. Funct. Mater.* 21 (2011) 3859–3867.
- [48] L.Y. Yang, H.Z. Li, J. Liu, S.S. Tang, Y.K. Lu, S. Te Li, J. Min, N. Yan, M. Lei, Li₄Ti₅O₁₂ nanosheets as high-rate and long-life anode materials for sodium-ion batteries, *J. Mater. Chem. A* 3 (2015) 24446–24452.
- [49] M.D. Slater, D. Kim, E. Lee, C.S. Johnson, Sodium-ion batteries, *Adv. Funct. Mater.* 23 (2013) 947–958.
- [50] C. Chen, Y. Wen, X. Hu, X. Ji, M. Yan, L. Mai, P. Hu, B. Shan, Y. Huang, Na⁺ intercalation pseudocapacitance in graphene-coupled titanium oxide enabling ultra-fast sodium storage and long-term cycling, *Nat. Commun.* 6 (2015).
- [51] Z. Le, F. Liu, P. Nie, X. Li, X. Liu, Z. Bian, G. Chen, H.B. Wu, Y. Lu, Pseudocapacitive sodium storage in mesoporous single-crystal-like TiO₂-graphene nanocomposite enables high-performance sodium-ion capacitors, *ACS Nano* 11 (2017) 2952–2960.

- [52] S. Dong, L. Shen, H. Li, P. Nie, Y. Zhu, Q. Sheng, X. Zhang, Pseudocapacitive behaviours of $\text{Na}_2\text{Ti}_3\text{O}_7$ @CNT coaxial nanocables for high-performance sodium-ion capacitors, *J. Mater. Chem. A* 3 (2015) 21277–21283.
- [53] A. Balducci, R. Dugas, P.-L. Taberna, P. Simon, D. Plee, M. Mastragostino, S. Passerini, High temperature carbon–carbon supercapacitor using ionic liquid as electrolyte, *J. Power Sources* 165 (2007) 922–927.
- [54] R. Lin, P.-L. Taberna, S. Fantini, V. Presser, C.R. Pérez, F. Malbosc, N.L. Rupasinghe, K.B. Teo, Y. Gogotsi, P. Simon, Capacitive energy storage from–50 to 100 C using an ionic liquid electrolyte, *J. Phys. Chem. Lett.* 2 (2011) 2396–2401.
- [55] W.-Y. Tsai, R. Lin, S. Murali, L.L. Zhang, J.K. McDonough, R.S. Ruoff, P.-L. Taberna, Y. Gogotsi, P. Simon, Outstanding performance of activated graphene based supercapacitors in ionic liquid electrolyte from–50 to 80 C, *Nano Energy* 2 (2013) 403–411.
- [56] V. Ruiz, T. Huynh, S. Sivakkumar, A. Pandolfo, Ionic liquid–solvent mixtures as supercapacitor electrolytes for extreme temperature operation, *RSC Adv.* 2 (2012) 5591–5598.

1. Supplemental material characterization

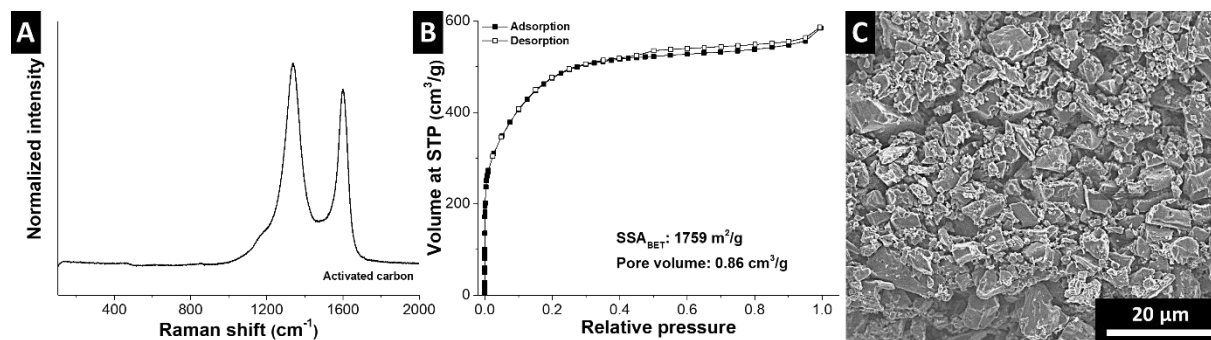


Fig. S1: (A) Raman spectrum and (B) nitrogen sorption isotherm and (C) scanning electron micrograph of AC electrodes. Replotted from Ref. [1].

Table S1: Properties of PMPyrr-TFSI as given by the supplier.

Ionic liquid	Viscosity	Conductivity
PMPyrr-TFSI	58.7 cP at 25 °C	4.924 mS/cm at 30 °C

2. Supplemental electrochemical data

2.1 Half-cell data: Activated carbon

To choose a suitable ionic liquid for our study, we evaluated the stability limits of various ionic liquids by so-called R-value testing,[2] [3] which calculates the number of parasitic reactions; an R-value above 0.1 is defined as a non-stable behavior. The results for PMPyrr-TFSI are depicted in **Fig. S2**, where an anodic stability limit of about +2 V vs. carbon is determined.

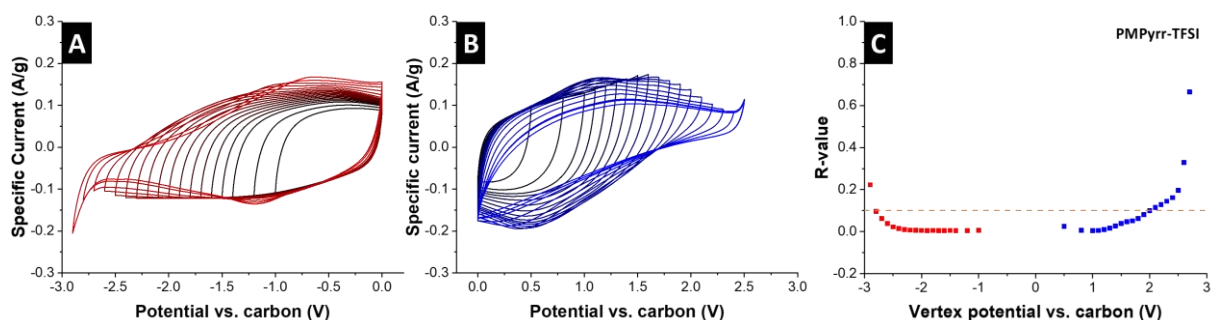


Fig. S2: (A) Cathodic stability test at 1 mV/s, (B) anodic stability test at 1 mV/s, and (C) calculated R-values for PMPyrr-TFSI electrolyte.

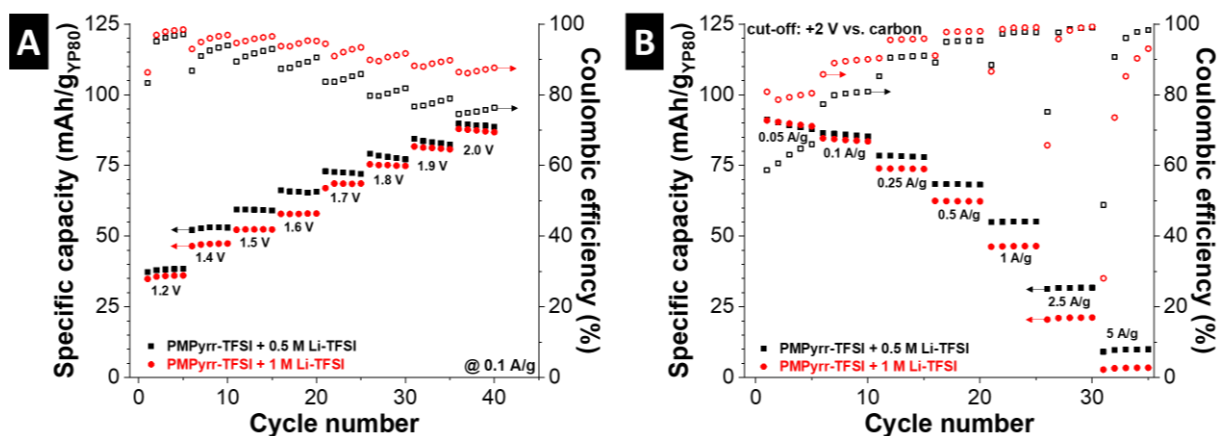


Fig. S3: (A) Testing anodic stability between +1.2 V and +2.0 V vs. carbon and (B) rate handling at rates from 50 mA/g to 5 A/g in 0.5 M and 1.0 M Li-TFSI in PMPyrr-TFSI electrolytes.

2.2 Half-cell data: Lithium titanate electrodes

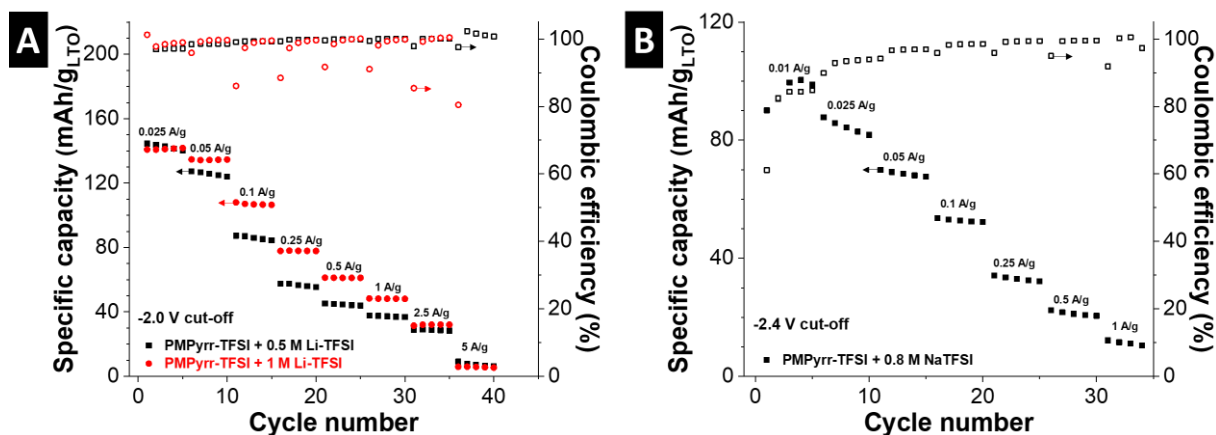


Fig. S4: (A) Rate handling from galvanostatic cycling between 0 V and -2.0 V vs. carbon from 25 mA/g to 5 A/g for Li-TFSI electrolytes and (B) rate handling from galvanostatic cycling between 0 V and -2.4 V vs. carbon from 10 mA/g to 1 A/g for Na-TFSI electrolytes, including corresponding Coulombic efficiency.

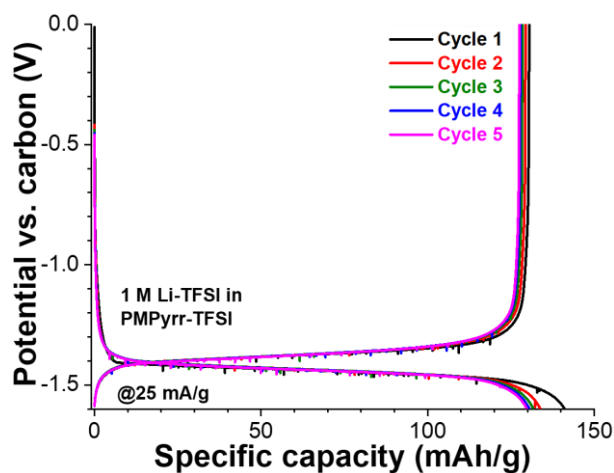


Fig. S5: Comparison of first 5 galvanostatic cycles in 1 M Li-TFSI in PMPyrr-TFSI electrolyte at a specific current of 25 mA/g.

2.3 AHSC full-cells

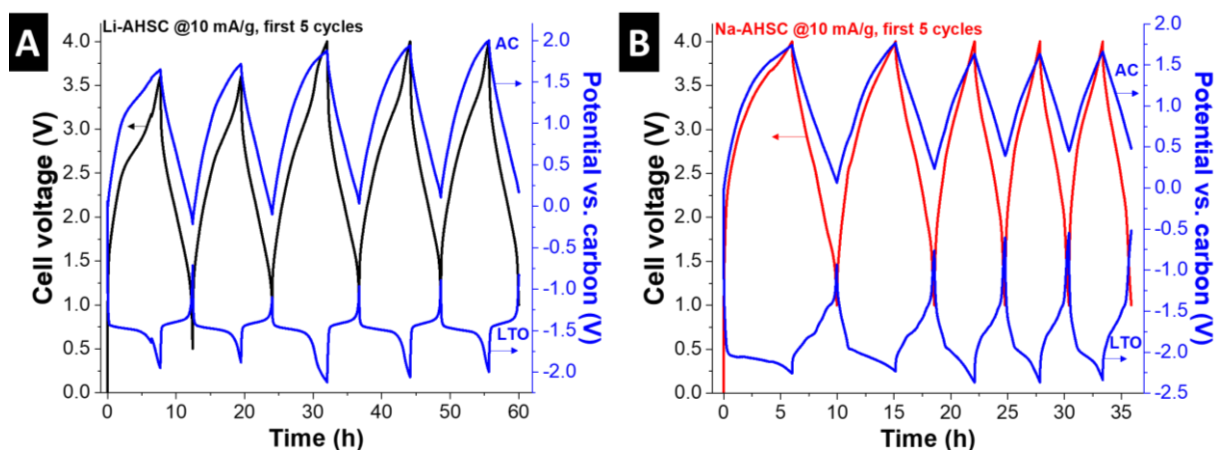


Fig. S6: Voltage profiles of first 5 galvanostatic cycles at 10 mA/g for (A) Li-AHSC cell and (B) Na-AHSC cell including potential development at negative and positive electrodes monitored via activated carbon quasi-reference electrode.

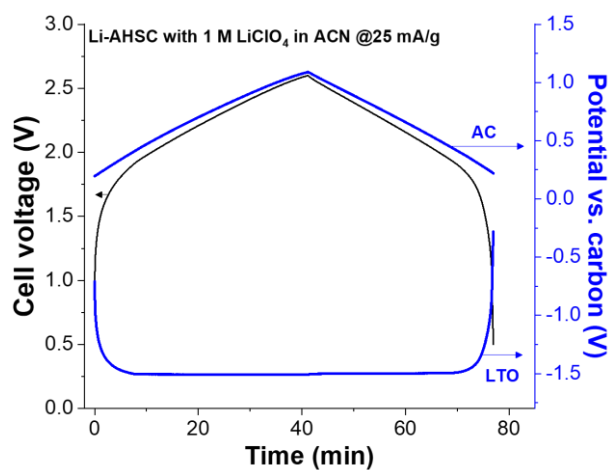


Fig. S7: Voltage profile of AHSC cell assembled the same way as described Li-AHSC cells, using 1 M LiClO₄ in acetonitrile electrolyte and not an IL-based electrolyte. Potential development is monitored by activated carbon spectator quasi-reference electrode.

2.4 High temperature operation

For measurements of Li-AHSC cells at 80 °C, we limited the maximum cell voltage to 3.2 V for stable cycling over 3,000 cycles at 2.5 A/g. The first three cycles are shown in **Fig. S8A**. The AC electrode mass of this cell was increased by a factor of 1.76 compared to LTO. When cycling at 80 °C with lower rates between 0.05 A/g and 0.5 A/g (**Fig. S8B-C**), the AC mass was increased by a factor of 2.3 compared to LTO to balance the higher capacity of LTO at lower rates. Also, the maximum cell voltage was decreased to 2.8 V (for 0.05 A/g and 0.1 A/g) or to 3.0 V (for 0.25 A/g and 0.5 A/g) to stay within the stable potential range of +1.2 V vs. carbon for the AC electrode at this temperature.

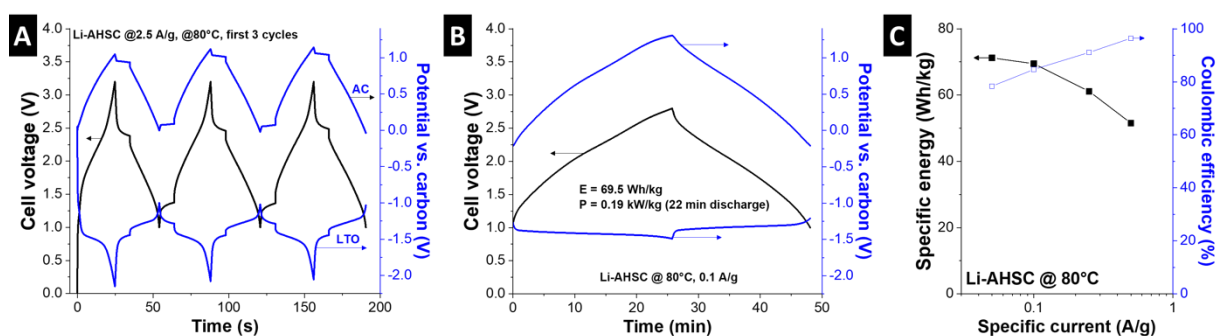


Fig. S8: Voltage profiles of (A) first 3 galvanostatic cycles at 2.5 A/g for the stability test and (B) a profile at 0.1 A/g for Li-AHSC cell at 80 °C including potential development at negative and positive electrodes monitored via activated carbon quasi-reference electrode. (C) Rate-handling plot of Li-AHSC cell at 80 °C at rates between 0.05 A/g and 0.5 A/g, including values of the Coulombic efficiency.

Supplemental References

- [1] S. Fleischmann, N. Jäckel, M. Zeiger, B. Krüner, I. Grobelsek, P. Formanek, S. Choudhury, D. Weingarh, V. Presser, Enhanced electrochemical energy storage by nanoscopic decoration of endohedral and exohedral carbon with vanadium oxide via atomic layer deposition, *Chem. Mater.* 28 (2016) 2802-2813.
- [2] D. Weingarh, H. Noh, A. Foelske-Schmitz, A. Wokaun, R. Kötz, A reliable determination method of stability limits for electrochemical double layer capacitors, *Electrochim. Acta* 103 (2013) 119-124.
- [3] K. Xu, S. P. Ding, T. R. Jow, Toward reliable values of electrochemical stability limits for electrolytes, *J. Electrochem. Soc.* 146 (1999) 4172-4178.

5 Conclusions and outlook

My PhD work has investigated and developed an optimized concept for the design of hybrid materials and hybrid supercapacitor cell architectures. As the main tool for materials synthesis, atomic layer deposition was employed. It allowed synthesizing materials with well-defined properties to investigate fundamental structural and electrochemical aspects of carbon/metal oxide hybrid materials. Specifically, ALD synthesis allowed to investigate (1) the influence of carbon substrate porosity, (2) targeted manipulation of the metal oxide crystal structure by doping with various amounts of foreign atoms, and (3) post-deposition annealing to adjust the metal oxide oxidation states. As a more economical and easier scalable method, I further explored the hydrothermal synthesis of carbon onion/vanadium oxide hybrid materials, and the properties were compared to conventionally fabricated composite electrode materials. All synthesized hybrid materials were used as Faradaic electrodes in hybrid supercapacitor cells, and valuable insights were gained concerning the material requirements that result in high energy, power, efficiency, and longevity of the devices. With the gathered knowledge, a fundamentally new hybrid supercapacitor cell concept was developed that relied on a novel ionic liquid electrolyte formulation.

We found that desired properties for a carbon substrate used for hybrid material synthesis should be prioritized in this order:^{15, 110}

1. Choosing reactant-accessible pore sizes, according to the chosen synthesis method, to avoid any pore blocking and increased diffusion paths at high metal oxide mass loadings. For ALD, the limiting pore size is around 2 nm, pores above 2-3 nm are accessible for coating.
2. Maximizing the specific surface area, enabling thin coatings, small diffusion paths, and large electrode-electrolyte interfaces to promote pseudocapacitive charge storage characteristics.
3. Preferring open, internal pores that confine the metal oxide coating, prevent particle coarsening during thermal annealing, and mitigate disintegration during prolonged cycling.
4. Preferring carbons with high structural ordering for enhanced electrical conductivity.

Following these design guidelines, it was possible to especially tailor a mesoporous carbon substrate with internal pores. Depositing various amounts of vanadium oxide via ALD, it was shown that the lithium intercalation properties were superior compared to other substrates

in terms of maximum capacity and rate handling. The mesoporous carbon/vanadium oxide hybrid materials also enabled highly stable, pseudocapacitive intercalation of larger sodium atoms at high rates, which was traced back to the homogeneously distributed vanadium oxide domains locally confined in the mesopores. These materials were among the most stable sodium intercalation hosts reported so far in literature.¹⁰² Future work should include the use of mesoporous carbon substrates for other Faradaic materials that experience large volume expansion during cycling (such as materials exhibiting alloying or conversion chemistries), as the mesopore confinement shows promise to prevent disintegration of the material.

During hybridization, carbon is already present during the formation of the Faradaic metal oxide component. In classic battery research, the Faradaic material is synthesized separately, and a conducting carbon is mechanically mixed afterward to obtain a composite electrode. Hydrothermal synthesis is a way for large-scale and economical production of Faradaic material. The impact of hybridization was analyzed by comparing the hydrothermal synthesis of vanadium oxide with either carbon onions present during synthesis or by adding them afterward. The hybrid approach yielded a highly intergrown network of carbon onions and vanadium oxide, whereas post-synthesis addition of carbon onions led to clustering of the separate components. The study systematically demonstrated that hybridization offers an enhanced rate handling for lithium intercalation compared to the composite approach. Also, the intercalation behavior can be tuned from pseudocapacitive to battery-like potential profiles depending on the amount of carbon onion substrate added during the synthesis, since the nucleation behavior of vanadium oxide is affected. In situ electrochemical dilatometry revealed that different macroscopic expansion behavior of vanadium oxide relates to the charge storage mechanisms: pseudocapacitive = small expansion, battery-like = large expansion.¹⁵² This study demonstrated the simplicity of scale-up for the hybrid material approach, making it of potential interest for large-scale applications.

While the choice of the carbon substrate primarily affected the power and cycling stability of the material, the maximum charge storage capacity is mainly determined by the ion intercalation capacity of the Faradaic material. Capitalizing on the cyclic character of ALD, alternating stacks of vanadium oxide and titanium oxide were deposited on carbon onions. By closely packing atomic layers of vanadium oxide and titanium oxide in alternating sequences, a post-deposition annealing step incorporated up to 50 % Ti into the monoclinic VO₂ lattice. The replacement of vanadium by slightly larger titanium atoms led to an expansion of the VO₂

unit cell, which resulted in an almost doubled lithium intercalation capacity compared to pure VO_2 or TiO_2 coatings.¹³⁸ In this first study on the electrochemical intercalation properties of mixed metal oxides synthesized by ALD, the large potential of this synthesis technique for mixed metal oxides in EES applications was revealed. It introduces the possibility to obtain mixed metal oxides at much higher precision and with increased contents of foreign atoms compared to other synthesis paths. That way, crystallographic changes can be selectively introduced, and charge storage properties can be improved. In the future, this approach is of particular promise for the use of larger and/or multivalent intercalation ions "beyond lithium", such as sodium, potassium, or magnesium, as it allows to adjust the lattice parameters to "fit" the desired ion. Future studies need to include simulations to predict optimized compositions and mixtures of different Faradaic materials.

Thermal annealing after the ALD process allows tuning of the metal oxide crystal structure. Carbon nanotube/molybdenum oxide hybrids were fabricated by ALD and annealed in both synthetic air or argon to obtain orthorhombic MoO_3 or monoclinic MoO_2 , respectively. Used as anodes in hybrid supercapacitor cells, the hybrid materials caused vastly different electrochemical properties of the cell. It was demonstrated that especially the high rate handling capability and small overpotential between lithiation and delithiation reaction of the carbon nanotube/ MoO_2 hybrid material was the determining factor to enable the most favorable full-cell performance. Though MoO_3 provided the higher initial capacity, its slower kinetics prohibited a high energy efficiency of the hybrid supercapacitor cell.¹²² The study demonstrated the importance of fast charge storage kinetics of the Faradaic material on the resulting cell performance, especially concerning energy efficiency values, being the determining factor for an economically viable transfer to the application. Crystal growth during post-deposition annealing led to relatively large MoO_2 particles (up to 100 nm) within the entangled carbon nanotube network of the hybrid material. Future studies should include the use of more optimized carbon substrates that may prevent particle coarsening, as smaller domain sizes could lead to improved power performances of the MoO_2 /carbon hybrid material in the hybrid supercapacitor setup.

Finally, lithium- and sodium-containing ionic liquid electrolytes were used in hybrid supercapacitors with an LTO anode and an activated carbon cathode. With this study, we made use of all virtues of ionic liquids to have a transformative impact on state-of-the-art hybrid supercapacitor technology:⁴³ (1) For the first time, a hybrid supercapacitor cell with an

LTO anode showed stable operation at 4 V without the need of any prelithiation and circumventing the formation of the solid electrolyte interphase. This was due to the expansion of the electrochemical stability window at the activated carbon cathode compared to conventional organic electrolytes. (2) The approach is universally adaptable as it was demonstrated for lithium- and sodium-intercalating hybrid supercapacitor setups, using only commercially available electrode materials. Using more advanced electrodes, such as hybrid materials presented earlier in this thesis, further performance improvement is expected for this cell setup. (3) High-temperature operation of hybrid supercapacitors up to 80 °C was enabled for the first time, and the cell safety was significantly enhanced because of use of a non-flammable electrolyte, which is particularly important for applications in the mobility sector. This new and innovative cell design holds high potential for further improvement, as the study only included non-optimized, commercially available materials as a proof-of-concept. Further work needs to include the use of hybrid materials as the anode material, which will further enhance the power of the hybrid supercapacitor cell. Also, the composition of the ionic liquid electrolyte needs to be improved either by variation of the ionic liquid itself, mixtures of different ionic liquids, or mixtures of ionic liquids with different solvents such as carbonates or water.

References

1. *Adoption of the Paris Agreement*, FCCC/CP/2015/L9/Rev.1 (UNFCCC, 2015).
2. G. A. Meehl, W. M. Washington, W. D. Collins, J. M. Arblaster, A. Hu, L. E. Buja, W. G. Strand and H. Teng, *How much more global warming and sea level rise?*, *Science*, **2005**, 307, 1769-1772.
3. L. Hughes, *Biological consequences of global warming: is the signal already apparent?*, *Trends in ecology & evolution*, **2000**, 15, 56-61.
4. D. R. Easterling, G. A. Meehl, C. Parmesan, S. A. Changnon, T. R. Karl and L. O. Mearns, *Climate extremes: observations, modeling, and impacts*, *science*, **2000**, 289, 2068-2074.
5. I. P. o. C. Change, *Climate Change 2013: The Physical Science Basis. Contribution of Working Group I to the Fifth Assessment Report on the Intergovernmental Panel on Climate Change*, Cambridge Univ. Press, 2013.
6. M. Meinshausen, N. Meinshausen, W. Hare, S. C. Raper, K. Frieler, R. Knutti, D. J. Frame and M. R. Allen, *Greenhouse-gas emission targets for limiting global warming to 2 °C*, *Nature*, **2009**, 458, 1158.
7. S. I. Seneviratne, M. G. Donat, A. J. Pitman, R. Knutti and R. L. Wilby, *Allowable CO₂ emissions based on regional and impact-related climate targets*, *Nature*, **2016**, 529, 477.
8. J. Huang, H. Yu, A. Dai, Y. Wei and L. Kang, *Drylands face potential threat under 2 °C global warming target*, *Nature Climate Change*, **2017**, 7, 417.
9. H. S. Baker, R. J. Millar, D. J. Karoly, U. Beyerle, B. P. Guillod, D. Mitchell, H. Shiogama, S. Sparrow, T. Woollings and M. R. Allen, *Higher CO₂ concentrations increase extreme event risk in a 1.5 °C world*, *Nature Climate Change*, **2018**, 1.
10. Z. Yang, J. Zhang, M. C. Kintner-Meyer, X. Lu, D. Choi, J. P. Lemmon and J. Liu, *Electrochemical Energy Storage for Green Grid*, *Chem. Rev.*, **2011**, 111, 3577-3613.
11. B. Dunn, H. Kamath and J.-M. Tarascon, *Electrical energy storage for the grid: a battery of choices*, *Science*, **2011**, 334, 928-935.
12. F. Béguin, V. Presser, A. Balducci and E. Frackowiak, *Carbons and electrolytes for advanced supercapacitors*, *Adv. Mater.*, **2014**, 26, 2219-2251.
13. H. Chen, T. N. Cong, W. Yang, C. Tan, Y. Li and Y. Ding, *Progress in electrical energy storage system: A critical review*, *Progress in Natural Science*, **2009**, 19, 291-312.
14. M. R. Lukatskaya, B. Dunn and Y. Gogotsi, *Multidimensional materials and device architectures for future hybrid energy storage*, *Nat. Commun.*, **2016**, 7, 12647.
15. S. Fleischmann, A. Tolosa and V. Presser, *Design of carbon/metal oxide hybrids for electrochemical energy storage*, *Chem. - Eur. J.*, **2018**, DOI: 10.1002/chem.201800772.
16. P. Simon and Y. Gogotsi, *Materials for electrochemical capacitors*, *Nat. Mater.*, **2008**, 7, 845-854.
17. H. v. Helmholtz, *Ueber einige Gesetze der Vertheilung elektrischer Ströme in körperlichen Leitern, mit Anwendung auf die thierisch-elektrischen Versuche (Schluss.)*, *Annalen der Physik*, **1853**, 165, 353-377.
18. D. Qu and H. Shi, *Studies of activated carbons used in double-layer capacitors*, *J. Power Sources*, **1998**, 74, 99-107.
19. H. Shi, *Activated carbons and double layer capacitance*, *Electrochim. Acta*, **1996**, 41, 1633-1639.

20. B. Hu, K. Wang, L. Wu, S. H. Yu, M. Antonietti and M. M. Titirici, *Engineering carbon materials from the hydrothermal carbonization process of biomass*, *Adv. Mater.*, **2010**, 22, 813-828.
21. D. Montané, V. Fierro, J.-F. Marêché, L. Aranda and A. Celzard, *Activation of biomass-derived charcoal with supercritical water*, *Microporous Mesoporous Mater.*, **2009**, 119, 53-59.
22. N. Jäckel, D. Weingarth, M. Zeiger, M. Aslan, I. Grobelsek and V. Presser, *Comparison of carbon onions and carbon blacks as conductive additives for carbon supercapacitors in organic electrolytes*, *J. Power Sources*, **2014**, 272, 1122-1133.
23. K. S. Sing, *Reporting physisorption data for gas/solid systems with special reference to the determination of surface area and porosity (Recommendations 1984)*, *Pure Appl. Chem.*, **1985**, 57, 603-619.
24. N. Jäckel, D. Weingarth, A. Schreiber, B. Krüner, M. Zeiger, A. Tolosa, M. Aslan and V. Presser, *Performance Evaluation of Conductive Additives for Activated Carbon Supercapacitors in Organic Electrolyte*, *Electrochim. Acta*, **2016**, 191, 284–298.
25. R. Saliger, U. Fischer, C. Herta and J. Fricke, *High surface area carbon aerogels for supercapacitors*, *J. Non-Cryst. Solids*, **1998**, 225, 81-85.
26. O. Barbieri, M. Hahn, A. Herzog and R. Kötz, *Capacitance limits of high surface area activated carbons for double layer capacitors*, *Carbon*, **2005**, 43, 1303-1310.
27. J. Chmiola, G. Yushin, Y. Gogotsi, C. Portet, P. Simon and P.-L. Taberna, *Anomalous increase in carbon capacitance at pore sizes less than 1 nanometer*, *Science*, **2006**, 313, 1760-1763.
28. J. Chmiola, C. Largeot, P. L. Taberna, P. Simon and Y. Gogotsi, *Desolvation of Ions in Subnanometer Pores and Its Effect on Capacitance and Double-Layer Theory*, *Angew. Chem.*, **2008**, 120, 3440-3443.
29. T. A. Centeno, O. Sereda and F. Stoeckli, *Capacitance in Carbon Pores of 0.7 to 15 nm: A Regular Pattern*, *PCCP*, **2011**, 13, 12403-12406.
30. N. Jäckel, M. Rodner, A. Schreiber, J. Jeongwook, M. Zeiger, M. Aslan, D. Weingarth and V. Presser, *Anomalous or Regular Capacitance? The Influence of Pore Size Dispersity on Double-Layer Formation*, *J. Power Sources*, **2016**, 326, 660-671.
31. N. Jäckel, P. Simon, Y. Gogotsi and V. Presser, *The increase in capacitance by subnanometer pores in carbon*, *ACS Energy Lett.*, **2016**, 1, 1262-1265.
32. J. Huang, B. G. Sumpter and V. Meunier, *Theoretical model for nanoporous carbon supercapacitors*, *Angew. Chem. Int. Ed.*, **2008**, 47, 520-524.
33. J. Huang, B. G. Sumpter and V. Meunier, *A universal model for nanoporous carbon supercapacitors applicable to diverse pore regimes, carbon materials, and electrolytes*, *Chem. - Eur. J.*, **2008**, 14, 6614-6626.
34. J. Huang, B. G. Sumpter, V. Meunier, G. Yushin, C. Portet and Y. Gogotsi, *Curvature Effects in Carbon Nanomaterials: Exohedral versus Endohedral Supercapacitors*, *J. Mater. Res.*, **2010**, 25, 1525-1531.
35. M. D. Stoller, C. W. Magnuson, Y. Zhu, S. Murali, J. W. Suk, R. Piner and R. S. Ruoff, *Interfacial capacitance of single layer graphene*, *Energy Environ. Sci.*, **2011**, 4, 4685-4689.
36. L. L. Zhang, R. Zhou and X. Zhao, *Graphene-based materials as supercapacitor electrodes*, *J. Mater. Chem.*, **2010**, 20, 5983-5992.
37. J. K. McDonough, A. I. Frolov, V. Presser, J. Niu, C. H. Miller, T. Ubieto, M. V. Fedorov and Y. Gogotsi, *Influence of the structure of carbon onions on their electrochemical performance in supercapacitor electrodes*, *Carbon*, **2012**, 50, 3298-3309.

38. D. Pech, M. Brunet, H. Durou, P. Huang, V. Mochalin, Y. Gogotsi, P.-L. Taberna and P. Simon, *Ultrahigh-Power Micrometre-Sized Supercapacitors Based on Onion-Like Carbon*, *Nat. Nanotechnol.*, **2010**, 5, 651-654.
39. M. Zeiger, N. Jäckel, V. N. Mochalin and V. Presser, *Review: Carbon Onions for Electrochemical Energy Storage*, *J. Mater. Chem. A*, **2016**, 4, 3172-3196.
40. E. Frackowiak, K. Jurewicz, S. Delpoux and F. Beguin, *Nanotubular Materials for Supercapacitors*, *J. Power Sources*, **2001**, 97, 822-825.
41. E. Frackowiak, K. Metenier, V. Bertagna and F. Beguin, *Supercapacitor electrodes from multiwalled carbon nanotubes*, *Appl. Phys. Lett.*, **2000**, 77, 2421-2423.
42. M. Zeiger, N. Jäckel, D. Weingarth and V. Presser, *Vacuum or Flowing Argon: What is the Best Synthesis Atmosphere for Nanodiamond-Derived Carbon Onions for Supercapacitor Electrodes?*, *Carbon*, **2015**, 94, 507-517.
43. S. Fleischmann, M. Widmaier, A. Schreiber, H. Shim, F. M. Stiemke, T. J. Schubert and V. Presser, *High voltage asymmetric hybrid supercapacitors using lithium-and sodium-containing ionic liquids*, *Energy Storage Materials*, **2019**, 16, 391-399.
44. A. Burke, *Ultracapacitors: why, how, and where is the technology*, *J. Power Sources*, **2000**, 91, 37-50.
45. L. Demarconnay, E. Raymundo-Piñero and F. Béguin, *A symmetric carbon/carbon supercapacitor operating at 1.6 V by using a neutral aqueous solution*, *Electrochem. Commun.*, **2010**, 12, 1275-1278.
46. M. Bichat, E. Raymundo-Piñero and F. Béguin, *High voltage supercapacitor built with seaweed carbons in neutral aqueous electrolyte*, *Carbon*, **2010**, 48, 4351-4361.
47. K. Fic, G. Lota, M. Meller and E. Frackowiak, *Novel insight into neutral medium as electrolyte for high-voltage supercapacitors*, *Energy Environ. Sci.*, **2012**, 5, 5842-5850.
48. Q. Gao, L. Demarconnay, E. Raymundo-Piñero and F. Béguin, *Exploring the large voltage range of carbon/carbon supercapacitors in aqueous lithium sulfate electrolyte*, *Energy Environ. Sci.*, **2012**, 5, 9611-9617.
49. M. Ue, *Chemical capacitors and quaternary ammonium salts*, *Electrochemistry*, **2007**, 75, 565-572.
50. M. Arulepp, L. Permann, J. Leis, A. Perkson, K. Rumma, A. Jänes and E. Lust, *Influence of the solvent properties on the characteristics of a double layer capacitor*, *J. Power Sources*, **2004**, 133, 320-328.
51. M. Armand, F. Endres, D. R. MacFarlane, H. Ohno and B. Scrosati, *Ionic-liquid materials for the electrochemical challenges of the future*, *Nat. Mater.*, **2009**, 8, 621-629.
52. A. Balducci, W. A. Henderson, M. Mastragostino, S. Passerini, P. Simon and F. Soavi, *Cycling stability of a hybrid activated carbon//poly(3-methylthiophene) supercapacitor with N-butyl-N-methylpyrrolidinium bis(trifluoromethanesulfonyl) imide ionic liquid as electrolyte*, *Electrochim. Acta*, **2005**, 50, 2233-2237.
53. V. L. Martins and R. M. Torresi, *Ionic liquids in electrochemical energy storage*, *Current Opinion in Electrochemistry*, **2018**.
54. A. Balducci, R. Dugas, P.-L. Taberna, P. Simon, D. Plee, M. Mastragostino and S. Passerini, *High temperature carbon-carbon supercapacitor using ionic liquid as electrolyte*, *J. Power Sources*, **2007**, 165, 922-927.
55. D. R. MacFarlane, N. Tachikawa, M. Forsyth, J. M. Pringle, P. C. Howlett, G. D. Elliott, J. H. Davis, M. Watanabe, P. Simon and C. A. Angell, *Energy applications of ionic liquids*, *Energy Environ. Sci.*, **2014**, 7, 232-250.
56. N. Jäckel, S. Patrick Emge, B. Krüner, B. Roling and V. Presser, *Quantitative information about electrosorption of ionic liquids in carbon nanopores from electrochemical*

- dilatometry and quartz crystal microbalance measurements*, J. Phys. Chem. C, **2017**, 121, 19120-19128.
57. K. L. Van Aken, M. Beidaghi and Y. Gogotsi, *Formulation of Ionic-Liquid Electrolyte To Expand the Voltage Window of Supercapacitors*, Angew. Chem. Int. Ed., **2015**, 54, 4806-4809.
 58. R. Lin, P.-L. Taberna, S. Fantini, V. Presser, C. R. Pérez, F. Malbosc, N. L. Rupesinghe, K. B. Teo, Y. Gogotsi and P. Simon, *Capacitive energy storage from -50 to 100 °C using an ionic liquid electrolyte*, The Journal of Physical Chemistry Letters, **2011**, 2, 2396-2401.
 59. M. Armand and J.-M. Tarascon, *Building better batteries*, Nature, **2008**, 451, 652.
 60. A. Volta, *On the electricity excited by the mere contact of conducting substances of different kinds. In a letter from Mr. Alexander Volta, FRS Professor of Natural Philosophy in the University of Pavia, to the Rt. Hon. Sir Joseph Banks, Bart. KBPRS*, Philosophical transactions of the Royal Society of London, **1800**, 403-431.
 61. M. S. Whittingham, *Electrical energy storage and intercalation chemistry*, Science, **1976**, 192, 1126-1127.
 62. K. Mizushima, P. Jones, P. Wiseman and J. B. Goodenough, *Li_xCoO₂ (0<x<1): A new cathode material for batteries of high energy density*, Mater. Res. Bull., **1980**, 15, 783-789.
 63. G.-A. Nazri and G. Pistoia, *Lithium batteries: science and technology*, Springer Science & Business Media, 2008.
 64. B. Scrosati and J. Garche, *Lithium batteries: Status, prospects and future*, J. Power Sources, **2010**, 195, 2419-2430.
 65. J.-M. Tarascon and M. Armand, *Issues and challenges facing rechargeable lithium batteries*, Nature, **2001**, 414, 359-367.
 66. Y. Qi and S. J. Harris, *In situ observation of strains during lithiation of a graphite electrode*, J. Electrochem. Soc., **2010**, 157, A741-A747.
 67. J. B. Goodenough and K.-S. Park, *The Li-ion rechargeable battery: a perspective*, J. Am. Chem. Soc., **2013**, 135, 1167-1176.
 68. P. Verma, P. Maire and P. Novák, *A review of the features and analyses of the solid electrolyte interphase in Li-ion batteries*, Electrochim. Acta, **2010**, 55, 6332-6341.
 69. J. Besenhard, M. Winter, J. Yang and W. Biberacher, *Filming mechanism of lithium-carbon anodes in organic and inorganic electrolytes*, J. Power Sources, **1995**, 54, 228-231.
 70. K. Xu, *Nonaqueous liquid electrolytes for lithium-based rechargeable batteries*, Chem. Rev., **2004**, 104, 4303-4418.
 71. T. Ohzuku, A. Ueda and N. Yamamoto, *Zero-strain insertion material of Li[Li_{1/3}Ti_{5/3}]O₄ for rechargeable lithium cells*, J. Electrochem. Soc., **1995**, 142, 1431-1435.
 72. E. Zhao, C. Qin, H.-R. Jung, G. Berdichevsky, A. Nese, S. Marder and G. Yushin, *Lithium Titanate Confined in Carbon Nanopores for Asymmetric Supercapacitors*, ACS Nano, **2016**, 10, 3977-3984.
 73. N. Nitta, F. Wu, J. T. Lee and G. Yushin, *Li-ion battery materials: present and future*, Mater. Today, **2015**, 18, 252-264.
 74. J. N. Reimers and J. Dahn, *Electrochemical and in situ X-ray diffraction studies of lithium intercalation in Li_xCoO₂*, J. Electrochem. Soc., **1992**, 139, 2091-2097.
 75. C. K. Chan, H. Peng, G. Liu, K. McIlwrath, X. F. Zhang, R. A. Huggins and Y. Cui, in *Materials for Sustainable Energy: A Collection of Peer-Reviewed Research and Review Articles from Nature Publishing Group*, World Scientific, 2011, pp. 187-191.
 76. X. Ji and L. F. Nazar, *Advances in Li-S batteries*, J. Mater. Chem., **2010**, 20, 9821-9826.

77. P. G. Bruce, S. A. Freunberger, L. J. Hardwick and J.-M. Tarascon, *Li-O₂ and Li-S batteries with high energy storage*, Nat. Mater., **2012**, 11, 19.
78. N. S. Choi, Z. Chen, S. A. Freunberger, X. Ji, Y. K. Sun, K. Amine, G. Yushin, L. F. Nazar, J. Cho and P. G. Bruce, *Challenges facing lithium batteries and electrical double-layer capacitors*, Angew. Chem. Int. Ed., **2012**, 51, 9994-10024.
79. A. Eftekhari, *Energy efficiency: A critically important but neglected factor in battery research*, Sustainable Energy Fuels, **2017**, 1, 2053-2060.
80. B. E. Conway, *Electrochemical supercapacitors: scientific fundamentals and technological applications*, Springer Science & Business Media, 2013.
81. S. Ardizzone, G. Fregonara and S. Trasatti, "Inner" and "outer" active surface of RuO₂ electrodes, Electrochim. Acta, **1990**, 35, 263-267.
82. J. Zheng, P. Cygan and T. Jow, *Hydrous ruthenium oxide as an electrode material for electrochemical capacitors*, J. Electrochem. Soc., **1995**, 142, 2699-2703.
83. H. Y. Lee and J. B. Goodenough, *Supercapacitor behavior with KCl electrolyte*, J. Solid State Chem., **1999**, 144, 220-223.
84. M. Toupin, T. Brousse and D. Bélanger, *Charge storage mechanism of MnO₂ electrode used in aqueous electrochemical capacitor*, Chem. Mater., **2004**, 16, 3184-3190.
85. J.-G. Wang, F. Kang and B. Wei, *Engineering of MnO₂-based nanocomposites for high-performance supercapacitors*, Prog. Mater. Sci., **2015**, 74, 51-124.
86. B. Conway, V. Birss and J. Wojtowicz, *The role and utilization of pseudocapacitance for energy storage by supercapacitors*, J. Power Sources, **1997**, 66, 1-14.
87. J. W. Kim, V. Augustyn and B. Dunn, *The effect of crystallinity on the rapid pseudocapacitive response of Nb₂O₅*, Adv. Energy Mat., **2012**, 2, 141-148.
88. A. Tolosa, B. Krüner, S. Fleischmann, N. Jäckel, M. Zeiger, M. Aslan, I. Grobelsek and V. Presser, *Niobium carbide nanofibers as a versatile precursor for high power supercapacitor and high energy battery electrodes*, J. Mater. Chem. A, **2016**, 4, 16003-16016.
89. V. Augustyn, J. Come, M. A. Lowe, J. W. Kim, P.-L. Taberna, S. H. Tolbert, H. D. Abruna, P. Simon and B. Dunn, *High-rate electrochemical energy storage through Li⁺ intercalation pseudocapacitance*, Nat. Mater., **2013**, 12, 518-522.
90. T. Brezesinski, J. Wang, S. H. Tolbert and B. Dunn, *Ordered mesoporous [alpha]-MoO₃ with iso-oriented nanocrystalline walls for thin-film pseudocapacitors*, Nat. Mater., **2010**, 9, 146-151.
91. V. Augustyn, P. Simon and B. Dunn, *Pseudocapacitive Oxide Materials for High-Rate Electrochemical Energy Storage*, Energy Environ. Sci., **2014**, 7, 1597-1614.
92. P. Srimuk, F. Kaasik, B. Krüner, A. Tolosa, S. Fleischmann, N. Jäckel, M. C. Tekeli, M. Aslan, M. E. Suss and V. Presser, *MXene as a novel intercalation-type pseudocapacitive cathode and anode for capacitive deionization*, J. Mater. Chem. A, **2016**, 4, 18265-18271.
93. P. Srimuk, J. Lee, S. Fleischmann, S. Choudhury, N. Jäckel, M. Zeiger, C. Kim, M. Aslan and V. Presser, *Faradaic deionization of brackish and sea water via pseudocapacitive cation and anion intercalation into few-layered molybdenum disulfide*, J. Mater. Chem. A, **2017**, 5, 15640-15649.
94. N. Shpigel, M. D. Levi, S. Sigalov, T. S. Mathis, Y. Gogotsi and D. Aurbach, *Direct assessment of nano-confined water in 2D Ti₃C₂ (MXene) electrode interspaces by a surface acoustic technique*, J. Am. Chem. Soc., **2018**.
95. P. Simon, Y. Gogotsi and B. Dunn, *Where Do Batteries End and Supercapacitors Begin?*, Science Magazine, **2014**, 343, 1210-1211.

96. T. Brousse, D. Bélanger and J. W. Long, *To be or not to be pseudocapacitive?*, J. Electrochem. Soc., **2015**, 162, A5185-A5189.
97. Q. Jiang, N. Kurra, M. Alhabeb, Y. Gogotsi and H. N. Alshareef, *All Pseudocapacitive MXene-RuO₂ Asymmetric Supercapacitors*, Adv. Energy Mat., **2018**, 8, 1703043.
98. M. Okubo, E. Hosono, J. Kim, M. Enomoto, N. Kojima, T. Kudo, H. Zhou and I. Honma, *Nanosize effect on high-rate Li-ion intercalation in LiCoO₂ electrode*, J. Am. Chem. Soc., **2007**, 129, 7444-7452.
99. S. Boukhalifa, K. Evanoff and G. Yushin, *Atomic layer deposition of vanadium oxide on carbon nanotubes for high-power supercapacitor electrodes*, Energy Environ. Sci., **2012**, 5, 6872-6879.
100. H.-S. Kim, J. B. Cook, H. Lin, J. S. Ko, S. H. Tolbert, V. Ozolins and B. Dunn, *Oxygen vacancies enhance pseudocapacitive charge storage properties of MoO_{3-x}*, Nat. Mater., **2016**, 16, 454-460.
101. H. Lindström, S. Södergren, A. Solbrand, H. Rensmo, J. Hjelm, A. Hagfeldt and S.-E. Lindquist, *Li⁺ ion insertion in TiO₂ (anatase). 2. Voltammetry on nanoporous films*, J. Phys. Chem. B, **1997**, 101, 7717-7722.
102. S. Fleischmann, D. Leistenschneider, V. Lemkova, B. Krüner, M. Zeiger, L. Borchardt and V. Presser, *Tailored mesoporous carbon/vanadium pentoxide hybrid electrodes for high power pseudocapacitive lithium and sodium intercalation*, Chem. Mater., **2017**, 29, 8653-8662.
103. D. M. Anjos, J. K. McDonough, E. Perre, G. M. Brown, S. H. Overbury, Y. Gogotsi and V. Presser, *Pseudocapacitance and Performance Stability of Quinone-Coated Carbon Onions*, Nano Energy, **2013**, 2, 702-712.
104. T. C. Liu, W. Pell, B. Conway and S. Roberson, *Behavior of molybdenum nitrides as materials for electrochemical capacitors comparison with ruthenium oxide*, J. Electrochem. Soc., **1998**, 145, 1882-1888.
105. J. Wang, J. Polleux, J. Lim and B. Dunn, *Pseudocapacitive Contributions to Electrochemical Energy Storage in TiO₂ (Anatase) Nanoparticles*, J. Phys. Chem. C, **2007**, 111, 14925-14931.
106. M. Opitz, J. Yue, J. Wallauer, B. Smarsly and B. Roling, *Mechanisms of charge storage in nanoparticulate TiO₂ and Li₄Ti₅O₁₂ anodes: new insights from scan rate-dependent cyclic voltammetry*, Electrochim. Acta, **2015**, 168, 125-132.
107. D. Dubal, O. Ayyad, V. Ruiz and P. Gómez-Romero, *Hybrid energy storage: the merging of battery and supercapacitor chemistries*, Chem. Soc. Rev., **2015**, 44, 1777-1790.
108. J. J. Vilatela and D. Eder, *Nanocarbon composites and hybrids in sustainability: a review*, ChemSusChem, **2012**, 5, 456-478.
109. M. Kerlau, M. Marcinek, V. Srinivasan and R. M. Kostecky, *Studies of local degradation phenomena in composite cathodes for lithium-ion batteries*, Electrochim. Acta, **2007**, 52, 5422-5429.
110. S. Fleischmann, N. Jäckel, M. Zeiger, B. Krüner, I. Grobelsek, P. Formanek, S. Choudhury, D. Weingarh and V. Presser, *Enhanced electrochemical energy storage by nanoscopic decoration of endohedral and exohedral carbon with vanadium oxide via atomic layer deposition*, Chem. Mater., **2016**, 28, 2802-2813.
111. G. G. Amatucci, F. Badway, A. Du Pasquier and T. Zheng, *An asymmetric hybrid nonaqueous energy storage cell*, J. Electrochem. Soc., **2001**, 148, A930-A939.
112. V. Khomenko, E. Raymundo-Piñero and F. Béguin, *High-energy density graphite/AC capacitor in organic electrolyte*, J. Power Sources, **2008**, 177, 643-651.

113. T. Aida, K. Yamada and M. Morita, *An advanced hybrid electrochemical capacitor that uses a wide potential range at the positive electrode*, *Electrochem. Solid-State Lett.*, **2006**, 9, A534-A536.
114. V. Khomenko, E. Raymundo-Pinero and F. Béguin, *Optimisation of an asymmetric manganese oxide/activated carbon capacitor working at 2 V in aqueous medium*, *J. Power Sources*, **2006**, 153, 183-190.
115. J. Yan, Z. Fan, W. Sun, G. Ning, T. Wei, Q. Zhang, R. Zhang, L. Zhi and F. Wei, *Advanced asymmetric supercapacitors based on Ni(OH)₂/graphene and porous graphene electrodes with high energy density*, *Adv. Funct. Mater.*, **2012**, 22, 2632-2641.
116. S. Sivakkumar and A. Pandolfo, *Evaluation of lithium-ion capacitors assembled with pre-lithiated graphite anode and activated carbon cathode*, *Electrochim. Acta*, **2012**, 65, 280-287.
117. P. Jeżowski, O. Crosnier, E. Deunf, P. Poizot, F. Béguin and T. Brousse, *Safe and recyclable lithium-ion capacitors using sacrificial organic lithium salt*, *Nat. Mater.*, **2017**, 17, 167.
118. K. Xu, S. P. Ding and T. R. Jow, *Toward reliable values of electrochemical stability limits for electrolytes*, *J. Electrochem. Soc.*, **1999**, 146, 4172-4178.
119. D. Weingarh, H. Noh, A. Foelske-Schmitz, A. Wokaun and R. Kötz, *A reliable determination method of stability limits for electrochemical double layer capacitors*, *Electrochim. Acta*, **2013**, 103, 119-124.
120. W. G. Pell and B. E. Conway, *Peculiarities and requirements of asymmetric capacitor devices based on combination of capacitor and battery-type electrodes*, *J. Power Sources*, **2004**, 136, 334-345.
121. E. Lim, C. Jo and J. Lee, *A Mini Review of Designed Mesoporous Materials for Energy-Storage Applications: From Electric Double-Layer Capacitors to Hybrid Supercapacitors*, *Nanoscale*, **2016**, 8, 7827-7833.
122. S. Fleischmann, M. Zeiger, A. Quade, A. Kruth and V. Presser, *Atomic layer deposited molybdenum oxide/carbon nanotube hybrid electrodes: Influence of crystal structure on lithium-ion capacitor performance*, *ACS Appl. Mater. Interfaces*, **2018**, 10, 18675-18684.
123. R. L. Puurunen, *Surface chemistry of atomic layer deposition: A case study for the trimethylaluminum/water process*, *J. Appl. Phys.*, **2005**, 97, 9.
124. M. Groner, J. Elam, F. Fabreguette and S. M. George, *Electrical characterization of thin Al₂O₃ films grown by atomic layer deposition on silicon and various metal substrates*, *Thin Solid Films*, **2002**, 413, 186-197.
125. Y. J. Lee, *Low-impurity, highly conformal atomic layer deposition of titanium nitride using NH₃-Ar-H₂ plasma treatment for capacitor electrodes*, *Mater. Lett.*, **2005**, 59, 615-617.
126. J. Musschoot, Q. Xie, D. Deduytsche, S. Van den Berghe, R. L. Van Meirhaeghe and C. Detavernier, *Atomic layer deposition of titanium nitride from TDMAT precursor*, *Microelectron. Eng.*, **2009**, 86, 72-77.
127. B. S. Lim, A. Rahtu and R. G. Gordon, *Atomic layer deposition of transition metals*, *Nat. Mater.*, **2003**, 2, 749.
128. H. Kim, *Atomic layer deposition of metal and nitride thin films: Current research efforts and applications for semiconductor device processing*, *Journal of Vacuum Science & Technology B: Microelectronics and Nanometer Structures Processing, Measurement, and Phenomena*, **2003**, 21, 2231-2261.

129. M. Mattinen, T. Hatanpää, T. Sarnet, K. Mizohata, K. Meinander, P. J. King, L. Khriachtchev, J. Räisänen, M. Ritala and M. Leskelä, *Atomic Layer Deposition of Crystalline MoS₂ Thin Films: New Molybdenum Precursor for Low-Temperature Film Growth*, *Advanced Materials Interfaces*, **2017**, 4, 1700123.
130. S. Shin, Z. Jin, D. H. Kwon, R. Bose and Y.-S. Min, *High turnover frequency of hydrogen evolution reaction on amorphous MoS₂ thin film directly grown by atomic layer deposition*, *Langmuir*, **2015**, 31, 1196-1202.
131. H. G. Kim and H.-B.-R. Lee, *Atomic Layer Deposition on 2D Materials*, *Chem. Mater.*, **2017**, 29, 3809-3826.
132. T. Suntola.
133. S. M. George, *Atomic Layer Deposition: An Overview*, *Chem. Rev.*, **2009**, 110, 111-131.
134. R. W. Johnson, A. Hultqvist and S. F. Bent, *A brief review of atomic layer deposition: from fundamentals to applications*, *Mater. Today*, **2014**, 17, 236-246.
135. D. B. Farmer and R. G. Gordon, *ALD of high- κ dielectrics on suspended functionalized SWNTs*, *Electrochem. Solid-State Lett.*, **2005**, 8, G89-G91.
136. K. Kim, R. W. Johnson, J. T. Tanskanen, N. Liu, M.-G. Kim, C. Pang, C. Ahn, S. F. Bent and Z. Bao, *Selective metal deposition at graphene line defects by atomic layer deposition*, *Nat. Commun.*, **2014**, 5.
137. D. B. Farmer and R. G. Gordon, *Atomic layer deposition on suspended single-walled carbon nanotubes via gas-phase noncovalent functionalization*, *Nano Lett.*, **2006**, 6, 699-703.
138. S. Fleischmann, A. Tolosa, M. Zeiger, B. Krüner, N. J. Peter, I. Grobelsek, A. Quade, A. Kruth and V. Presser, *Vanadia–Titania Multilayer Nanodecoration of Carbon Onions via Atomic Layer Deposition for High Performance Electrochemical Energy Storage*, *J. Mater. Chem. A*, **2017**, 5, 2792-2801.
139. T. Suntola, *Handbook of Crystal Growth 3*, Thin films and Epitaxy, Part B: Growth, **1994**.
140. J. Aarik, A. Aidla, T. Uustare, M. Ritala and M. Leskelä, *Titanium isopropoxide as a precursor for atomic layer deposition: characterization of titanium dioxide growth process*, *Appl. Surf. Sci.*, **2000**, 161, 385-395.
141. J. W. Elam, N. P. Dasgupta and F. B. Prinz, *ALD for clean energy conversion, utilization, and storage*, *MRS Bull.*, **2011**, 36, 899-906.
142. D. M. Mattox, *Handbook of physical vapor deposition (PVD) processing*, William Andrew, 2010.
143. K. Choy, *Chemical vapour deposition of coatings*, *Prog. Mater. Sci.*, **2003**, 48, 57-170.
144. X. Wang and G. Yushin, *Chemical vapor deposition and atomic layer deposition for advanced lithium ion batteries and supercapacitors*, *Energy Environ. Sci.*, **2015**, 8, 1889-1904.
145. J. R. Bakke, K. L. Pickrahn, T. P. Brennan and S. F. Bent, *Nanoengineering and interfacial engineering of photovoltaics by atomic layer deposition*, *Nanoscale*, **2011**, 3, 3482-3508.
146. J. P. C. Baena, L. Steier, W. Tress, M. Saliba, S. Neutzner, T. Matsui, F. Giordano, T. J. Jacobsson, A. R. S. Kandada and S. M. Zakeeruddin, *Highly efficient planar perovskite solar cells through band alignment engineering*, *Energy Environ. Sci.*, **2015**, 8, 2928-2934.
147. S. Albrecht, M. Saliba, J. P. C. Baena, F. Lang, L. Kegelmann, M. Mews, L. Steier, A. Abate, J. Rappich and L. Korte, *Monolithic perovskite/silicon-heterojunction tandem solar cells processed at low temperature*, *Energy Environ. Sci.*, **2016**, 9, 81-88.

148. J. H. Shim, C.-C. Chao, H. Huang and F. B. Prinz, *Atomic layer deposition of yttria-stabilized zirconia for solid oxide fuel cells*, Chem. Mater., **2007**, 19, 3850-3854.
149. Y. S. Jung, A. S. Cavanagh, L. A. Riley, S. H. Kang, A. C. Dillon, M. D. Groner, S. M. George and S. H. Lee, *Ultrathin direct atomic layer deposition on composite electrodes for highly durable and safe Li-ion batteries*, Adv. Mater., **2010**, 22, 2172-2176.
150. A. C. Kozen, C.-F. Lin, A. J. Pearse, M. A. Schroeder, X. Han, L. Hu, S.-B. Lee, G. W. Rubloff and M. Noked, *Next-generation lithium metal anode engineering via atomic layer deposition*, ACS Nano, **2015**, 9, 5884-5892.
151. M. Yu, A. Wang, F. Tian, H. Song, Y. Wang, C. Li, J.-D. Hong and G. Shi, *Dual-protection of a graphene-sulfur composite by a compact graphene skin and an atomic layer deposited oxide coating for a lithium-sulfur battery*, Nanoscale, **2015**, 7, 5292-5298.
152. S. Fleischmann, M. Zeiger, N. Jäckel, B. Krüner, V. Lemkova, M. Widmaier and V. Presser, *Tuning pseudocapacitive and battery-like lithium intercalation in vanadium dioxide/carbon onion hybrids for asymmetric supercapacitor anodes*, J. Mater. Chem. A, **2017**, 5, 13039-13051.